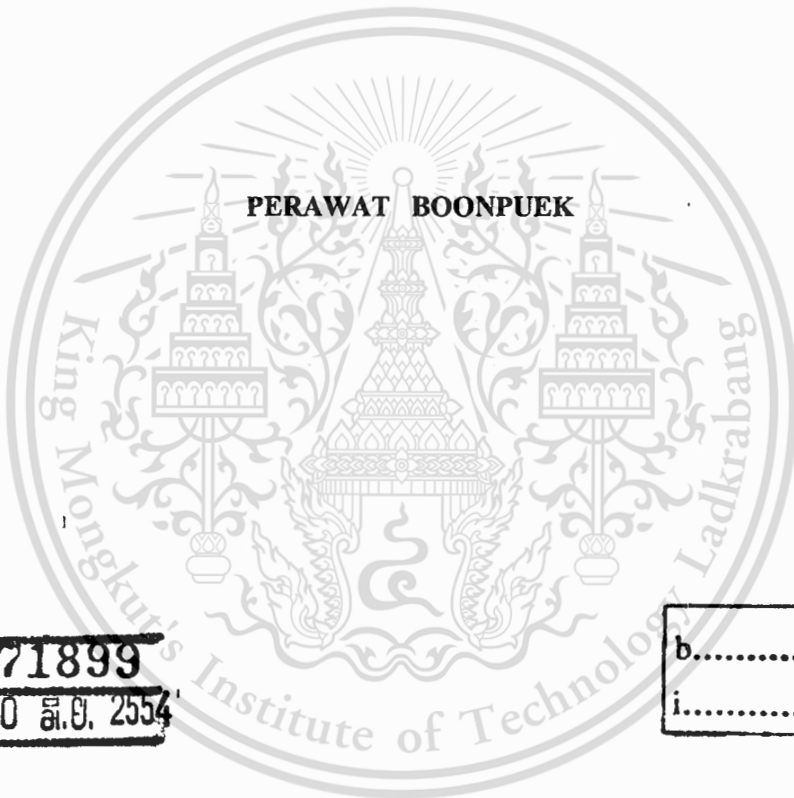


สำนักหอสมุดกลาง พระจอมเกล้าลาดกระบัง

FLOW STRESS DETERMINATION OF STEEL TUBE  
FOR HYDROFORMABILITY EVALUATION



E071899



สาขา.....  
เลขทะเบียน..... 71899  
วันเดือนปี 30 ส.ย. 2554

b.....
i.....

A THESIS SUBMITTED IN PARTIAL FULFILLMENT  
OF THE REQUIREMENT FOR THE DEGREE OF MASTER  
OF ENGINEERING IN AUTOMOTIVE ENGINEERING  
(INTERNATIONAL PROGRAM)  
INTERNATIONAL COLLEGE  
KING MONGKUT'S INSTITUTE OF TECHNOLOGY LADKRABANG

2011

KMITL-2011-IC-M-004-001



**COPYRIGHT 2011**

**INTERNATIONAL COLLEGE**

**KING MONGKUT'S INSTITUTE OF TECHNOLOGY LADKRABANG**

**NATIONAL SCIENCE AND TECNHLOGY DEVELOPMENT AGENCY**

This material is reserved for educational use only, not allowed for commercial use.

Forbidden to modify the content, and cite the document when use.

<b>Thesis Title</b>	Flow Stress Determination of Steel Tube for Hydroformability Evaluation
<b>Student</b>	Mr. Perawat Boonpuek
<b>Student ID</b>	51061913
<b>Degree</b>	Master of Engineering
<b>Program</b>	Automotive Engineering (International Program)
<b>Year</b>	2011
<b>Thesis Advisor</b>	Asst. Prof. Dr. Nattawut Depaiwa
<b>Thesis Coordinate Advisor</b>	Prof. Dr. Naoto Ohtake
<b>Thesis Coordinate Advisor</b>	Dr. Suwat Jirathearanat
<b>Thesis Reference Number</b>	KMITL-2011-IC-M-004-001

### ABSTRACT

This research aims to determine flow stress of steel tube by using hydraulic bulge test. A developed SPB analytical model for analyzing bulge shapes of hydroformed tubes is postulated. Bulge test apparatus is specially designed by using FEA simulation of hydroformability evaluation, and then manufactured for use in the hydraulic bulge test. STKM 11A steel tube, outside diameter = 28.6 mm and thickness = 1.2 mm, is used for the free bulge test. Test tubes are deformed under a biaxial stress state. Bulge heights and internal pressures are continuously measured during experimentation. Tube thicknesses at vertex of the bulge shapes are measured by a dial caliper gauge. Bulge shape curvature and contact points are measured by taking digital photos of the bulge shapes combined with measurement methods in CAD software. Effective stress - strain relationships are obtained from the developed SPB analytical model using those measured values. Flow stress curves obtained from the effective stress – strain relationships are compared with those by YingYot's model, Hwang's model and a tensile test. FEA methods are used to conduct simulation of tube hydroforming using those flow stress curves obtained. The predicted internal pressures versus the bulge heights and the tube thicknesses are compared with the experimental results. The flow stress curve obtained from stress-strain relation at Neck Point of the hydroformed tube is determined.

## ACKNOWLEDGEMENT

This research would not be complete without the assistance and financial support from academic affiliation. I would like to express my appreciation to them.

Firstly, I would like to sincerely thank Asst. Prof. Dr. Nattawut Depaiwa and Prof. Dr. Naoto Ohtake who are a thesis advisor and a coordinate advisor from TAIST Tokyo Tech program, King Mongkut's Institute of Technology Ladkrabang (KMITL) and Tokyo Institute of Technology, Japan. They give me many helpful suggestions and useful discussions on this research. I would like to sincerely thank Dr. Suwat Jirathearanat who is a coordinate thesis advisor and researcher from the hydroforming laboratory, National Metal and Material Technology Center (MTEC). He gives me many helpful suggestions and more knowledge concerned with useful information during undertaken research. I would like to thank MTEC team members that help me with all the experiments.

Secondly, I would like to acknowledge an affiliation to TAIST Tokyo Tech program that is academic collaboration between King Mongkut's Institute of Technology Ladkrabang (KMITL), National Science and Technology Development Agency (NSTDA), Thailand and Tokyo Institute of Technology, Japan. They kindly provide a scholarship for this research.

Finally, I would like to sincerely thank and appreciate my family in caring, opportunity, understanding and motivation throughout my life. I would like to bless my parents in bliss, healthy and happiness. These virtue and beneficence belong to my parents and Boonpuek's family forever.

Perawat Boonpuek

# Contents

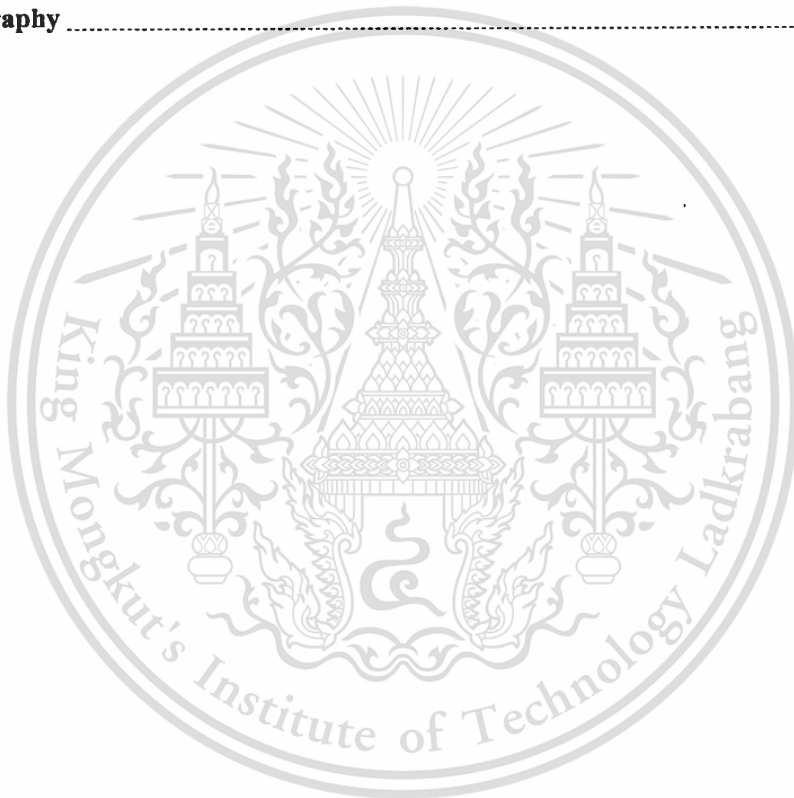
	Page
<b>Abstract</b> .....	I
<b>Acknowledgement</b> .....	II
<b>Contents</b> .....	III
<b>List of Tables</b> .....	VI
<b>List of Figures</b> .....	VII
<b>Chapter 1 Introduction</b> .....	1
1.1 Background and Problem Statement .....	1
1.2 Objective of Research .....	4
1.3 Hypothesis of Research .....	4
1.4 Scope of Research .....	4
1.5 Methodology of Research .....	5
<b>Chapter 2 Theory and Literature Review</b> .....	6
2.1 Tube Hydroforming Technology .....	6
2.1.1 Background of hydroforming .....	7
2.1.2 Tube hydroforming systems and tooling .....	9
2.1.3 Tubular material for tube hydroforming .....	12
2.2 Finite Element of Thin-Walled Vessel .....	12
2.3 Mechanical Properties of Material .....	15
2.3.1 Stress and strain .....	15
2.3.2 Plasticity .....	20
2.3.3 Plastic anisotropy .....	27
2.4 Determination of Stress - Strain Curve of Sheet Metal .....	29
2.5 Literature Review .....	30

## Contents (cont.)

	Page
<b>Chapter 3 Research Methodology</b> .....	34
3.1 Tooling Design for Free Bulge Test .....	34
3.1.1 Design for die inserts .....	34
3.1.2 Design for die stands .....	46
3.1.3 Design for axial punches .....	48
3.2 Tooling Set for Free Bulge Test .....	53
<b>Chapter 4 Experiment and Result</b> .....	55
4.1 Free Bulge Tests .....	55
4.1.1 Tooling construction and hydroforming system .....	55
4.1.2 Measuring instrument .....	59
4.1.3 Test tubes .....	59
4.1.4 Experimentation and results .....	61
4.2 Determinations of Flow Stress Curves .....	74
4.2.1 Flow stress curves by SPB analytical model .....	75
4.2.2 Flow stress curves by YingYot's analytical model .....	76
4.2.3 Flow stress curves by Hwang's analytical model .....	78
4.3 Tensile Tests of Flattened Tube Specimen .....	79
4.3.1 Flow stress curve of the tube by tensile tests .....	82
<b>Chapter 5 Comparison and Analysis</b> .....	83
5.1 Comparison of Flow Stress Curves .....	83
5.2 Validation of Developed Analytical Models Using Flow Stress Curves .....	84
5.2.1 Tube hydroformability evaluation with finite element simulations .....	84
5.2.2 Comparison between FEA simulation result and experimental result .....	85
5.2.3 Analysis of flow stress curves .....	91
5.2.4 Study of anisotropy effects on materials .....	94
5.3 Usability Evaluation of Determined Flow Stress Curve .....	97

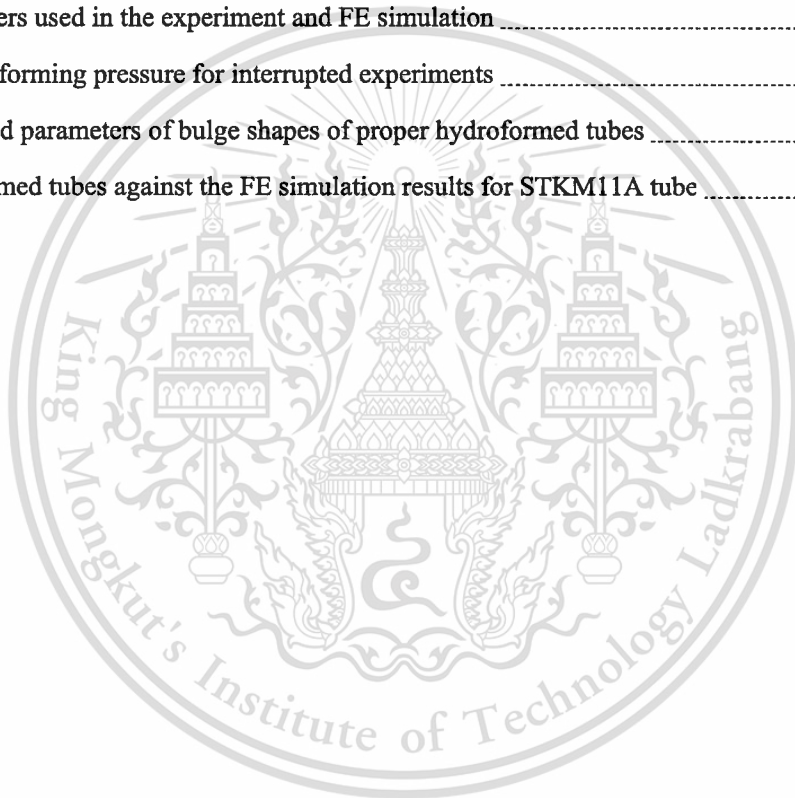
## Contents (cont.)

	Page
<b>Chapter 6 Conclusion and Suggestions</b> .....	100
6.1 Conclusion .....	100
6.2 Suggestions .....	101
<b>Reference</b> .....	102
<b>Appendix</b> .....	104
<b>Author Biography</b> .....	143



## List of Tables

Table	Page
3.1 Parameters for die insert design and flow stress determination .....	34
3.2 Parameters of finite element model for die insert design .....	37
3.3 Punch dimensions of finite element model for tube swaging .....	48
3.4 Punch dimensions of finite element model for tube fixing evaluation .....	51
4.1 Material properties of STKM 11A steel tube .....	60
4.2 Parameters used in the experiment and FE simulation .....	60
4.3 Internal forming pressure for interrupted experiments .....	63
4.4 Measured parameters of bulge shapes of proper hydroformed tubes .....	73
5.1 Real formed tubes against the FE simulation results for STKM11A tube .....	86



## List of Figures

Figure	Page
1.1 A specimen of a uniaxial tensile test .....	2
1.2 A tube bulge shape with thickness measurement positions .....	3
1.3 Schematic of a tube deformed under a biaxial stress state .....	3
2.1 Typical steps of tube hydroforming .....	6
2.2 Hydroformed parts in automobile structure .....	6
2.3 Classification of hydroforming .....	7
2.4 Schematic diagrams of sheet hydroforming operations .....	8
2.5 Parameters of the hydroformed tube .....	9
2.6 A schematic diagram of tube hydroforming system, tools, controls, pumps, and clear tank .....	9
2.7 A tube hydroforming sealing method .....	10
2.8 A schematic diagram of fluid hydroforming system .....	11
2.9 A schematic diagram of gas hydroforming system .....	12
2.10 An element of an axisymmetric shell .....	13
2.11 A yield diagram of principal tensions .....	13
2.12 Shell element analysis .....	14
2.13 Forces acting on a shell element .....	14
2.14 Deformation of a line in a material .....	16
2.15 Specimen of tensile test .....	16
2.16 A load–extension diagram of sheet tensile test .....	17
2.17 True stress–strain curved from the load–extension .....	19
2.18 True stress–strain plotted in a logarithmic diagram .....	19
2.19 Tresca criterion in six sectors by the following conditions .....	22
2.20 Von Mises yield locus .....	23
2.21 Tresca and von Mises loci showing certain loading paths .....	23
2.22 Schematic diagrams of yield locus .....	24
2.23 R value effect on the shape of the yield loci for textured materials .....	28

## List of Figures (Cont.)

Figure	Page
2.24 A schematic diagram of a sheet bulge test .....	30
3.1 A schematic diagram of a tube bulge test .....	35
3.2 A schematic diagram of free bulge test and design parameters .....	36
3.3 A half model of finite element simulation on symmetry plane .....	38
3.4 Flow stress curve used for the tube bulging test .....	38
3.5 Fluid internal pressure curve used for the tube bulging test .....	39
3.6 A half model of FE simulation of tube bulge test .....	39
3.7 Intermediate forming steps with thickness distributions .....	40
3.8 Comparison of predicted bulge shapes with different die insert geometry .....	40
3.9 Bulge heights versus thickness at the vertex (P) of the bulge shape .....	41
3.10 Deviation of simulated bulge curvatures from Hwang's model .....	42
3.11 Comparison between meridian radius obtained from FE simulation result and meridian radius calculated by Hwang's model .....	43
3.12 Comparison between circumferential radius obtained from FE simulation result and circumferential radius calculated by Hwang's model .....	43
3.13 A flow chart of die-insert design .....	44
3.14 Features of lower die inserts .....	45
3.15 Features of upper die inserts .....	45
3.16 A typical feature of a left die stand .....	46
3.17 Finite element analysis (a) compression loads applied, (b) deflection analysis result .....	47
3.18 Geometry of a punch for tube swaging .....	48
3.19 FEA model for tube swaging process .....	49
3.20 Thickness distributions of the swaged tube .....	50
3.21 Thinning of the swaged tube .....	50
3.22 FEA results of tube fix ability evaluation, (a) before bulge and (b) after bulge .....	52
3.23 FEA results of tube fixing, (a) thickness distribution and (b) maximum von Mises contours .....	53
3.24 Geometry of the axial punch (Model # 2) for hydraulic bugle test .....	53

## List of Figures (Cont.)

Figure	Page
3.25 Exploded view of tooling set for hydraulic bulge test .....	54
4.1 A feature of tooling structure, (a) front view and (b) isometric view .....	56
4.2 Wireframe of tooling structure, (a) front view and (b) isometric view .....	56
4.3 Real tool set, (a) lower tool set and (b) upper tool set .....	57
4.4 Hydroforming tools set on T.M.C 200 Ton press machine .....	57
4.5 Axial punches fix the ends of the test tube, (a) front view and (b) back view .....	58
4.6 Central control units of (a) hydroforming system and (b) a press machine .....	58
4.7 A schematic diagram of tube hydroforming system .....	59
4.8 A typical STKM 11A tube produced by roll forming with ERW process .....	60
4.9 Internal forming pressures versus bulge heights of the hydroformed tubes .....	61
4.10 Hydroformed tubes (STKM11A) versus test numbers .....	62
4.11 Internal forming pressure curve of Test #1 in plastic state of the hydroformed tube .....	63
4.12 Certain pressure curve for interrupted experiments .....	64
4.13 Proper hydroformed tubes (STKM11A) corresponding forming pressure levels .....	65
4.14 Pressure sensor .....	66
4.15 OptoNCDT1302 laser sensor .....	66
4.16 Internal forming pressures versus bulge heights from continuous forming .....	66
4.17 A typical hydroformed tube on lower die set .....	67
4.18 Tube thickness measurement using KASEDA dial caliper gauge .....	67
4.19 Polar coordinate circle grid .....	68
4.20 Thickness distributions of the hydroformed tubes versus internal pressure levels .....	68
4.21 Thickness distributions of the proper hydroformed tubes versus internal pressure levels .....	69
4.22 Bulge heights of the hydroformed tubes versus internal pressure levels .....	70
4.23 Bulge heights of the proper hydroformed tubes versus internal pressure levels .....	71
4.24 A support table for taking photos of bulge shapes .....	71
4.25 A typical bulge shape with geometrical parameter measurement .....	72
4.26 Points for flow-stress determination, (a) Neck, NearbyWeldline and (b) OppositeWeldline .....	73

## List of Figures (Cont.)

Figure	Page
4.27 Internal pressures versus circumferential radius of curvature of the bulge shapes .....	74
4.28 Internal pressures versus meridian radius of curvature the bulge shapes .....	75
4.29 Flow stress curves of STKM11A steel tube by SPB model .....	76
4.30 Flow stress curves of STKM11A steel tube by Ying Yot's model .....	77
4.31 Flow stress curves of STKM11A steel tube by Hwang's model .....	79
4.32 A typical tube cut in longitudinal direction, (a) a cut tube and (b) wall-separated tubes .....	80
4.33 A typical flattened tube workpiece .....	80
4.34 Finite element simulation of tube flattening process .....	80
4.35 Finite element simulation result of tube flattening .....	80
4.36 A typical specimen for tensile test, (a) standard dimension and (b) a fine specimen .....	81
4.37 Comparison between width strain and thickness strain for anisotropy value calculation .....	81
4.38 Flow stress curves of STKM 11A steel tube obtained from tensile test .....	82
5.1 Flow stress curves of STKM 11A steel tube .....	83
5.2 Finite element simulation model .....	85
5.3 A real hydroformed tube at $P_5$ (Level #5 in Figure 4.13, $P = 336$ bar) .....	88
5.4 Thickness distributions in longitudinal direction of the tube .....	89
5.5 Thickness comparison between the FEA results and the real tube (Level#5, Figure 4.13) .....	89
5.6 Bulge height comparison between the FEA results and the real tube (Level#5, Figure 4.13) .....	90
5.7 Bulge shape comparison between the FEA model and the real tube (Level #5, Figure 4.13) .....	91
5.8 A flow chart of flow stress determination .....	93
5.9 Flow stress curves obtained from consideration of anisotropic materials .....	95
5.10 Thickness comparison of FEA models varied in anisotropy values .....	96
5.11 Bulge height comparison of FEA models varied in anisotropy values .....	96
5.12 FEA model shown by section cut for hydroformability evaluation of Oil Filler Pipes .....	97
5.13 Feeding distance curve .....	98
5.14 FE simulation result of Oil Filler Pipe .....	98
5.15 FEA results, (a) tube thickness distribution and (b) Forming Limit Diagram (FLD).....	99

# Chapter 1

## Introduction

### 1.1 Background and Problem Statement

Tubular materials have been used for part production in several industries such as automotive, aerospace, appliance, etc. Due to increasing demands of lightweight and seamless parts with high strength, many manufacturers applied specifically high technology for quality part production. One of high technologies is hydroforming process. With more complex shape forming, this process gives better results compared with conventional productions (rolling, forging or stamping) [1-3]. This technology is relatively new manufacturing process for developing countries to produce the component parts of automobiles. Therefore, the hydroforming process is prospective manufacturing for reducing disadvantage of conventional forming processes.

Tube HydroForming (THF) is one of hydroforming technology that uses a pressurized fluid (liquid or gas) in cavity of die whereby a tubular blank (straight or pre-bent) is formed into the cavity using simultaneous application of internal forming pressure. The tube hydroforming usually has compressive and axial punches which can exert on both or either ends of the tube. This hydroforming process has some advantages such as (1) reduction in the number of workpieces, tool cost and the product weight, (2) quality improvement of the formed parts, (3) more complex shapes and more uniform thickness distribution, (4) fewer secondary operations, etc. On the other hand, this process has some disadvantages such as slow cycle time, expensive equipment, heavy tooling, lack of database for tool and process designs, etc [1].

As the tube hydroforming is cold forming work, stiff metal forming with high internal pressure is consequently used. Therefore, dies and tooling are made from high strength materials, and designed for closed block to prevent metal scrap bursting out and damage to tools during the hydroforming. A tube workpiece is plastically deformed by internal hydraulic pressure. The forming tube has sequential tendency to easy crack because of unbalanced strain-hardening ( $n$ ) and residual stress effects. Hence, qualified tooling selection and process design with tube hydroformability prediction are substantial factors. The dies and tooling should be specifically designed by computational

optimization. In process and die designs, feasibility is widely used for study of plastic deformation of the tubular materials. Material properties of the tubes, stress – strain relationship (flow stress) are important data for this study and influence on its hydroformability. Unfortunately, the data based on that flow stress of the specific tube produced in Thailand are not available for tube hydroformability evaluation with feasibility studies.

In several fields, studies mostly concern with evaluation of expansive deformation of the tubular materials by hydraulic bulge test. The flow stress data obtained from a uniaxial tensile test are mostly used for prediction of tube deformation with Finite Element (FE) simulation [2-3]. Their studies were found that the FEA simulations gave the effective results of the formed parts and approximated to experimental results. However, the above-mentioned flow stresses used in such FEA models were only specific data of sheet metal formed under a uniaxial stress state as shown in Figure 1.1.

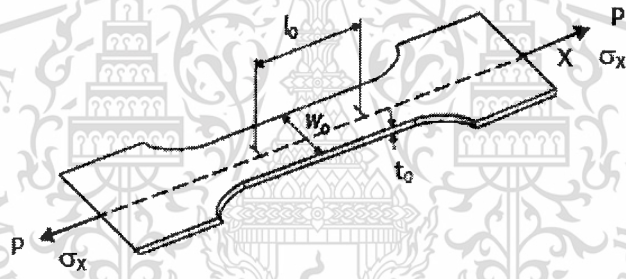
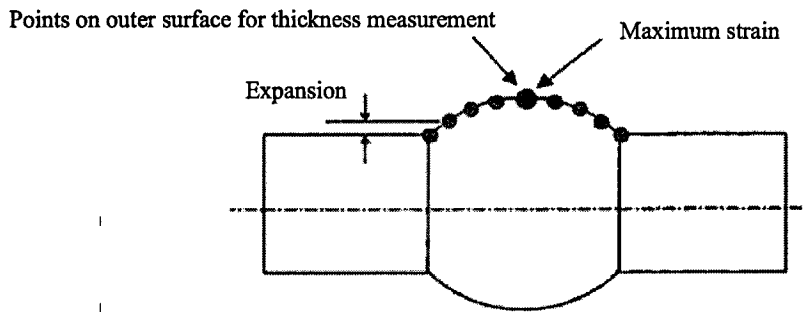
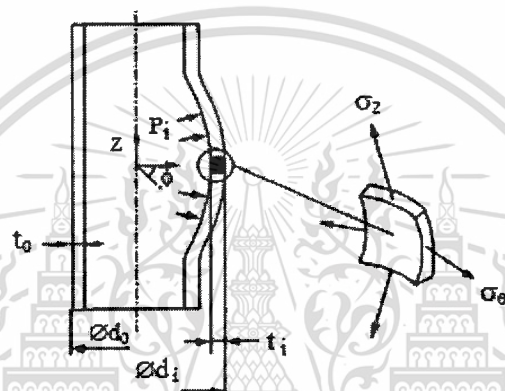


Figure 1.1 A specimen of a uniaxial tensile test

Figure 1.1 shows a specimen of tensile test under the uniaxial stress state. The obtained flow stress is not mechanical property of the tube deformed under the biaxial stress state [6-12]. From their studies, analytical results are just verified that FEA simulations were rather close to the experimental results. The simple approach were only restricted to the uniaxial tension test. The analytical models could not be able to determine the effective flow stress of the tubes in the biaxial stress state. Consequently, better evaluation of tube deformation would be explicit FEA simulation by using the flow stress obtained from the biaxial stress state. The analytical results would be closer to the experimental result. The simple approach to the flow stress determination of the tubes could be the free bulge test which corresponds to the biaxial stress testing as shown in Figure 1.2 and Figure 1.3 [6-12].



**Figure 1.2** A tube bulge shape with thickness measurement positions



**Figure 1.3** Schematic of a tube deformed under a biaxial stress state

Yeong – Maw Hwang, Yi - Kai Lin and T. Altan [10, 11], their study directly related to the determination of the flow stress curve obtained from the biaxial stress state. The analytical model of the bulge shape was considered for die entrance radius. An assumption of the elliptical surface for the bulge profile was made. Internal forming pressure versus thickness distribution of the formed tubes was shown. Tube thickness of the bulge shape seemed to have quadratic distribution. However, they did not consider influences of  $R_d/t$  and  $L/OD$  ratios which are important effects on bulge formability of the thin – walled tube.

This study consequently aims for research on the evaluation of the tube hydroformability by using the free bulge test and reliable methods of the FEA simulation. Firstly, Hwang's model is used for die insert design by considering the effects of  $R_d/t$  and  $L/OD$  ratios, where,  $R_d$ ,  $L$ ,  $t$  and  $OD$  are the die entrance radius, the bulge length, the thickness and the outer diameter of the tube, respectively. Those designed die inserts are manufactured. Secondly, the hydraulic bulge test and the tensile test are conducted from the specific test tubes. SPB model (new analytical model) is postulated

to analyze the bulge shapes of the formed tubes for flow stress determinations. SPB model, Ying Yot's model, Hwang's model and the tensile test are used to determine the flow stress curves of the formed tubes. Then, all of the flow stress curves are compared and specified as material properties in the FEA simulations. Finally, verification of this analytical model with the obtained flow stress curves is presented. Comparison of the FE simulation results and the experimental results are performed. The author hopes that this study will be useful information on the subject of die insert design, the simple approach to flow stress determination and tube hydroformability evaluation.

## 1.2 Objective of Research

1. To design and implement proper tube bulge test approach.
2. To determine flow stress of steel tube (STKM 11A steel tube).
3. To validate new analytical model for flow stress determination of tubular materials for hydroformability evaluation of automotive tubular parts

## 1.3 Hypothesis of Research

The free bulge test for testing mechanical property of the steel tube is a better method than the tensile test. The developed SPB analytical model can accurately evaluate the flow stress curve of the tube (STKM 11A steel tubing).

## 1.4 Scope of Research

1. STKM 11A steel tube (OD=28.6 mm. and t= 1.2 mm.) are used.
2. INSTRON, a universal testing machine is used for the tensile tests.
3. DDP 200 Ton, a press machine is used for hard tooling support in hydroforming process.
4. Data Acquisition System combined with sensors is used for parameter measurement.
5. DYNAFORM with LS-Dyna solver is employed to conduct simulation of hydroforming.
6. Laboratory at National Metal and Material Technology Center (MTEC), National Science and Technology Development Agency (NSTDA), Thailand

## 1.5 Methodology of Research

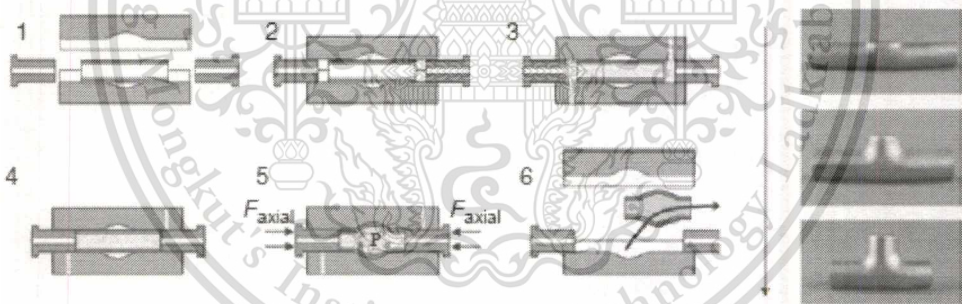
1. Designing die inserts and tools for free bulge test by using CAD and FEA Software,
2. Determining the die inserts suitable for the free bulge-test by investigating the proper bulge shape of the hydroformed tube through FEA simulation software,
3. Implementing designed die inserts and tools for use in the free bulge tests,
4. Conducting the hydraulic bulge test with simultaneously measurements of internal pressure, tube thickness at the vertex, contact points and bulge heights of the tube being tested,
5. Conducting the tensile tests using simultaneous measurements of load cell and elongation,
6. Determining effective stress-strain relationship curves (flow stress curves) by using SPB analytical model, Hwang's model, Ying Yot's model and data from the tensile test,
7. Running the FE models of the tube free bulge test using DYNAFORM software by specifying the flow stress data obtained from the experiments,
8. Analyzing the behavior of tube deformation in form of the bulge shape by LS-Dyna solver,
9. Comparing FEA simulation results with the experimental results,
10. Evaluating the hydroformability of an automotive part by using FEA simulation with the determined flow stress curve

## Chapter 2

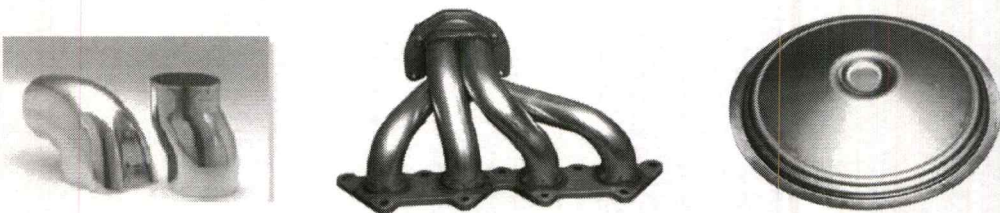
### Theory and Literature Review

#### 2.1 Tube Hydroforming Technology

Tube HydroForming (THF) is one of high technology that uses hydraulic pressurized fluid (liquid or gas) in the die cavity to form a tubular material. This process has different characteristics of forming from conventional processes (stamping and drawing) as illustrated in **Figure 2.1**. The conventional processes can form a tubular material by using the object force. The tube hydroforming on the other hand uses hydraulic pressure. In this process, more complex shapes with increased strength and lightweight part can be manufactured. Moreover, this process can finalize a part with more complex shapes by a single step. Additional post-processing step (boring or trimming) is sometimes used in this step. The tube hydroforming has been popularly used in various industries such as appliance, aerospace and automotive parts as shown in **Figure 2.2**.



**Figure 2.1** Typical steps of tube hydroforming (Siempelkamp Pressen Systems)

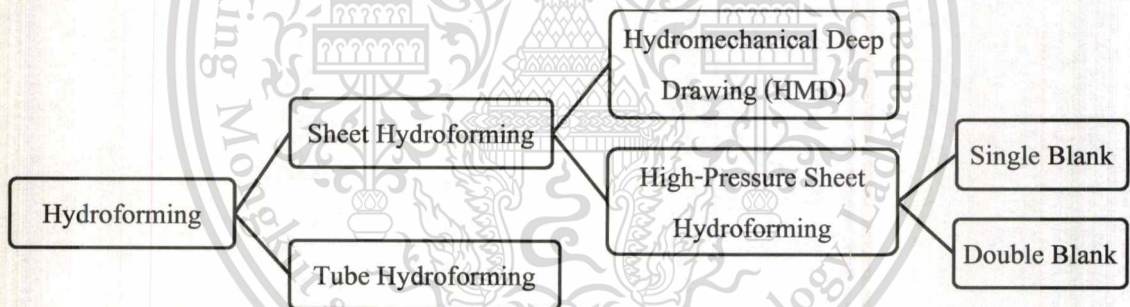


**Figure 2.2** Hydroformed parts in automobile structure (Schuler Press, DCX, Vari-form)

The advantage of the hydroforming technology are weight and cost reducing through part consolidation in case of elimination of additional metal, reduction of assembly operations via tight part consolidation with dimensional tolerances, more complex shape and reduced post-forming processes such as welding and piercing. In contrast, the hydroforming process has some disadvantages, such as weaknesses in terms of process cycle times, limitation of existing data-base knowledge and tools design [1-3].

### 2.1.1 Background of hydroforming

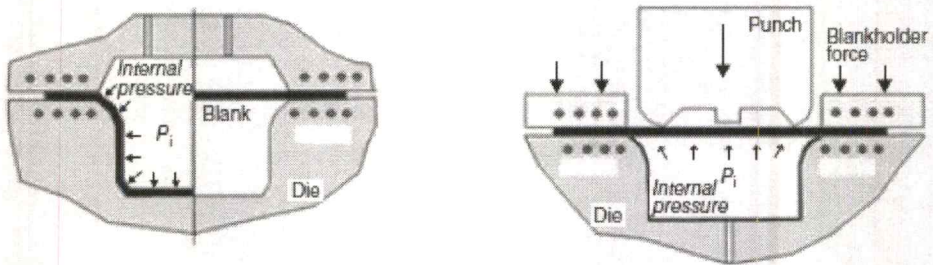
The hydroforming process was established in 1940s. Hydroforming applications were firstly used in boiler manufacturing and musical instruments. The patented application was obtained by Milton Garvin of the Schaible Company of Cincinnati, Ohio, USA, for producing kitchen spouts in the 1950s and used effectively in the 1990s due to advantage of computer controls, hydraulic systems and design guidelines. It can be classified by two categories: (1) sheet hydroforming and (2) tube hydroforming (Figure 2.3) [1].



**Figure 2.3** Classification of hydroforming (Schmoeckel, 1999)

#### 2.1.1.1 Sheet hydroforming

The principles of the sheet hydroforming can be briefly described as follows: a sheet blank is formed into the die cavity by the hydraulic pressure as illustrated in **Figure 2.4**. This forming method allows a deeper drawing than normal stamping. The sheet hydroforming process can be normally classified by two categories: (1) hydro-mechanical deep drawing and (2) high-pressure sheet hydroforming with single and multiple blanks [1].



**Figure 2.4** Schematic diagrams of sheet hydroforming operations (Schuler Inc., 1998)

### 1 Hydromechanical deep drawing

Hydro-mechanical deep drawing (HMD) and conventional deep drawing processes are similar in common except the application of counter pressure on other punch side. Hydro-mechanical deep drawing process has not lower dies. It applies the hydraulic pressure instead of the lower dies after the punch forces the sheet blank. The hydraulic pressure improves for deeper drawing to fill the sheet into the complex corner of the die cavity [1].

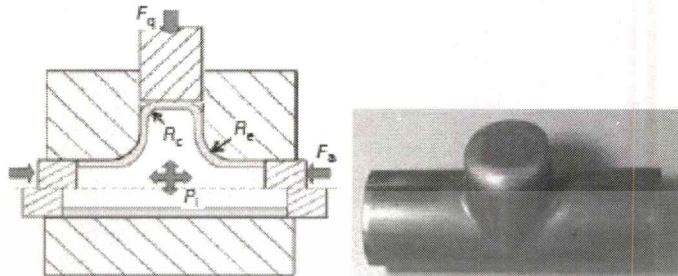
### 2 High-pressure sheet hydroforming

High-pressure sheet hydroforming consists of two types, i.e. a single sheet hydroforming and double sheet hydroforming. For the single sheet, a sheet blank laid on side holder is first fixed by dies. Then, forming pressure is used to fill a sheet into the die cavity. For the double sheet, the hydraulic fluid pressure is pumped in the gap of the workpiece after they have been formed by the conventional deep drawing. The blank sheets are deformed by internal pressure and contoured by the upper and the lower die. Both processes can form the material by deeper drawing with metal flow control [1].

#### 2.1.1.2 Tube hydroforming

The principle of the tube hydroforming is that the tube blank is formed into the die cavity using simultaneous application of the internal pressure and axial compressive punches. Either axial feeding punch or non-axial feeding punch is used. Tube hydroforming can be classified by two ideal forming characteristics i.e. (1) hydromechanical tube feeding and (2) Hydromechanical tube fixing. For the hydromechanical tube feeding, the axial punches (both or either ends of the tube) compress the tube blank into the die cavity. Feeding distance of the axial punch can be controlled by feeding load. In contrast, the hydromechanical tube fixing, the tube blank is fixed by the axial

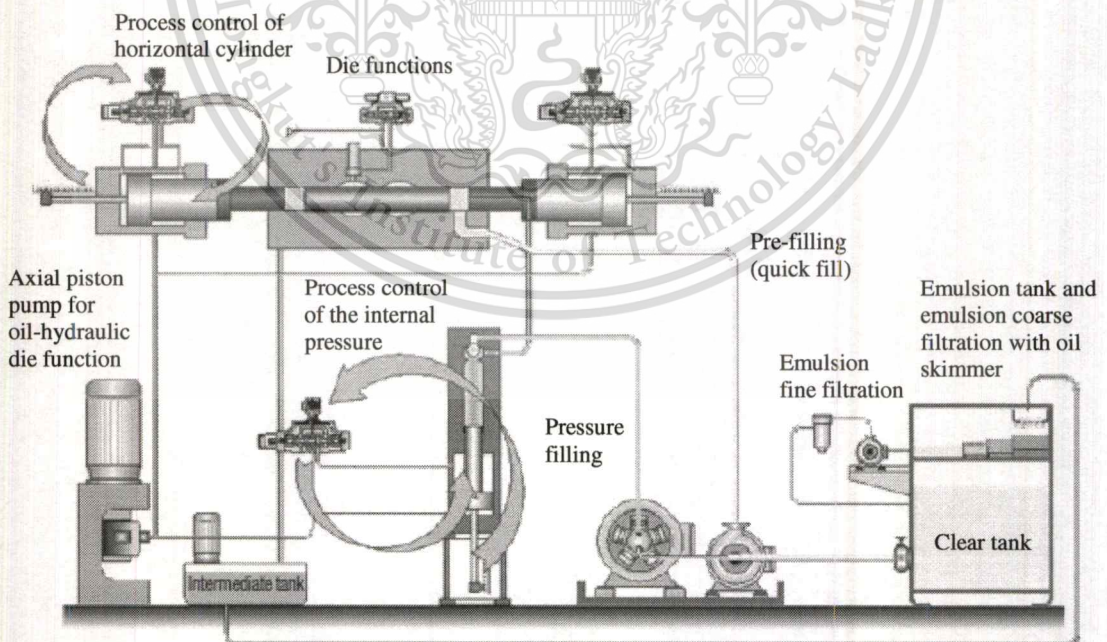
punches (both or either ends of the tube) combined with loading control. Geometry and parameters of the hydroformed parts are shown in **Figure 2.5** [1].



**Figure 2.5** Parameters of the hydroformed tube and die geometry, die radius ( $R_e$ ), contact radius ( $R_c$ ), axial force ( $F_a$ ), counter force ( $F_q$ ) and internal pressure ( $P_i$ )

### 2.1.2 Tube Hydroforming System and Tooling

Control, design, and maintenance of tube hydroforming are important subject to prevent damage because of exceed internal pressure. Typical configuration of tube hydroforming process is illustrated in **Figure 2.6**.



**Figure 2.6** A schematic diagram of tube hydroforming system, tools, controls, pumps, and clear tank

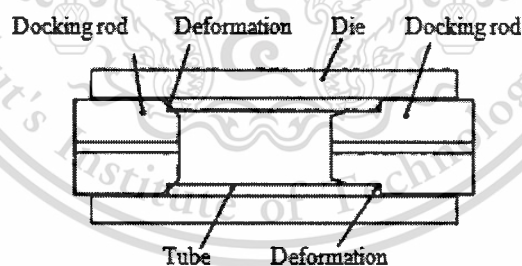
Tube hydroforming tools normally consist of die holders, dies, insert, punches, counter punches and sealing systems. Due to high internal pressure of the THF process, tooling systems with tight tool tolerance are required to reduce die and part separations. The special characteristics of the tooling are defined as follows: (1) high strength, (2) finish surface to minimize friction, (3) flexibility by interchangeable inserts and guiding systems, (4) balanced design to minimize the closing force. The upper die, the lower die and other cams or punches suitable for feeding tube are used. For the sealing method, the axial punch positions for fixing the ends of the tube are illustrated in **Figure 2.7**. In this way, the axial punches are used for compression to seal the internal fluid and feed the tube into the die cavity. The required force can be expressed as **Equation 2.1**.

$$F_s = PA \quad (2.1)$$

where  $F_s$ ,  $P$  and  $A$  are the sealing force (N), the forming pressure (Pa), the cross sectional area of the tube ( $m^2$ ), respectively. The punch feeding force can be expressed as **Equation 2.2**.

$$F_y = (Y_s)A \quad (2.2)$$

where  $F_y$ ,  $A$  tube and  $Y_s$  are the force required to yield the tube material (N), the cross-sectional area of the tube only ( $m^2$ ), the yield strength of the tube (Pa) [1].



**Figure 2.7** A tube hydroforming sealing method (Muammer Koç)

### 2.1.2.1 Clamping and pressing

The hydraulic press machine is directly used to open and close the die with high clamping force for preventing die separation. The closing force should be values in the range of 7000 – 10000 tons. The special clamping has to increase capabilities on process control, obtain better dimensional accuracy of the formed part, reduce cycle time and increase of flexibility for different

parts. Press machine must have the following features: (1) appropriate closing force and table area for die support, (2) adjustable punch with computer control and adjustable counter punch with position control, (3) automatic workpiece handling, (4) high internal pressure (2000 to 5000 bar/200–500 MPa) and fluid-pumping capability with tight dimension control [1].

### 2.1.2.2 Hydraulic pressure system

The hydraulic power supply (HPS) provides high pressure for actuator operation and the compression intensification. The hydraulic cylinders with the axial punches are used for compression to seal the internal fluid and fix the two ends of the tube. Loading condition should be optimized by investigation methods for pressure versus time and axial force versus time. The applied internal pressure should be investigated values in the range from 1000 bar (30 ksi/100 MPa) to 10000 bar (150 ksi/1000 MPa), depending on the workpiece. The high-pressure hydroforming systems normally operate in the range from 15000 psi (1034 bar) to 60 000 psi (4137 bar). Figure 2.8 shows a schematic diagram of fluid hydroforming system. Figure 2.9 shows a schematic diagram of gas hydroforming system. The control systems of hydroforming normally consist of two types i.e. open-loop control and closed-loop control on the clamp actuator [1].

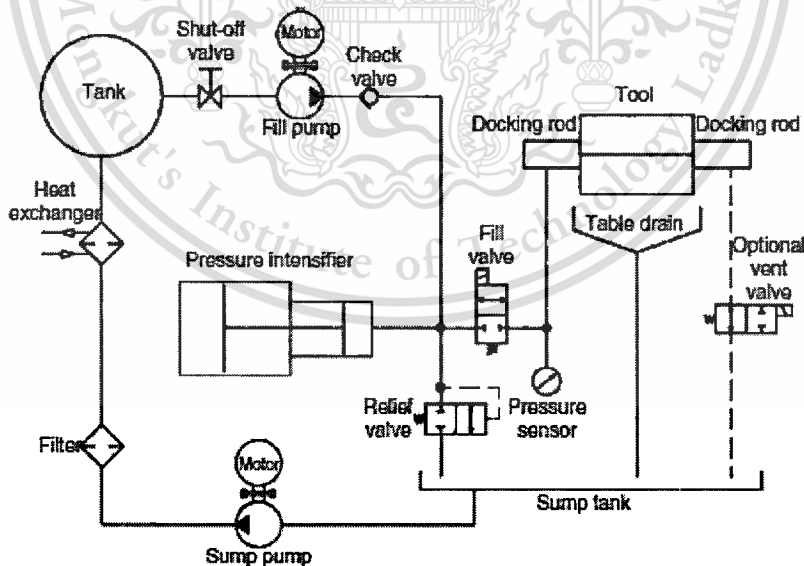


Figure 2.8 A schematic diagram of fluid hydroforming system (Muammer Koç)

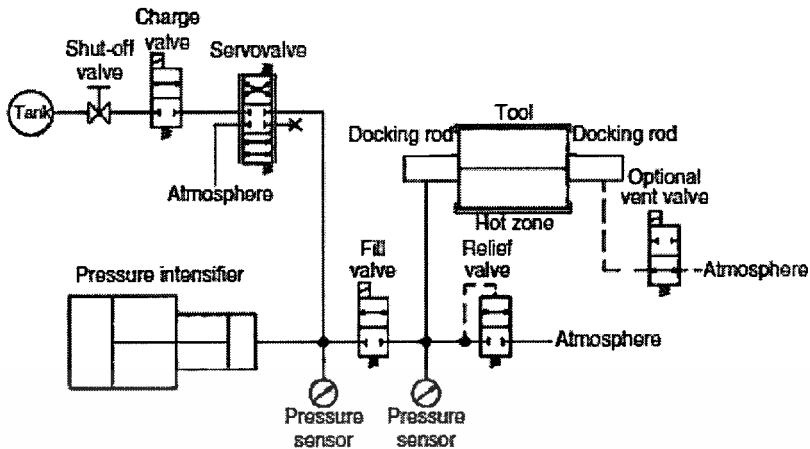


Figure 2.9 A schematic diagram of gas hydroforming system (Muammer Koç)

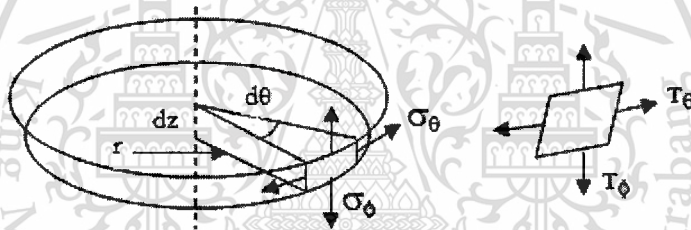
### 2.1.3 Tubular Material for tube hydroforming

Stress-strain relationship, weld type, yield and tensile strength, ductility and anisotropy are material properties that are mainly considered for tube hydroforming. The required characteristics of raw materials for the quality production are defined as follows: (1) high and uniform elongation, high strain hardening exponent and low anisotropy, (2) strong mechanical and surface properties of seam line to the base material, (3) finish surface quality without scratches, close dimensional tolerances (thickness, diameter), (4) burr free ends and tube edges perpendicular to the longitudinal axis. Therefore, the hydroforming for tube production necessitates that the alloy steel tube are suitable for semi-finished part forming. Low-carbon steel tubes with yield strength between 200 MPa and 430 MPa are common in automotive component. The special testing methods have been conducted to study the material quality. There are the following items: (a) tensile test, (b) expansion test, (c) cone test and (d) bulge test. Yield and ultimate tensile strength, elastic modulus (E), strength coefficient (K), strain hardening (n) and anisotropy (r) can be obtained. The tubular materials, outer diameters ( $d_o$ ) = 20 - 140 mm and ratios of thickness and outer diameter ( $t_o/d_o$ ) = 0.012 - 0.16 are mostly used [1].

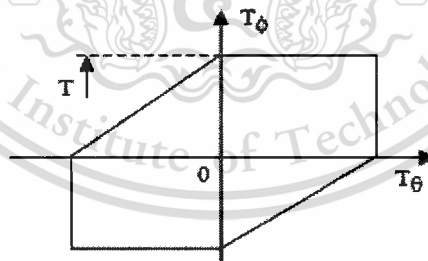
## 2.2 Finite Element of Thin – Walled Vessel

Thinning, thickening, strain and stress on deformed tubes can be evaluated by feasibility study. Different parameters can be investigated by varying dimensions and loading conditions on part and dies. Appropriately selected FEA software should display accurate forming results. Furthermore, the success of efficacious hydroforming without defects is dependent on the selection of proper loading

path, the pressure versus time, lubrication, part and tooling design. LS-DYNA solver that is FEA software for nonlinear and plasticity problem solution is widely used. The employed element model is the response surface method (RSM), shell element (Koç, 2001, Asnafi et al, 2000) [1] that can be considered as an axisymmetric shell illustrated in **Figure 2.10**. The surface element is at a radius ( $r$ ) and subtends an angle ( $d\theta$ ). The thickness ( $t$ ) and the principal stresses in the hoop and meridian directions, ( $\sigma_\theta$  and  $\sigma_\phi$ ), are postulated. The radial stress perpendicular to the element is considered as small. Acting on the element are the principal tensions,  $T_\theta = \sigma_\theta t$  and  $T_\phi = \sigma_\phi t$ . If the element is deforming plastically, the principal stresses will reach to the yield condition. The element structure of planar stress is illustrated in **Figure 2.11**. We identify an effective tension function  $T$ . The major assumption here is that the yielding tension  $T$  will remain constant throughout the process. This implies that strain-hardening balance material thinning (i.e.,  $\sigma_r t = T$  constant) [4].

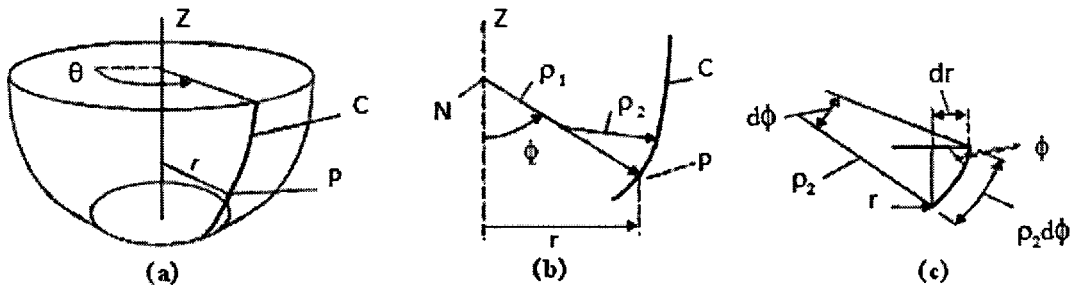


**Figure 2.10** An element of an axisymmetric shell



**Figure 2.11** A yield diagram of principal tensions ( $T$  is constant)

An axisymmetric shell or surface of revolution is illustrated in **Figure 2.12(a)**. A point on the surface ( $P$ ) can be described in terms of cylindrical coordinates,  $r$ ,  $\theta$ ,  $z$ . The curve generating shell,  $C$ , is illustrated in **Figure 2.12(b)** and the outward normal to the curve at  $P$  is  $NP$ . An angle  $\phi$  can be made by the axis. The curvature of the curve at  $P$  is  $\rho_2$  that is one of the principal radii of curvature of the surface. The other principal radius of curvature of the surface is  $\rho_1$ .



**Figure 2.12** Shell element analysis (a) surface of revolution swept out by rotation of a curve C, (b) principal radii of curvature at the point P, (c) geometric relations at P

The arc length of the element along the meridian is  $d\phi = \rho_2 d\phi$ . Figure 2.12(b) and (c), the following geometric relations can be identified as Equation 2.3.

$$r = \rho_1 \sin\phi \tag{2.3}$$

$$dr = \rho_2 d\phi \cos\phi \tag{2.4}$$

Equilibrium equation of shell element in Figure 2.13, we can consider a shell element of sides,  $r d\theta$  and  $\rho_2 d\phi$ . The pressure (P) acting on this element exerts an outward along the normal surface. It can be defined as relation shown in Equation 2.5

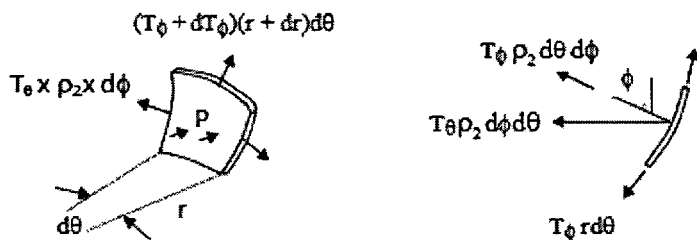
$$P r d\theta \rho_2 d\phi \tag{2.5}$$

Due to the curvature of the shell, the forces on the element,  $T_\theta \rho_2 d\phi$  in the hoop direction exert in the horizontal direction. It can be defined as relation shown in Equation 2.6.

$$T_\theta \rho_2 d\phi d\theta \tag{2.6}$$

The component of the force along the normal direction is expressed as Equation 2.7.

$$T_\theta \rho_2 d\phi d\theta \sin\phi \tag{2.7}$$



**Figure 2.13** Force acting on a shell element

The component tangential to the surface in the meridian is expressed as **Equation 2.8**.

$$T_{\theta} \rho_2 d\phi d\theta \cos\phi \quad (2.8)$$

Due to the curvature of the shell, the forces along the meridian  $T_{\phi} r d\theta$  exert in the normal direction to the surface. It can be defined as relation shown in **Equation 2.9**. So, the equation of equilibrium force in normal direction to the surface is expressed as **Equation 2.10**.

$$T_{\phi} r d\theta d\phi \quad (2.9)$$

$$Pr d\theta \rho_2 d\phi = (T_{\theta} \rho_2 d\phi d\theta) \sin \varphi + T_{\phi} r d\theta d\phi \quad (2.10)$$

Combining with Equation 2.3, the equation of equilibrium force reduces to **Equation 2.11**.

$$P = (T_{\theta} / \rho_1) + (T_{\phi} / \rho_2) \quad (2.11)$$

Then, the equilibrium equation in the meridian direction is expressed as **Equation 2.12**.

$$(T_{\phi} + dT_{\phi})(r + dr)d\theta - T_{\phi} r d\theta - T_{\theta} \rho_2 d\phi d\theta \cos \phi = 0 \quad (2.12)$$

Combining with Equation 2.4, the equation of equilibrium force reduces to **Equation 2.13**.

$$(dT_{\phi} / dr) - [(T_{\theta} - T_{\phi}) / r] = 0 \quad (2.13)$$

## 2.3 Mechanical Properties of Material

### 2.3.1 Stress and Strain

An understanding of stress and strain is essential for analyzing metal forming operations. In engineering, stress is the intensity of force acting on metal. Strain is the amount of deformation in the body of metal [5].

#### 2.3.1.1 Stress

The stress is defined as the intensity of the force,  $F$ , at a point. If the stress is the same everywhere, it can be expressed as **Equation 2.14**.

$$\sigma = F/A \quad (2.14)$$

where,  $A$  and  $F$  are current cross-sectional area, force on cross-sectional area, respectively.

### 2.3.1.2 Strain

The points in that body are displaced when the body is deformed. The strain must be defined in such a way that it excludes effects of rotation and translation. **Figure 2.14** shows lines in the material that is extended and rotated. Deformation is characterized by engineering strain  $e$ :

$$e = (l - l_0) / l_0 = \Delta l / l_0 \quad (2.15)$$

An alternative definition is result of true or logarithmic strain,  $\epsilon$ , defined as **Equation. 2.16**.

$$d\epsilon = dl / l \quad (2.16)$$

The integrated strain expression gives **Equation 2.17**. That means the true strain and the engineering strain are almost equal when they are small.

$$\epsilon = \ln(l / l_0) = \ln(1 + e) \quad (2.17)$$

Expressing  $\epsilon$  as  $\epsilon = \ln(l / l_0) = \ln(1 + e)$  and expanding,  $\epsilon = e - e^2/2 + e^3/3! \dots$  so as  $e \rightarrow 0$ ,  $\epsilon \rightarrow e$ .



**Figure 2.14** Deformation of a line in a material (Z. Marciniak, J.L. Duncan, S. J. Hu)

### 2.3.1.3 Stress - strain relationship

Tensile test is widely used for studying material properties of metal. **Figure 2.15** shows a typical workpiece for the tensile test having a parallel. The reduced section of a normal length is the indent width,  $w_0$ . Initial thickness ( $t_0$ ) and load on specimen at the instant point (P) are measured by a load cell of the testing machine. In the middle of the specimen, a gauge length ( $l_0$ ) and current gauge length ( $l$ ) are monitored by an extensometer. The extensional length is  $\Delta l = l - l_0$ . In various tests, a transverse extensometer may also be used to measure the change in width, i.e.  $\Delta w = w - w_0$ . During the test, load and extension will be recorded in a data acquisition system. This is then analyzed and material property diagrams can be curved.

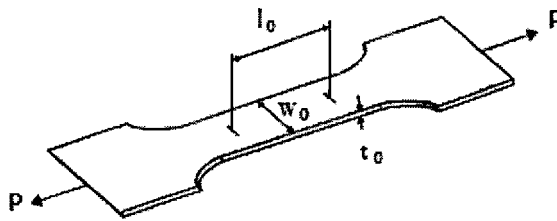


Figure 2.15 A specimen of tensile test (Z. Marciniak, J.L. Duncan, S. J. Hu)

### 1 Load extension diagram

Figure 2.16 shows a typical load–extension diagram of the tested part. The elastic extension is so small that it cannot be seen. One feature is initial yielding load,  $P_y$ . The initial yielding is followed by a gage length region in which the deformation is uniform and the load increases. The increasing load is due to strain-hardening ( $n$ ), which is a phenomenon exhibited by most metal and alloys when the strength or hardness of the material increases with plastic deformation. During the tensile test, the cross-sectional area at the indent decreases while the length increases. When load reaches a maximum  $P_{max}$ , deformation at the indent area decreases continuously. That means the ultimate tensile strength of the material occurs. Then, the indent area would be necking — it develops in non-uniform extension until the strip fractures.

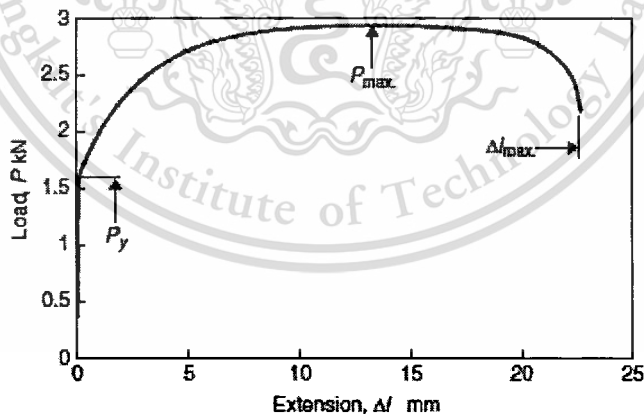


Figure 2.16 A load–extension diagram of sheet tensile test (Z. Marciniak, J.L. Duncan, S. J. Hu)

### 2 True stress and true strain curve (flow stress curve)

Engineering stress–strain curve is unsuitable for use in the metal forming analysis because the stress is based on the initial cross-sectional area of the workpiece, rather than the

current value. The engineering strain is not a satisfactory measure of strain because it is based on the original gauge length. Therefore, the study of forming processes is mostly based on true stress and strain. The true stress can be obtained from the load-extension diagram between initial yielding and the maximum load or ultimate tension. When the gauge section is constant, initial volume and any volume can be expressed as **Equation 2.18**.

$$A_0 l_0 = Al \quad (2.18)$$

and the true stress can be expressed as **Equation 2.19**.

$$\sigma = \left(\frac{P}{A_0}\right)\left(\frac{l}{l_0}\right) \quad (2.19)$$

For the deformation of the workpiece, if the gauge length increases by a small amount,  $dl$ , a suitable definition is the strain increment, extensional length per current length as shown in **Equation 2.20**.

$$d\varepsilon = dl/l \quad (2.20)$$

For every small strains (where  $l \approx l_0$ ), the strain increment is very similar to the engineering strain. If the straining process continues uniformly in the one direction as it does in the tensile test, the strain increment can be integrated as the true strain:

$$\varepsilon = \int d\varepsilon = \int_{l_0}^l \frac{dl}{l} = \ln(l/l_0) \quad (2.21)$$

The true stress-strain curve obtained from the load-extension diagram is shown in **Figure 2.17**. The true stress could also be obtained from the engineering stress-strain equation:

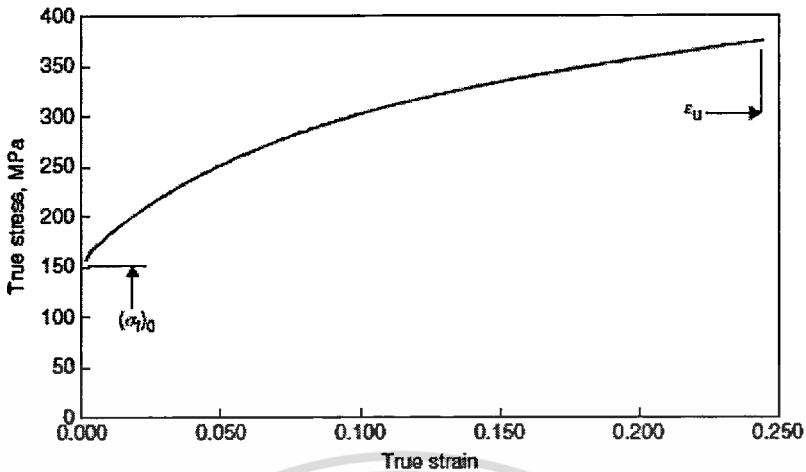
$$\sigma = \frac{F}{A} = \frac{P}{A_0} \times \frac{A_0}{A} = \sigma_{eng} \frac{l}{l_0} = \sigma_{eng} \left(1 + \frac{e_{eng}}{100}\right) \quad (2.22)$$

and

$$\varepsilon = \ln\left(1 + \frac{e_{eng}}{100}\right) \quad (2.23)$$

It can be seen that the true stress-strain curve does not reach a maximum as strain hardening is continuous increase. When necking starts, deformation in the gauge length is no longer uniform. So, Equation 2.23 is no longer valid. The curve (**Figure 2.17**) cannot be calculated on a strain corresponding to maximum load; this strain is called the maximum uniform strain:

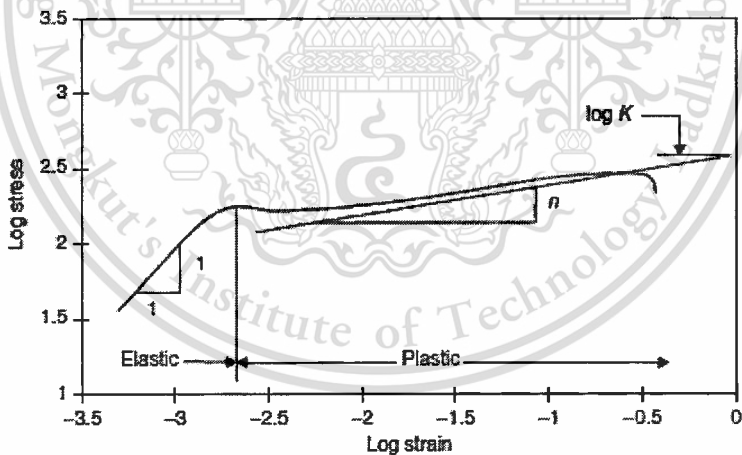
$$\varepsilon_u = \ln\left(1 + \frac{E_u}{100}\right) \quad (2.24)$$



**Figure 2.17** True stress-strain curved from the load–extension (Z. Marciniak, J.L. Duncan, S. J. Hu)

If the true stress-strain is plotted on logarithmic scales, sample of the sheet metal shows the characteristics as illustrated in **Figure 2.18**. At low strain in the elasticity, the curve is approximately linear. This relation corresponds to an equation for the elasticity as **Equation 2.25**.

$$\sigma = E\epsilon \text{ or } \log \sigma = \log E + \log \epsilon \quad (2.25)$$



**Figure 2.18** True stress–strain plotted in a logarithmic diagram (Z. Marciniak, J.L. Duncan, S. J. Hu)

At higher strains, the curve can be fitted by a power law expression:

$$\sigma = K\epsilon^n \quad (2.26a)$$

or

$$\log \sigma = \log K + n \log \epsilon \quad (2.26b)$$

The fitted curve has a slope of strain-hardening index ( $n$ ) and strength coefficient ( $K$ ). The power law equation 2.26(a) is often used to describe the plasticity of low carbon steel sheet. When metal are

deformed plastically at temperatures lower than causes of recrystallization, this phenomenon is called cold work. Cold working increases the strength and hardness, but it decreases the ductility. When the true stress ( $\sigma$ ), and true strain ( $\epsilon$ ) in a tension test are the effective stress and effective strain, the flow stress can be expressed as **Equation 2.27**.

$$\bar{\sigma} = K \bar{\epsilon}^n \quad (2.27)$$

In the other strain hardening approximations, expressions are more accuracy mathematically for cold working. The appropriate expressions are shown in **Equation 2.28** and **Equation 2.29**.

$$\bar{\sigma} = K (\epsilon_0 + \bar{\epsilon})^n \quad (2.28)$$

or

$$\bar{\sigma} = \sigma_0 + K \bar{\epsilon}^n \quad (2.29)$$

where ,  $K$  ,  $\epsilon_0$  ,  $\epsilon$  ,  $\sigma_0$  ,  $n$  are the strength coefficient, the initial strain, the true strain, the initial stress and the strain –hardening , respectively.

### 2.3.2 Plasticity

With elastic deformation, a sheet body returns to its original shape when the stress is removed. The stress and strain under elastic loading are related through Hooke's laws. Any stress also causes some strains. Indeed, no plastic deformation occurs until the stress reaches the yield strength. Afterwards, large amounts of plastic deformation occur under continually increasing stress from yield point to fracture point. Yield criteria are mathematical description of combination for stresses necessary to cause yielding [5].

#### 2.3.2.1 Yield criterion

A yield criterion is a postulated mathematical expression of the stress state that causes yielding. The general form is shows in **Equation 2.30**.

$$f(\sigma_x, \sigma_y, \sigma_z, \tau_{yz}, \tau_{zx}, \tau_{xy}) = C \quad (2.30)$$

where  $C$  is constant. For isotropic material, Equation 2.30 can be expressed by principal stresses:

$$f(\sigma_1, \sigma_2, \sigma_3) = C \quad (2.31)$$

For most isotropic ductile metals, the following assumptions are commonly made. Namely, (1) yield strengths in tension and compression are the same ideal deformation analysis. (2) A volume remains constant during plastic deformation. (3) Magnitude of the normal stress is mean expression as shown in **Equation 2.32**.

$$\sigma_m = (\sigma_1 + \sigma_2 + \sigma_3) / 3 \quad (2.32)$$

Assumption of yielding is independent of mean normal stress ( $\sigma_m$ ) that is reasonable because deformation usually occurs by slip area (mechanical shear stresses). Therefore, the yield criteria for isotropic materials consequently have the normal form as shown in **Equation 2.33**.

$$f [(\sigma_2 - \sigma_3), (\sigma_3 - \sigma_1), (\sigma_1 - \sigma_2)] = C. \quad (2.33)$$

If the stress state  $\sigma_1$ ,  $\sigma_2$  and  $\sigma_3$  cause yielding, another stress state that differs only by  $\sigma_m$  causes yielding. The stresses  $\sigma'_1$ ,  $\sigma'_2$ ,  $\sigma'_3$  are called the deviatoric stresses, **Equation 2.34**.

$$\sigma'_1 = \sigma_1 - \sigma_m, \sigma'_2 = \sigma_2 - \sigma_m, \sigma'_3 = \sigma_3 - \sigma_m \quad (2.34)$$

### 2.3.2.2 Tresca criterion

The Tresca criterion postulates that yielding depends on the largest shear stress in the body. With the convention of  $\sigma_1 \geq \sigma_2 \geq \sigma_3$ , this term can be expressed as  $\sigma_1 - \sigma_3 = C$ . The constant C can be found by considering a tension test. In this case,  $\sigma_3 = 0$  and  $\sigma_1 = Y$ , the yield strength at yielding is  $C = Y$ . Therefore this criterion can be expressed as **Equation 2.35**.

$$\sigma_1 - \sigma_3 = Y. \quad (2.35)$$

Yielding in pure shear occurs when the largest shear stress is  $\sigma_1 = k$  and  $\sigma_3 = -\sigma_1 = -k$ , where k is the yield strength in shear. A yield locus is a plot of a yield criterion. **Figure 2.19** is a plot of the Tresca yield locus,  $\sigma_x$  versus  $\sigma_y$ , for  $\sigma_z = 0$ , where  $\sigma_x$ ,  $\sigma_y$ , and  $\sigma_z$  are principal stresses.

$$\sigma_1 - \sigma_3 = 2k. \quad (2.36)$$

### 2.3.2.3 Von Mises criterion

Von Mises criterion postulates that yielding will occur when the value of the root-mean-square of shear stress reaches a critical value. The principal stress expression is **Equation 2.37**.

$$[(\sigma_2 - \sigma_3)^2 + (\sigma_3 - \sigma_1)^2 + (\sigma_1 - \sigma_2)^2] / 3 = C_1 \quad (2.37)$$

or equivalently

$$(\sigma_2 - \sigma_3)^2 + (\sigma_3 - \sigma_1)^2 + (\sigma_1 - \sigma_2)^2 = C_2 \quad (2.38)$$

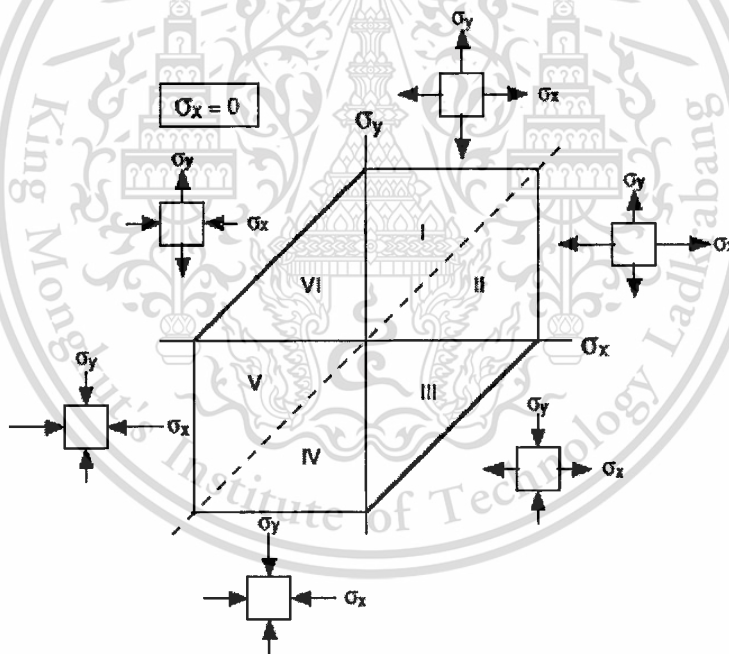
$C_2$  value can be found by a uniaxial tension in a single direction. Substituting  $\sigma_1 = Y$ ,  $\sigma_2 = \sigma_3 = 0$  at yielding, the von Mises criterion postulates yield equation as **Equation 2.39**.

$$(\sigma_2 - \sigma_3)^2 + (\sigma_3 - \sigma_1)^2 + (\sigma_1 - \sigma_2)^2 = 2Y^2 = 6k^2. \quad (2.39)$$

**Figure 2.20** shows the yield locus with  $\sigma_2 = 0$ . In a general form for shear stress consideration, Equation 2.39 can be expressed as **Equation 2.40**.

$$(\sigma_Y - \sigma_Z)^2 + (\sigma_Z - \sigma_X)^2 + (\sigma_X - \sigma_Y)^2 + 6(\tau_{YZ} + \tau_{ZX} + \tau_{XY}) = 2Y^2 = 6k^2. \quad (2.40)$$

Eventually, Tresca and von Mises yield loci are plotted together in **Figure 2.21** for the same values of  $Y$ . The greatest differences point occur for  $\alpha = \sigma_3 / \sigma_1 = -1, 1/2$  and  $2$ . Three-dimensional plots of the Tresca and von Mises yield criteria are shown in **Figure 2.22(a)**. Tresca criterion is a regular hexagonal prism. But, von Mises criterion is a cylinder. Both criteria are centered on a line  $\sigma_1 = \sigma_2 = \sigma_3$ . A projection of these parameters on a plane  $\sigma_1 + \sigma_2 + \sigma_3 = \text{constant}$ . The projective chart is shown in **Figure 2.22(b)**.



**Figure 2.19** Tresca criterion in six sectors by the following conditions:

- I :  $\sigma_y > \sigma_x > 0$ , so  $\sigma_y = Y$
- II :  $\sigma_x > \sigma_y > 0$ , so  $\sigma_x = Y$
- III :  $\sigma_x > 0 > \sigma_y$ , so  $\sigma_x - \sigma_y = Y$
- IV :  $0 > \sigma_x > \sigma_y$ , so  $\sigma_y = -Y$
- V :  $0 > \sigma_y > \sigma_x$ , so  $\sigma_x = -Y$
- VI :  $\sigma_y > 0 > \sigma_x$ , so  $\sigma_y - \sigma_x = Y$

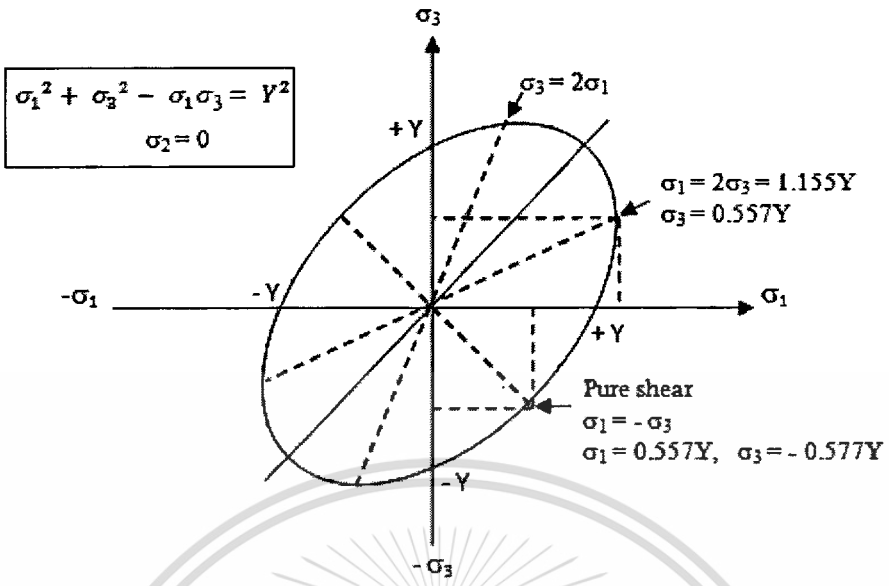


Figure 2.20 Von Mises yield locus

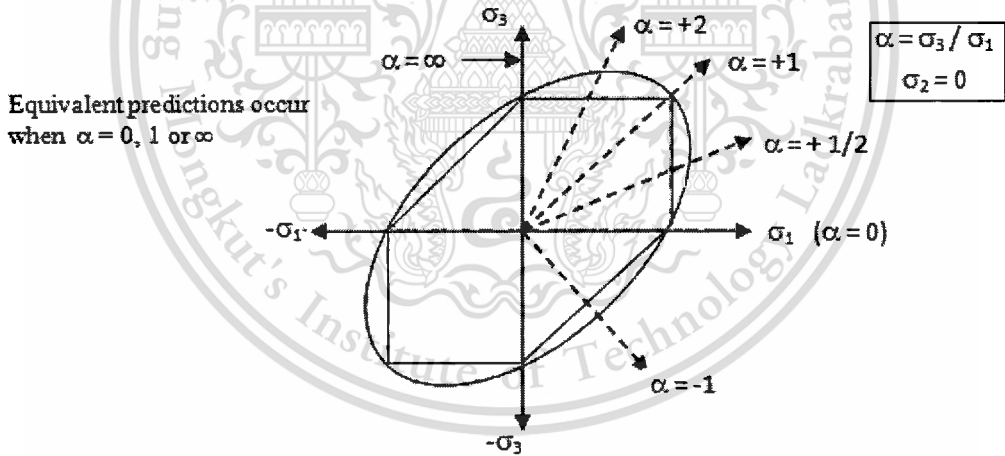
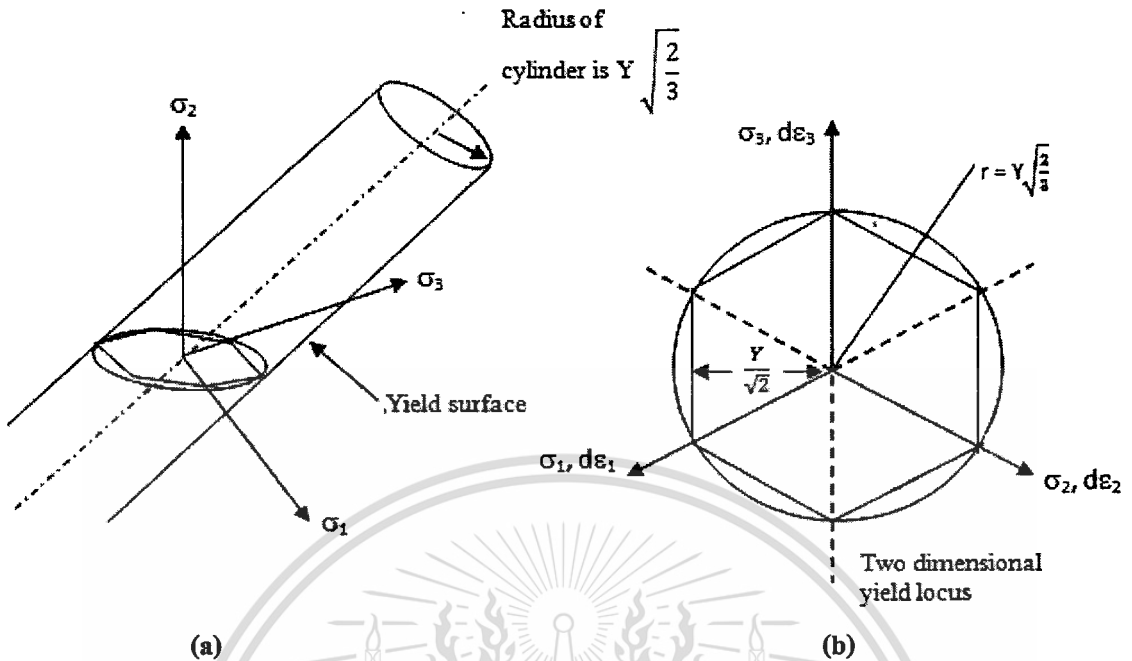


Figure 2.21 Tresca and von Mises loci showing certain loading paths



**Figure 2.22** Schematic diagrams of yield locus, (a) three-dimensional plot of Tresca and von Mises yield criteria, (b) projection of Tresca and von Mises yield criteria onto a plane  $\sigma_1 + \sigma_2 + \sigma_3 = \text{constant}$

#### 2.3.2.4 Plastic work

The differential amount of plastic work per volume associated with strain  $d\epsilon$  of a bar of length ( $l_0$ ), subjected to a force acting on an area is a plastic work equation, **Equation 2.41**.

$$dw = F dl / Al_0 = \sigma d\epsilon \quad (2.41)$$

In the general case, there are three normal stresses and three shear stresses. The plastic work per volume can be expressed as **Equation 2.42**.

$$dw = \sigma_x d\epsilon_x + \sigma_y d\epsilon_y + \sigma_z d\epsilon_z + \tau_{yz} d\gamma_{yz} + \tau_{zx} d\gamma_{zx} + \tau_{xy} d\gamma_{xy} \quad (2.42)$$

Term of principal stresses and strains can be expressed as **Equation 2.43**.

$$dw = \sigma_1 d\epsilon_1 + \sigma_2 d\epsilon_2 + \sigma_3 d\epsilon_3 \quad (2.43)$$

#### 2.3.2.5 Effective stress

Effective stress for a yield criterion is defined that yielding occurs when the magnitude of effective stress reaches a critical value. Von Mises criterion is shown in **Equation 2.44**.

$$\bar{\sigma} = \sqrt{\left(\frac{1}{2}\right) [(\sigma_2 - \sigma_3)^2 + (\sigma_3 - \sigma_1)^2 + (\sigma_1 - \sigma_2)^2]} \quad (2.44)$$

This can be also expressed as **Equation 2.45**.

$$\bar{\sigma} = \sqrt{\left(\frac{1}{2}\right) [(\alpha^2 + 1 + (1 - \alpha)^2)\sigma_1^2]} = \sqrt{1 - \alpha + \alpha^2}\sigma_1 \quad (2.45)$$

where  $\alpha = \sigma_2 / \sigma_1$  and  $\sigma_2 \gg \sigma_3$ ,  $\sigma_3 \approx 0 = \sigma_1$ . Finally, the effective stress of von Mises criterion is shown in **Equation 2.46**.

$$\bar{\sigma} = \sqrt{\sigma_1^2 - \sigma_1\sigma_2 + \sigma_2^2} \quad (2.46)$$

For the Tresca criterion, it is different form (**Equation. 2.47**).

$$\bar{\sigma} = \sigma_1 - \sigma_3 \quad (2.47)$$

where  $\sigma_1 \geq \sigma_2 \geq \sigma_3$

### 2.3.2.6 Effective Strain

The effective strain is incremental plastic work per volume, **Equation 2.48**.

$$dw = \sigma_1 d\varepsilon_1 + \sigma_2 d\varepsilon_2 + \sigma_3 d\varepsilon_3 = \bar{\sigma} d\bar{\varepsilon} \quad (2.48)$$

The von Mises effective strain can be actually expressed as **Equation 2.49**.

$$d\bar{\varepsilon} = \sqrt{[(d\varepsilon_2 - d\varepsilon_3)^2 + (d\varepsilon_3 - d\varepsilon_1)^2 + (d\varepsilon_1 - d\varepsilon_2)^2]}/3} \quad (2.49)$$

or more simply form as

$$d\bar{\varepsilon} = \sqrt{\left(\frac{2}{3}\right) (d\varepsilon_1^2 + d\varepsilon_2^2 + d\varepsilon_3^2)} \quad (2.50)$$

For proportional straining with a constant ratio of  $d\varepsilon_1 : d\varepsilon_2 : d\varepsilon_3$ , the total effective strain is

$$\bar{\varepsilon} = \sqrt{\left(\frac{2}{3}\right) (\varepsilon_1^2 + \varepsilon_2^2 + \varepsilon_3^2)} \quad (2.51)$$

In planar deformation, materials normally have the incremental strain in two or three direction with volume constancy ( $\varepsilon_x + \varepsilon_y + \varepsilon_z = 0$ ). Therefore, strain in each axis is  $\varepsilon_x = \varepsilon_1$ ,  $\varepsilon_y = \varepsilon_2$ ,  $\varepsilon_z = \varepsilon_3$  and  $\varepsilon_3 = -\varepsilon_1 - \varepsilon_2$ . Substituting those strains into **Equation 2.51**, its form becomes **Equation 2.52**. When the von Mises criterion and the effective stress are used, the von Mises effective strain must be used.

$$\bar{\varepsilon} = \frac{2}{\sqrt{3}} \sqrt{(\varepsilon_1^2 + \varepsilon_1 \varepsilon_2 + \varepsilon_2^2)} \quad (2.52)$$

This result should be realized that the  $\sigma - \varepsilon$  relationship curve in a tension test is the  $\bar{\sigma} - \bar{\varepsilon}$  curve, since  $\bar{\sigma}$  reduces to  $\sigma$  and  $\bar{\varepsilon}$  reduces to  $\varepsilon$  in the tension test. The strain hardening exponent and the strength coefficient can also be obtained by the  $\bar{\sigma} - \bar{\varepsilon}$  curve found in a tension test.

### 2.3.2.7 Derivation of the von Mises effective strain

The incremental work per volume is  $dw = \sigma_1 d\varepsilon_1 + \sigma_2 d\varepsilon_2 + \sigma_3 d\varepsilon_3 = \bar{\sigma} d\bar{\varepsilon}$ . Simple form that considers a stress state with  $\sigma_3 = 0$  is Equation 2.53.

$$\bar{\sigma} d\bar{\varepsilon} = \sigma_1 d\varepsilon_1 + \sigma_2 d\varepsilon_2 = \sigma_1 d\varepsilon_1 (1 + \alpha \rho) \quad (2.53)$$

Where  $\alpha = \sigma_2 / \sigma_1$  and  $\rho = d\varepsilon_2 / d\varepsilon_1$ . Then, the reduced form is shown in Equation 2.54.

$$d\bar{\varepsilon} = d\varepsilon_1 (\sigma_1 / \bar{\sigma}) (1 + \alpha \rho) \quad (2.54)$$

Form the flow rule,  $\rho = d\varepsilon_2 / d\varepsilon_1 = [\sigma_2 - (1/2)\sigma_1] / [\sigma_1 - (1/2)\sigma_2] = (2\alpha - 1) / (2 - \alpha)$  or

$$\alpha = (2\rho + 1) / (2 + \rho) \quad (2.55)$$

Combining Equation 2.54 and Equation 2.55, we can get Equation 2.56:

$$d\bar{\varepsilon} = d\varepsilon_1 (\sigma_1 / \bar{\sigma}) [2(1 + \rho + \rho^2) / (2 + \rho)] \quad (2.56)$$

With  $\sigma_3 = 0$ , the von Mises expression for  $\bar{\sigma}$  is Equation 2.57.

$$\bar{\sigma} = \sqrt{\sigma_1^2 - \sigma_1 \sigma_2 + \sigma_2^2} = (1 - \alpha + \alpha^2)^{1/2} \sigma_1 \quad (2.57)$$

Combining Equation 2.55 and Equation 2.56, we can get Equation 2.58.

$$\frac{\sigma_1}{\bar{\sigma}} = \left( \frac{2+\rho}{\sqrt{3}} \right) / (1 + \rho + \rho^2)^{1/2} \quad (2.58)$$

Since  $\rho = d\varepsilon_2 / d\varepsilon_1$ ,

$$d\bar{\varepsilon} = \frac{2}{\sqrt{3}} \sqrt{(d\varepsilon_1^2 + d\varepsilon_1 d\varepsilon_2 + d\varepsilon_2^2)} \quad (2.59)$$

Now since with constant value is  $d\varepsilon_1^2 + d\varepsilon_2^2 + d\varepsilon_3^2 = 0$ .

From volume consistency of axial strains, therefore, we get the incremental strain as Equation 2.60.

$$d\varepsilon_1^2 + d\varepsilon_2^2 + (-d\varepsilon_1 - d\varepsilon_2)^2 = 2(d\varepsilon_1^2 + d\varepsilon_1 d\varepsilon_2 + d\varepsilon_2^2) \quad (2.60)$$

Finally, Equation 2.59 becomes Equation 2.61.

$$d\bar{\epsilon} = \sqrt{\left(\frac{2}{3}\right) (d\epsilon_1^2 + d\epsilon_2^2 + d\epsilon_3^2)} \quad (2.61)$$

This derivation also holds where  $\sigma_3 \neq 0$ , since this is equivalent to a stress state as

$$\sigma_1' = \sigma_1 - \sigma_3, \quad \sigma_2' = \sigma_2 - \sigma_3, \quad \sigma_3' = \sigma_3 - \sigma_3 = 0$$

### 2.3.2.8 Thin – walled structure of cylindrical pressure vessel

The longitudinal stress in thin – walled structure of cylindrical vessel that is forced by internal hydraulic pressure can be expressed as Equation 2.62.

$$\sigma_{\phi p} = \frac{P_i r_0}{2t_p} \quad (2.62)$$

## 2.3.3 Plastic Anisotropy

### 2.3.3.1 Crystallographic basis

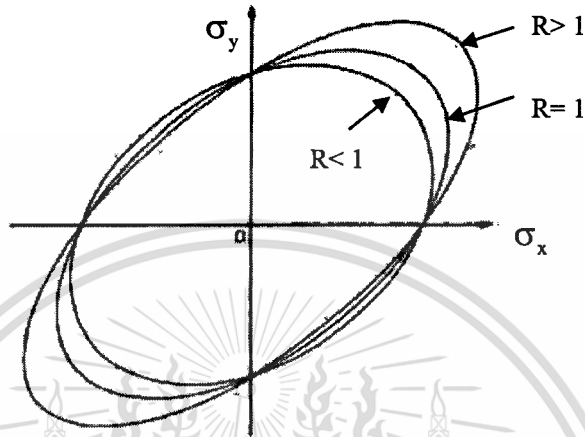
The primary cause of anisotropy of plastic properties is preferred orientation of grains. Mechanical working of metals produces preferred orientations or crystallographic textures. Recrystallization during annealing usually changes the crystallographic texture but it doesn't cause randomness. When a tensile specimen cut from a sheet is extended, slip can easily occur on the prism planes. Even though the yield strength may be almost unchanged with the orientation of the tensile specimen relative to the rolling direction, the material is not isotropic. Slip on the prism planes causes contraction in the plane of the sheet. A useful parameter to describe this sort of anisotropy is the ratio  $R$  of the plastic strain in the width direction to that in the thickness direction,

$$R = \frac{\epsilon_w}{\epsilon_t} \quad (2.63)$$

Where,  $\epsilon_w$  and  $\epsilon_t$  are the contractile strains in the width and thickness directions. For an isotropic material, the ratio  $R$  is 1. A high  $R$ -value suggests that there is a high resistance to thinning and a high strength in biaxial tension state of the sheet. Figure 2.23 illustrates schematically how  $R$  value affects shapes of yield loci for textured materials with rotational symmetry. Although the  $R$ -value is defined as the ratio of width-to-thickness strains, the thickness strain of a thin sheet cannot be measured. Instead the thickness strain is found from width and length strains,  $\epsilon_t = (\epsilon_w + \epsilon_l)$ . The  $R$ -values vary

with the test direction in the plane of the sheet. It is customary to define an average value as **Equation 2.64**.

$$\bar{R} = \frac{R_0 + 2R_{45} + R_{90}}{4} \quad (2.64)$$



**Figure 2.23** *R* values effect on the shapes of the yield loci for textured materials

### 2.3.3.2 Hill's anisotropic plasticity theory

In 1948, Hill advanced a quantitative treatment of plastic anisotropy without regard to its crystallographic basis. He assumed materials with three orthogonal axes of anisotropy,  $x$ ,  $y$ , and  $z$  about which the properties have two-fold symmetry. The  $yz$ ,  $zx$ , and  $xy$  planes are planes of mirror symmetry. In a rolled sheet, it is conventional to take the  $x$ ,  $y$ , and  $z$  axes as the rolling direction, the transverse direction, and the sheet-plane normal. Theory also assumes equal tensile and compressive yield strengths in every direction. The proposed yield criterion is a generalization of the von Mises criterion,

$$F(\sigma_Y - \sigma_Z)^2 + G(\sigma_Z - \sigma_X)^2 + H(\sigma_X - \sigma_Y)^2 + 2L\tau_{YZ}^2 + 2M\tau_{ZX}^2 + 2N\tau_{XY}^2 = 2f(\sigma_{ij})^2 \quad (2.65)$$

where,  $F$ ,  $G$ ,  $H$ ,  $L$ ,  $M$ , and  $N$  are constants that describe anisotropy values. Note that if  $F = G = H = 1$  and  $L = M = N = 3$ , this reduces to von Mises criterion. The constants  $F$ ,  $G$ , and  $H$  can be evaluated from simple tension tests. Let  $x$  direction yield strength be  $X$ . At yielding in an  $x$ -direction tension test,  $\sigma_x = X$  and  $\sigma_y = \sigma_z = \tau_{ij} = 0$ . Substituting into equation 2.65,  $(G + H)X^2 = 1$ . Similarly,

$$X^2 = \frac{1}{G+H} \quad , \quad Y^2 = \frac{1}{H+F} \quad \text{and} \quad Z^2 = \frac{1}{F+G} \quad (2.66)$$

Solving simultaneously,

$$\begin{aligned} F &= (1/Y^2 + 1/Z^2 - 1/X^2) / 2 \\ G &= (1/Z^2 + 1/X^2 - 1/Y^2) / 2 \\ H &= (1/X^2 + 1/Y^2 - 1/Z^2) / 2 \end{aligned} \quad (2.67)$$

where, Y and Z are the y and z direction yield strengths. However, measurement of Z is not feasible for sheets. Using **Equation 2.68**

$$d\varepsilon_{ij} = d\lambda [\partial f(\sigma_{ij}) / \partial \sigma_{ij}] \quad (2.68)$$

The flow rules are

$$\begin{aligned} d\varepsilon_x &= d\lambda [H(\sigma_x - \sigma_y) + G(\sigma_x - \sigma_z)], \quad d\varepsilon_{yz} = d\varepsilon_{zy} = d\lambda L \tau_{yz} \\ d\varepsilon_y &= d\lambda [H(\sigma_y - \sigma_z) + G(\sigma_y - \sigma_x)], \quad d\varepsilon_{zx} = d\varepsilon_{xz} = d\lambda M \tau_{zx} \\ d\varepsilon_z &= d\lambda [H(\sigma_z - \sigma_x) + G(\sigma_z - \sigma_y)], \quad d\varepsilon_{xy} = d\varepsilon_{yx} = d\lambda N \tau_{xy} \end{aligned} \quad (2.69)$$

To derive these flow rules the yield criterion must be written with the shear stress terms appearing as

$$L(\tau_{yz}^2 + \tau_{zy}^2) + M(\tau_{zx}^2 + \tau_{xz}^2) + N(\tau_{xy}^2 + \tau_{yx}^2) \quad (2.70)$$

Note that in case of constant volume:  $d\varepsilon_x + d\varepsilon_y + d\varepsilon_z = 0$ . The constant N can be found from a tension test made at an angle  $\theta$  to the x - axis.

## 2.4 Determination of Stress – Strain Curve of Sheet Metal

The simple approach to stress – strain curve determination has various methods depending on workpiece shape, force action and loading condition. The objective of testing is to determine true stress and true strain of the materials for use in deformation study. The hydraulic bulge testing is popularly alternative method. With testing sheet metal, the workpiece is deformed under the biaxial stress state whereby the workpiece is clamped around edges by fluid pressure as illustrated in **Figure 2.24**. The bulge shape is assumed as spherical dome. The tensile stresses are **Equation 2.71**.

$$\bar{\sigma} = \sigma_\theta = \sigma_\varphi = P_\rho / 2t \quad (2.71)$$

where, P is the forming pressure,  $\rho$  is the radius of curvature, t is the thickness. The effective strain can be expressed as **Equation 2.72**.

$$\bar{\varepsilon} = -2\varepsilon_\theta = 2\varepsilon_\varphi = \ln(t / t_0) \quad (2.72)$$

The advantage of bulge testing is that it can be carried out to much higher strains than tension testing.

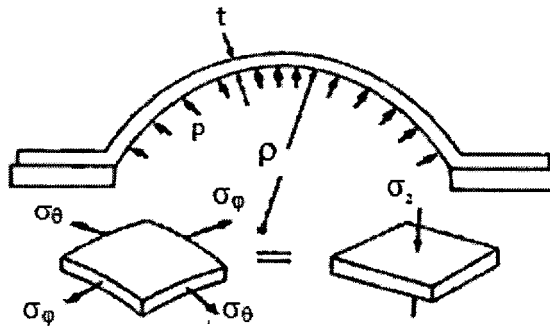


Figure 2.24 A schematic diagram of a sheet bulge test

## 2.5 Literature Reviews

Fuchizawa and Narazaki, “Bulge test for determining stress-strain characteristics of thin-walled tubes”, in their study, a simple approach for determining flow stress curve is the hydraulic bulge test. They proposed a mathematical model suitable for determination of effective stress-strain relationship (flow stress curve). Material properties of the tubes obtained from the bulge test such as flow stress, strain hardening, anisotropy, yield strength, etc. are not the same value as the sheet tensile test, because the tensile test applies a uniaxial tension. On the other hand, the tube bulge test applies tension in a biaxial stress state. The total strain and membrane theories to derive a differential equation of the relationships between the thin-walled tube profile, the thickness distribution, and the forming pressure were analyzed. The tube profile at the free bulge region was assumed as a circular arc. In their experiment, mechanical property with the material definition is that the testing methods (i.e. tensile test and bulge test) were used. Internal pressure forms the tube whereby the tube blank was stretched under the biaxial stress state. Two ends of the tube were fixed. The effective stress-strain relationship was obtained from meridian radius ( $\rho_\phi$ ) and hoop radius ( $\rho_\theta$ ) of curvature of the deformed tube. The meridian radius ( $\rho_\phi$ ) and hoop radius ( $\rho_\theta$ ) were required to calculate stress components on the basis of force equilibrium equations. Consequently, the system of tube bulge testing must be equipped with devices capable of measuring the meridian radius. Finally, flow stress data obtained from the bulge test was defined as mechanical properties of the tube in FEA simulation. FE simulation was found that result of the FEA simulation showed of accurately plastic deformation that was approximate to the experimental result.

**YingYot Aue-u-lan, Muammer Koc, Taylan Altan, “On the characteristics of tubular materials for hydroforming experimentation and analysis”**, their study is about characterization and specification of tubular material properties under hydroforming conditions. An analytical model that was made by T. Sokolowski Model [8] is used for flow stress determination. The sheet tensile test is done under a uniaxial state, but, the tube bulge test is the biaxial state. The required tubing has normal properties as follows: (1) high expansion, uniform deformation characteristics, (2) low anisotropy, high strength coefficient (K) and high strain hardening exponent (n), (3) straight and parallel edges, (4) good finish surface and free of scratches for, (5) better feeding, (f) tight dimensional tolerances. In their experiment, two ends of the tubes were fixed by axial load ( $F_a$ ). The tube was bulged by hydraulic pressure. Internal pressure, bulge diameter and thickness distribution were measured. Measured parameter values were converted into true stress–strain by power law. Measurement of curvature radius in hoop direction ( $r_q$ ) and longitudinal direction ( $r_z$ ), internal pressure ( $P_i$ ), axial load ( $F_a$ ), and thickness ( $t$ ) were performed. The bulge test methods for flow stress determinations were proposed as follows:

1. **Method A: all parameters were measured**, for measurement method, lasers, ultrasonic or non-touching sensors were used to measure the internal pressure and the bulge shape. Bulge height was measured (‘on-line’) in different stages of bulging for the same tube. Finite strains ( $\epsilon_q$ ), ( $\epsilon_z$ ), and ( $\epsilon_r$ ) were calculated for the incremental strains. Effective strain was obtained from relationship between hoop strain and longitudinal strain. Stresses in hoop and longitudinal directions were calculated. Effective stress and effective strain were curved by Power law. SS 304 tubular materials were conducted to the hydraulic bulge test.

2. **Method B: all parameters were measured ‘off-line’ and  $r_z$  was calculated**, Method B was used when Method A (on-line), measure of thickness ( $t_p$ ) and ( $r_z$ ) was not possible. All parameters were measured after the tubes were bulged and taken out of the apparatus. Longitudinal radius ( $r_z$ ) was calculated by exact equation because it is difficult to measure. SS 304 tubular materials were conducted to the bulge test.

3. **Method C:  $r_z$  and  $t_p$  were calculated, the remaining values were measured**, the thickness at the pole ( $t_p$ ) and longitudinal radius ( $r_z$ ) could be derived from analytical model. The Levy– Mises plastic equation was used to find  $P_i$ ,  $r_z$ ,  $F_a$  values. Thickness at the pole ( $t_p$ ) was

obtained. Low carbon steel 1008, SS 304 and aluminum alloy 6260-T4 tubes were used. From their study, Method A results great deformation predictions over Methods B and C.

**Yeong-Maw Hwang, Yi-Kai Lin, Taylan Altan, “Evaluation of tubular materials by a hydraulic bulge test”**, their study aimed to evaluate mechanical properties of two tubes by using hydraulic bulge tests combined with a new analytical model. They proposed that the test tube in the bulge test is deformed under the biaxial stress state and different from the tensile test. The tensile test is a uniaxial stress state. For determination of effective stress – strain curve, the bulge shape of the tube is assumed as follows: (1) profile of the bulge shape of the formed tube is considered as an elliptical surface. (2) The two ends of the tube with a forming length ( $L$ ) are fixed completely. Bulge test apparatus based on simple stand alone hydraulic tooling was referred to Sokolowski’s paper. The internal forming pressure could reach as high as 100MPa. Materials used in their experiment are AA6011 ( $D_0 = 51.91\text{mm}$  and  $t_0 = 1.86\text{ mm}$ ) and SUS409 tubes ( $D_0 = 50.86\text{ mm}$  and  $t_0 = 1.46\text{ mm}$ ). The die entry radius and bulge length for the bulge test were  $R_d = 15\text{ mm}$  and  $L = 60\text{ mm}$ . Six pressure levels versus bulge height ( $h_p$ ) were set.  $P_i$  and  $t_p$  for each level were measured. Tube thickness at the pole, bulge height and internal forming pressure were directly measured simultaneously during the bulge test. The bulge heights were read from a dial-gauge through a modified transmission rod. The tube thickness at the pole ( $t_p$ ) of the tube was measured by a dial gauge combined with a self-designed mechanism. A micrometer was used to measure the bulge diameter of the bulge shape. Circumferential and meridian radii of curvature ( $\rho_\theta$  and  $\rho_\phi$ ) and strains in the hoop and thickness directions were obtained from an analytical model. Von Mises yield criterion, volume constancy theory were used for plastic deformation analysis led to flow stress curve determination. The flow stress curves were obtained from Swift’s law. From their result, FEA simulations with DEFORM 2D”software using flow stress data obtained from the bulge test and the tensile test were used. The internal pressure curve, bulge heights and tube thickness were closer to the experimental results than those by using the flow stress data obtained by Fuchizawa’s model and the tensile test.

For imperfection of the analytical model and FEA simulation, Ying Yot’s model (analytical model) assumed that the tube bulge shape is a perfect profile like a circular arc. Then, Ying Yot’s model considered an inner surface of the bulge shape for flow stress calculations. Ying Yot’s model

did not consider an outer surface of the bulge shape. On the other hand, Hwang's model assumed that the bulge shape of the formed tube is a perfect profile like an elliptical arc. Hwang's model considered a middle surface of the bulge shape for flow stress calculations. The contact point ( $e$ ) and contact angle ( $\phi_e$ ) were calculated for meridian radius of the bulge shape and effective stress – strain relationship. However, Ying Yot's model and Hwang's model did not consider contact angles ( $\phi_e$ ) and effects of  $L/OD$  and  $Rd/t$  ratios for die insert design. These parameters have effects on hydroformability of the tube inside the die cavity.

This study attempts to obtain better research result considering abovementioned parameters with new developed analytical model (SPB model). Die insert and tool design, process design and measurement method are performed. Abovementioned literatures are referred in this research. However, die inserts and forming process designs are investigated by considering the effects of  $Rd/t$  and  $L/OD$ . Namely, proper dimensions of the die insert and the test tube,  $Rd/t$ ,  $L/OD$ , and the pressure loading curve that are the influential parameters for tube free bulge test are obtained. This study presents useful information of parameter definition, tooling selection, guideline design in order to achieve the free bulge test with tube hydroforming process.

## Chapter 3

# Research Methodology

### 3.1 Tooling Design for Free Bulge Test

#### 3.1.1 Design for die inserts

To research on effective validation of an analytical model for flow stress determination of the tubular material, the tube free bulge test is adopted. Special apparatus with the hydroforming process capability consequently is used for this test. The following die designs are first studied by using Finite Element simulation.

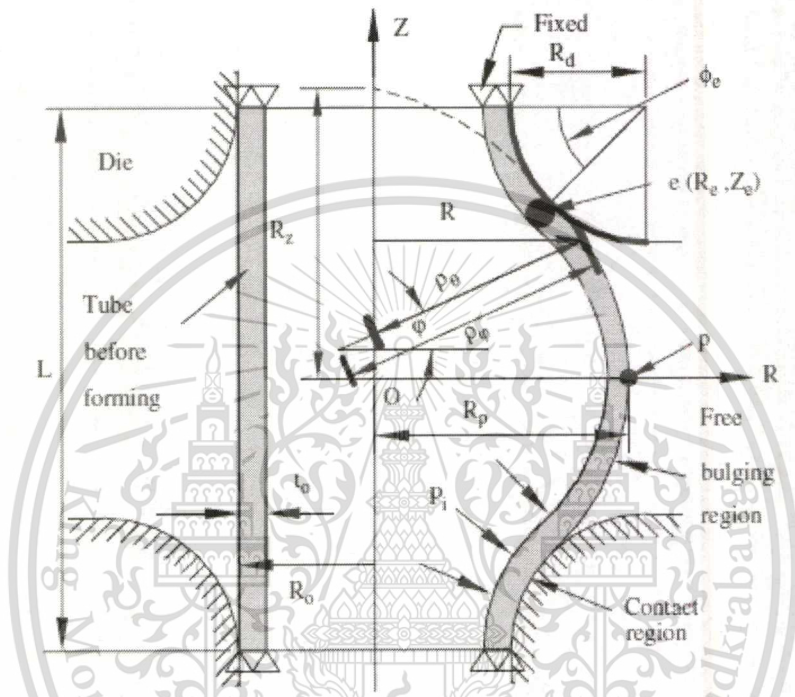
##### 3.1.1.1 Analytical model

An assumption of an elliptical surface of a tube bulge shape is analyzed by considering effects of  $R_d/t$  and  $L/OD$  ratios. All parameters involved to the die insert design and determination of flow stress of tubular materials are shown in **Table 3.1**.

**Table 3.1** Parameters for die insert design and flow stress determination

Nomenclature	
$P_i$ internal pressure	$D_p$ diameter of the bulge profile at vertex (P)
$L_b$ bulge length	$\rho_\theta$ circumferential radius of curvature of the bulge shape
$R_o$ initial outer radius of tube	$\rho_\phi$ meridian radius of curvature of the bulge shape
$R_d$ entrance radius of die inserts	$\rho_{\theta p}$ circumferential radius of curvature of the bulge shape at the vertex (P)
$t_p$ thickness at vertex (p) of bulge	$\rho_{\phi p}$ meridian radius of curvature the bulge shape at the vertex (P)
$R_e, Z_e$ coordinates of contact point e	$\epsilon_o$ initial yield strain of material
$K$ strength coefficient of material	$\epsilon_{\theta p}$ strain in the hoop direction at vertex (P)
$n$ strain hardening of material	$\epsilon_{tp}$ strain in thickness direction at vertex (P)
$\phi_e$ contact angle at the die surface	$\sigma_{\theta p}$ stress in circumferential direction at vertex (P)
$R_p$ half length of minor axes of an elliptical tube surface	$\sigma_{\phi p}$ stress in meridian direction at vertex (P)
$R_z$ half length of major axes	$\bar{\sigma}, \bar{\epsilon}$ effective stress and effective strain
$t_o$ initial tube thickness	

In Hwang's model [1], effective stress and effective strain are derived from the hydraulic bulge profile of the tube combined with internal forming pressure. The assumptions of the free bulge profile are the following items. (1) The bulge shape of the forming tube is assumed to be an elliptical surface (see **Figure 3.1**). (2) Two ends of the tube with a bulge length ( $L_b$ ) are completely fixed.



**Figure 3.1** A schematic diagram of tube bulge test [10 - 12]

The coordinate of contact point  $e$ ,  $R_e$  and  $Z_e$  can be expressed as **Equation 3.1** and **Equation 3.2**.

$$R_e = R_0 + R_d(1 - \cos\phi_e) \quad (3.1)$$

$$Z_e = L_0/2 - R_d \sin\phi_e \quad (3.2)$$

where,  $\phi_e$ ,  $L_b$ ,  $R_0$ ,  $R_d$  are the contact angle, the bulge length, the tube outer diameter and the die entrance radius, respectively. The half length of minor and major axes of the elliptical surface,  $R_p$ ,  $R_z$  can be expressed as **Equation 3.3** and **Equation 3.4**.

$$R_p = \sqrt{R_e(R_e + Z_e \tan\phi_e)} \quad (3.3)$$

$$R_z = \sqrt{Z_e(Z_e + R_e \cot\phi_e)} \quad (3.4)$$

Circumferential and meridian radii of curvature at the vertex (p) of the tube bulge shape,  $\rho_{\theta p}$  and  $\rho_{\varphi p}$  can be expressed, respectively, as **Equation 3.5** and **Equation 3.6**.

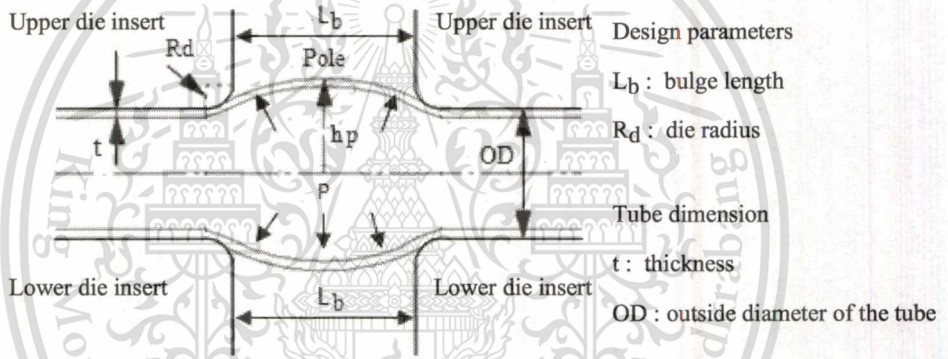
$$\rho_{\theta p} = R_p \quad (3.5)$$

$$\rho_{\varphi p} = R_z^2 / R_p \quad (3.6)$$

These parameters will be used to obtain the flow stress curve of the test tube in next section.

### 3.1.1.2 Finite Element analysis with varied dimension of die inserts

The objective of this FEA simulation for tooling design is to investigate dimensions of the die inserts ( $R_d$  and  $L_b$ ) that allow tube to form a proper free bulge shape. The schematic diagram of the free bulge shape is shown in **Figure 3.2**.



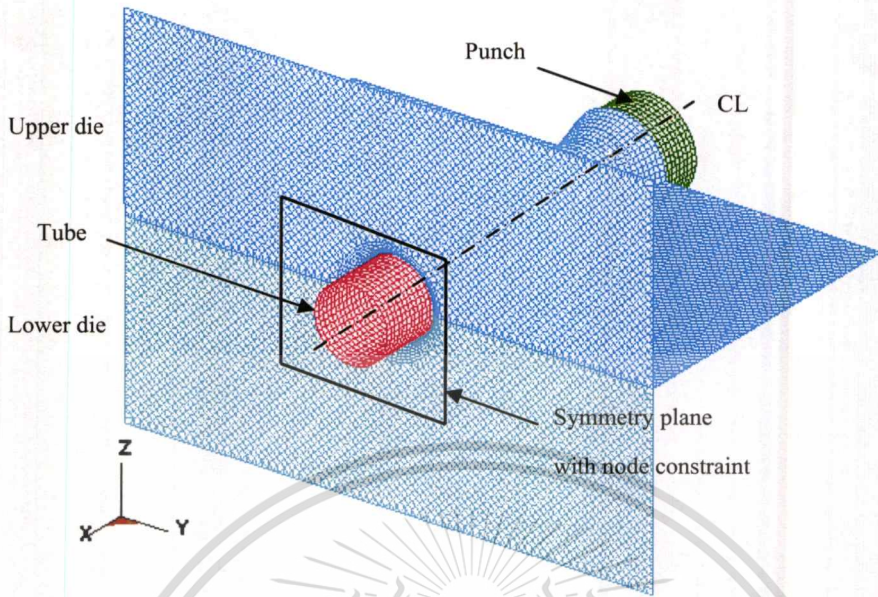
**Figure 3.2** A schematic diagram of free bulge test and design parameters

For **Figure 3.2**,  $R_d$  and  $L_b$  values are die radius and bulge length.  $R_d$  signifies mobility of the tubes into the die cavity.  $L_b$  signifies a bulge ability of the tubes. These factors have effects on tube thickness distributions also. Dimensions of the investigated die insert for FEA simulation are defined in **Table 3.2**.  $R_d$  and  $L_b$  are varied to investigate the forming of the bulge shapes ranging from initial bulge to cracking. Features of the tube and the tools (i.e. tube, upper die, lower die and axial fixing punch) are created by CAD software, UG NX 6. Then each feature is exported to FEA simulation software. All FEA models mainly are created to be a fully meshed model. In order to achieve accurate simulation result with fast explicit analysis, each of FEA model is performed using a half model with nodal constraints on the symmetry plane as shown in **Figure 3.3**.

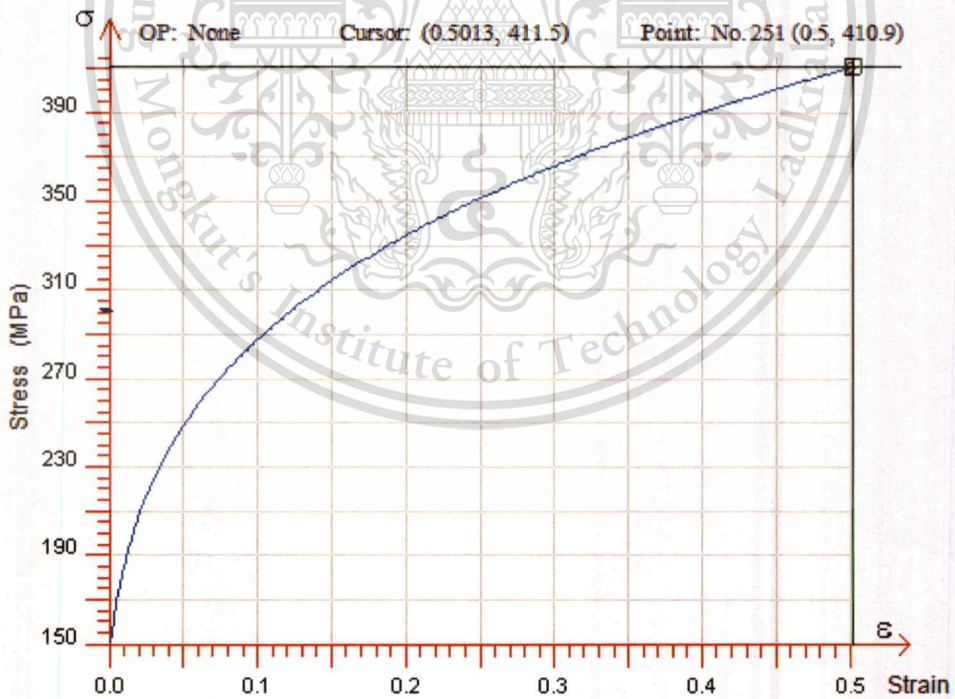
**Table 3.2** Parameters of finite element model for die insert design

Model	R <sub>d</sub> (mm)	t <sub>0</sub> (mm)	R <sub>d</sub> / t <sub>0</sub>	L <sub>b</sub> (mm)	OD (mm)	L <sub>b</sub> / OD
1	5	1	5	25.4	25.4	1
2	5	1	5	38.1	25.4	1.5
3	5	1	5	50.8	25.4	2
4	15	1	15	25.4	25.4	1
5	15	1	15	38.1	25.4	1.5
6	15	1	15	50.8	25.4	2
7	25	1	25	25.4	25.4	1
8	25	1	25	38.1	25.4	1.5
9	25	1	25	50.8	25.4	2

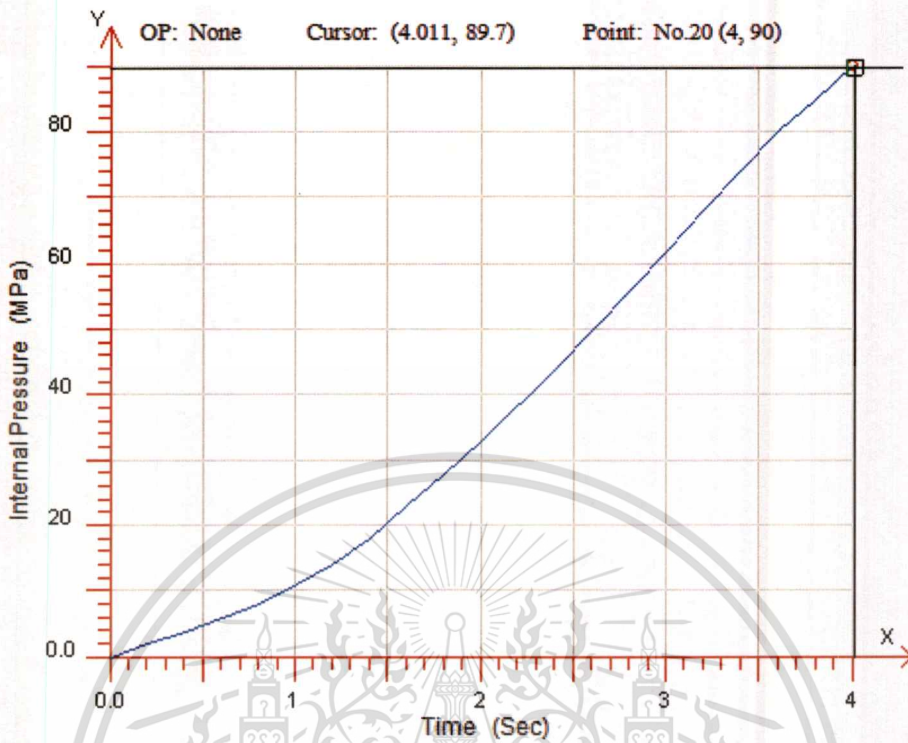
For process simulation of all models, DYNIFORM 5.6.1 is used to conduct the FEA simulations of hydroforming processes. LS - Dyna solver is directly adopted to solve nonlinear problems. FEA model is shown like **Figure 3.3**. The material used for tube blank model is mild steel: CQ (USA Standard), OD = 25.4 mm, thickness = 1 mm. Mechanical properties of tubular material are defined as default of software. Flow stress curve of material is shown in **Figure 3.4**, Yield stress ( $\sigma_y$ ) = 274 MPa, Strength coefficient (K) = 648 MPa and Strain hardening (n) = 0.22. Fluid internal pressure curve (see **Figure 3.5**) that is properly defined values for computational iteration is applied for THF simulation. Heat and temperature are neglected. A constant friction coefficient ( $\mu$ ) of 0.125 is assumed at the interface between the tube and the die insert set. Models of die inserts are assumed to be rigid. The model of the tube is meshed by shell elements at the middle surface. Element size of die mesh is maximum size = 2 mm, minimum size = 0.5 mm. Element size of the tube mesh is maximum size = 1 mm, minimum size = 0.5 mm. Feeding distance of the horizontal punches is zero (fixed). Two ends of the tube are fixed in the closed die. Density of Water =  $9.95e^{-7}$  kg/mm<sup>3</sup> and Bulk modulus = 2200 GPa. Plastic deformation of the tube is in the biaxial stress state.



**Figure 3.3** A half model of finite element simulation on symmetry plane



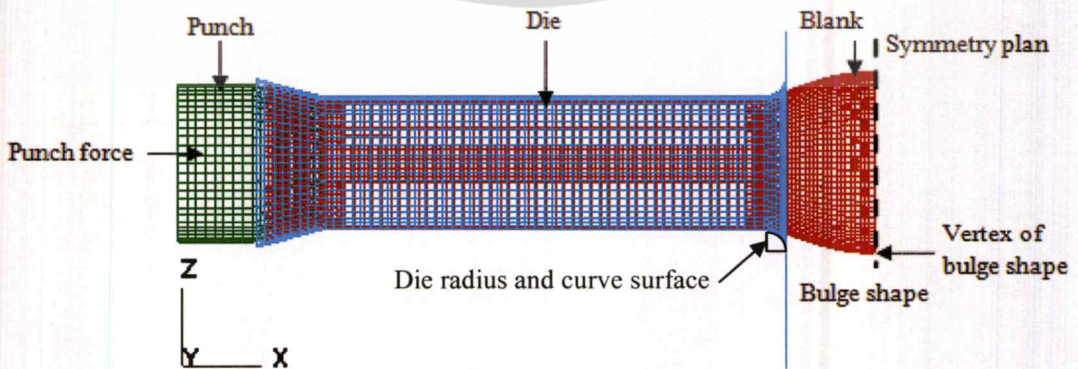
**Figure 3.4** Flow stress curve used for the tube bulging test



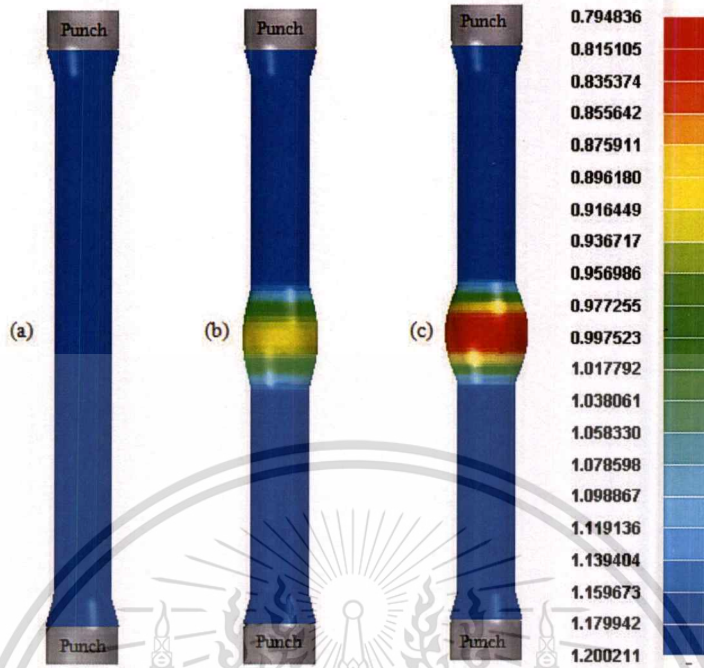
**Figure 3.5** Fluid internal pressure curve used for the tube bulging test

### 3.1.1.3 Results of Finite Element Simulations

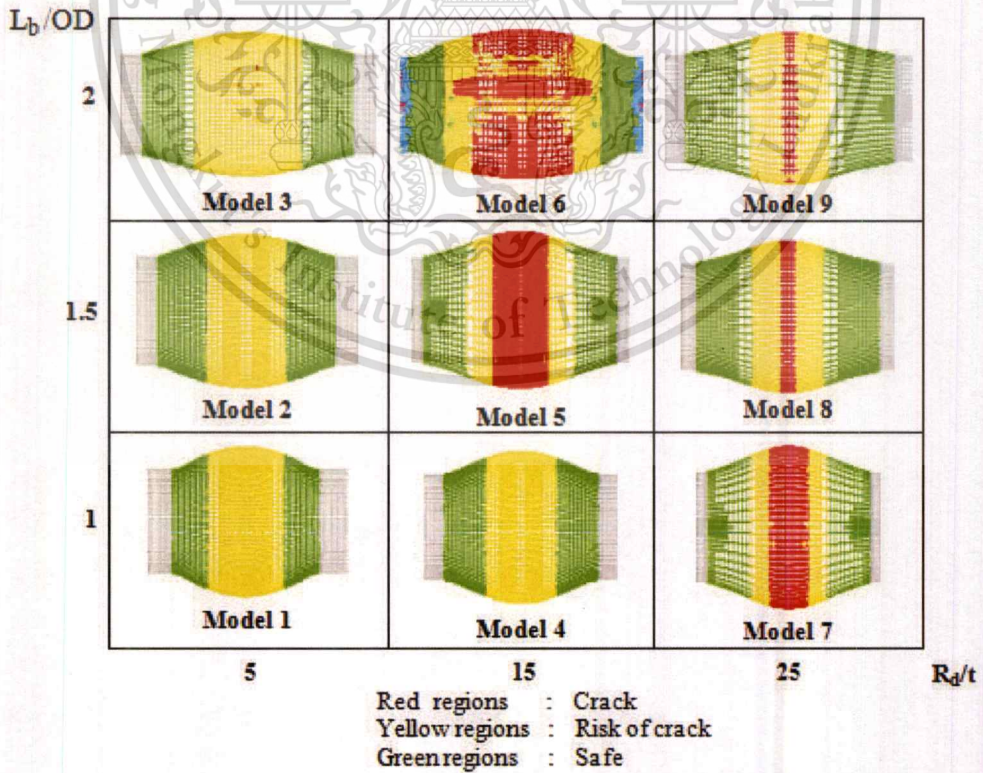
All FEA results of the tube bulging are summarized. The free bulge shape of the tube is considered at the time when a crack is first predicted as shown in **Figure 3.6**. **Figure 3.7** shows the forming tube at various intermediate forming steps. Tube thickness in each model is measured simultaneously while tube is yielding with continuous bulging step.



**Figure 3.6** A half model of FE simulation of tube bulge test

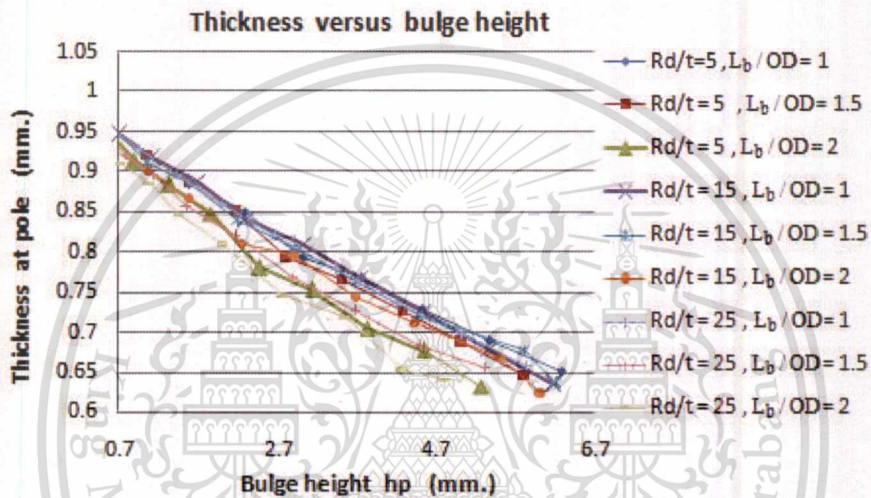


**Figure 3.7** Intermediate forming steps with thickness distributions: (a) tube ends are fixed by punches (b) early deformation by internal pressurization, (c) end of free bulge forming



**Figure 3.8** Comparison of predicted bulge shapes with different die insert geometry

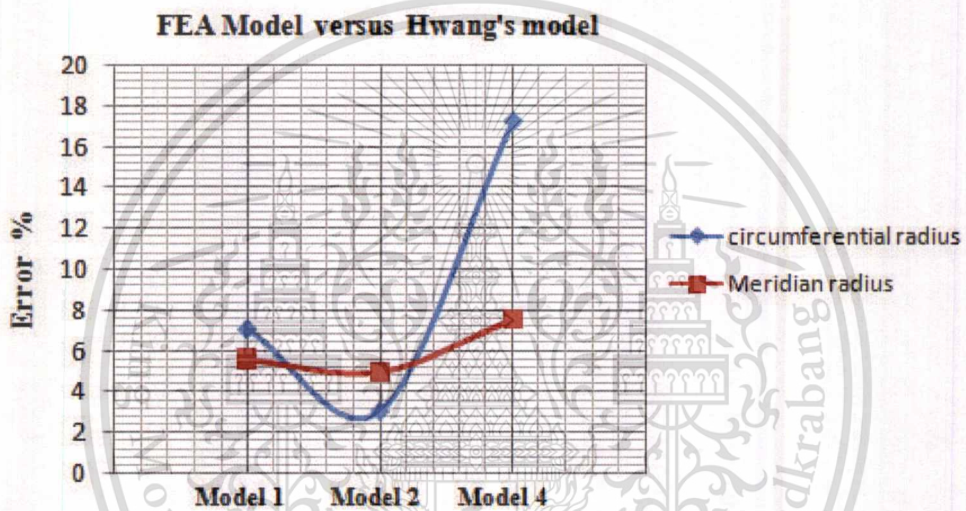
The measured tube thickness at the vertex of the bulge shape along the circumferential direction is considered for all the cases. Moreover, the elliptical surface and risk of cracks at the vertex from nine FEA models are compared and shown in **Figure 3.8**. The thickness versus bulge heights at the vertex is compared with different ratios of  $R_d / t$  and  $L_b / OD$ , in order to determine the bulge shape suitable for flow stress curve determination of the tubes, thus selecting proper die insert dimensions. For comparison of thinning, the thickness versus bulge heights is shown in **Figure 3.9**.



**Figure 3.9** Bulge heights versus thickness at the vertex (P) of the bulge shape

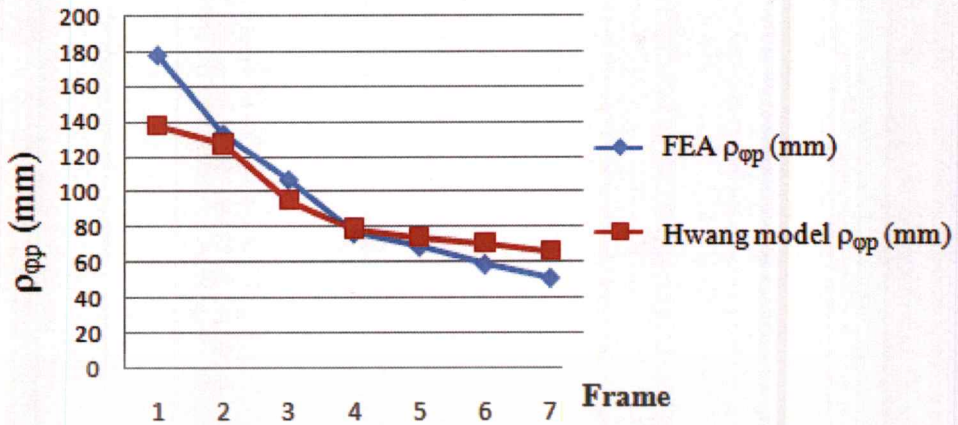
From **Figure 3.8**, it can be seen that Model #3, Model #5, Model #6, Model #7, Model #8, Model #9 have improper bulge shapes because they do not resemble the elliptical shape or the circular shape. Therefore, 6 out of 9 models (i.e. Model #3, Model #5-Model #9) have cracked by the end of the simulation. This leads to a conclusion that Model #1, Model #2, Model #4 seem to be suitable for the testing as they form to be large bulges without any cracks. This is confirmed by larger wall thickness of the three models compared to the rest of the FEA simulation, **Figure 3.9**. In order to select only the best model among the Model #1, Model #2 and Model #4, radii of curvature of the bulge shape, i.e. circumferential radius ( $\rho_{\theta p}$ ) and meridian radius ( $\rho_{\phi p}$ ) are compared with those calculated by Hwang's model. With measurements of the bulge shapes, final bulge shape profiles of three simulated models are exported to be special file (i.e. file nastran.nas) compatible with CAD software. Parameter values ( $R_e$ ,  $Z_e$ ,  $R_p$ ,  $R_z$  and  $\phi_e$ ) of each imported model are measured in CAD software. The

circumferential radius ( $\rho_{\theta p}$ ) and the meridian radius ( $\rho_{\phi p}$ ) are calculated by substituting those measured values for **Equation 3.5** and **Equation 3.6**, respectively. In Hwang's model,  $R_e$ ,  $Z_e$ ,  $R_p$  and  $R_z$  are calculated by substituting known parameters (i.e.  $R_0$ ,  $L_0$ ,  $R_0$ ,  $\phi_e$ ) for Equation 3.1 – Equation 3.4. Then, the circumferential radius ( $\rho_{\theta p}$ ) and the meridian radius ( $\rho_{\phi p}$ ) are calculated by substituting calculated values (i.e.  $R_p$  and  $R_z$ ) for **Equation 3.5** and **Equation 3.6**, respectively. Consequently, comparison of the evaluated curvature between FEA simulation and Hwang's model is shown in **Figures 3.10**, **3.11** and **3.12**.

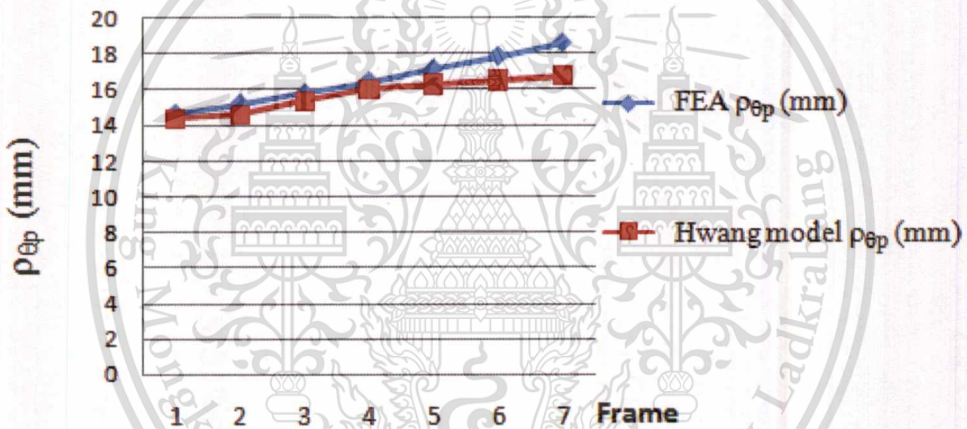


**Figure 3.10** Deviation of simulated bulge curvatures from Hwang's model

**Figure 3.10** graphs the curvature deviations of the simulated Model #1, Model #2, and Model #4 from the corresponding analytical results based on Hwang's model. Model #2 best fits Hwang's model as it shows the least curvature deviations. **Figure 3.11** and **Figure 3.12** show comparisons of the simulated (i.e. from Model #2) and exact curvature (i.e. from Hwang's model). It can be seen that the bulge curvatures (i.e. both circumferential and meridian radii) are approximately close to Hwang's model. Therefore, the model #2 ( $R_d / t = 5$  and  $L_b / OD = 1.5$ ) is the proper die insert geometry for flow stress curve determination experiment. Those values are then chosen for the free bulge test tooling manufacturing.

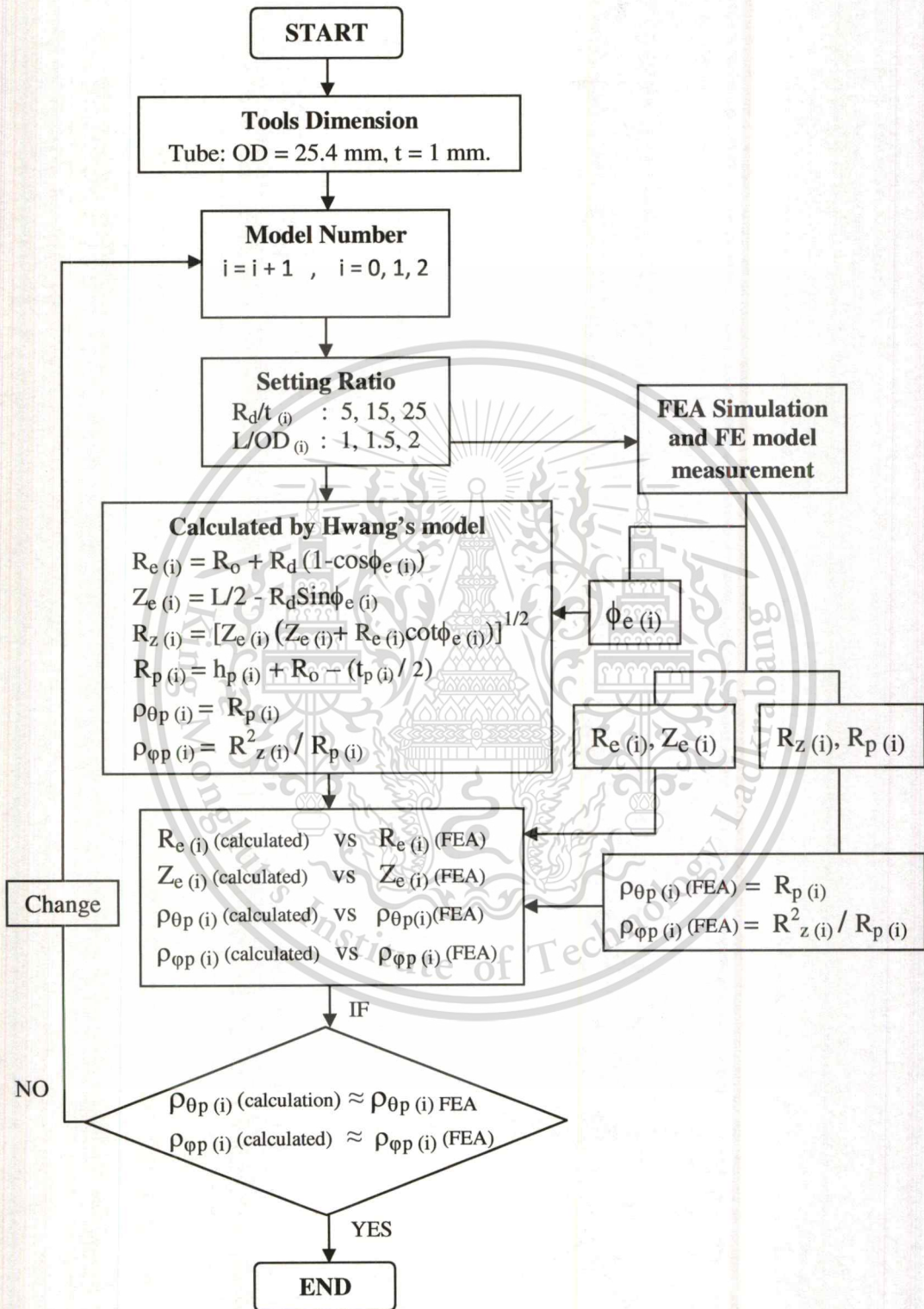


**Figure 3.11** Comparison between meridian radius obtained from FE simulation result and meridian radius calculated by Hwang's model



**Figure 3.12** Comparison between circumferential radius obtained from FE simulation result and circumferential radius calculated by Hwang's model

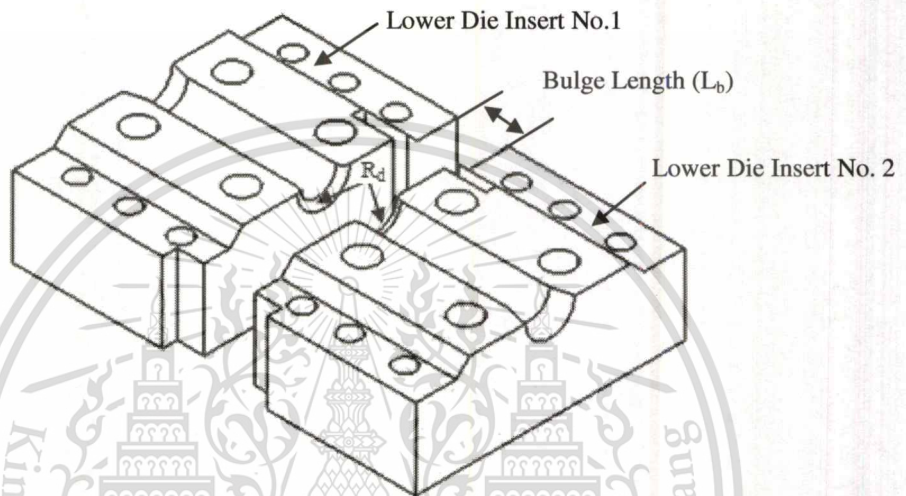
From the die insert design, the die entrance radius ( $R_d$ ) and the bulge length ( $L_b$ ) are investigated by using finite element simulation. The circumferential and meridian radii obtained from FEA simulation are compared with the circumferential and meridian radii calculated by Hwang's model. Finally, the die inserts suitable for free bulge test is model #2 ( $R_d = 5$  mm,  $L_b = 38.1$  mm). A flow chart of die insert design is shown in **Figure 3.13**.



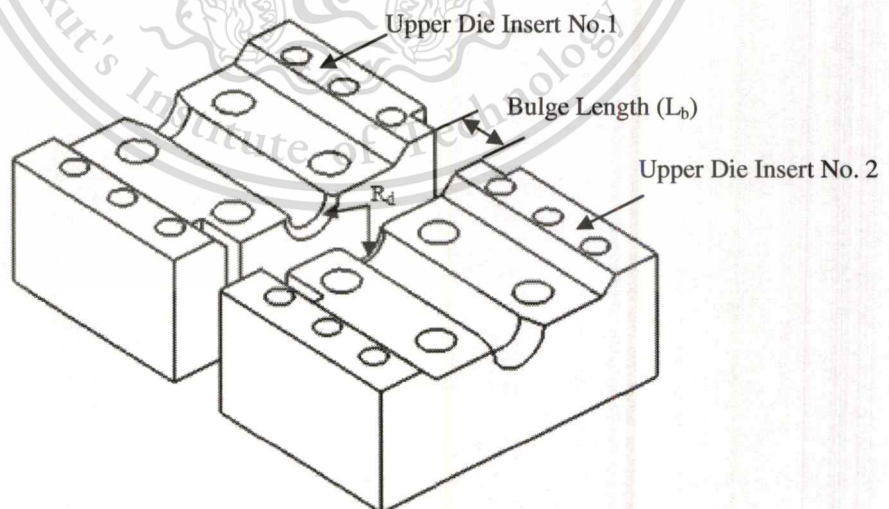
**Figure 3.13** A flow chart of die-insert design

### 3.1.1.4 Features of die inserts

Die inserts in the free bulge test consist of four parts, i.e. upper die inserts No. 1 and No. 2, lower die inserts No. 1 and No. 2. The die inserts are drafted by proper dimensions of the designed model (Model#2 in **Table 3.2**) and manufactured. The features of the die inserts are shown in **Figure 3.14** and **Figure 3.15**.



**Figure 3.14** Features of lower die inserts



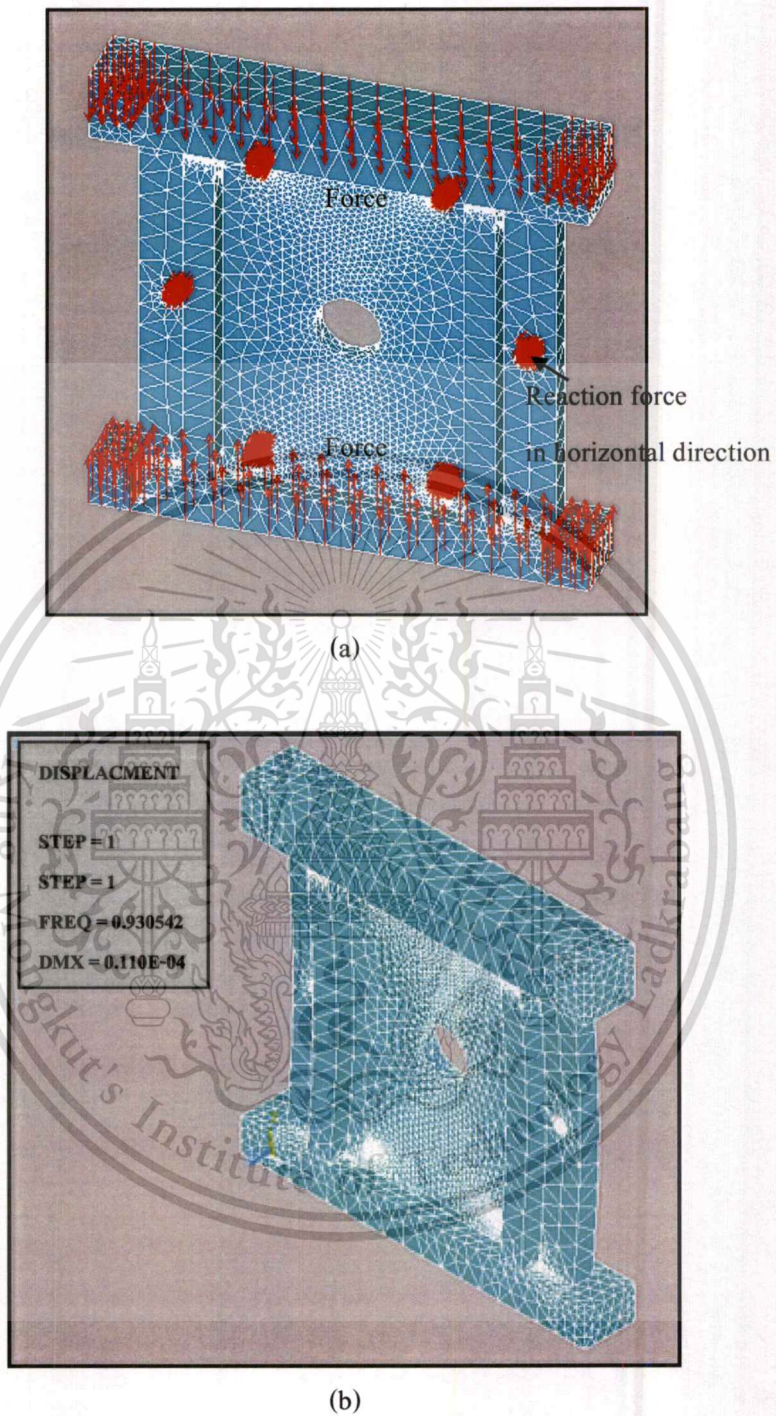
**Figure 3.15** Features of upper die inserts

### 3.1.2 Design for die stands

Maximum vertical loading of 200 ton from the press machine in hydroforming process can potentially destroys die stands and die bases (upper die base and lower die base) in this study. Therefore, the die stands are important parts of bulge test tooling in the hydroforming process. The die stands must be designed suitably for sufficient loading support. For die stand designs, the features and mesh size are created using CAD software with FEA simulation (ANSYS v.12). Principle of mechanics analysis helps to evaluate the part deflection condition and proper geometry parameters. The designed die stand is the solid part of the rectangular shape as shown in **Figure 3.16**. Right-left die stands are specifically designed for optimal supports for maximum punch forces of 50 tons and vertical pressing forces of 200 Tons. In FEA simulation, the vertically applied load is 200 Ton as actual capacity of compressive force. The horizontally applied load of axial punch is 50 Ton and it exerts on the bolt positions. The workpiece is fixed by large bolts. Result of solid mechanics solution is shown in **Figure 3.17**. It is found that the designed die stand can withstand the high compressive force with an insignificant deflection of  $0.11 \times 10^{-4}$  m. in the horizontal direction.



**Figure 3.16** A typical feature of a left die stand



**Figure 3.17** Finite element analysis, (a) compression loads applied, (b) deflection analysis result (Deflection maximum =  $0.110e^{-04}$  m.)

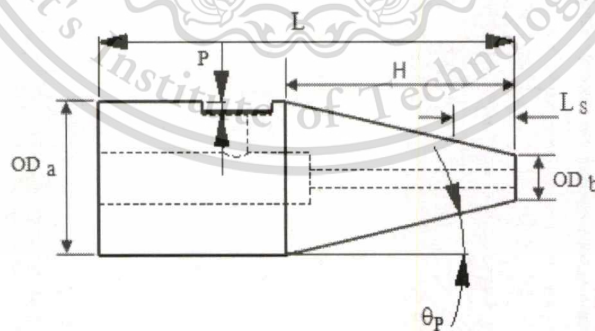
### 3.1.3 Design for axial punches

#### 3.1.3.1 Finite element simulation of tube swaging process

The die design (in Title 3.1.1) considers fixing of two ends of the tube. The axial punches fix the tube ends and seal the internal pressurized water. Therefore, the axial punches must withstand fixing reaction force and sealing force against the internal pressure. In this study, the swaging method is used to expand the two ends of the test tube. The FEA method is used to conduct the simulation of the swaging process for investigating proper taper angles and length of the axial punches. The taper angle and the taper length are defined in each of the FEA model as shown in Table 3.3. Geometry of the axial-punch (swage) is shown in Figure 3.18. The features of the axial punches are created by CAD software, UG NX 6, and exported to explicit FEA software.

**Table 3.3** Punch dimensions of finite element model for tube swaging

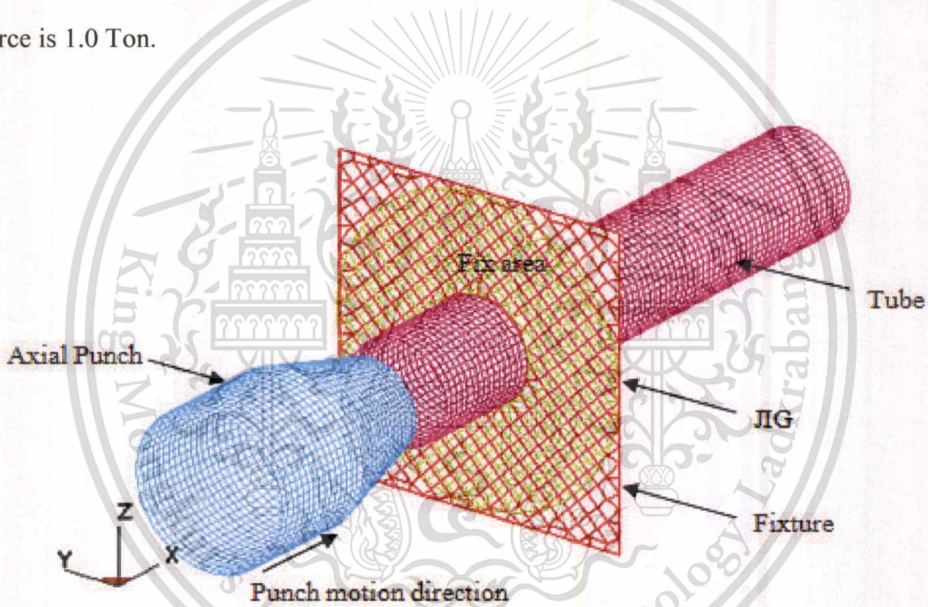
Model	$\theta_p$ (degree)	OD <sub>a</sub> (mm)	OD <sub>b</sub> (mm)	L <sub>s</sub> (mm)
1	10	59.77	20.00	15.00
2	15	59.77	20.00	15.00
3	20	59.77	20.00	15.00
4	25	59.77	20.00	15.00
5	30	59.77	20.00	15.00



**Figure 3.18** Geometry of a punch for tube swaging

Where,  $\theta_p$ , L, L<sub>s</sub>, H, P, OD<sub>a</sub> and OD<sub>b</sub> are the swaging angle, the punch length, the swaging length, the chamfer length, the pocket depth, the initial outer diameter and the final outer diameter of the punch, respectively. OD<sub>a</sub> size is constant and OD<sub>b</sub> must be smaller than inner diameter of the tube

so that the end of the swage can be inserted into the tube.  $H$  value depends on swaging angle ( $\theta_p$ ).  $L_s$  can be defined by axial feeding displacement. FEA model is meshed as shown in **Figure 3.19**. DYNAFORM 5.6.1 is used to conduct the FEA simulations of swaging processes. LS - Dyna solver is directly adopted to solve the nonlinear problem. The tube is fixed by a created JIG FE model. FE Models of tube and punch are assumed as rigid body. The tubular material is mild steel: CQ (USA Standard), OD = 25.4 mm, thickness = 1 mm. Mechanical properties of the tube and punch are defined as default of software (see **Figure 3.4**). The FE models of the tube and the punch are meshed by shell elements at the middle surface of the tube. Element size of the tube and punch meshes is maximum = 1 mm, minimum = 0.5 mm. Feeding distance is defined as values in **Table 3.3**. Punch force is 1.0 Ton.



**Figure 3.19** FEA model for tube swaging process

From FEA simulation results, swaged area of FE tube model (in **Table 3.3**) is measured to evaluate the thickness distributions and swage ability of the axial punch. Thickness distributions of the swaged tube are shown in **Figure 3.20**. It is found that the Model #2 ( $\theta = 15^\circ$  and  $L_s = 15$  mm) and Model #3 ( $\theta = 20^\circ$  and  $L_s = 15$  mm) show optimal stability of thickness distribution and thinning is not over 20 % as shown in **Figure 3.21**. Therefore, Model #2 and Model #3 are suitable for use in fixability evaluation of the axial punch.

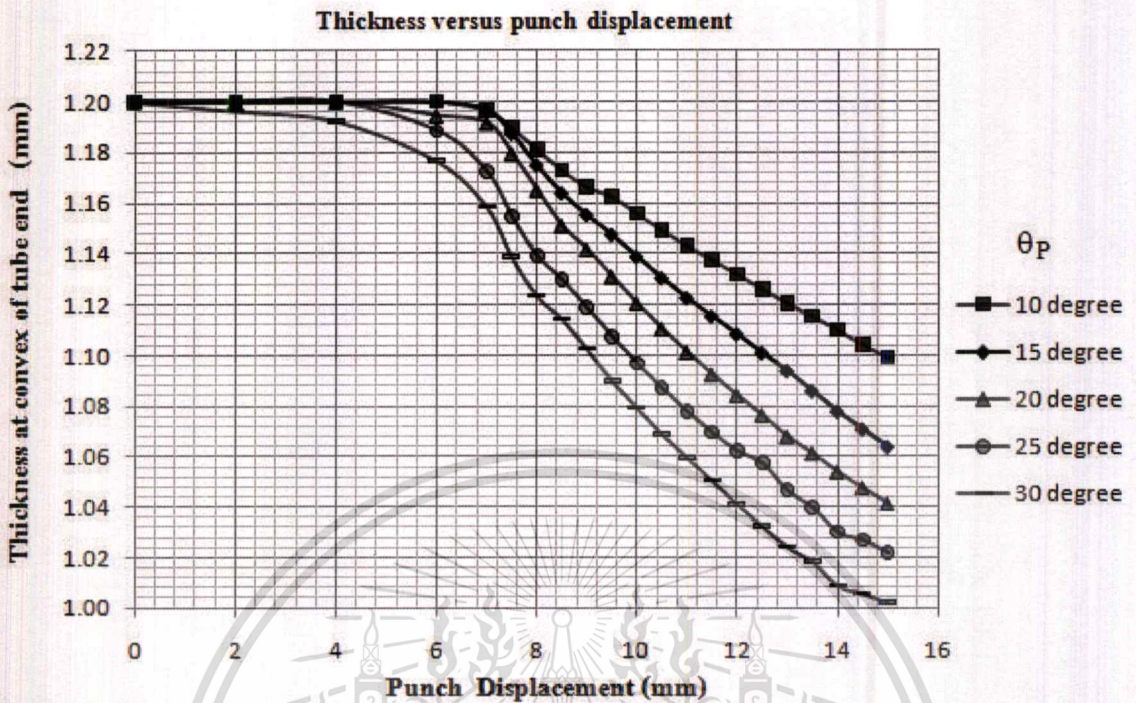


Figure 3.20 Thickness distributions of the swaged tube

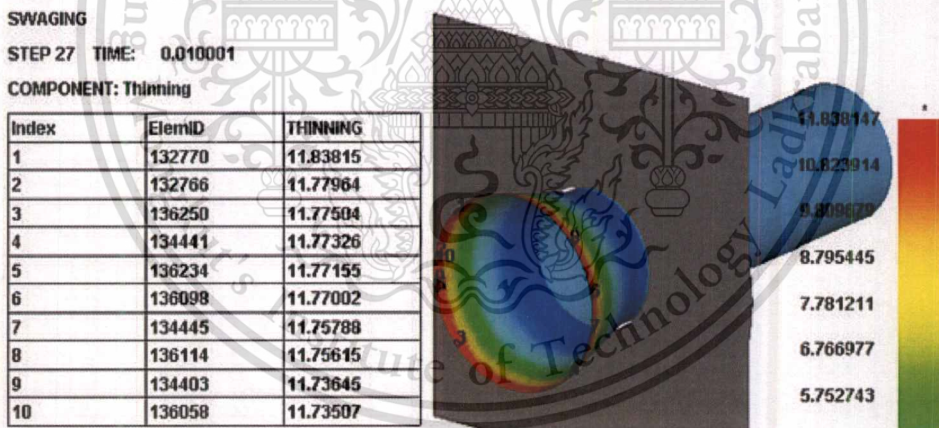


Figure 3.21 Thinning of the swaged tube

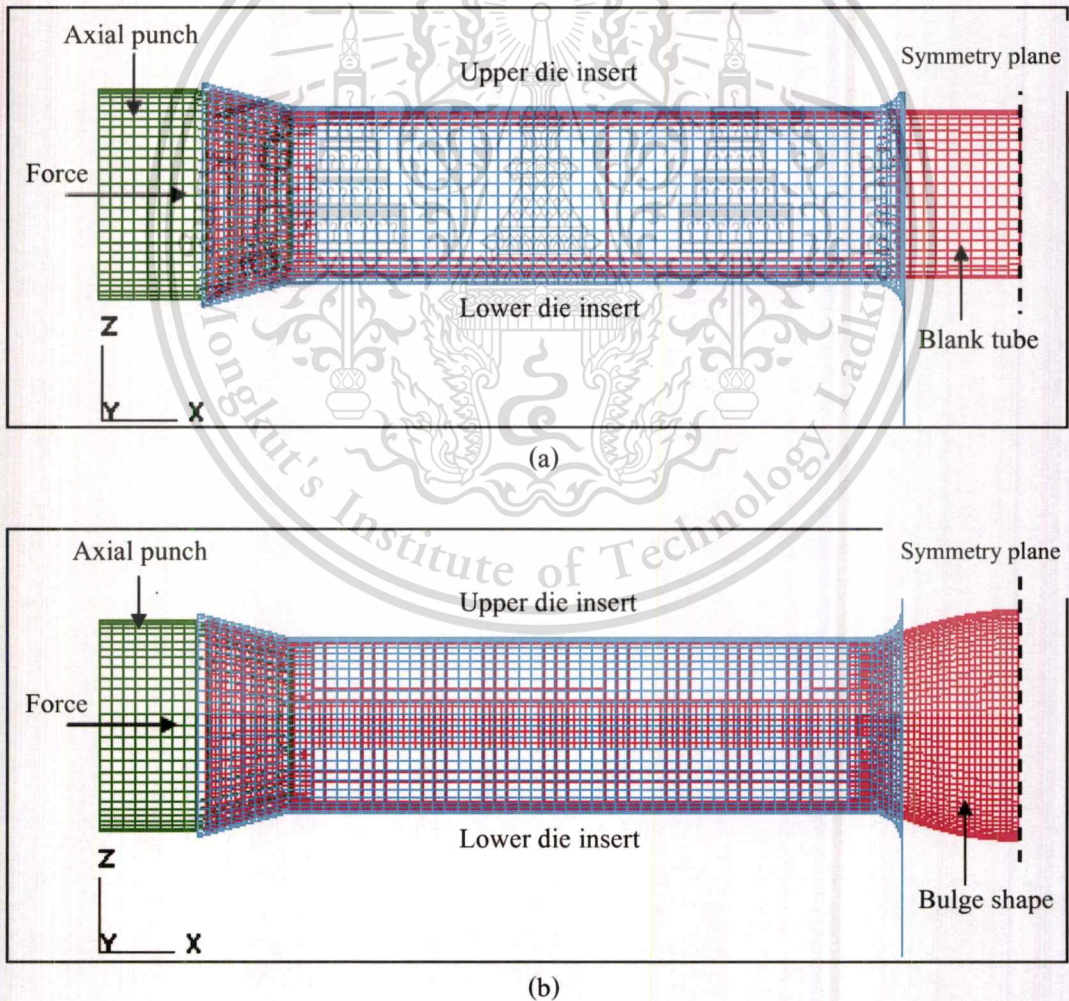
### 3.1.3.2 Finite element simulation for fixability evaluation of the axial punch

With tube hydroforming, high internal forming pressure up to 100 MPa, the axial punches must exert the tube ends with enough for sealing the fluid pressure inside the tube. In FEA simulation, the punches and swaged tubes (in Title 3.1.3.1, Model #2 and Model #3) are used to conduct new FEA simulations (i.e., two FEA models) with tube hydroforming process. To select the proper punch and swaged tube, FEA simulation has the same hydroforming process as the FEA

model of the die insert design (in **Title 3.1.1**). But, the axial punches and swaged tubes of Model # 2 and Model # 3 (in **Table 3.4**) are imported. The axial punch exerts the end of the tube with 1.0 Ton. All of FE simulation models are created using a full mesh. In order to achieve accurate simulation with fast explicit analysis, each of FEA models is performed using a half meshed model with nodal constraints on the symmetry plane as shown in **Figure 3.22**.

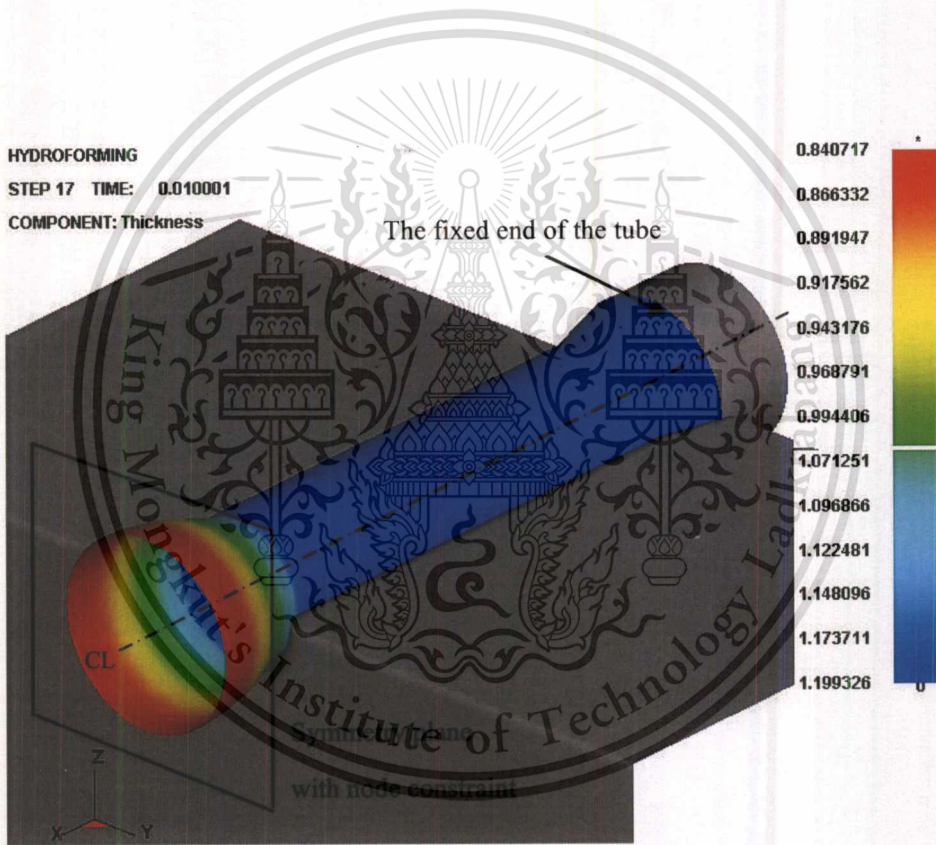
**Table 3.4** Punch dimensions of finite element model for tube fixing evaluation

Model	$\theta_P$ (degree)	$L_S$ (mm)	$OD_a$ (mm)	$OD_b$ (mm)	Punch Force (Ton)
2	15	15.00	59.77	20.00	1.00
3	20	15.00	59.77	20.00	1.00



**Figure 3.22** FEA results of tube fix ability evaluation, (a) before bulge and (b) after bulge

As results of FEA simulation, tube thicknesses throughout fixed areas between Model #2 and Model #3 are compared. Maximum von Mises stresses between Model #2 and Model #3 are compared as shown in **Figure 3.23**. It is found that Model #2 shows the result of reasonable fixability evaluation of the axial punch. Model #2 has the tube thickness values (blue) and the von Mises stress values (light blue) at the end of the swaged tube more than Model#3. Moreover, the swaged end of the tube of Model #2 has more thickness than Model #3 (see **Figure 3.20**). Hence, Model #2 with punch geometry (**Figure3.24**) is the best part and it is manufactured for use in the hydraulic bulge test.

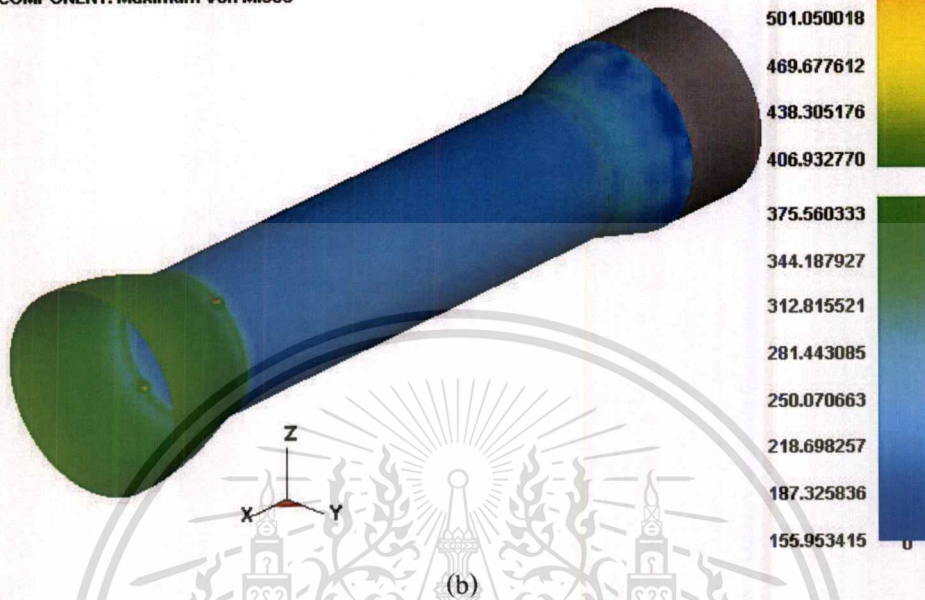


(a)

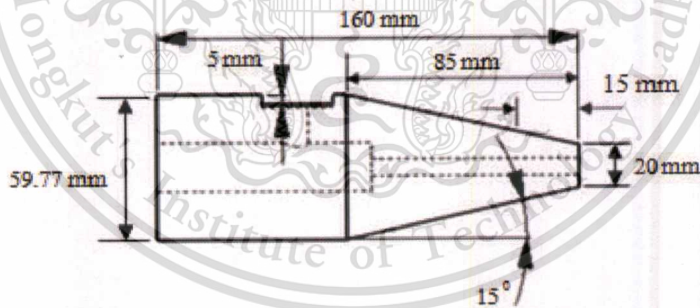
HYDROFORMING

STEP 17 TIME: 0.010001

COMPONENT: Maximum Von Mises



**Figure 3.23** FEA results of Model #2 at the final forming step 17, time : 0.01 msec, (a) thickness distribution contour and (b) maximum Von Mises stress contour

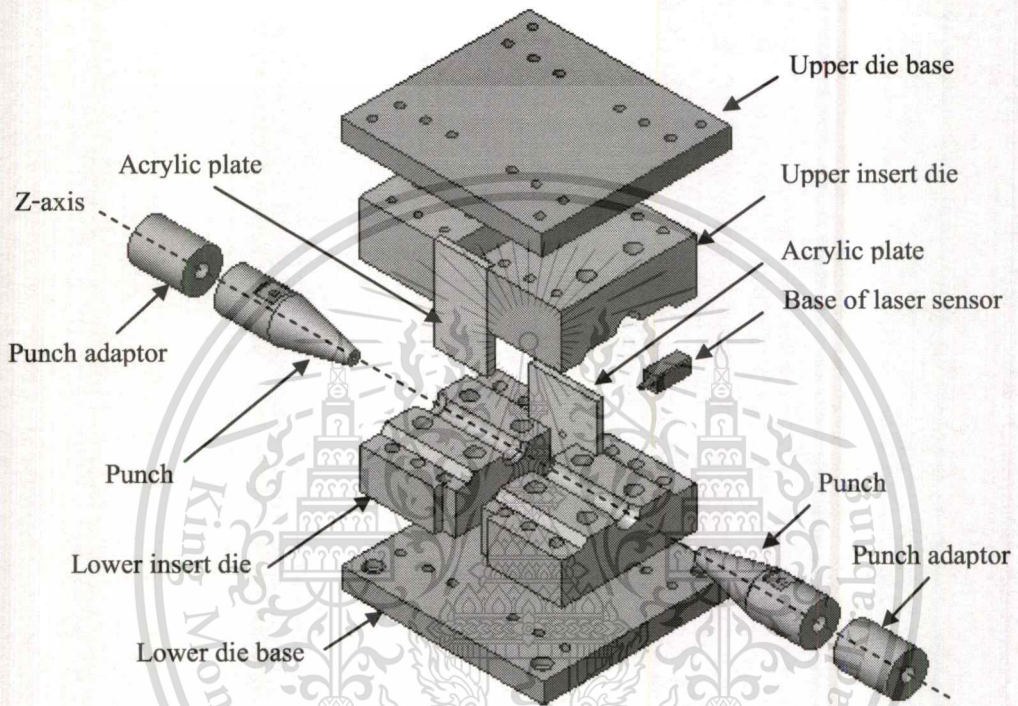


**Figure 3.24** Geometry of the axial punch (Model # 2) for hydraulic bulge test

### 3.2 Tooling Set for Free Bulge Test

The hydroforming tool set for the free bulge test consists of eight parts: (1) two upper dies, (2) two lower dies, (3) two axial punches, (4) upper die and lower die bases, (5) two punch adaptors, (6) base of laser sensor, (7) two acrylic plates and (8) two die stands. In die manufacturing, the materials for die inserts and axial punches are SKD50C steel and S400 steel, respectively. Exploded view of the

tool set is shown in **Figure 3.25**. The designed dies is used for the tube free bulge test in hydroforming process (see **Chapter 4**). Die insert design data and tooling structure are detailed and shown in **Appendix- D**.



**Figure 3.25** Exploded view of tooling set for the hydraulic bulge test

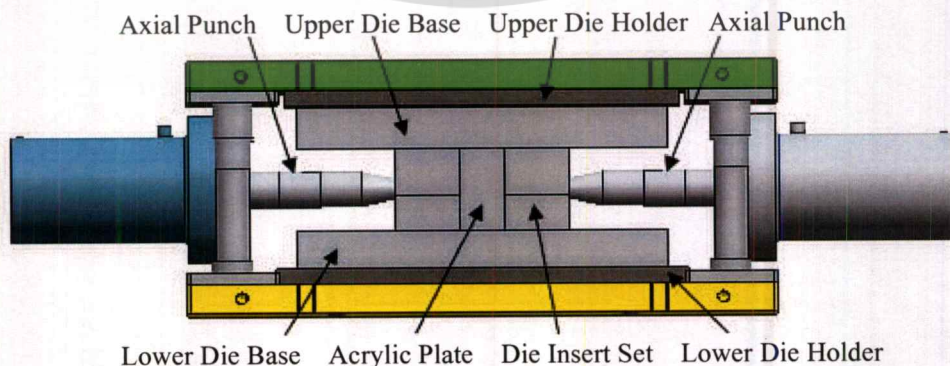
## Chapter 4

# Experiment and Result

### 4.1 Free Bulge Test

#### 4.1.1 Tooling construction and hydroforming system

Designed tools are manufactured as special parts available for implementing a tube hydroforming process. To obtain the experimental result required for flow stress determination of the tube, these pieces of parts are used for the free bulge tests, combining with main tooling in laboratory of hydroforming technology, MTEC pilot plant. There are T.M.C. 200 Ton hydraulic press machine and composition of heavy tools (i.e. a water pressurization circuit, a pressure intensifier). Advantage of this tooling feature is high flexibility in the application, so that different test tubes (material type and size in terms of thickness and length) can be conducted simply by changing positions of die inserts. Therefore, the die inserts that have different entrance radii and bulge lengths can be used. For the tooling construction, the manufactured die inserts (upper die and lower die in **Title 3.1**) are set on two die bases. Bulge length ( $L_b$ ) is 38.1 mm. **Figure 4.1 (a)** and **(b)** shows the features of assembled tools, including two acrylic plates and laser sensor fixed by large screws. The objective of acrylic plate installation is to prevent the water and metal scrape bursting out. **Figure 4.2 (a)** and **(b)** shows wireframe of tooling structure. **Figure 4.3 (a)** and **(b)** shows the real tool sets that are set on the large die bases. The hydroforming tool set is installed in the T.M.C. 200 ton press machine and fixed by large screws as shown in **Figure 4.4**.



(a)

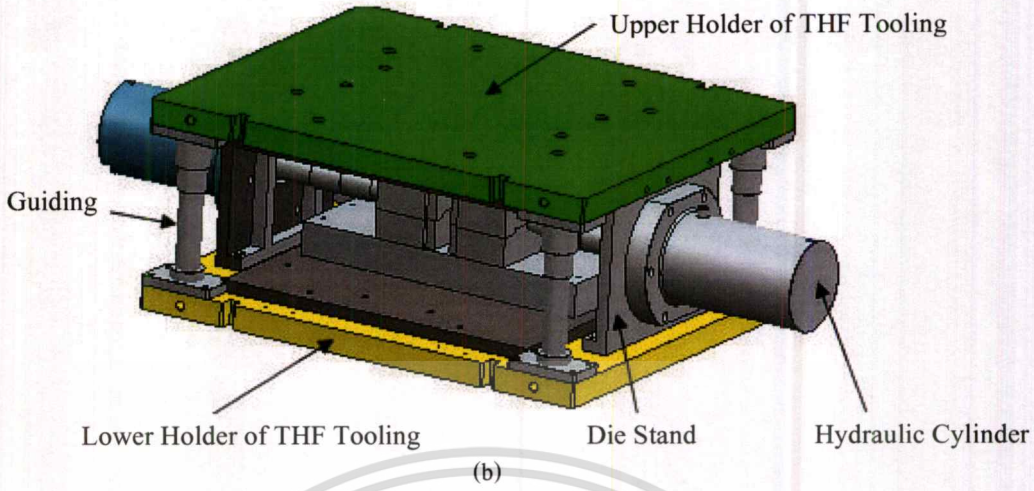


Figure 4.1 A feature of tooling structure, (a) front view and (b) isometric view

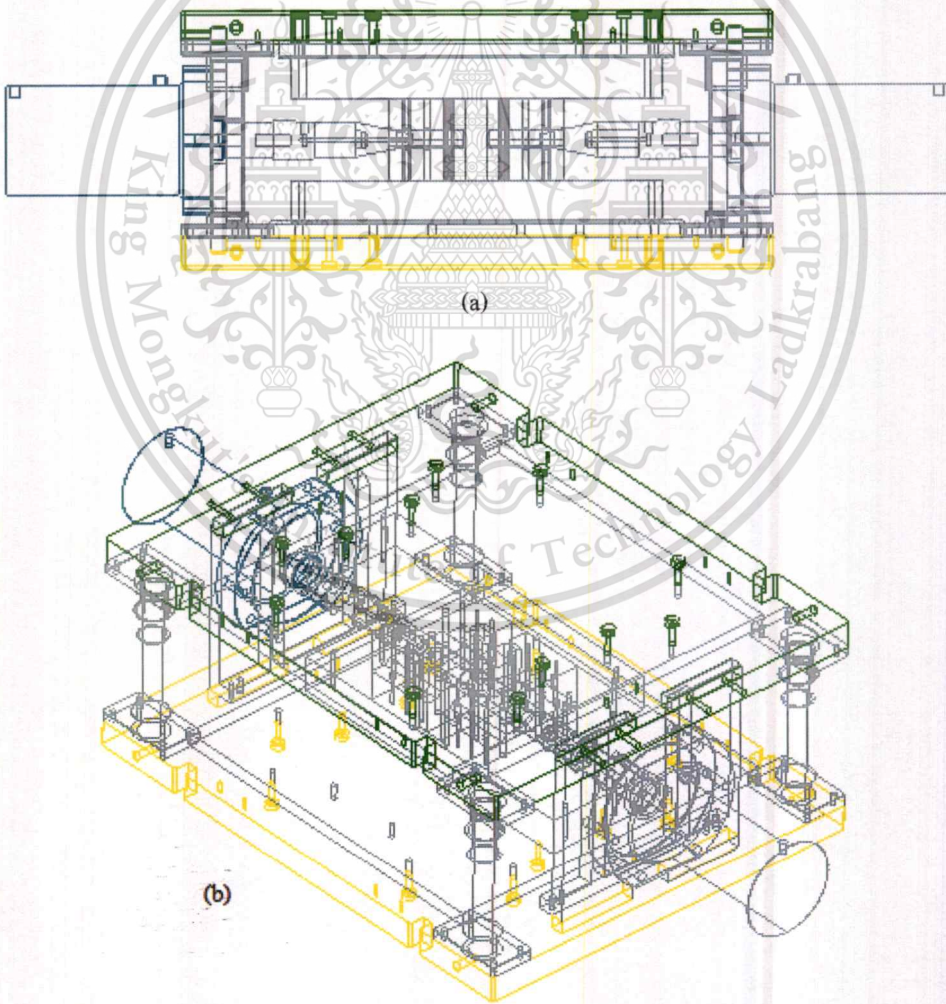
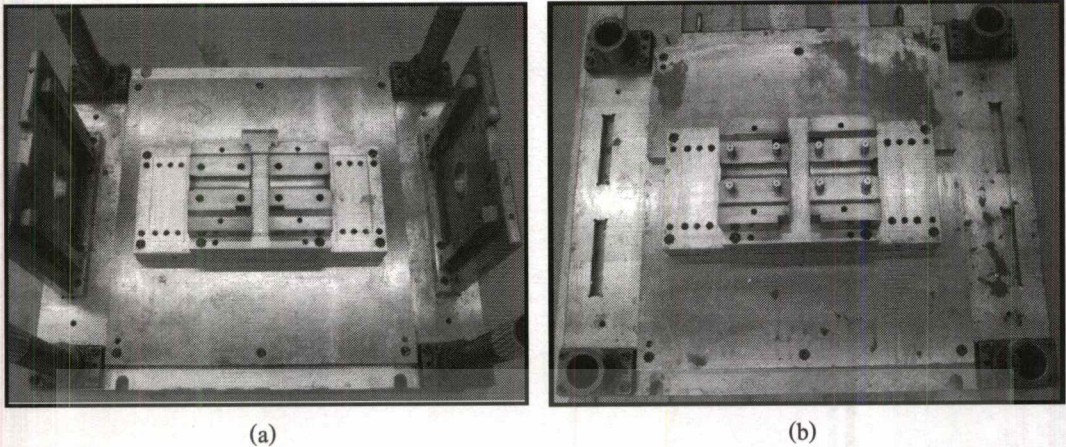
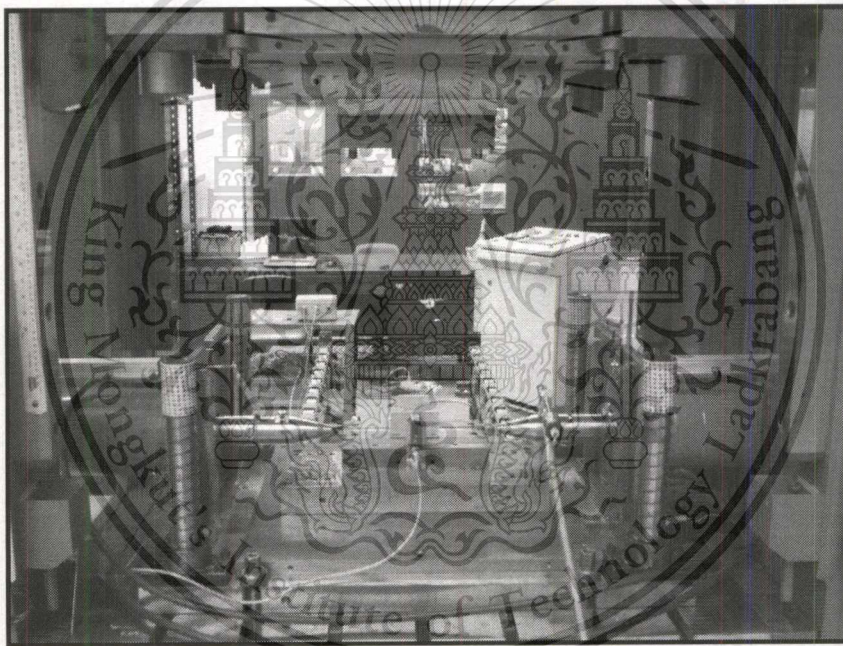


Figure 4.2 Wireframe of tooling structure, (a) front view and (b) isometric view



**Figure 4.3** Real tool sets, (a) lower tool set and (b) upper tool set

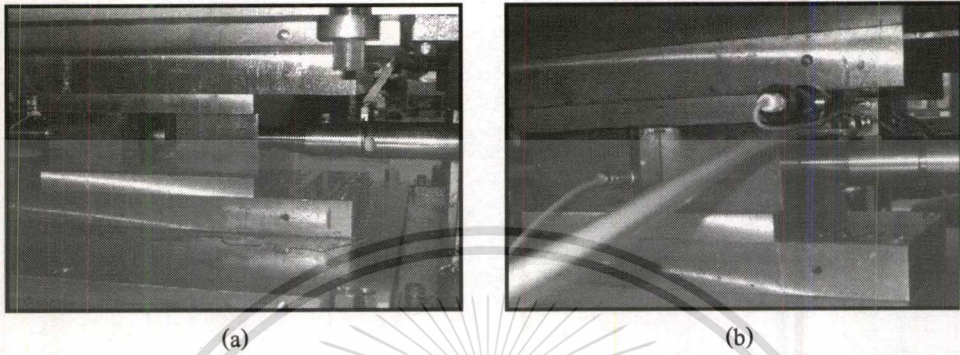


**Figure 4.4** Hydroforming tools set on T.M.C 200 Ton press machine

#### **4.1.1.1 Tooling and press machine operation**

The press machine vertically presses the upper tool set to close the tube workpiece. Consequently, the tube workpiece is closed by main tool set (upper and lower die sets). In order to fix the ends of the tube being closed in the die set, each punch is moved and compressed by hydraulic cylinders. The compression force of the punch is accomplished with a pair of hydraulic cylinders of 50 ton. After forming, two axial punches in left hand side and right hand side will be

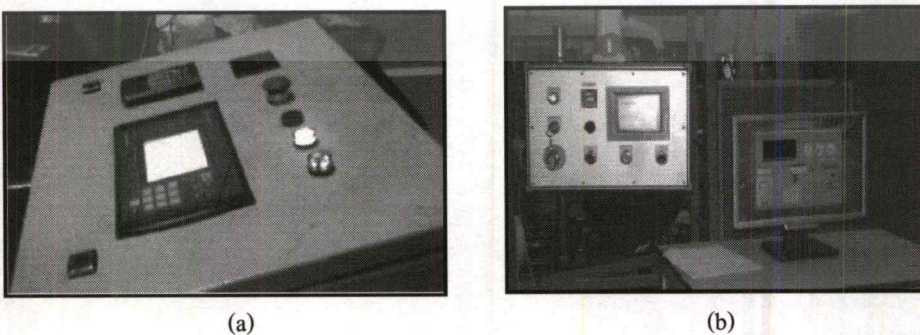
retracted to original positions. The press machine raises the upper tool set for opening die inserts. The punches with adaptors are installed in the hydraulic cylinder per side as shown in **Figure 4.5**. The adaptors are composed for minor adjustment of the feeding distance of the axial punches.



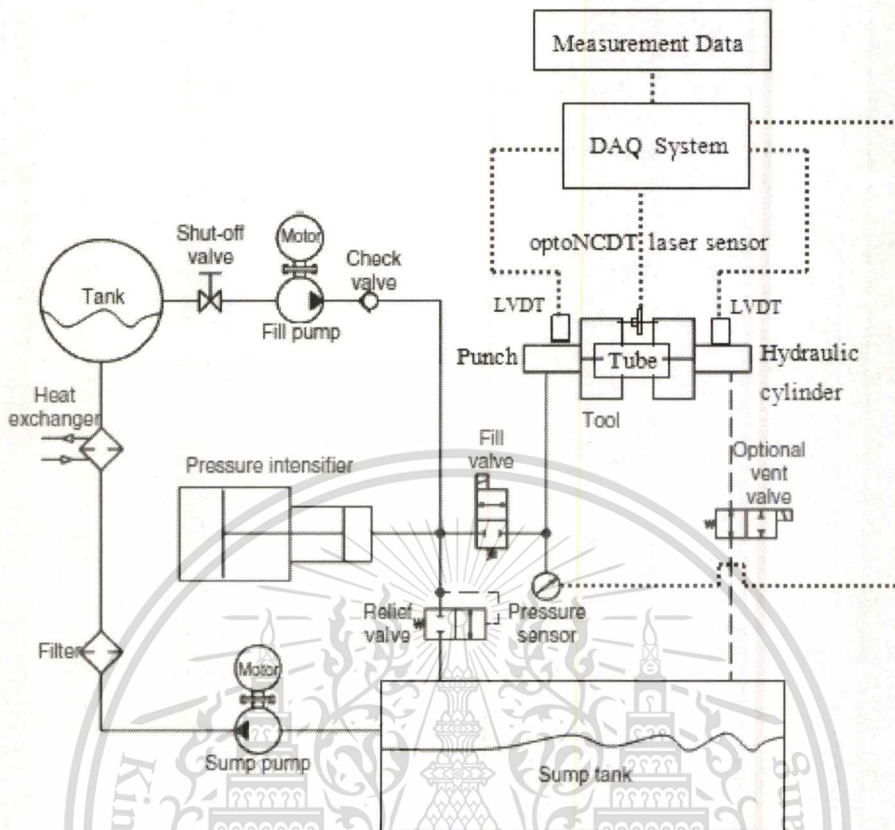
**Figure 4.5** Axial punches fix the ends of the test tube, (a) front view and (b) back view

#### 4.1.1.2 Tube hydroforming and pressurization system

The tube hydroforming process is used to form the tube. A schematic diagram of hydroforming operating system is shown in **Figure 4.7**. The hydroforming control unit and the press machine control unit are shown in **Figure 4.6 (a)** and **(b)**. Measuring instrument connected with data acquisition system is used for detecting bulge heights and internal pressure. The pressurized fluid (water) continuously flows into the tube, along straight hole of the axial punches till the test tube is cracked. The internal forming pressure is generated by pressure intensifier. The internal forming pressure can reach 100 MPa. However, the optimal values of internal forming pressure must be investigated for use in proper forming process.



**Figure 4.6** Central control units of (a) hydroforming system and (b) a press machine



**Figure 4.7** A schematic diagram of tube hydroforming system

#### 4.1.2 Measuring instrument

Measuring instruments in this study consist of sensors, hand tools and electronic devices as follows: 1) Linear Variable Differential Transformer (LVDT) for feeding distance measurement, 2)  $\mu\text{E}$  Laser sensor, optoNCDT1302 for bulge height measure, 3) Dial caliper gauge, KASEDA F-180 series for thickness measure, 4) JIG and Fixture for workpiece holding, 5) DAQ system for data acquisition and 6) a digital camera with micro lens for taking photos of the bulge shape.

#### 4.1.3 Test tubes

The required tubular material for this experimentation is STKM11A steel tube that has specific dimensions, i.e. outside diameter = 28.6 mm and thickness = 1.2 mm. This steel tube is generally produced by electrical resistance welding (ERW) process as shown in **Figure 4.8**. **Table 4.1** shows material properties of STKM11A steel grade from datasheet. **Table 4.2** shows parameters of the test tube and the die inserts. That is initial regulation for the free bulge test and FEA simulation.

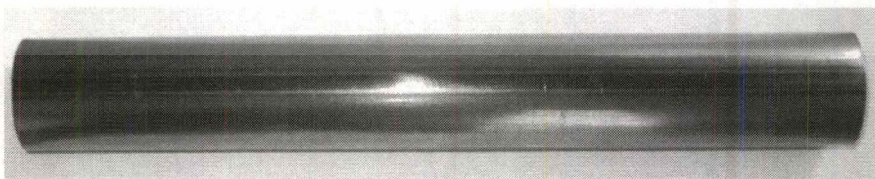
Before conducting the free bulge test, two ends of the tube are swaged by the designed axial punch as detailed in **Chapter 3**.

**Table 4.1** Material properties of STKM 11A steel tube

Chemical composition (%)	Mechanical properties
Carbon = 0 - 1.2	Ultimate Tensile Strength = 294 MPa / 42500 Psi
Silicon = 0 - 0.35	Elongation = 35 %
Manganese = 0 - 0.6	Flattening Strength = 1/2 D
Phosphorus = 0 - 0.04	Max. Bending = 180°
Sulfur = 0 - 0.04	

**Table 4.2** Parameters used in the experiment and FEA simulation

Parameters	Values
Total length of tube (L)	130.00 mm
Bulge length ( $L_b$ )	38.10 mm
Initial tube thickness ( $t_0$ )	1.20 mm
Initial outside diameter of tube (OD)	28.60 mm
Die radius ( $R_d$ )	5.00 mm
Maximum pressure level ( $P_{max}$ )	100 MPa
Friction coefficient ( $\mu$ ) between die insert and outer surface of tube	0.125



**Figure 4.8** A typical STKM 11A tube produced by roll forming with ERW process

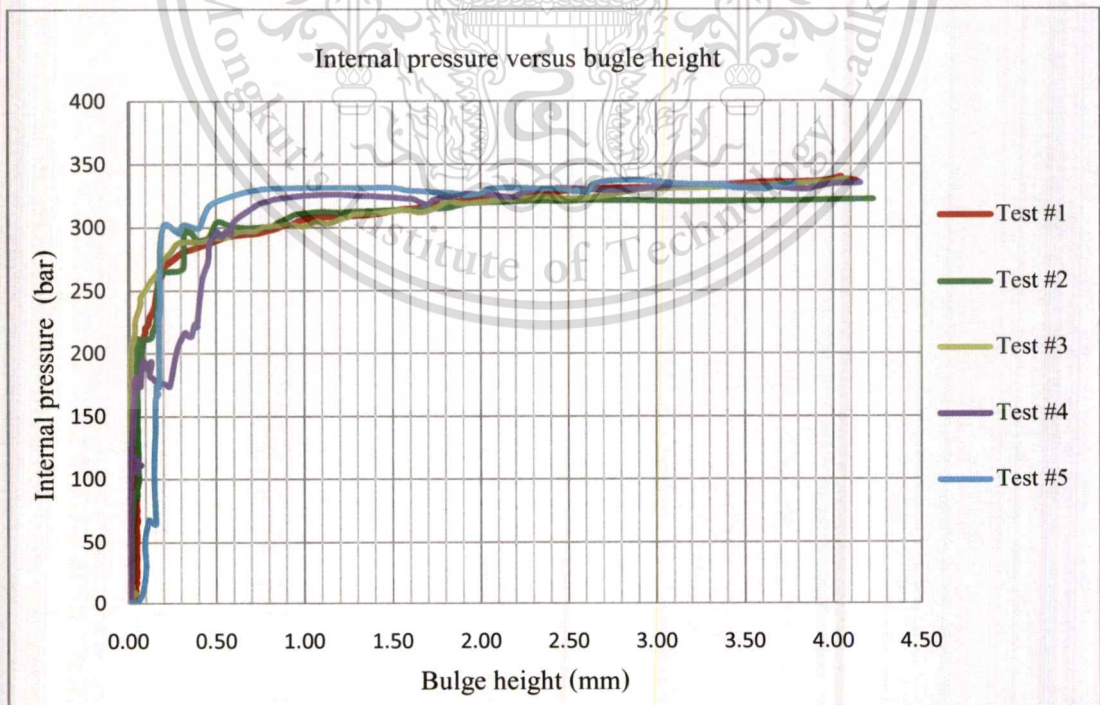
## 4.1.4 Experimentation and Results

### 4.1.4.1 Investigation of internal pressure with continuous forming

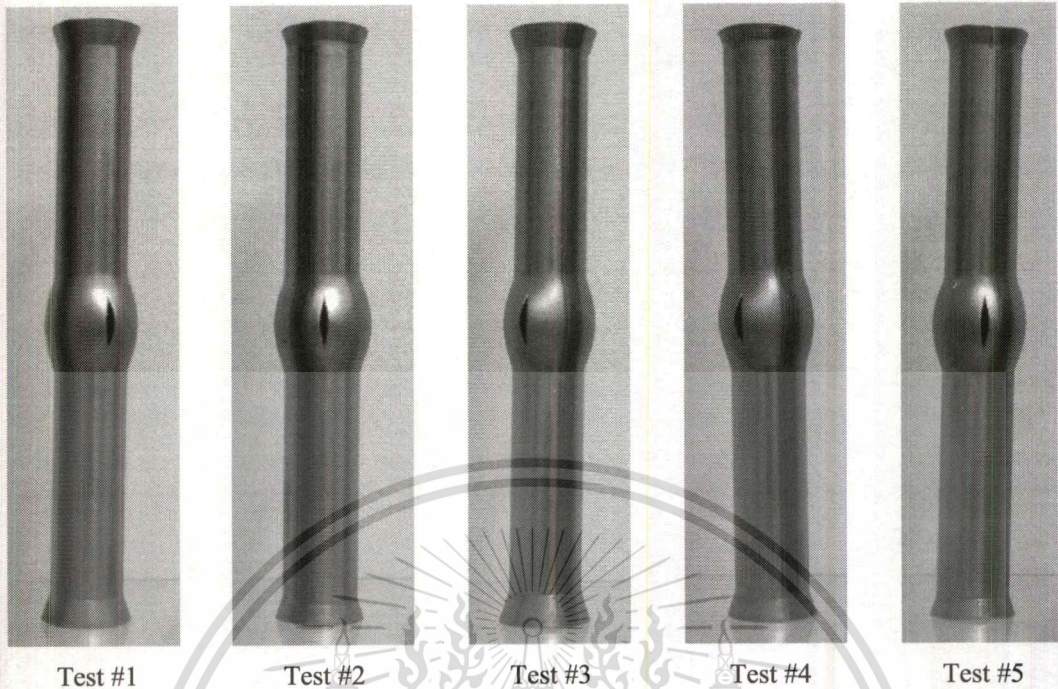
Firstly, free bulge tests using STKM11A tubes are performed by continuous forming. The hydraulic pressures can reach about 340.00 bar. The continuous forming pressures can be obtained by the pressure sensor. The axial punches can successfully seal the water pressure and fix the left-right ends of the tube.

#### 1. Test result

The forming tube displays the continuously expansive deformation during the hydraulic bulge test. At the end of forming process, the formed tube reveals the bulge shape inside the die cavity. The curvatures of the bulge shape correspond to initial assumption of the elliptical surface. As result, five pressure curves obtained from the continuous forming tests (Test #1, Test #2, Test #3, Test #4 and Test #5) are shown in **Figure 4.9**. The internal forming pressures and bulge heights of the hydroformed tubes are plotted. Fluctuations of internal pressure curves indicate leakages of the water during bulging. **Figure 4.10** shows the hydroformed tubes with test numbers from the continuous forming tests.



**Figure 4.9** Internal forming pressures versus bulge heights of the hydroformed tubes



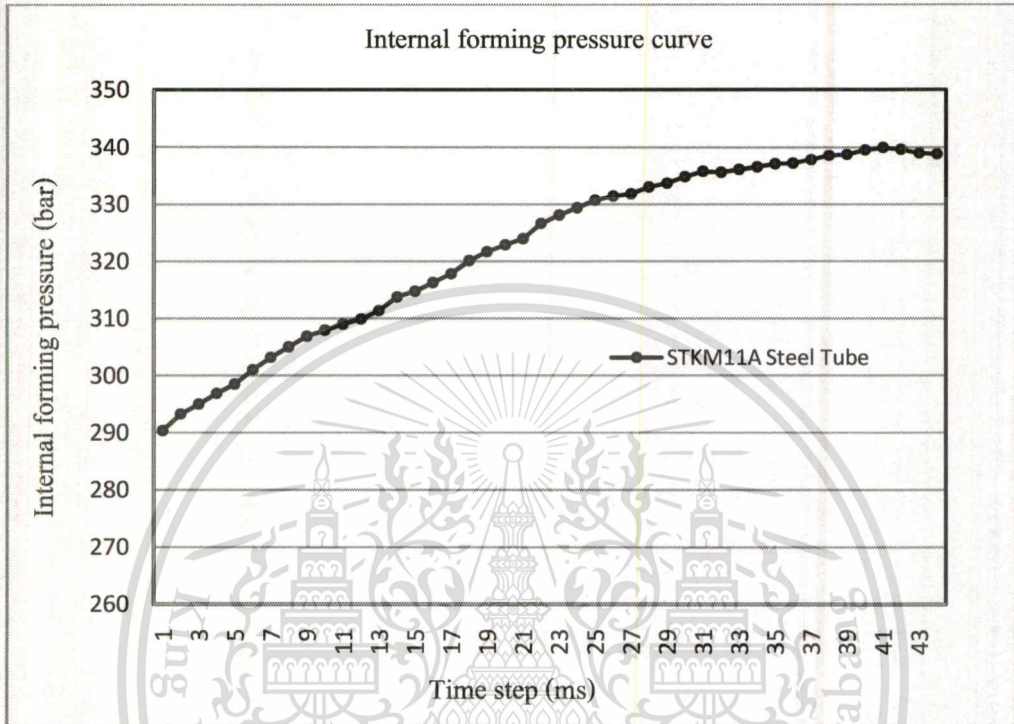
**Figure 4.10** Hydroformed tubes (STKM11A) versus test numbers

From Figure 4.9, it is found that the readable forming pressure of Test #1 (see Test #1 in **Figure 4.10**) is the best loading curve because it exhibits the most stable pressure curve. The internal forming pressure in plastic state of the tube is additionally shown in **Table B-1, Appendix B-5**.

## 2. Investigation of internal forming pressure

The proportional pressure levels are investigated from relationships between the internal forming pressures and the bulge heights in Figure 4.9. It can be seen that the internal pressure curve of Test #1 is more stable than the others. From the test #1 results, the internal forming pressure at the yield point of the tube,  $P_{\text{yield}}$ , is taken from an initial value of the pressure that first causes a change in the bulge height. The internal forming pressure at the burst point of the tube,  $P_{\text{burst}}$  is also taken at the bursting moment. As results, the internal forming pressures of Test#1 in plastic state of the hydroformed tube are chosen as shown in **Figure 4.11**. The estimated  $P_{\text{yield}}$  and  $P_{\text{burst}}$  levels are 29.00 MPa and 33.77 MPa, respectively. Then, the internal pressure levels,  $P_1$ ,  $P_2$ ,  $P_3$ ,  $P_4$ ,  $P_5$ , are chosen evenly between the yielding and the bursting pressures. The forming pressure curve is defined as the investigated pressure levels as shown **Figure 4.12**. These pressure values will be used for

interrupted forming experiments (step forming with process interruption). The experimentation procedure is referred as Design of Experiment (DOE) explained in **Appendix B-5**.



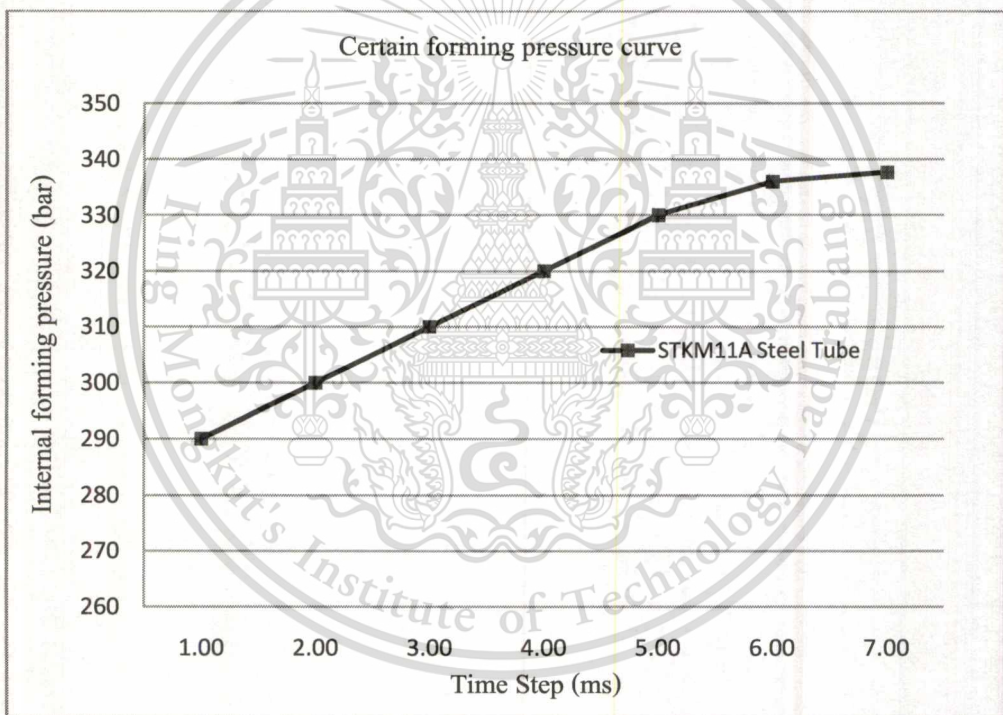
**Figure 4.11** Internal forming pressure curve of Test #1 in plastic state of the hydroformed tube

**Table 4.3** Internal forming pressure for interrupted experiments

Pressure level	STKM11A Steel Tube	
	Internal forming pressure (MPa)	Internal forming pressure (psi)
P <sub>yield</sub>	29.00	4205.00
P <sub>1</sub>	30.00	4350.00
P <sub>2</sub>	31.00	4495.00
P <sub>3</sub>	32.00	4640.00
P <sub>4</sub>	33.00	4785.00
P <sub>5</sub>	33.60	4872.00
P <sub>burst</sub>	33.77	4896.65

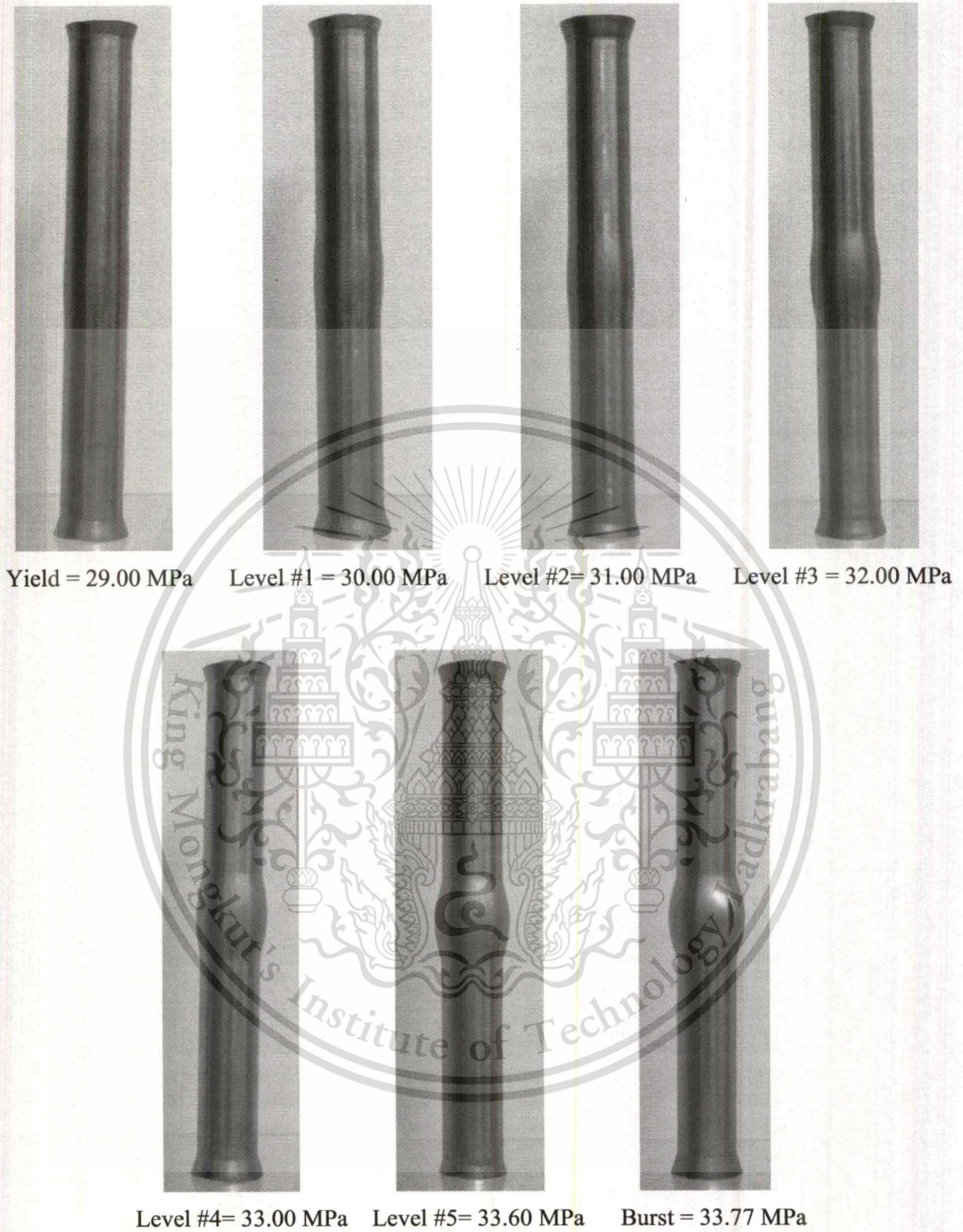
#### 4.1.4.2 Experiment with interrupted forming

In the interrupted experiment, the internal forming pressures in **Table 4.3** are used. The certain pressure curve for the interrupted forming test is shown in **Figure 4.12**. To obtain the proper hydroformed tubes and stable pressure curve per a forming step, four tube workpieces (Parts #1, #2, #3 and #4) per a pressure level are used for repeating the free bulge test of 4 times. After tube bulge test in each level, the hydroforming process is stopped. Then, the hydroformed tube is taken out of the die. The results of this experiment will lead to flow stress curve determination using analytical models (i.e., SPB's model, YingYot's model and Hwang's model). The measured parameters are described as analytical models (see **Appendix B**).



**Figure 4.12** Certain pressure curve for interrupted experiments

For result of the free bulge tests, the formed tube displays the nice bulge shape per the forming level number. Every tube cracks at the burst pressure level equal to 33.00 MPa approximately. **Figure 4.13** shows the proper hydroformed tubes versus internal forming pressures of 7 levels. It can be seen that the formed tubes have good bulge shapes without wrinkle and scratch.



**Figure 4.13** Proper hydroformed tubes (STKM11A) and corresponding forming pressure levels

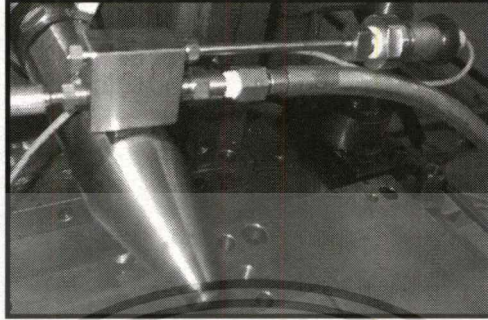
#### 4.1.4.3 Experimental data collection

The internal forming pressure in continuous forming test is detected by pressure sensor (**Figure 4.14**). The bulge height is detected by optoNCDT1302 laser sensor (**Figure 4.15**).

This material is reserved for educational use only, not allowed for commercial use.

Forbidden to modify the content, and cite the document when use.

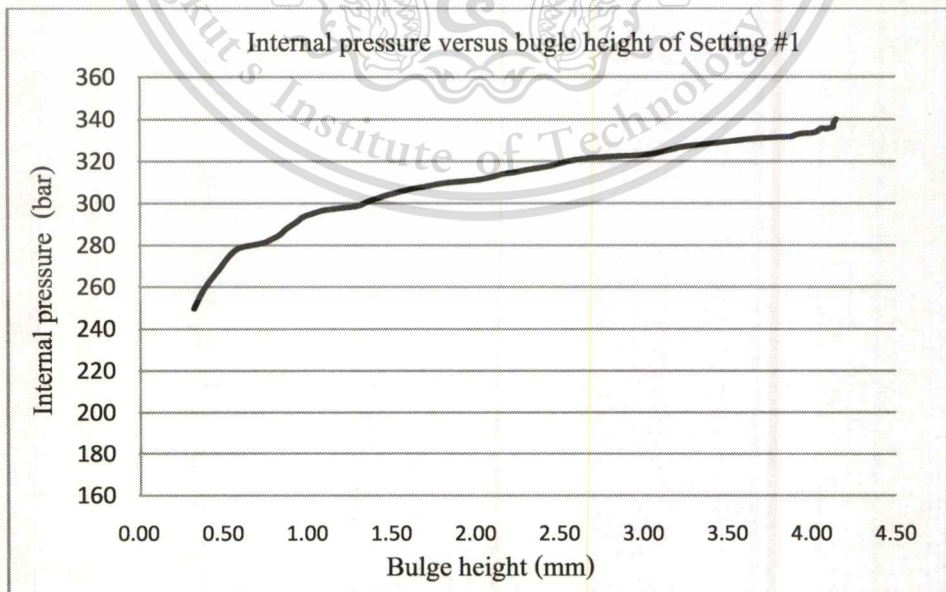
The internal forming pressures versus bulge heights in plastic state of the hydroformed tube are shown in **Figure 4.16**. The bulge heights at vertex of the bulge shape are measured.



**Figure 4.14** Pressure sensor

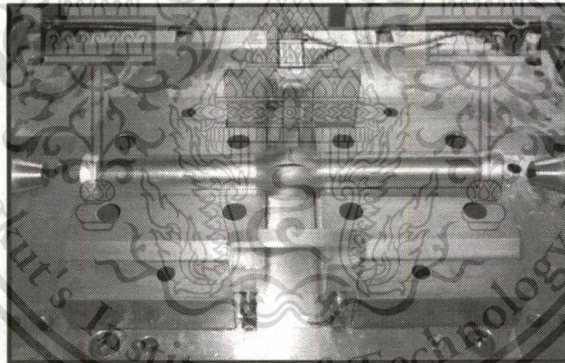


**Figure 4.15** OptoNCDT1302 laser sensor

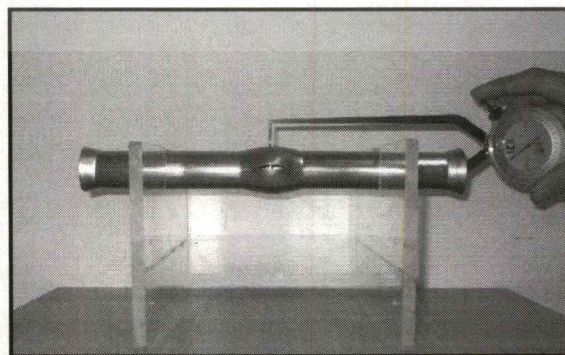


**Figure 4.16** Internal forming pressures versus bulge heights from continuous forming

For interrupted forming test, the pressure sensor is connected to a DAQ system for detecting the internal forming pressure that is defined as data in **Table 4.3**. The upper die set is raised up in vertical direction after tube hydroforming process is interrupted. The hydroformed tube which is on the lower die (**Figure 4.17**) is taken out of the die insert set for measuring the tube thickness and the bulge height. A self - designed JIG is used for tube work-piece support. KASEDA dial caliper gauge (accuracy = 20 Micron) is used for measuring the tube thickness as sample shown in **Figure 4.18**. For measurement methods, 36 target points that are thickness measuring positions at vertex of the bulge along the circumferential direction are divided by 10 degree. Those points are defined as angles of a circle grid shown in **Figure 4.19** whereby the formed tube workpiece (left side end and right side end) is put on the circle grid in vertical direction. Left side end of the tube touch the grid scale surface and it is marked with permanent ink for 36 measuring points. Next, right side end of the tube is done. Then, 36 measuring points in bulge area are marked straightly with two marked ends. As result, thickness distributions measured in clockwise direction are shown in **Figure 4.20**.



**Figure 4.17** A typical hydroformed tube on lower die set



**Figure 4.18** Tube thickness measurement using KASEDA dial caliper gauge

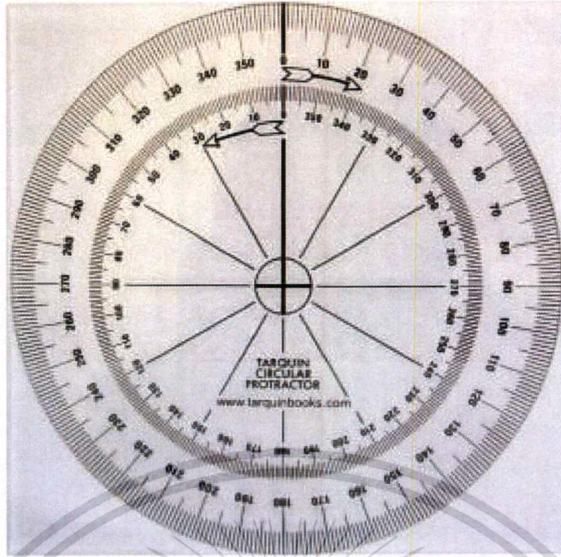


Figure 4.19 Polar coordinate circle grid

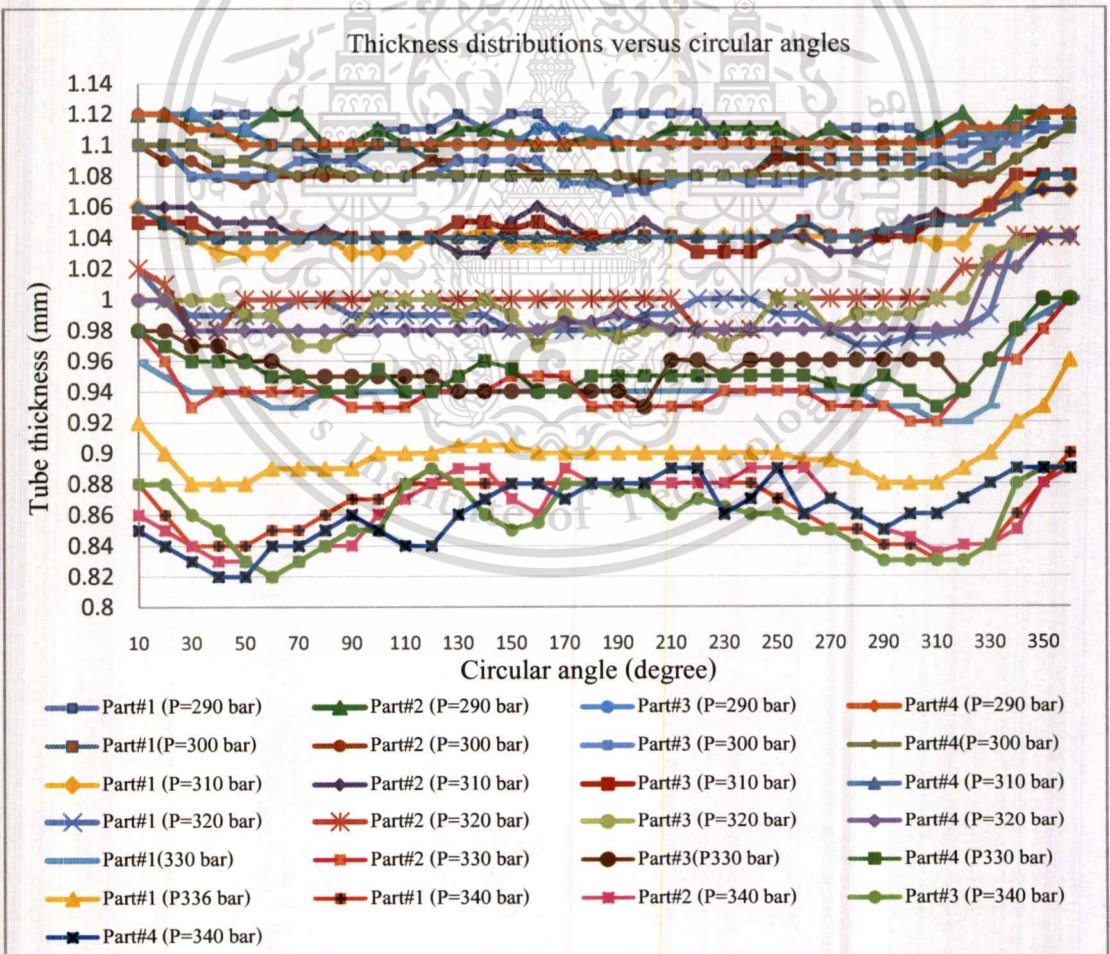
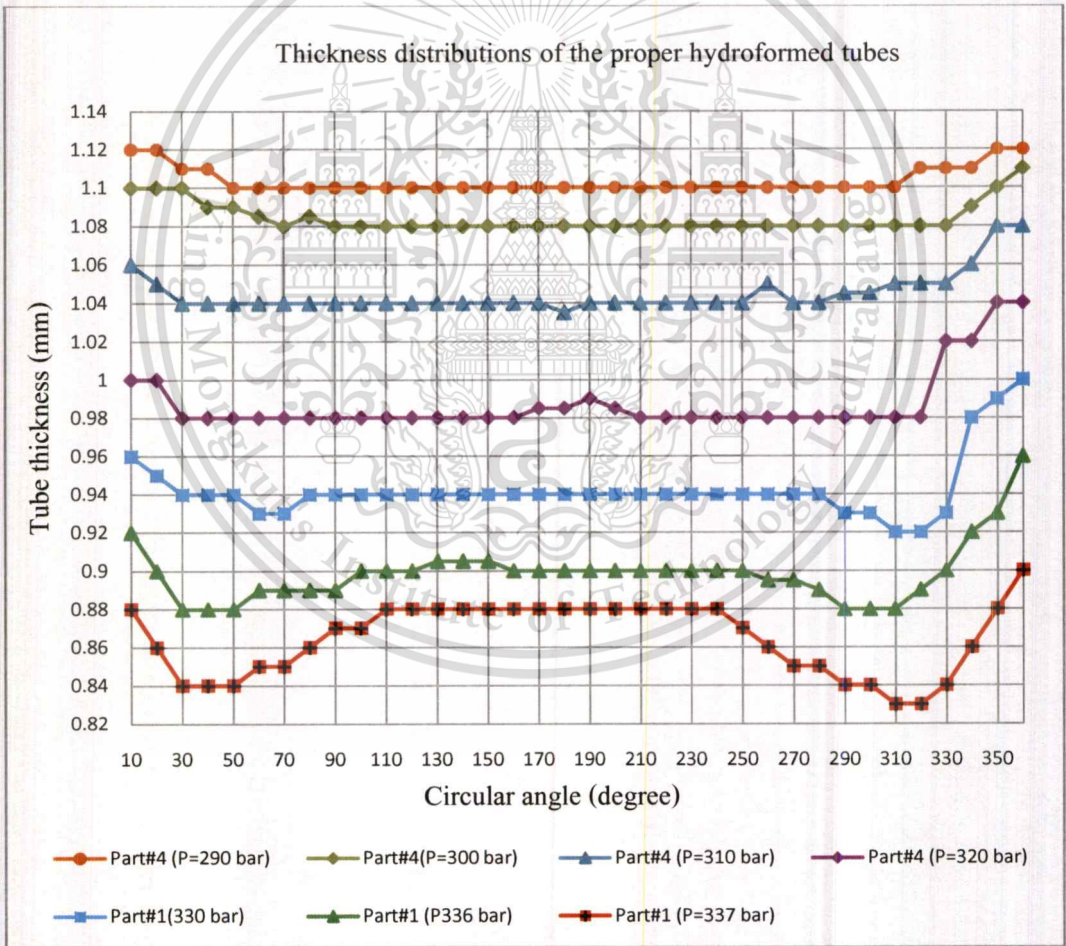
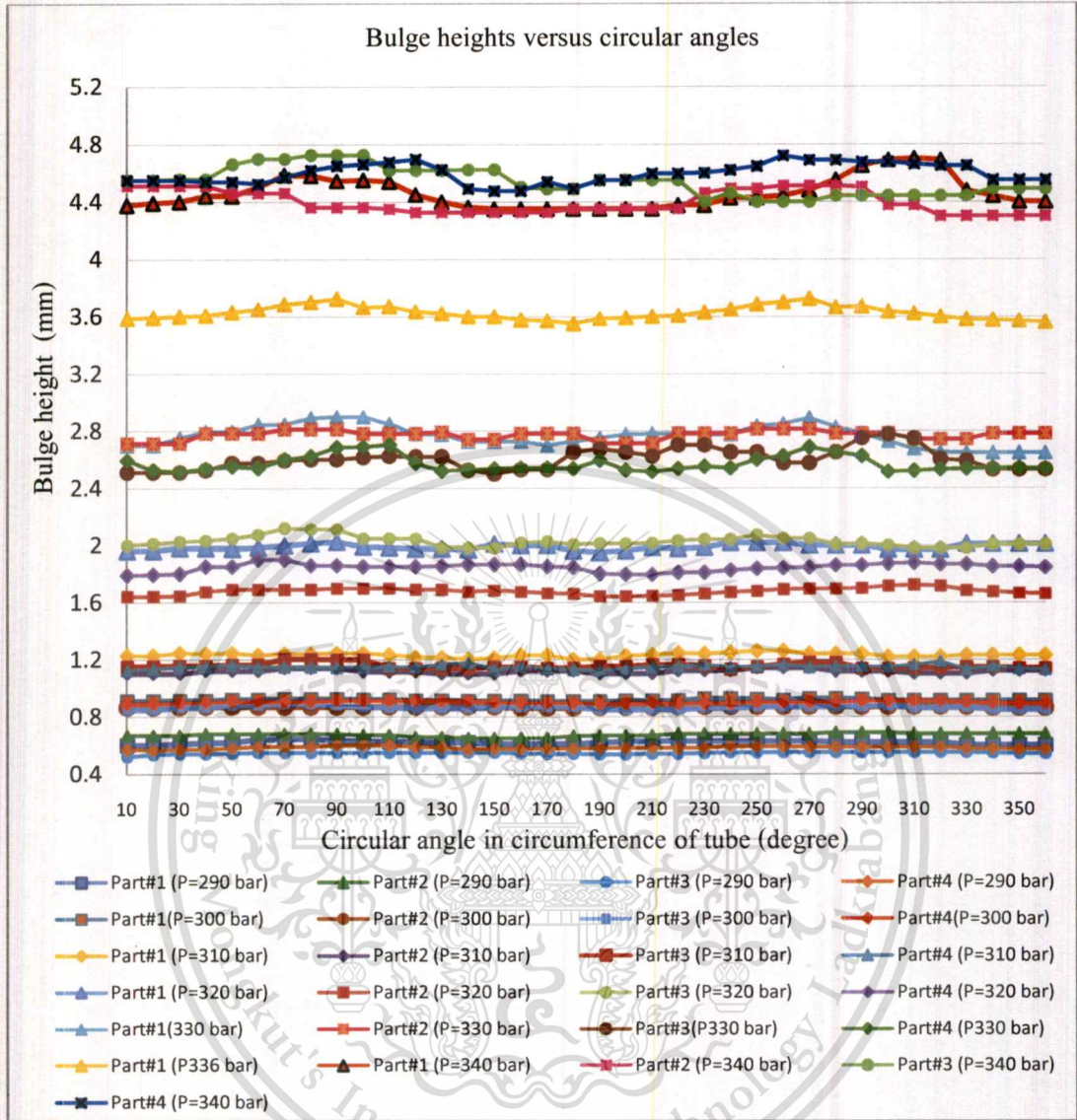


Figure 4.20 Thickness distributions of the hydroformed tubes against internal pressure levels

From Figure 4.20, it can be seen that in each internal pressure level, at which 4 tubes are tested, exists some hydroformed tubes that display thickness distribution corresponding to the behavior of tube radial expansion. The weakest area mostly occurs at the points nearby the weld line, at the right and left hand sides. Tendency to crack is clearly evident from the thickness distributions. It can be concluded that the following parts which have the proper bulge shapes and correspond to the real hydroformed tube, are Part #4 (P = 290 bar), Part #4 (P =300 bar), Part #4 (P =310 bar), Part #4 (P=320 bar), Part #1(P=330 bar), Part #1(P=336 bar) and Part #1 (P=377.7 bar). These thickness distribution curves of the hydroformed tubes versus internal pressure levels are chosen from **Figure 4.20** and plotted in **Figure 4.21**.

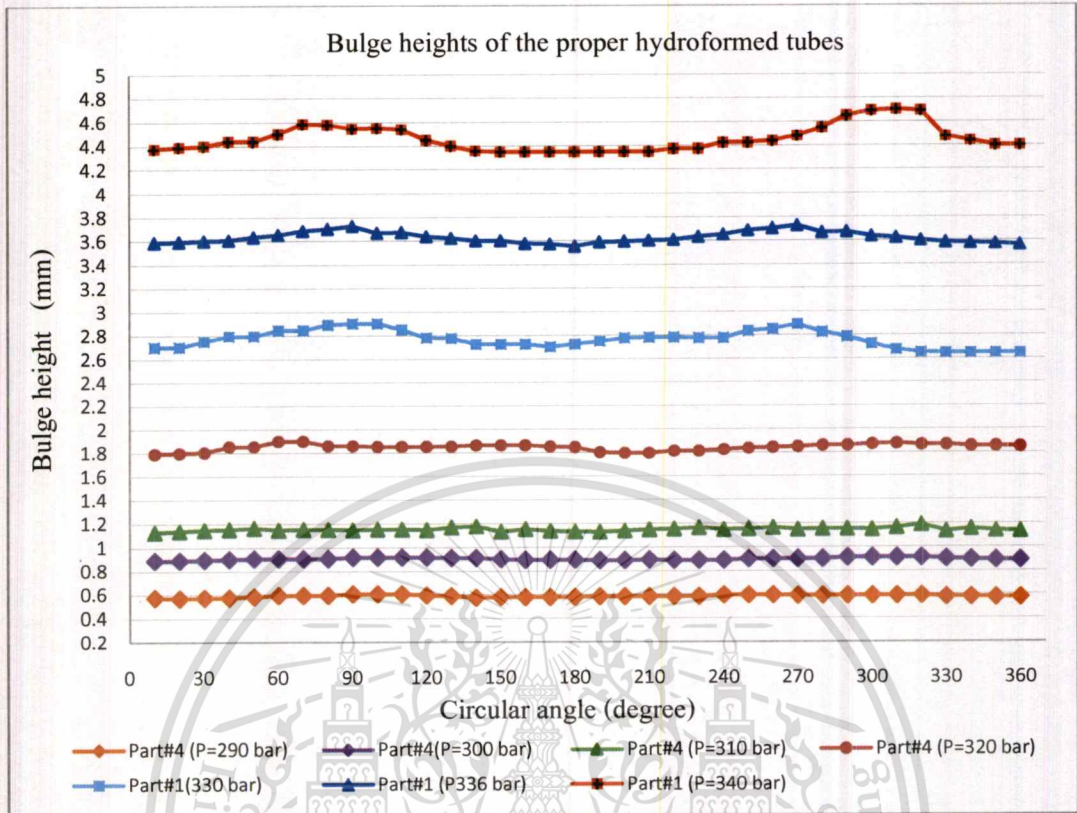


**Figure 4.21** Thickness distributions of the proper hydroformed tubes versus internal pressure levels



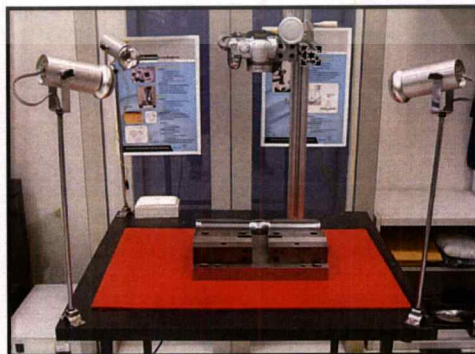
**Figure 4.22** Bulge heights of the hydroformed tubes against internal pressure levels

The bulge heights are measured by a vernier caliper using the same procedure as the thickness measurement. The bulge heights of the hydroformed tubes are shown in **Figure 4.22**. The best curves of the bulge height are shown in **Figure 4.23**.

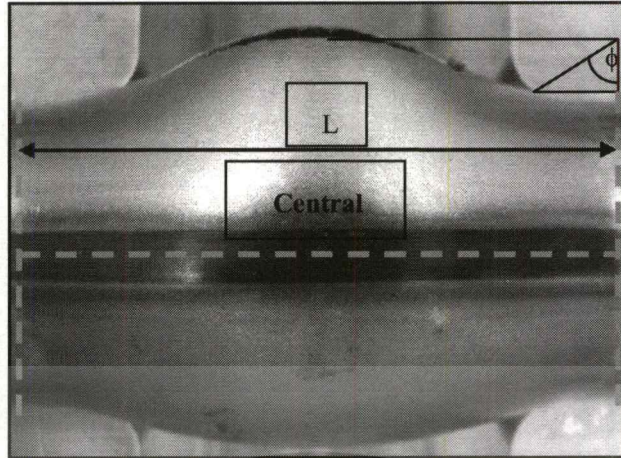


**Figure 4.23** Bulge heights of the proper hydroformed tubes versus internal pressure levels

In order to measure the contact angle on the bulge surface and meridian radius ( $\rho_{\phi p}$ ) of curvature of the bulge shape, the lower die set is used for supporting the workpiece. A digital camera with a micro lens is used for photography as shown in **Figure 4.24**. Finally, the contact point (e), geometrical parameters and meridian radius ( $\rho_{\phi p}$ ) of the bulge shapes in picture are found and measured in CAD software (see **Figure 4.25**), according to analytical models (**Appendix B**).

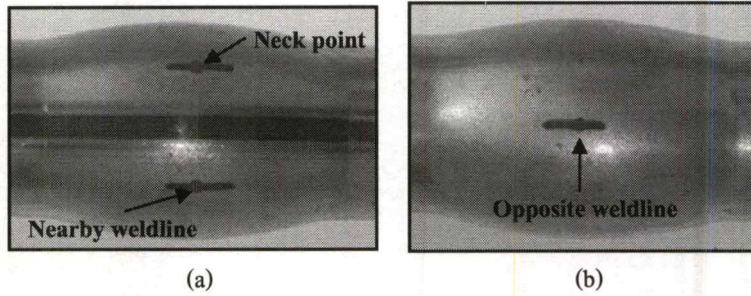


**Figure 4.24** A support table for taking photos of bulge shapes



**Figure 4.25** A typical bulge shape with geometrical parameter measurement

From **Figure 4.25**, it can be seen that the tube workpiece shows obvious shape of free expansive deformation with thickness reduction. Due to the fact that the tube workpiece is deformed by internal water pressure without counter punch, the metal throughout circumference of the tube is expanded by continuous forming pressure. Consequently, mechanical behavior of material properties (stress – strain relationship or flow stress) occurs progressively until the tube is cracked. The neck point indicates the upper limit of hydroformability of the tube. This study consequently aims at determination of flow stress suitable for tube hydroformability evaluation. Therefore, the flow stress at Neck point of the hydroformed tube should be determined. The thin-walled tube at Neck point has the most risk of cracking. However, other bulge vertexes along circumferential direction are also considered. Its thickness distributions (**Figure 4.21**) imply different flow stress curves which can be of three cases. Case #1, Case #2 and Case #3 are the thickness distributions at Neck, Nearby Weldline and Opposite Weldline Points, respectively as shown in **Figure 4.26**. Therefore, these points are representatives of necked area, thick area and thickest area, respectively for flow stress determination. From the measurement results in **Table 4.4**, the parameter values in Neck, Nearby Weldline and Opposite Weldline columns are measured at the abovementioned points along circumferential direction with circular angles ( $\theta = 310^\circ$ ,  $\theta = 50^\circ$  and  $\theta = 180^\circ$  in **Figure 4.19**). These values will be used to determine the flow stress of the proper hydroformed tube.



**Figure 4.26** Points for flow stress determination, (a)Neck, NearbyWeldline and (b)OppositeWeldline

**Table 4.4** Measured parameters of bulge shapes of proper hydroformed tubes

Internal pressure (MPa)	Neck point				Nearby Weldline				Opposite Weldline			
	Thickness at vertex $t_p$ (mm)	Bulge height $h_p$ (mm)	Contact angle $\phi$ (degree)	Meridian radius $\rho_{\phi P}$ (mm)	Thickness at vertex $t_p$ (mm)	Bulge height $h_p$ (mm)	Contact angle $\phi$ (degree)	Meridian radius $\rho_{\phi P}$ (mm)	Thickness at vertex $t_p$ (mm)	Bulge height $h_p$ (mm)	Contact angle $\phi$ (degree)	Meridian radius $\rho_{\phi P}$ (mm)
$P_{yield}$ 29.0	1.10	0.59	15.00	289.84	1.11	0.57	15.00	289.84	1.1	0.57	15.00	289.84
$P_1 =$ 30.0	1.08	0.91	18.00	232.85	1.09	0.9	18.00	232.85	1.08	0.89	18.00	232.85
$P_2 =$ 31.0	1.05	1.16	22.35	146.09	1.04	1.15	22.30	146.19	1.03	1.13	22.30	146.26
$P_3 =$ 32.0	0.98	1.88	41.00	97.00	0.98	1.85	40.99	102.14	0.98	1.84	40.93	102.04
$P_4 =$ 33.0	0.92	2.80	47.32	73.13	0.94	2.80	46.52	76.15	0.94	2.72	46.32	78.03
$P_5 =$ 33.6	0.88	3.62	50.14	58.18	0.88	3.60	48.91	60.58	0.9	3.55	48.14	63.20
$P_{burst}$ = 33.77	0.83	4.70	52.04	45.43	0.84	4.55	51.54	49.18	0.88	4.4	50.14	59.69

## 4.2 Determination of Flow Stress Curve

The internal forming pressure ( $P_i$ ), the bulge heights ( $h_p$ ), the tube thicknesses ( $t_p$ ) and the contact angle ( $\phi$ ) in Table 4.4 are used to calculate the effective stress and effective strain that are required for determination of the flow stress curves. By substituting those parameters into the analytical models (i.e. SPB model, YingYot model and Hwang model), the flow stress curves of STKM 11A steel tube will be obtained. Figure 4.27 and Figure 4.28 show the comparison of the internal pressure ( $P_i$ ), circumferential radius ( $\rho_{\theta p}$ ) and meridian radius ( $\rho_{\phi}$ ) of the bulge shapes that are obtained from those analytical models. It is found that the internal pressure directly influence on deformation of the tube to the bulge geometry. The circumferential radius increases when the internal pressure increases. On the other hand, the meridian radius decreases when the internal pressure increases. The tube thickness at the vertex decreases when the internal pressure increases. Derivations of those analytical models are respectively explained in Appendix B.

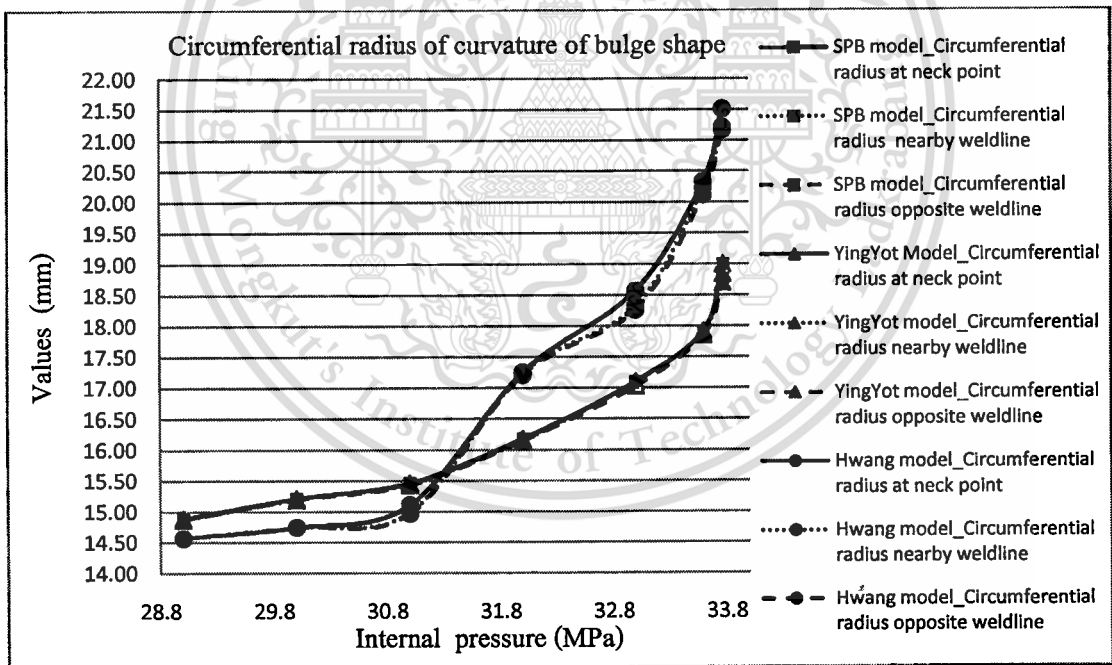


Figure 4.27 Internal pressures versus circumferential radius of curvature of the bulge shapes

For Figure 4.27 and Figure 4.28, the square, triangle and circle with different lines denote the circumferential and meridian radii of the bulge shapes obtained from SPB model, YingYot model and Hwang model, respectively.

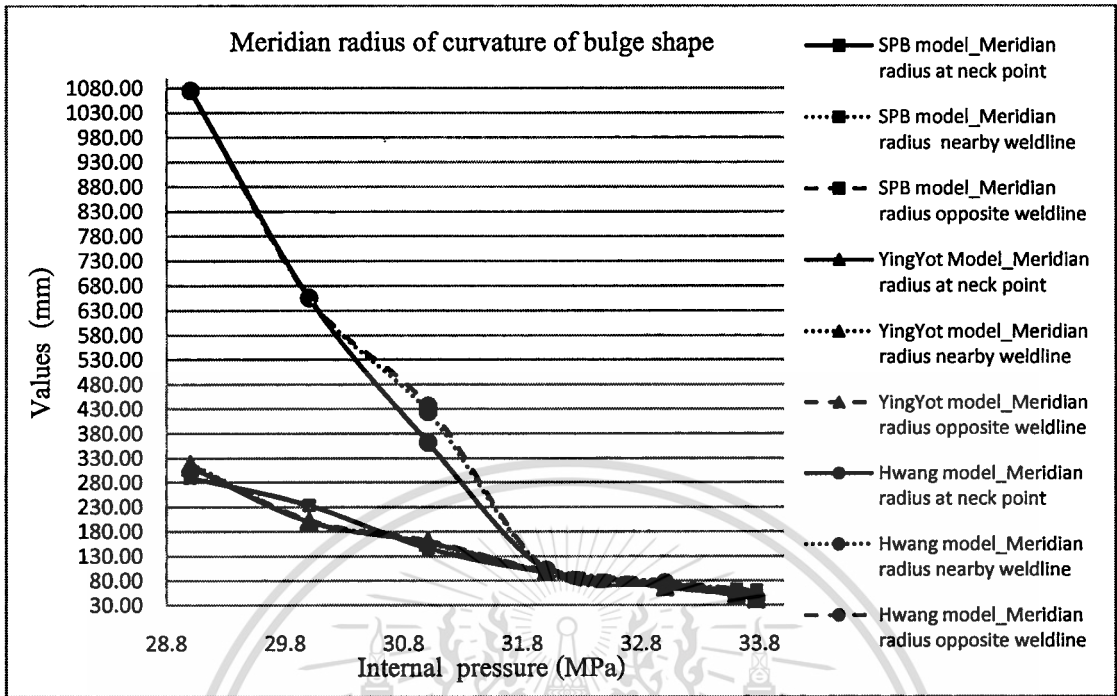


Figure 4.28 Internal pressures versus meridian radius of curvature of the bulge shapes

#### 4.2.1 Flow stress curves by SPB analytical model

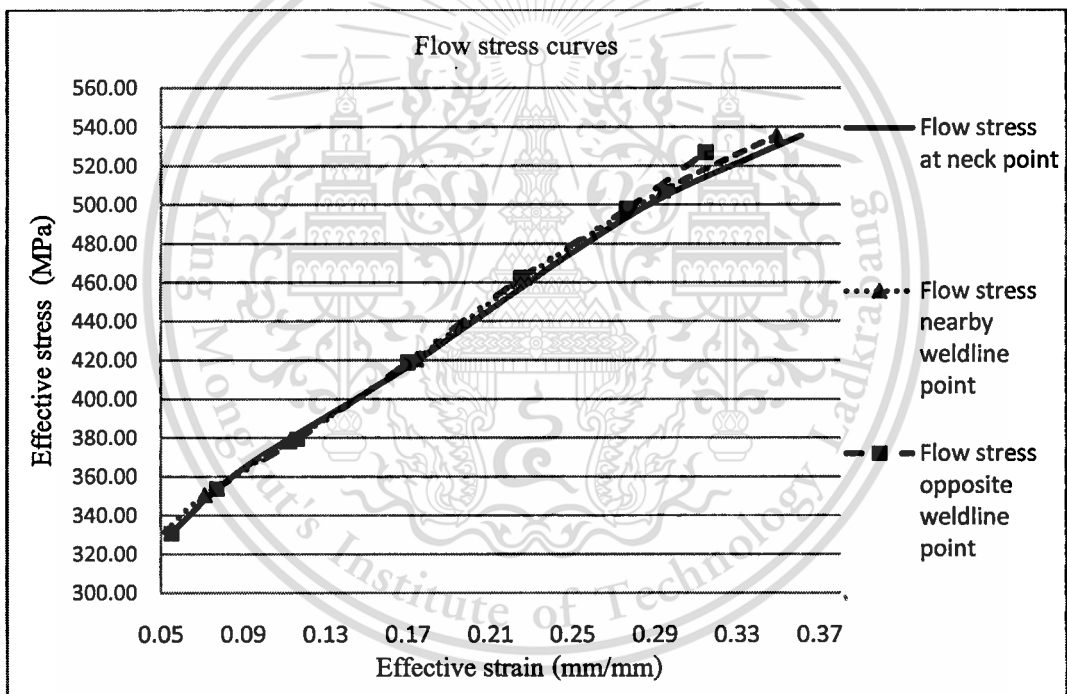
Considering geometry of the hydroformed tubes, curvature of the bulge shape is assumed as the circular arc, outer surface of the bulge shape with shell element. The above-mentioned experimental data, the initial thickness ( $t_0$ ) and current thickness ( $t_p$ ), initial tube radius ( $r_0$ ) and current tube radius ( $r_p$ ) are used for calculating strain in thickness direction and circumferential strain. Circumferential radius values ( $\rho_{0p}$ ) at Neck, Nearby Weldline and Opposite Weldline Points that are obtained from direct measurement are used for calculating meridian stress by taking equation of cylindrical pressure vessel. Meridian radius values ( $\rho_{qp}$ ) at Neck, Nearby Weldline and Opposite Weldline Points (Figure 4.28) that are obtained from direct measurement in CAD software (Figure 4.25) are used for calculating circumferential stress by taking equation of equilibrium of force. The flow stress curves of the tubes are obtained from Power law (Equation 21 in appendix B-1). Strength coefficient ( $K$ ) and strain hardening ( $n$ ) of material are numerically determined by the least mean square method. Eventually, the flow stresses are expressed as

$$\bar{\sigma} = 687.48 (\bar{\epsilon})^{0.2597} \quad (4.1)$$

$$\bar{\sigma} = 680.76 (\bar{\epsilon})^{0.2511} \quad (4.2)$$

$$\bar{\sigma} = 697.33 (\bar{\epsilon})^{0.266} \quad (4.3)$$

**Equation 4.1, Equation 4.2 and Equation 4.3** are expressions of flow stresses at Neck, Nearby Weldline and Opposite Weldline Points, respectively. Three flow stress curves are shown in **Figure 4.29**. Strength coefficients (K) of material at Neck, Nearby Weldline and Opposite Weldline Points are equal to 687.48 MPa, 680.76 MPa and 697.33 MPa, respectively. Strain hardenings (n) of material at Neck, Nearby Weldline and Opposite Weldline Points are equal to 0.2597, 0.2511 and 0.266, respectively. The concerned parameters and effective stress - strain values of STKM 11A steel tubes are shown in **Appendix B-6, Table B-4, Table B-5 and Table B-6**. The procedure of flow stress determination for SPB model is shown in **Appendix B-1**.



**Figure 4.29** Flow stress curves of STKM11A steel tube by SPB model

#### 4.2.2 Flow stress curves by YingYot's analytical model

The bulge shape is assumed as the circular arc, inner surface of thin-walled tube with shell element. All of the above-mentioned experimental data are used. From their geometrical parameters, meridian and radial radii,  $r_z$  and  $r_\theta$  (in **Figure 4.27** and **Figure 4.28**) are calculated by using geometrical relationship. Strains in longitudinal and hoop directions are calculated by using those

radius values. Thin-walled structure and plasticity theorem with meridian and radial radii are directly used for calculating hoop and longitudinal stresses. By substituting those calculated parameters into equations of Von-mises criterion (Equation 28 and Equation 31 in Appendix B-2), the effective stress and effective strain are obtained. The experimental data and calculated parameters are shown in Table B-7, Table B-8 and Table B-9 (see Appendix B-6), respectively. The flow stress curves of the tubes are obtained from Power law (Equation 32 in appendix B-2). Strength coefficient (K) and Strain hardening (n) of the tubes are determined by the least mean square method. As result, the flow stresses at Neck, Nearby Weldline and Opposite Weldline Points are expressed as Equation 4.4, Equation 4.5 and Equation 4.6. Strength coefficients (K) of material at Neck, Nearby Weldline and Opposite Weldline Points are equal to 659.41 MPa, 646.21 MPa and 644.7 MPa, respectively. Strain hardenings (n) of material at Neck, Nearby Weldline and Opposite Weldline Points are equal to 0.2441, 0.2319 and 0.2353, respectively. Three flow stress curves are shown in Figure 4.30.

$$\bar{\sigma} = 659.41(\bar{\epsilon})^{0.2441} \quad (4.4)$$

$$\bar{\sigma} = 646.21(\bar{\epsilon})^{0.2319} \quad (4.5)$$

$$\bar{\sigma} = 644.70(\bar{\epsilon})^{0.2353} \quad (4.6)$$

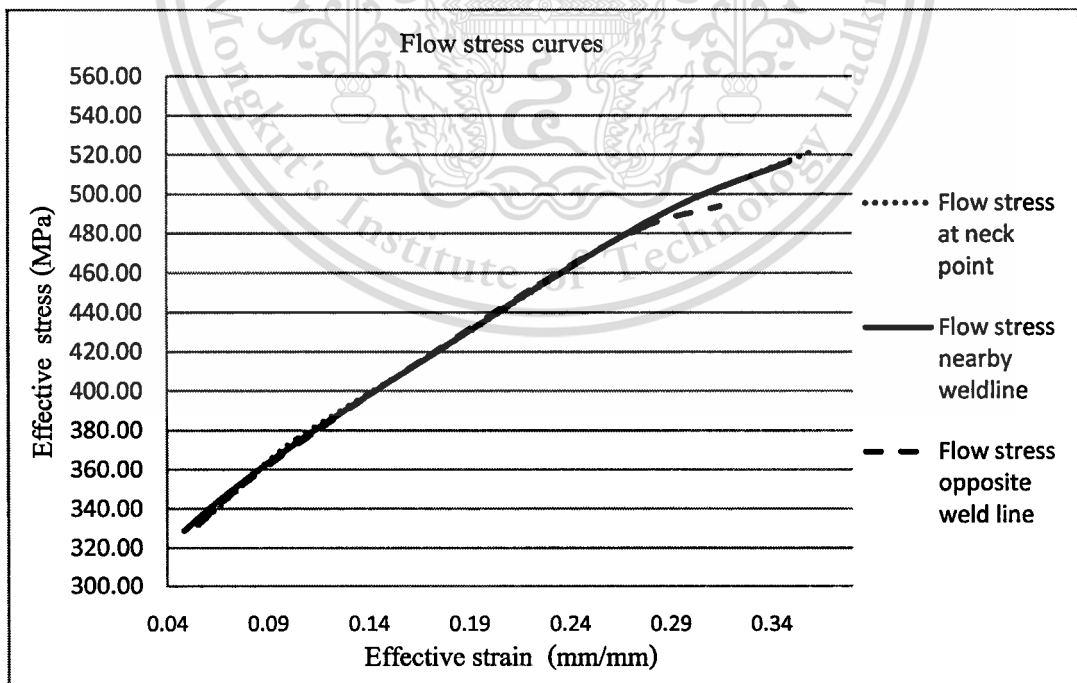


Figure 4.30 Flow stress curves of STKM11A steel tube by Ying Yot's model

### 4.2.3 Flow stress curves by Hwang's analytical model

The bulge shape is assumed as the elliptical surface, outer surface of thin-walled tube with shell element. All of the above-mentioned experimental data are used for flow stress calculation. From their analytical model, circumferential radius ( $\rho_{\theta p}$ ) and meridian radius ( $\rho_{\phi p}$ ) are calculated by using geometrical relation as shown in **Figure 4.27** and **Figure 4.28**. Circumferential strain and strain in thickness direction are obtained. The meridian stress and circumferential stress are calculated by taking equation of equilibrium of force. By substituting those calculated parameters into equations of Von-mises criterion (**Equation 40** and **Equation 46** in **Appendix B-3**), Effective stress and effective strain are obtained. As results, the effective stress and effective strain of STKM 11A steel are shown in **Table B-10**, **Table B-11** and **Table B-12** (see **Appendix B-6**). The flow stress curves of the tubes are obtained from Power law (**Equation 47** in **Appendix B-3**). Strength coefficient (K) and strain hardening (n) of the tubes are determined numerically by the least mean square method. As result, Strength coefficients (K) of material at Neck, Nearby Weldline and Opposite Weldline Points are equal to 744.52 MPa, 728.32 MPa and 728.32 MPa, respectively. Strain hardenings (n) of material at Neck, Nearby Weldline and Opposite Weldline Points are equal to 0.2664, 0.2505 and 0.2505, respectively. Therefore, the flow stresses at Neck, Nearby Weldline and Opposite Weldline Points are expressed as **Equation 4.7**, **Equation 4.8** and **Equation 4.9**.

$$\bar{\sigma} = 744.52 (\bar{\epsilon})^{0.2664} \quad (4.7)$$

$$\bar{\sigma} = 728.32 (\bar{\epsilon})^{0.2505} \quad (4.8)$$

$$\bar{\sigma} = 728.32 (\bar{\epsilon})^{0.2505} \quad (4.9)$$

The flow stress curves of STKM 11A steel tube are shown in **Figure 4.31**. All of calculated data according to the internal pressure levels are shown in **Appendix B-6** and

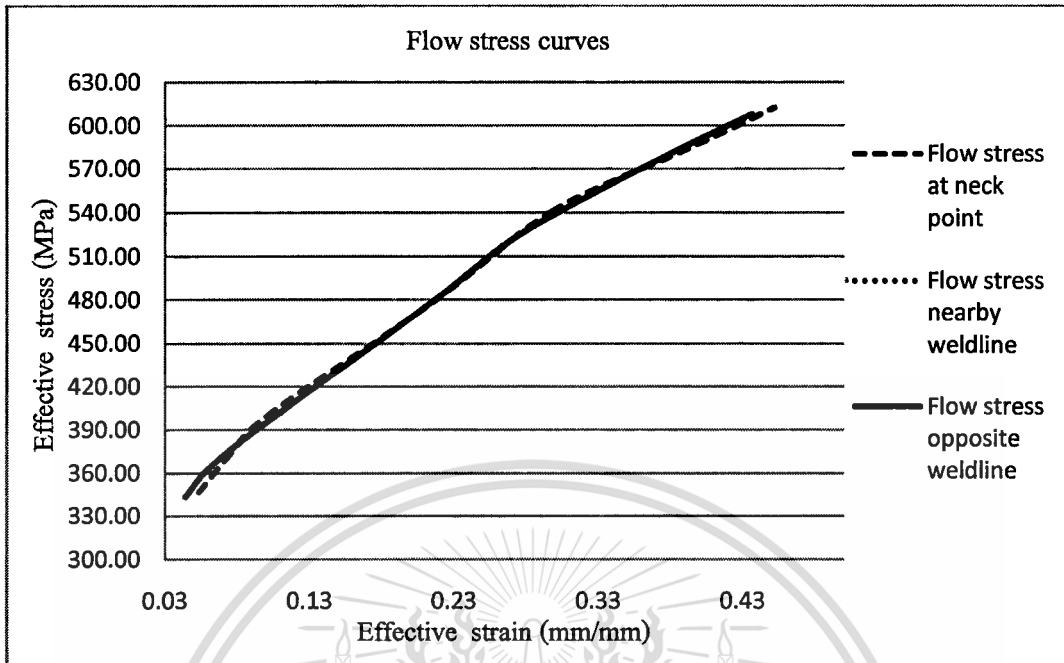


Figure 4.31 Flow stress curves of STKM11A steel tube by Hwang's model

### 4.3 Tensile Tests of Flattened Tube Specimen

In order to determine the flow stress data of the tubes by uniaxial tensile tests, STKM 11A tubes is slit and flattened as shown in Figure 4.32 (a) and (b). The cut tubes are flattened by the T.M.C. 200 ton press machine as shown in Figure 4.33. The pre-strain ( $\epsilon_0$ ) approximated from FEA simulation of the tube flattening (Figure 4.34 and Figure 4.35) is 5.10 percent approximately. This value will be used to substitute in the flow stress expression. The flattened tube specimens for tensile test are cut to shape referring to ASTM standard dimensions [15] as shown in Fig. 4.36 (a) and (b). The tensile tests of flattened tube are conducted under a constant strain rate of  $2 \times 10^{-3} \text{ s}^{-1}$  at room temperature using an INSTRON universal testing machine. As result, anisotropy value ( $r$ ) of material which is strain in width direction to that in thickness direction is obtained by calculating the slope of a straight line in Figure 4.37. The anisotropy value in the longitudinal direction of the tube is  $r_\phi = 1.74$ . But, the tube sheet tensile test in width direction is ignored because outer diameter of this tube is very small. It cannot be cut in width direction Thus, anisotropy value in width directions ( $r_\theta$ ) of the tube is assumed that it is equal to 1.74, same as that in the longitudinal direction.

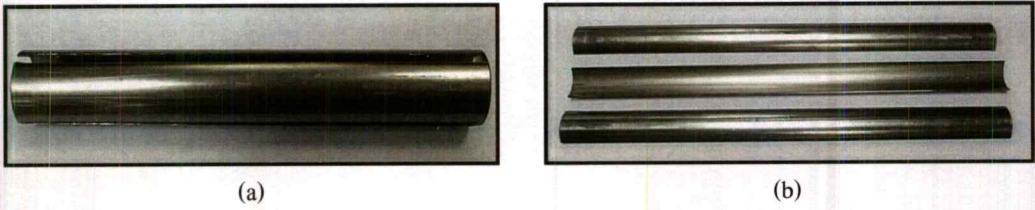


Figure 4.32 A typical tube cut in longitudinal direction, (a) a cut tube and (b) wall-separated tubes

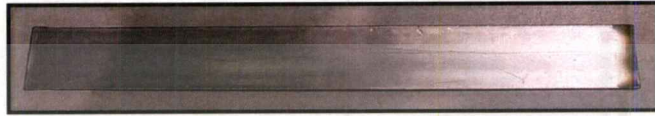


Figure 4.33 A typical flattened tube workpiece

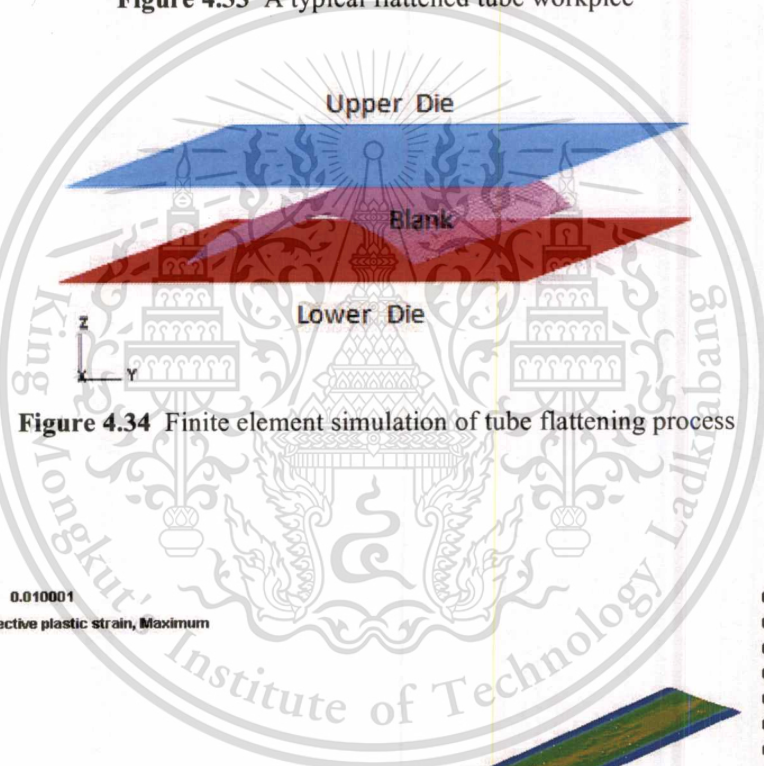


Figure 4.34 Finite element simulation of tube flattening process

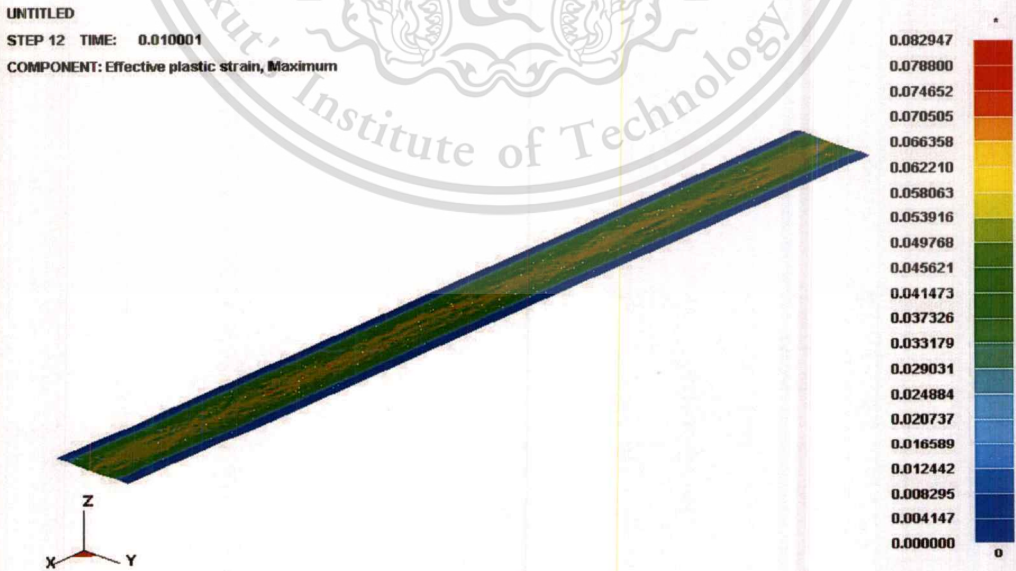
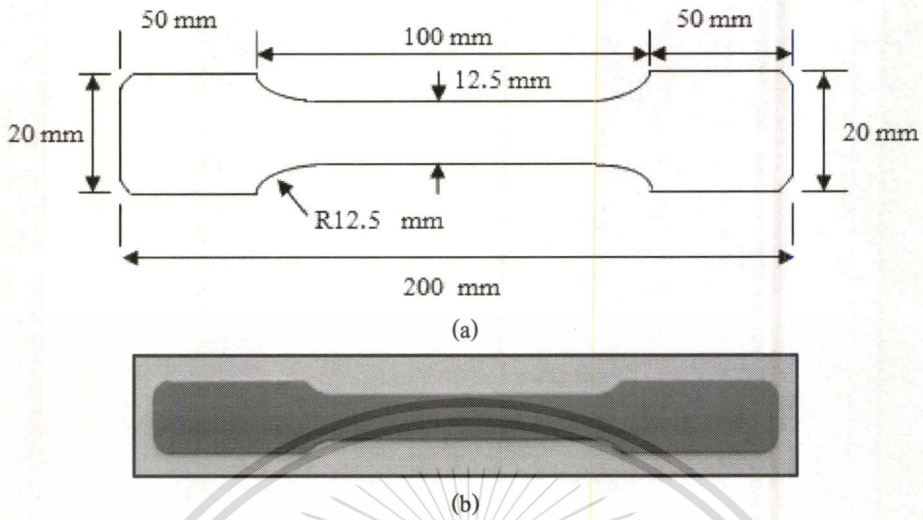
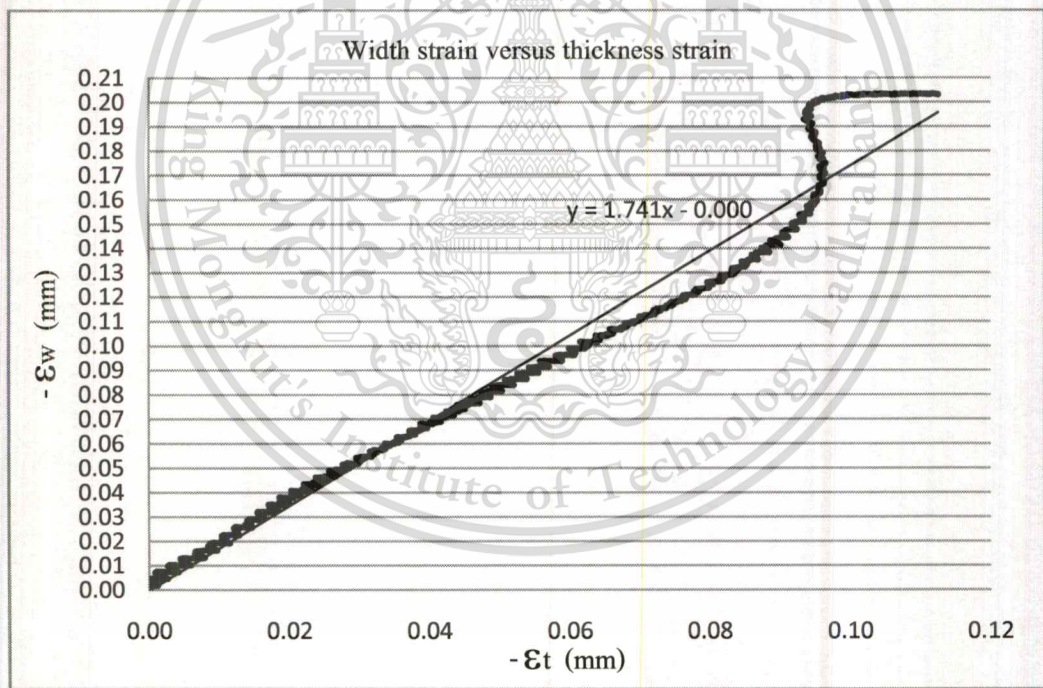


Figure 4.35 Finite element simulation result of tube flattening



**Figure 4.36** A typical specimen for tensile test, (a) standard dimension and (b) a fine specimen

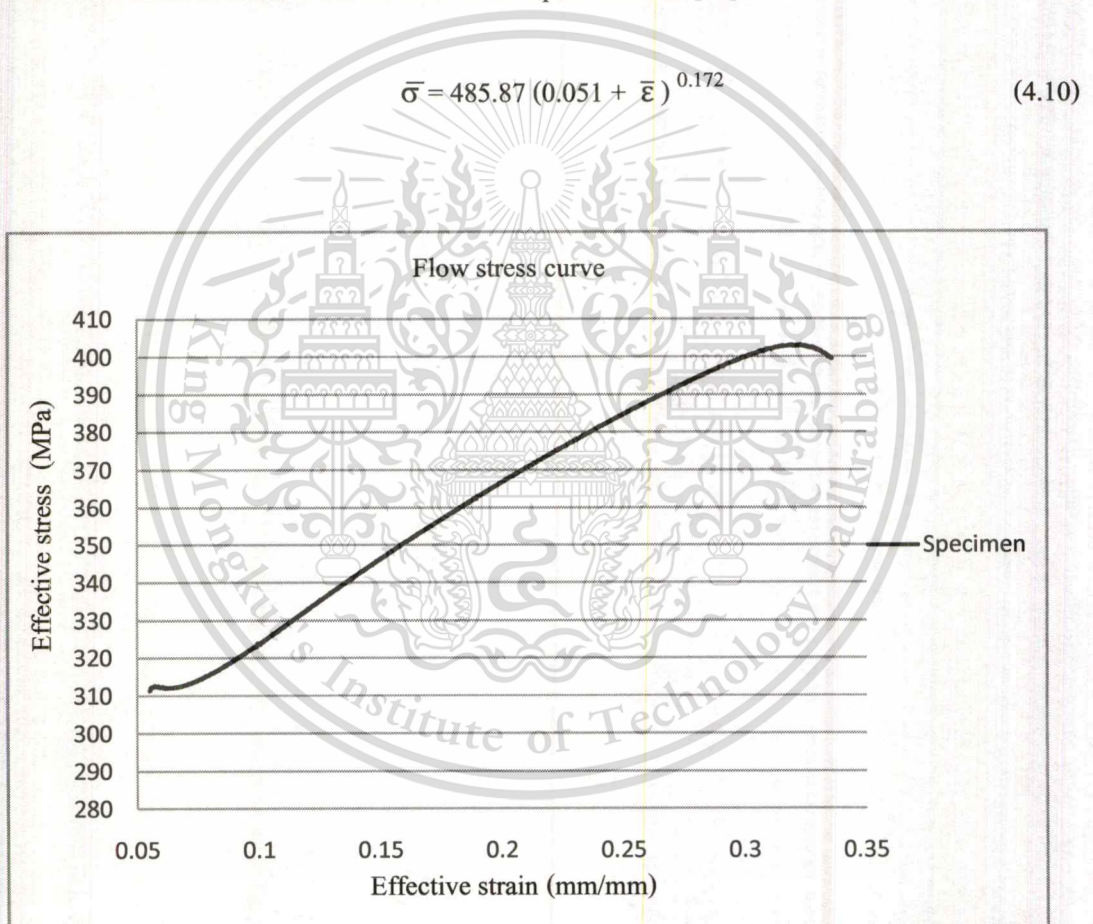


**Figure 4.37** Comparison between width strain and thickness strain for anisotropy value calculation

Elongations are recorded by a video extensometer. Tension forces, strain in longitudinal and width directions can also be obtained. The flow stress curve of the test tube can be determined by using relationship between extension load and elongation.

#### 4.3.1 Flow stress curve of the tube by tensile tests

After the tensile tests, the recorded tension load and elongation in longitudinal direction are calculated into true stress and true strain. The experimental data combined with a pre-strain ( $\epsilon_0$ ) of wall-flattened tube is used for the flow stress determination. An extrapolation from the Swift's law with the experimental data and available  $\epsilon_0$  value is performed, where,  $\epsilon_0 = 0.051$ . The flow stress curve of the STKM 11A tube that result is expressed as **Equation 4.10** without anisotropy value ( $R$ ) is shown in **Figure 4.38**. Strength coefficient ( $K$ ) = 485.87 MPa and strain-hardening exponent ( $n$ ) = 0.172 of material are obtained from the least mean square method [21].



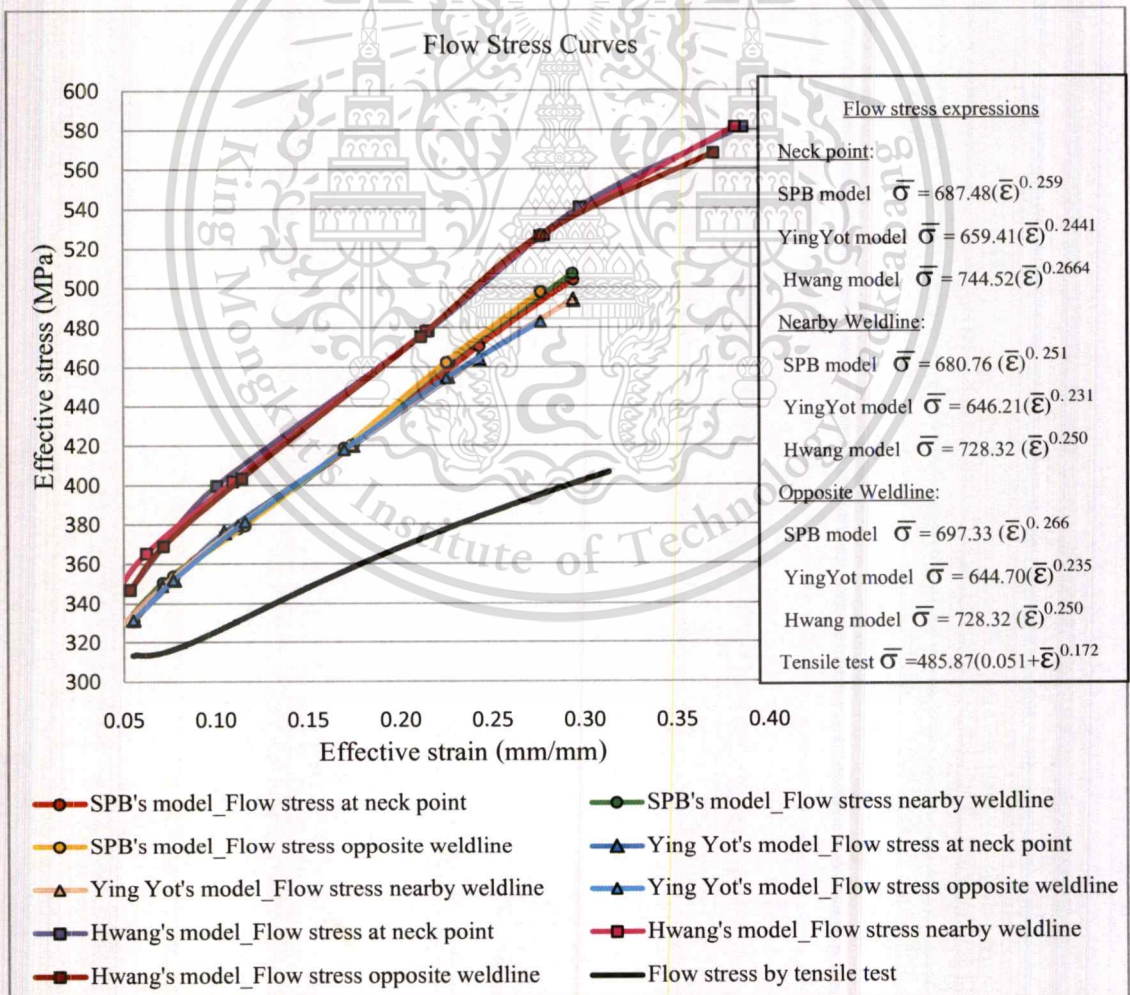
**Figure 4.38** Flow stress curve of STKM 11A steel tube obtained from tensile test

## Chapter 5

# Comparison and Analysis

### 5.1 Comparison of Flow Stress Curves

The flow stress curves obtained from the analytical models (SPB model, YingYot's model, Hwang's model) and tensile test are compared. **Figure 5.1** shows comparison results. The circular, triangular, square and linear symbols denote the flow stress curves obtained from SPB model, YingYot model, Hwang model and tensile test, respectively. The equivalent stress-strain relations with corresponding  $\epsilon_0$ , K and n are also compared.



**Figure 5.1** Flow stress curves of STKM 11A steel tube

From **Figure 5.1**, it is found that the flow stress curve obtained from the tensile test is quite different from those by the free bulge test. The flow stress curves obtained from SPB model reveal different characteristics from those by YingYot model, Hwang model and tensile test. Nevertheless, there are no significant discrepancies of flow stress curves between SPB model and YingYot model because both models have the same assumption of the bulge shape. That is, the curvature of the bulge shape seems to be the circular arc. The meridian radius of the bulge shape can be measured in form of the circular arc. On the other hand, Hwang model assumed that curvature of the bulge shape is ellipsoid. The meridian radius of the bulge shape is obtained from their equation. So, the flow stress curves obtained from Hwang model highly differs from SPB model and YingYot model. For strength coefficient ( $K$ ) and stain hardening ( $n$ ) values, SPB model obviously differs from other models. It can be seen that those analytical models and tensile test have large differences because of the influence on axial tension test. Namely, SPB and YingYot models analyze the plastic deformation behavior of the tube by using theory of the biaxial stress state. On the other hand, flow stress of tensile test is obtained from the uniaxial stress state. To determine the best representative of flow stress curve of the tube, these flow stress curves will be used for predicting the upper hydroformability limit of the tube (safety forming without crack) with the FEA simulation.

## 5.2 Validation of Developed Analytical Models Using Flow Stress Curves

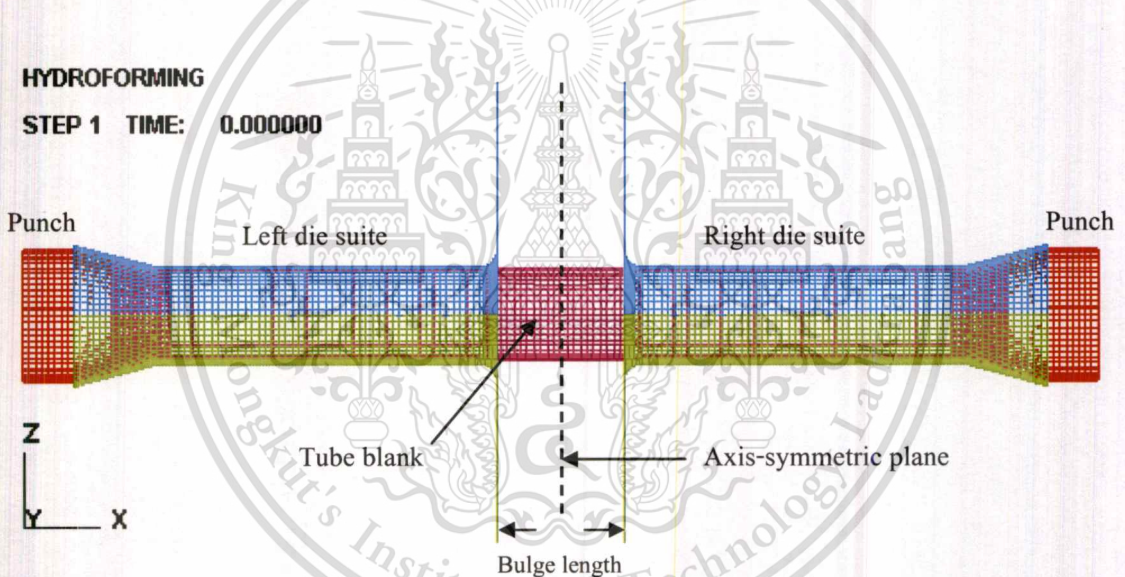
### 5.2.1 Tube hydroformability evaluation with finite element simulations

In order to validate the developed SPB model, Finite Element simulation methods are adopted for tube hydroformability evaluation. The explicit FEA software, i.e. DYNAFORM 5.6.1 with LS-Dyna solver (non-linear problem solver), is used to conduct the simulation of tube hydroforming process. For process design, the FEA model per the flow stress curve (**Figure 5.1** or data in **appendix B-6**) in each process is created as follows.

- 1) Model#1, Model#2 and Model#3 use Flow stress curves at Neckpoint, Nearby Weldline and Opposite Weldline of the formed tube, respectively, which are obtained from SPB model.
- 2) Model#4, Model#5 and Model#6 use Flow stress curves at Neckpoint, Nearby Weldline and Opposite Weldline of the formed tube, respectively, which are obtained from YingYot model.
- 3) Model#7, Model#8 and Model#9 use Flow stress curves at Neckpoint, Nearby Weldline and Opposite Weldline of the formed tube, respectively, which are obtained from Hwang model.

4) Model#10 use Flow stress curve obtained from tensile test.

FE simulation methods are shown in **Appendix C**. The die inserts are assumed to be rigid. A FE model of tube blank, outer diameter (OD) = 28.6 mm, thickness = 1.2 mm and bulge length = 38.1 mm is created and defined as a half model with nodal constraints on the symmetry plane. The mechanical properties of material are defined as abovementioned flow stress data. Internal pressures in **Table 4.3** are specified as pressure loading curve. Isotropic material is assumed ( $R_{00} = 1$ ,  $R_{45} = 1$  and  $R_{90} = 1$ ). Heat transfer and temperature are neglected. A constant friction coefficient ( $\mu$ ) of 0.125 is assumed at the interface between the tube surface and the die surface. Mesh sizes of tube blank and die inserts are described in **Appendix C**. Two ends of the tube are fixed by the axial punches, which have zero feeding distance. For instance, the created FEA model is shown in **Figure 5.2**.














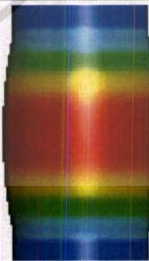

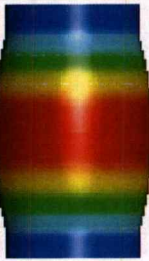
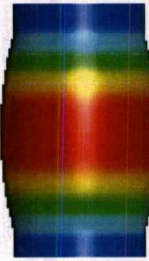
**Figure 5.2** Finite Element Simulation model

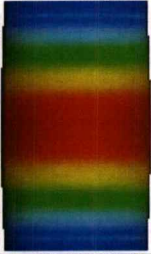


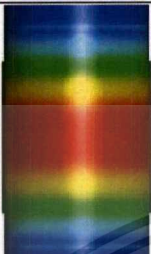

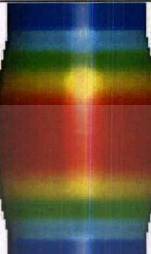








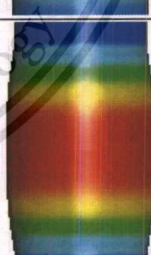



### 5.2.2 Comparison between FEA simulation result and experimental result

The explicit FEA results for STKM11A tube are compared with experimental results. **Table 5.1** shows real formed tubes against FEA results in partial forming levels. From **Table 5.1**, there are ten compared models which depend on internal pressure levels ( $P_{yield}$ ,  $P_5 = 336$  bar,  $P_{burst} = 337.7$  bar). The FE tube models in the simulation software mostly respond to the free bulge deformation except the FEA model using flow stress obtained from tensile test is cracked at  $P_3$  level

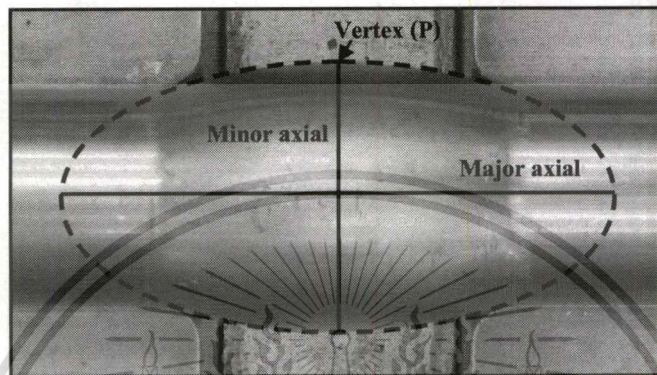
(320 bar). That means the tube hydroformability is too low. Moreover, another model shows that the every hydroformed tube at  $P_{burst}$  level ( $P = 337.7$  bar) is the biggest bulge shape. But, it is cracked.

**Table 5.1** Real formed tubes against the FE simulation results for STKM11A tube

Model	Internal forming pressure levels		
	$P_{yield} = 290$ bar	$P_5 = 336$ bar	$P_{burst} = 337.7$ bar
Real hydroformed tubes			
Model #1			
Model #2			
Model #3			
Model #4			

Model # 5			
Model # 6			
Model # 7			
Model # 8			
Model # 9			
Model #10			
<p><b>Remark :</b> Blue = Wrinkle tendency, Green = Safe, Yellow = Risk of crack, Red = Crack, Gray = Insufficient strength or burst</p>			

Therefore, the real hydroformed tube at  $P_5$  level (Level #5,  $P = 336$  bar) is compared with the FEA results ( $P_5$  level) in order to estimate effective parameters (i.e., maximum bulge height ( $h_p$ ), maximum tube thickness ( $t_p$ ) maximum internal pressure ( $P_i$ )). **Figure 5.3** shows minor and major axes of the elliptical surface corresponding to the real hydroformed tube (Level #5 in **Figure 4.13**).



**Figure 5.3** A real hydroformed tube at  $P_5$  (Level #5 in **Figure 4.13**,  $P = 336$  bar)

Tube thickness distributions in longitudinal direction (only section cut at  $\theta = 180^\circ$ ) at pressure level  $P_5$  are stable as shown in **Figure 5.4**. It can be seen that the FE tube model has the proper shape without wrinkle. Maximum thickness and bulge heights at the vertex of the bulge are compared with the real hydroformed tube (Level #5 in **Figure 4.13**) as shown in **Figure 5.5** and **Figure 5.6**.

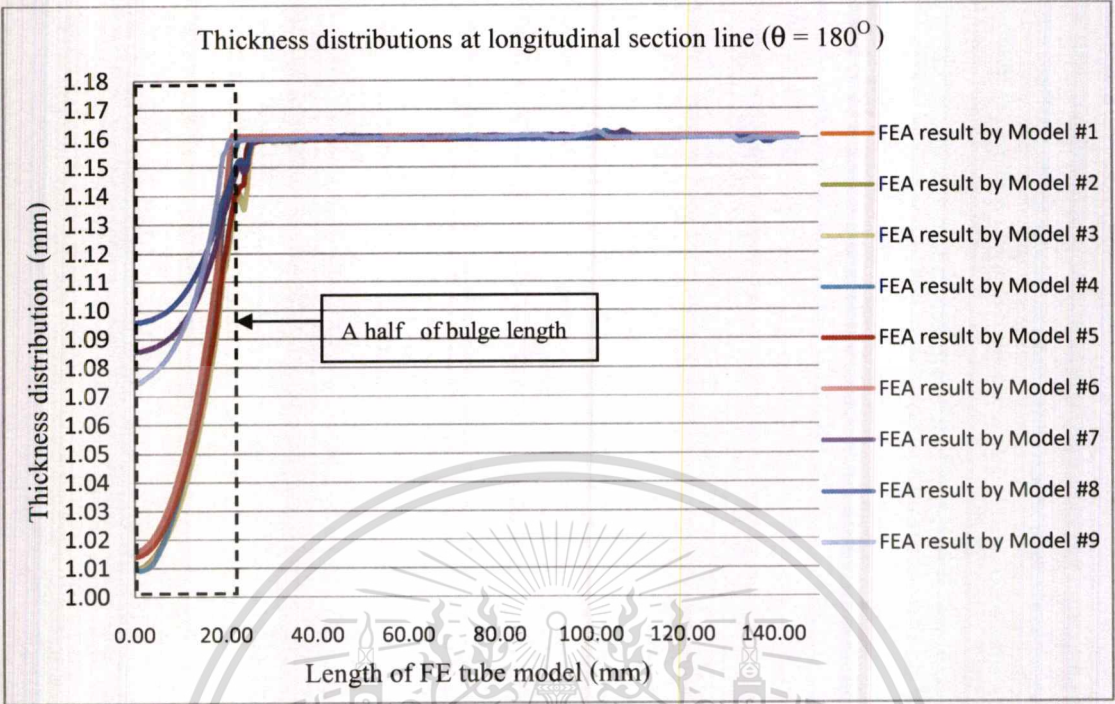


Figure 5.4 Thickness distributions in longitudinal direction of the tube

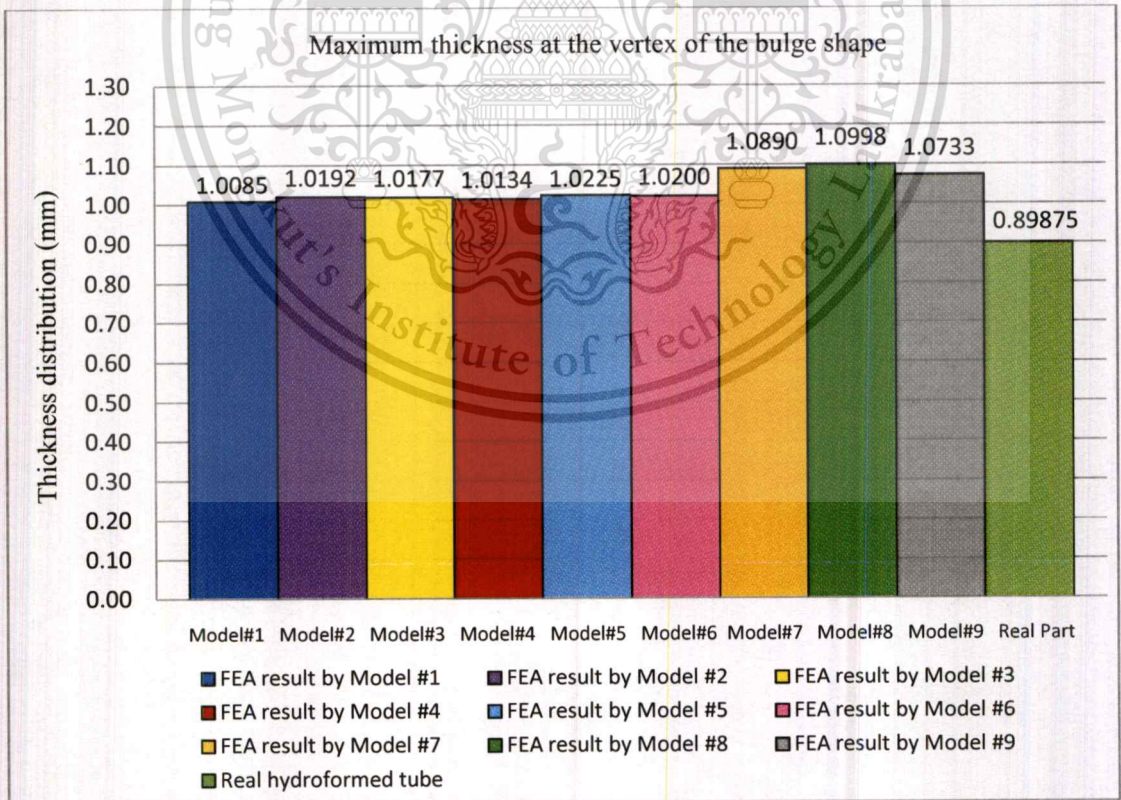
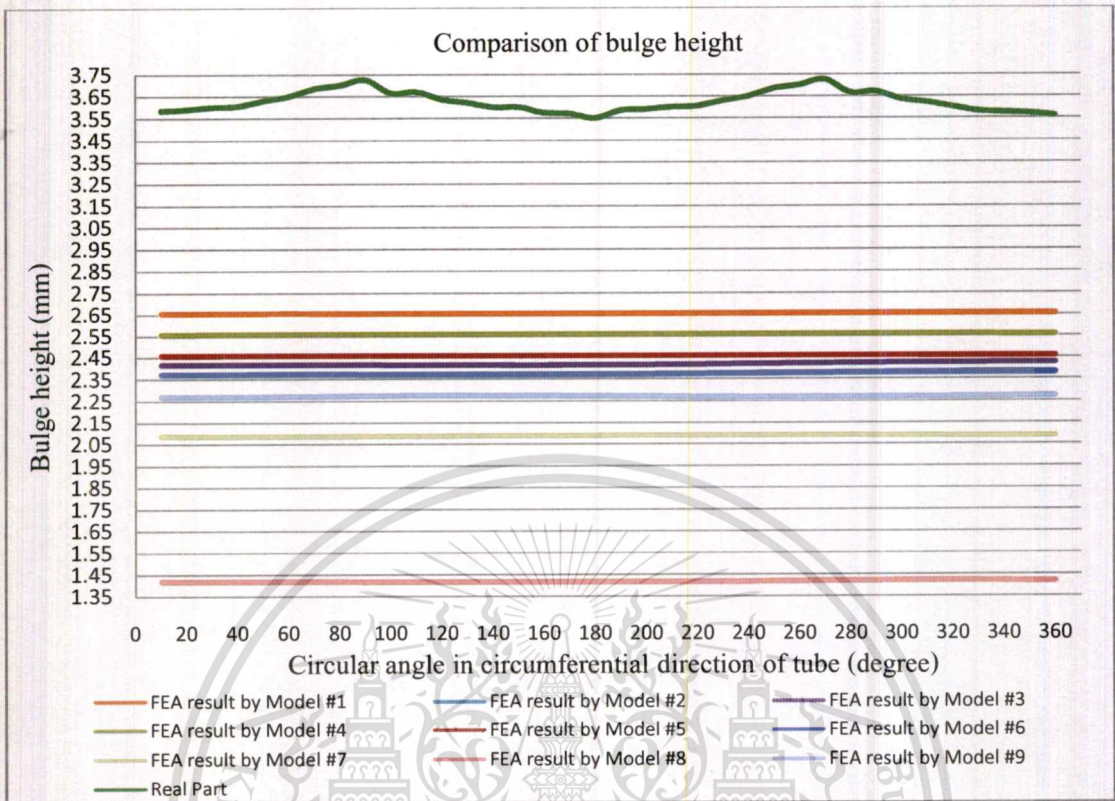


Figure 5.5 Thickness comparison between the FEA results and the real tube (Level#5 in Figure 4.13)

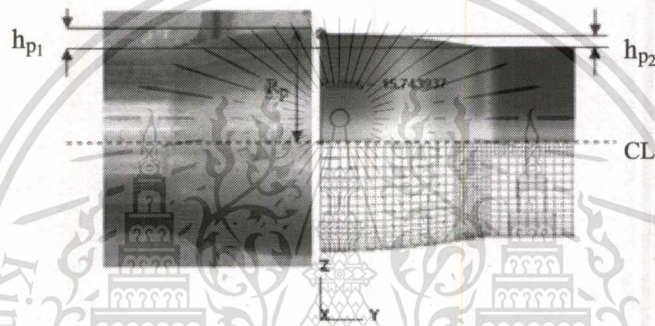


**Figure 5.6** Bulge height comparison between the FEA results and the real tube (Level#5, Figure 4.13)

For **Figure 5.5**, it can be seen that the thickness ( $t_p$ ) of Model #1 using SPB model\_Neck point flow stress is closest to the experimental result because SPB model directly measures the bulge shape parameters for flow stress calculation. On the other hand, another model approximates bulge shape parameters by using exact equations. Nevertheless, YingYot model has the same assumption of bulge shape as SPB model. Thus, Model #4 (YingYot's model\_Neck point flow stress) almost corresponds with SPB model. Both of analytical models deviate from the experimental results about 10.88 % and 11.31 %, respectively. Model #7, Model #8 and Model #9 (results from Hwang model) and other models are more different from the experimental results.

For **Figure 5.6**, it can be seen that the bulge height ( $h_p$ ) of Model #1 using SPB model\_Neck point flow stress) is closest to the experimental result because SPB model directly measures the bulge shape for flow stress calculation. On the other hand, another model approximates bulge shape parameters by using exact equations. Model #4 (YingYot's model\_Neck point flow stress) slightly differs from SPB model by 0.1 mm. Model #1 (SPB model\_Neck point flow stress) deviates from the

experimental result about 26.80 %. Model #4 (YingYot's model\_Neck point flow stress) deviates from the experimental result about 29.48 %. Model #7, Model #8, Model #9 (results from Hwang model) and other models are more different from the experimental results. **Figure 5.7** displays the analytically predicted bulge curvature which is alike the real shape of the hydroformed tube (Level #5 in **Figure 4.13**). It illustrates the real and predicted bulge heights ( $h_p$ ), the real and predicted circumferential radii ( $\rho_{pp}$ ) of the formed tube. It can be seen that the real formed tube is bigger bulge than FEA model that **Figure 5.7** shows apparent aspect correspond with the bulge height comparison result (**Figure 5.6**).



**Figure 5.7** Bulge shape comparison between the FEA model and the real tube (Level #5, Figure 4.13)

### 5.2.3 Analysis of flow stress curves

For SPB model, three flow stress curves are obtained from the free bulge test that the tube is deformed under a biaxial stress state. The curvature of the bulge shape is assumed as the outer surface. The meridian radius of the bulge shape can be measured in CAD software. The internal pressure, bulge height, thickness and circumferential radius are directly measured by measuring instruments. From **Figure 5.1**, the flow stress curves indicate that two measured points have the maximum strain near weldline (Neck and Nearbyweldline points) and more risk of crack. These points are caused by high strength of weldline. ERW method causes for preferred orientation of grains. Consequently, stress rather decreases when strain continuously increases. Moreover, strain at these points are more than the Opposite weldline point. Hence, the flow stress curves at Neck and Nearbyweldline points are longer curves, respectively as shown in **Figure 5.1**. However, stress at Oppositeweldline point is relatively similar to Neck and Nearbyweldline points. As comparison results, the thickness distribution of Model #1 is lower than Model #2 and Model #3 because strain of

Model #1 is more than Model #2 and Model #3. Moreover, the bulge height of Model #1 is more than Model #2 and Model #3. Therefore, FEA model of Model#1 is the biggest bulge shape. The thickness distribution of Model #2 is lower than Model #3. The bulge height of Model #2 and the bulge shape are bigger than Model #3.

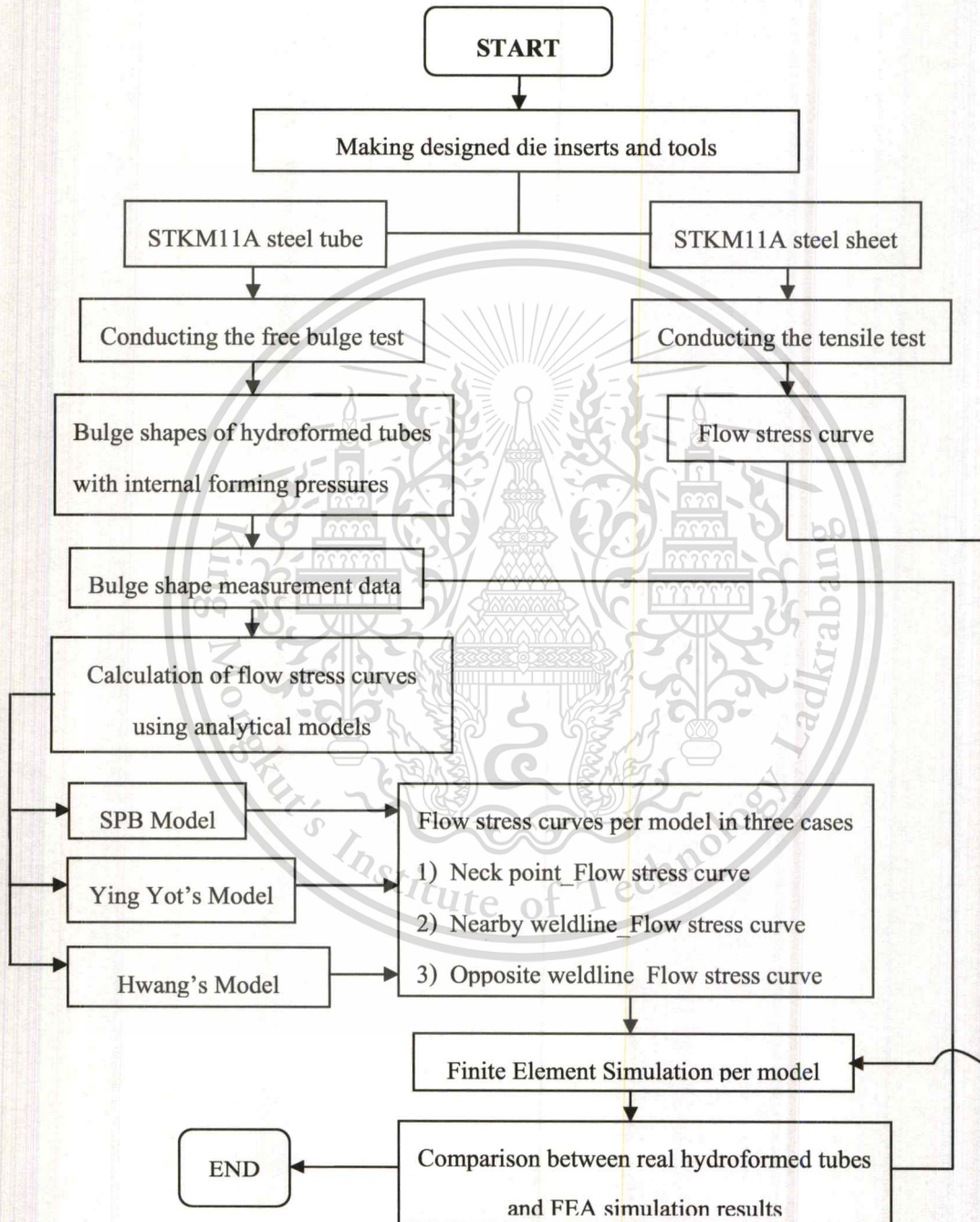
For YingYot model, three flow stress curves are obtained from the free bulge test. The bulge shape is assumed as circular arc. The curvature of the bulge shape is assumed as the inner surface. Circumferential and meridian radii are estimated by using their equations. Consequently, three flow stress curves are different from SPB model's flow stress curves as shown in **Figure 5.1**. However, effects of flow stress curves from different measured point can be explained as same as SPB model. From comparison results, thickness distributions and bulge heights of all FEA models certainly differ from the experimental results as shown in **Figure 5.1**.

For Hwang model, three flow stress curves are obtained from the free bulge test. The bulge shape is assumed as elliptical surface. The curvature of the bulge shape is assumed as the middle surface. Circumferential and meridian radii are estimated by using their equations. Their methodology is different from SPB model and YingYot model. Consequently, three flow stress curves absolutely differ from SPB model and YingYot model as shown in **Figure 5.1**. Thickness distributions and bulge heights of all FEA models highly differ from the experimental results. Effects of the flow stress curves from different measured point can be explained as same as SPB model. The bulge shapes of FEA models (i.e., Models #7, #8, #9) are smaller than the real formed tube, respectively. It is found that Hwang model overestimates the flow stress curves of the tube.

For tensile test result, the flow stress curve is too low. The FEA model cannot withstand the free bulging with high internal pressure (32 MPa). Besides, FEA simulation progress is early failed (see Model #10 in **Table 5.1**). It is found that the tensile test underestimates the flow stress curve that is not suitable for the free bulge test.

As results, SPB model seems to be the best analytical approach among all considered methods as it gives the best prediction results compared to the experimental result. Therefore, the representative of strain-strain relationship of STKM 11A steel tube is the flow stress curve at Neckpoint (see **Figure 4.26**) calculated by SPB model. A flow chart of flow stress determination is shown in **Figure 5.8**.

Nevertheless, the abovementioned discrepancies of analytical models and experimental results may be caused by material anisotropy.



**Figure 5.8** A flow chart of flow stress determination

### 5.2.4 Study of anisotropy effects on materials

Anisotropy is caused by preferred orientations or textures of grains due to manufacturing processes. This value indicates expansion ability of thin-walled tube. From Hwang papers [11, 12], effective stress-strain relationship obtained from tensile test can be expressed as **Equation 5.1** and **Equation 5.2**, respectively.

$$\bar{\sigma} = \sqrt{\frac{3}{2}} \left( \frac{1 + \left(\frac{1}{r_\phi}\right)}{\left(\frac{1}{r_\theta} + 1 + \frac{1}{r_\phi}\right)} \right)^{1/2} \cdot \sigma_\phi \quad (5.1)$$

$$\bar{\epsilon} = \sqrt{\frac{2}{3}} \left( \frac{\left(\frac{1}{r_\theta}\right) + 1 + \left(\frac{1}{r_\phi}\right)}{\left(1 + \frac{1}{r_\phi}\right)} \right)^{1/2} \cdot \epsilon_\phi \quad (5.2)$$

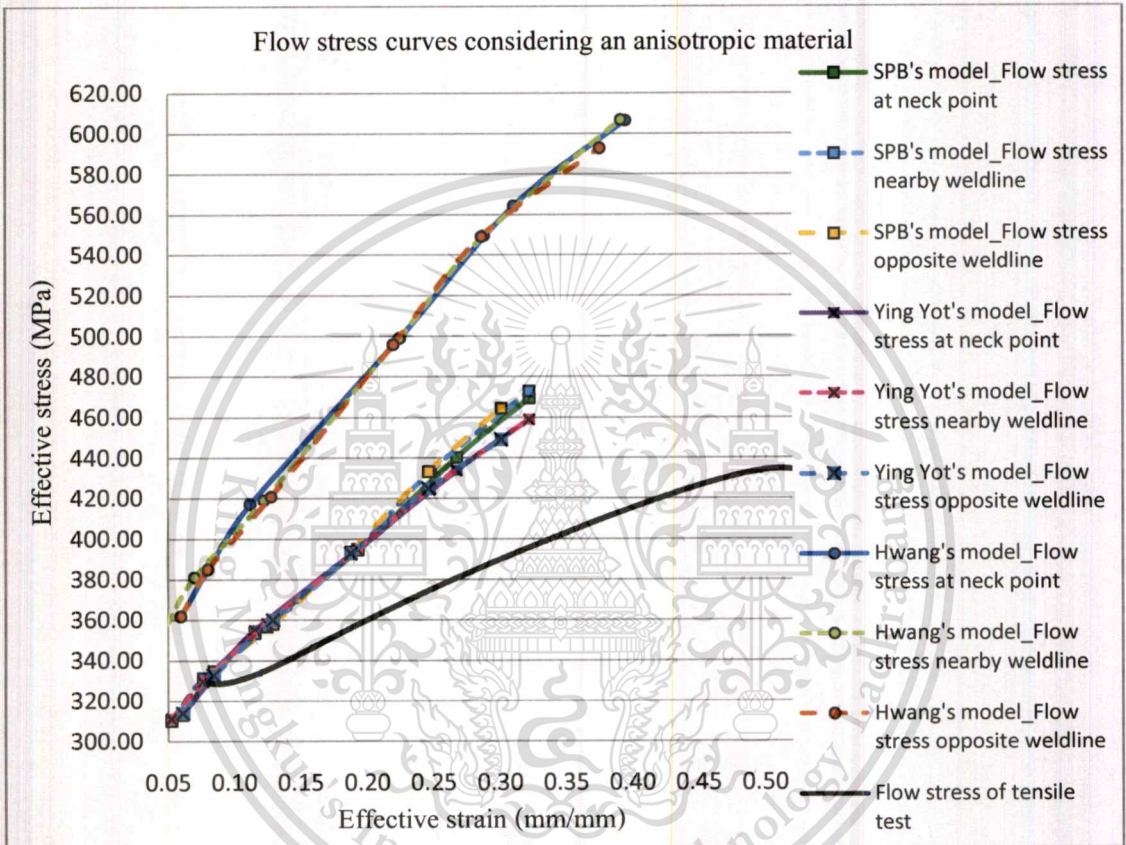
where,  $\sigma_\phi$  and  $\epsilon_\phi$  are axial stress and axial strain obtained from the tensile test, respectively. Equation 5.1 and Equation 5.2 are adopted when plotting the figure of the effective stress – strain relationship considering anisotropic materials. From Hill's orthogonal anisotropic theory (Hill, 1950) and theory of volume constancy, the effective stress and effective strain obtained from the free bulge test can be expressed as **Equation 5.3** and **Equation 5.4**, respectively.

$$\bar{\sigma} = \sqrt{\frac{3}{2}} \left[ \frac{\left(1 + \left(\frac{1}{r_\phi}\right)\right) \sigma_\phi^2 - 2\sigma_\phi \sigma_\theta + \left(1 + \left(\frac{1}{r_\theta}\right)\right) \sigma_\theta^2}{\left(\frac{1}{r_\theta} + 1 + \frac{1}{r_\phi}\right)} \right]^{1/2} \quad (5.3)$$

$$\bar{\epsilon} = \sqrt{\frac{2}{3}} \left\{ \frac{\left(\frac{1}{r_\theta}\right) + \left(\frac{1}{r_\phi}\right) + 1}{\left(\frac{1}{r_\theta r_\phi}\right) + \left(\frac{1}{r_\phi}\right) + \left(\frac{1}{r_\theta}\right)} \left[ \left(\frac{1}{r_\theta} + \frac{1}{r_\phi}\right) \epsilon_\theta^2 + \frac{2}{r_\theta} \epsilon_\theta \epsilon_t + \left(1 + \frac{1}{r_\theta}\right) \epsilon_t^2 \right] \right\}^{1/2} \quad (5.4)$$

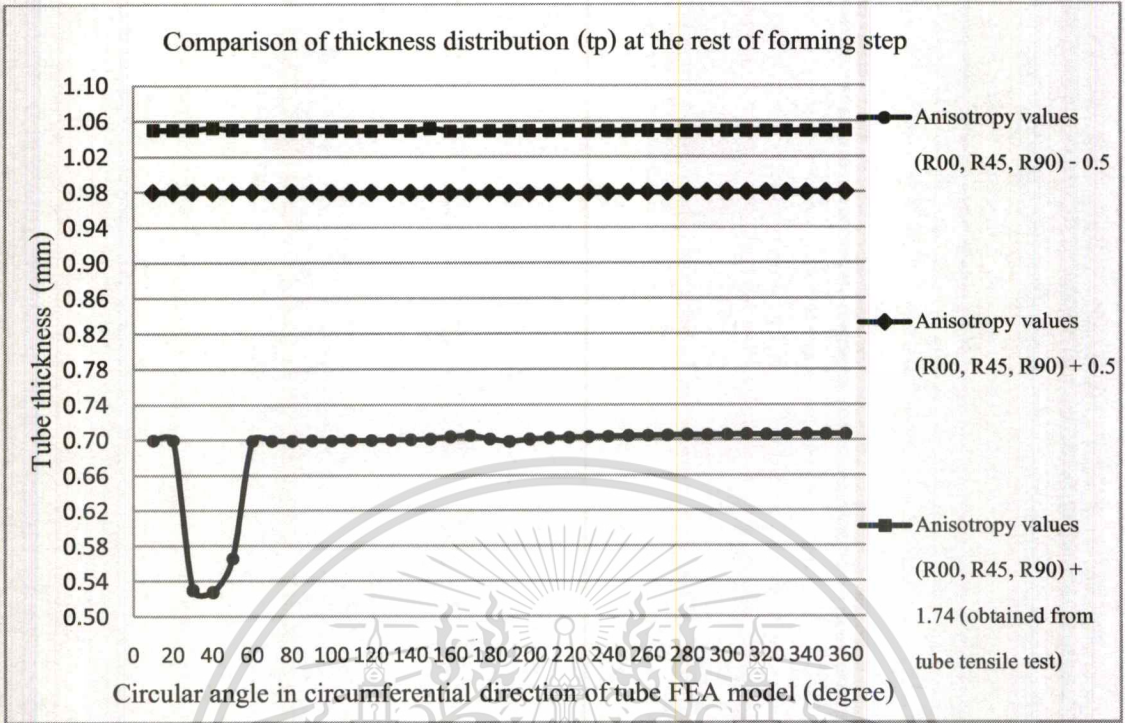
where,  $\sigma_\phi$  and  $\sigma_\theta$  are principal stresses in meridian and circumferential directions at the vertex of the bulge shape, respectively.  $\epsilon_\theta$  and  $\epsilon_t$  are principal strains in circumferential and thickness directions at the vertex of the bulge shape, respectively.  $r_\phi$  and  $r_\theta$  are anisotropy values of materials in meridian and circumferential directions (i.e.,  $r_\phi = r_\theta = 1.74$ ), which are obtained from tensile tests (**Title 4.3** in **Chapter 4**) in the corresponding directions. As result, the flow stress curves obtained from the tensile test and the bulge test considering the material anisotropy can be calculated as shown in **Figure 5.9**. The square, cross, circle and straight line denote the flow stress curves obtained from SPB model, YingYot model, Hwang model and tensile test, respectively. For the flow stress curves from SPB

model and YingYot's model, increased anisotropy values cause an increase of effective strain. In contrast, increased anisotropy values cause a decrease of effective stress. For the flow stress curves from Hwang model and tensile test, increased anisotropy values cause increases of effective stress and effective strain as shown in **Figure 5.9**.

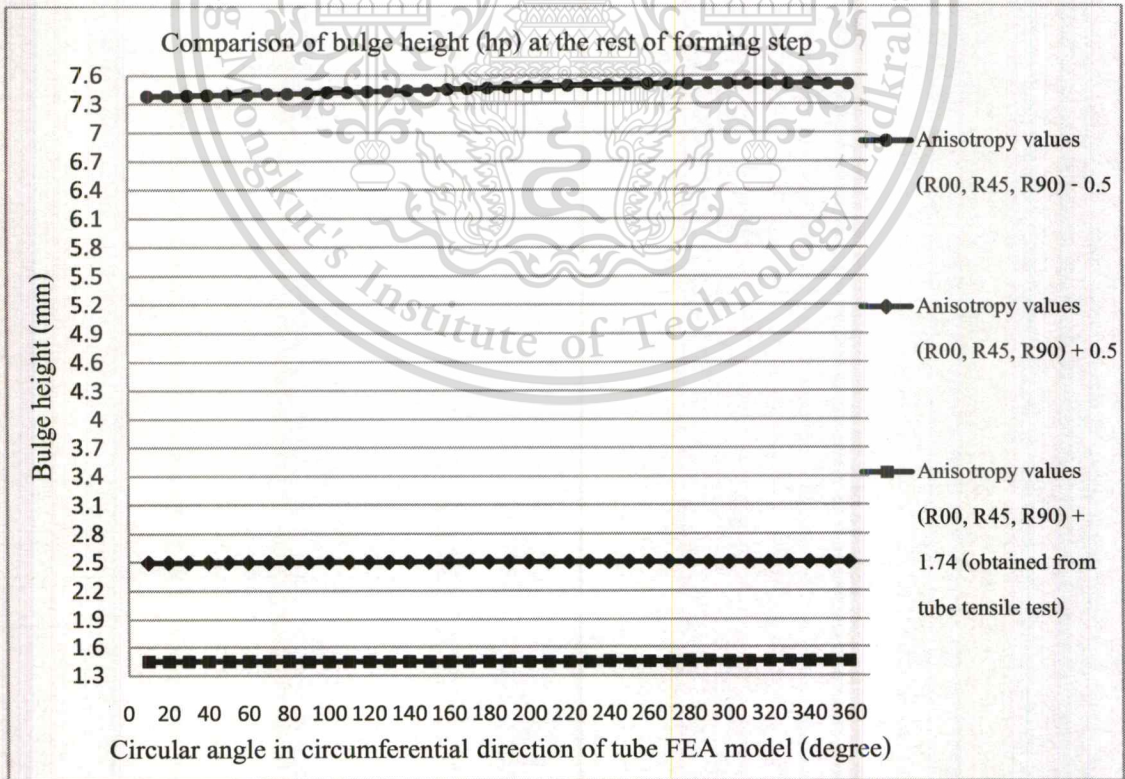


**Figure 5.9** Flow stress curves obtained from consideration of anisotropic materials

For FEA simulation, NeckPoint flow stress curve of the tube obtained from SPB model is specified to be mechanical properties of material. Designs of FEA model and THF process are described in Finite Element Simulation Method, **Table C-2** in **Appendix C**. Anisotropy values (R00, R45 and R90 in **Appendix C, Table C-2**) are varied from default (material type T36 SPCC, JIS standard) to study the anisotropy effects on tube deformation. The resulted deformation from finite element analysis, thickness distributions of Model#1, Model#2 and Model #3 are compared as shown in **Figure 5.10**. The bulge heights of Model #1, Model #2 and Model #3 are compared as shown in **Figure 5.11**.



**Figure 5.10** Thickness comparison of FEA models varied in anisotropy values

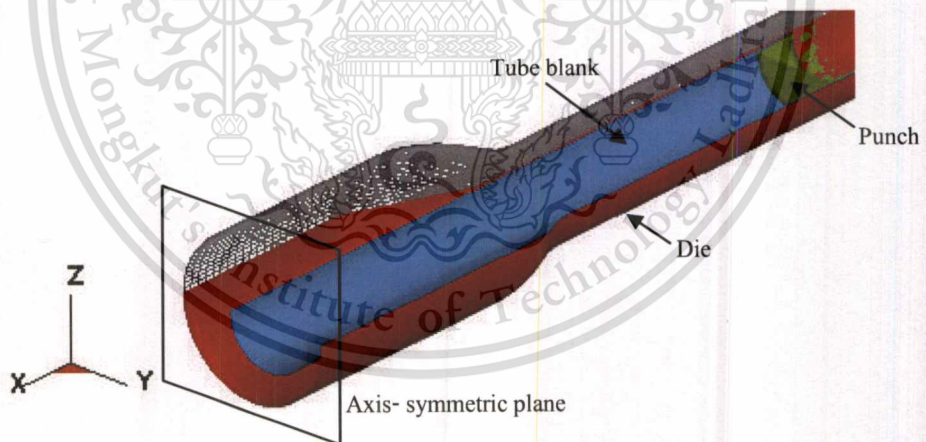


**Figure 5.11** Bulge height comparison of FEA models varied in anisotropy values

From **Figure 5.10** and **Figure 5.11**, equally increased anisotropy values in all three directions (R00, R45 and R90 in **Table C-2**) result in increased strength of materials. The tube can only be expanded slightly under the biaxial stress state. Thickness distribution is stable. In contrast, equally decreased anisotropy values in all three directions (R00, R45 and R90 in **Table C-2**) result in increased strength of materials. The tube can be expanded easily under the biaxial stress state. The material nearby weldline of the tube is easily cracked. Thickness distribution is less stable.

### 5.3 Usability Evaluation of Determined Flow Stress Curve

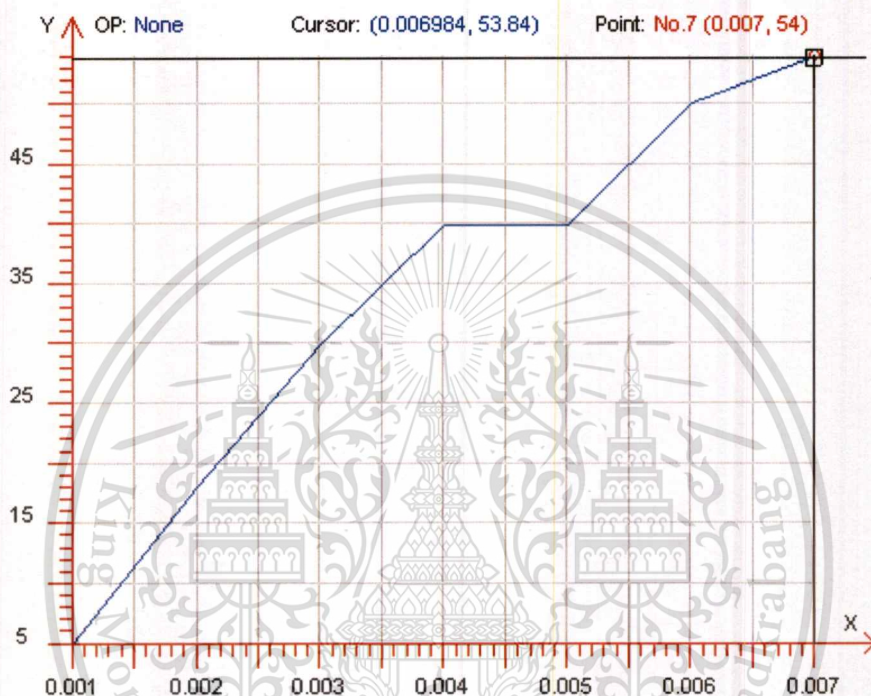
The determined flow stress data (flow stress at Neck point of the formed tube) from SPB model is used in the FE simulation for studying hydroformability of Oil Filler Pipe. A tube blank is defined as a half model with node constraint on symmetry plane. Hydroforming process design and dimension of a FE tube blank model in the simulation software is the same procedure as described details in **Title 5.2.1** except feeding distance is specified for punch function. The FEA model and feeding distance are shown in **Figure 5.12** and **Figure 5.13**. The FE simulation result is shown in **Figure 5.14**.



**Figure 5.12** FEA model shown by section cut for hydroformability evaluation of Oil Filler Pipe

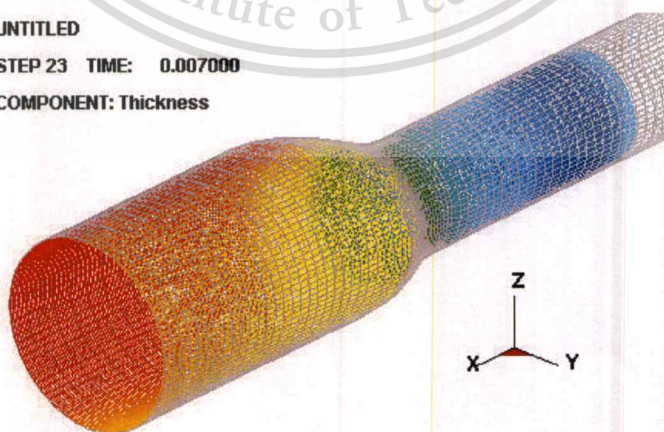
As result, the formed tube seems to be deforming properly. **Figure 5.15 (a)** and **(b)** shows the thickness distributions of Oil Filler Pipe and Forming Limit Diagram (FLD) with forming zones, respectively. Thicknesses around expansion area of Oil Filler Pipe are values in the range from 0.70 mm to 1.02 mm. It is found that the FEA model using the determined flow stress and internal pressure

curve clearly displays crack. However, this does not suggest failure of the determined flow stress curve. This flow stress curve still causes stable deformation of the tube without wrinkle. Other FEA models can be successfully applied by means of internal pressure of less than 33.77 Mpa. Nevertheless, this study (**Title 5.3**) should be useful information for further studies.



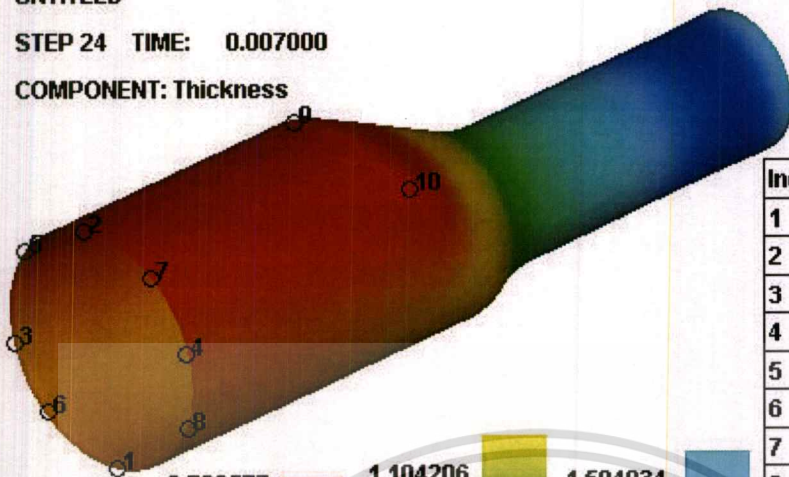
**Figure 5.13** Feeding distance curve

UNTITLED  
STEP 23 TIME: 0.007000  
COMPONENT: Thickness

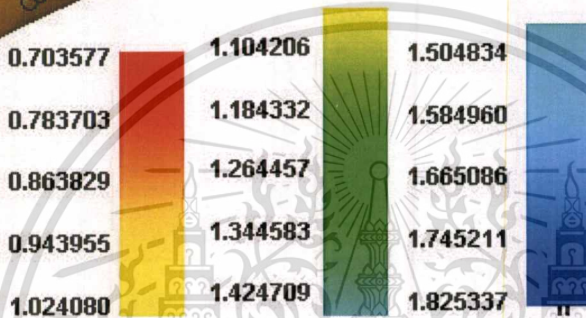


**Figure 5.14** FE simulation result of Oil Filler Pipe

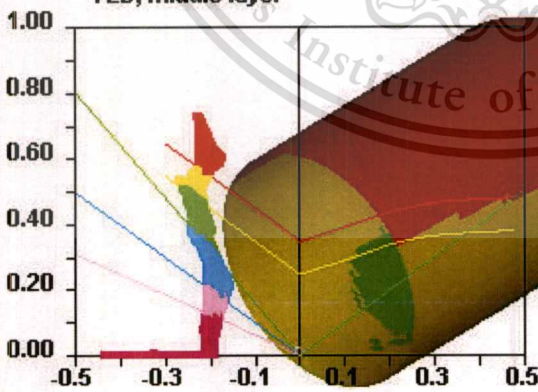
UNTITLED  
 STEP 24 TIME: 0.007000  
 COMPONENT: Thickness



Index	NodeID	THICKNESS
1	13577	0.889995
2	18046	0.806471
3	13598	0.883780
4	28593	0.910836
5	13478	0.803186
6	23492	0.894041
7	23930	0.866248
8	23476	0.890735
9	22492	0.708434
10	18853	0.758818



UNTITLED  
 STEP 23 TIME: 0.007000  
 FLD, middle layer



CRACK  
 RISK  
 OF CRACK  
 SAFE  
 WRINKLE  
 TENDENCY  
 WRINKLE  
 SEVERE  
 WRINKLE  
 INSUFFICIENT  
 STRETCH



(b)

**Figure 5.15** FEA results, (a) tube thickness distributions and (b) Forming Limit Diagram (FLD), middle layer with forming zones

## Chapter 6

# Conclusion and Suggestions

### 6.1 Conclusion

The die inserts are designed for the free bulge test to obtain the proper bulge shapes of the formed tubes for effective flow stress determination. The bulge shapes of the formed tubes in the range from the elliptical surface to the circular surface are investigated by considering effects of parameters ( $R_d/t$  and  $L_b/OD$ ) on hydroformability. The explicit dynamic FEA software, DYNIFORM 5.6.1 is used to conduct the simulation of tube hydroforming. From FEA results, the properly investigated dimensions of the die inserts are the bulge length ( $L_b$ ) = 38.1 mm and the die entrance radii ( $R_d$ ) = 5 mm. The manufactured die inserts and tools are used for the free bulge test.

The free bulge test and the tensile test are conducted. STKM 11A steel tube, OD = 28.6 mm, thickness = 1.2 mm is used for this study. The new developed analytical model (SPB model) with the flow stress determination is proposed. From the free bulge test result, those die inserts with investigated internal pressure levels can form the tubes well. The tube is deformed under the biaxial stress state. Maximum bulge height ( $h_p$ ) and minimum thickness at the vertex of the bulge shape ( $t_v$ ) are 4.7 mm and 0.83 mm, approximately. On the other hand, the flattened tube workpieces in the tensile test are stretched under a uniaxial stress state. A simple approach (SPB model) to the flow stress determination is compared with the referenced methods (YingYot's model, Hwang's model and the tensile test). The flow stress data of the tube obtained from SPB model and referenced methods are specified as the material property inputs of the tube in the FEA simulation software.

Finite Element simulation models using the flow stress curves of the tube display accurate results of tube hydroformability evaluation. It is found that the internal pressure, the bulge height and the thickness distribution of the formed tube from FEA model #1 (Neckpoint\_flow stress curve obtained from SPB model) are closest to the experimental results. Thickness distributions at the vertex of the bulge shape of FEA model #1 deviate from the real hydroformed tube about 10.88 %. The bulge heights at vertex of the bulge shape of FEA model #1 deviate from the real hydroformed tube about 26.80 %. From comparison result, the best representative of the stress-strain relationship

of the hydroformed tube (STKM 11A tube) is the flow stress curve determined at the Neck Point. Finite element simulation for hydroformability evaluation of Oil Filler Pipe displays a proper bulge shape with a stable thickness distribution. Thinning is about 20 % approximately.

## 6.2 Suggestions

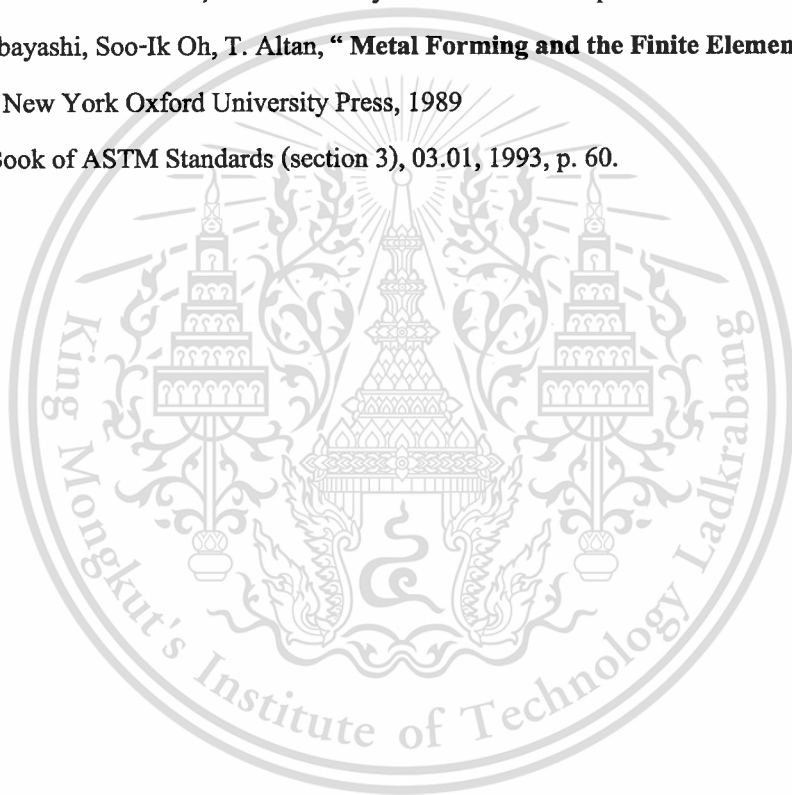
Although, the free bulge test is only conducted by using abovementioned specific tube, there are some suggestions for further studies on other material properties of the tube. The free bulge test for different material tubing should be possible as well. Die insert parameters and different forming conditions can be investigated by adjusting a few component of tooling. The optimization of the die inserts and forming pressure should be performed by considering the effects of  $R_d/t$  and  $L_b/OD$  on tube hydroformability. However, below are some suggestions for further studies in the field.

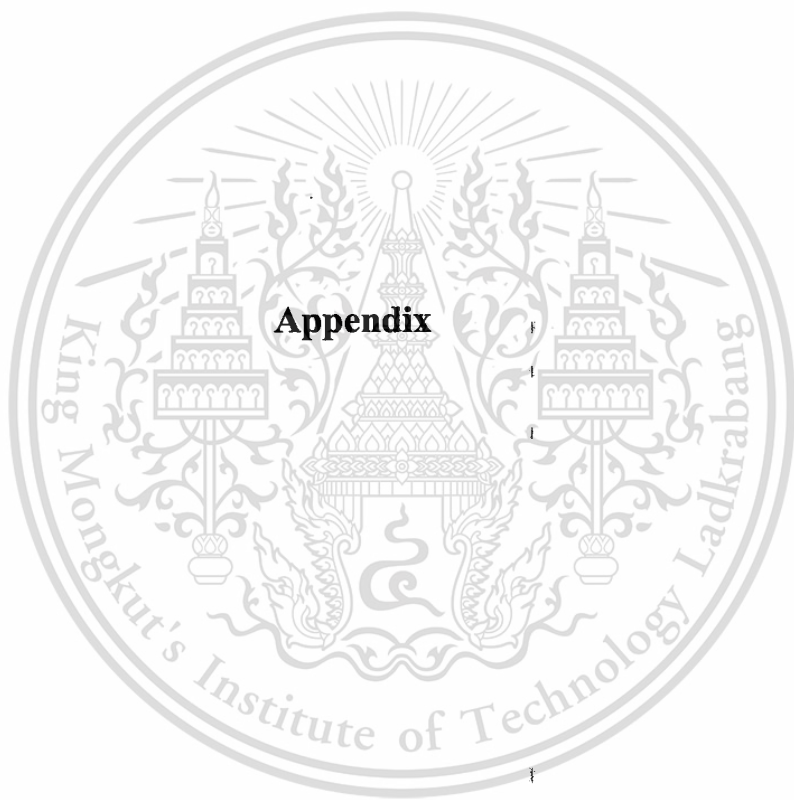
- 1) The special test for studies of mechanical property of the tube should correspond to deformation of real part forming process.
- 2) Due to high pressure nature of the test, tooling must be designed to be extra strong.
- 3) The test tube with high quality of weld line should be used for this bulge test.
- 4) The bulge test with statistical data collection should be used for flow stress determination.
- 5) The abovementioned die inserts (entrance radius ( $R_d$ ) = 5 mm, bulge length ( $L_b$ ) = 38.1 mm and outside diameter =  $29.1 \pm 0.5$  mm) may be tools suitable for the hydraulic free bulge test to study quality of STKM11A steel tube (OD = 25.4-28.6 mm, thickness = 1-1.2 mm) produced in Thailand.

## Reference

- [1] Muammer Koç, “ **Hydroforming for Advanced Manufacturing** ”, First Published, England: Woodhead Publishing Limited and CRC Press LLC. 2008
- [2] F. Dohmann, Ch. Hartl, “ **Liquid-Bulge Forming as a Flexible Production Method** ”, Journal of Materials Processing Technology, 45 (1994) 377
- [3] F. Dohmann, Ch. Hartl, “ **Hydroforming – a Method to Manufacture Light-Weight Parts** ”, Journal of Materials Processing Technology, 60 (1996) 669
- [4] Z. Marciniak, J.L. Duncan, S.J. Hu, “ **Mechanics of Sheet Metal Forming** ”, First published by Edward Arnold, London (1992), Second edition published by Butterworth Heinemann (2002)
- [5] William F. Hosford, Robert M. Caddell, “ **METAL FORMING Mechanics and Metallurgy** ”, Third Edition, First Published, Cambridge University Press, 2007
- [6] S. Fuchizawa, “ **Deformation of Metal Tubes under Hydrostatic Bulge Forming with Closed Die** ”, Advanced Technology of Plasticity, (1990) 1543
- [7] S. Fuchizawa, M. Narazaki, “ **Analysis of Bulge Deformation of Thin Tube with Cylindrical Die - Hydrostatic Tube Bulging with Closed Die I** ”, Journal of Japan Society for Technology of Plasticity, 30 (1989) 116
- [8] T. Sokolowski, K. Gerke, M. Ahmetoglu, T. Altan, “ **Evaluation of Tube Formability and Material Characteristic: Hydraulic Bulge Testing of Tubes** ”, Journal of Material Processing Technology, 2000, pp. 34-40
- [9] Muammer Koç, Yingyot Aue-u-lan, Taylan Altan, “ **On the Characteristics of Tubular Materials for Hydroforming - Experimentation and Analysis** ”, International Journal of Machine Tools & Manufacture, 41 (2001), pp. 761–772
- [10] Y.M. Hwang, Yi-Kai Lin, T. Altan, “ **Evaluation of Tubular Materials by a Hydraulic Bulge Test** ”, Journal of Machine Tools & Manufacture, 47 (2007), pp. 343-351
- [11] Y.M. Hwang, Yi-Kai Lin, “ **Analysis of Tube Bulge Forming in an Open Die Considering Anisotropic Effect of the Tubular Material** ”, Journal of Machine Tools & Manufacture 46 (2006), pp. 1921-1928

- [12] Y.M. Hwang, C.W.Wang, “ **Flow Stress Evaluation of Zinc Copper and Carbon Steel Tubes by Hydraulic Bulge Tests Considering Their Anisotropy** ”, Journal of Material Processing Technology, 6 October 2008
- [13] Yang Lianfa, Guo Cheng, “**Determination of Stress-Strain Relationship of Tubular Material with Hydraulic Bulge Test** ” , Thin-walled structure, 4 October 2007, pp.147-154
- [14] George T. Halmos, “ **Roll Forming Handbook (Manufacturing Engineering and Materials Processing; 67)** ” , Series Edition, Delta Engineering, Ontario, Canada, Published in 2006, CRC Press Taylor & Francis Group
- [15] Shiro Kobayashi, Soo-Ik Oh, T. Altan, “ **Metal Forming and the Finite Element Method** ” , New York Oxford University Press, 1989
- [16] Annual Book of ASTM Standards (section 3), 03.01, 1993, p. 60.





This material is reserved for educational use only, not allowed for commercial use.

Forbidden to modify the content, and cite the document when use.

## Appendix A

### International Publication

# 14th International ANnual Symposium on Computational Science and Engineering 2010 (ANSCSE14)

# ANSCSE14

14th International ANnual Symposium on Computational Science and Engineering  
on the occasion of the 12th anniversary of the founding of Mae Fah Luang University

**23 - 26 March 2010**

**Mae Fah Luang University, Chiang Rai, Thailand**

Organized by

**Mae Fah Luang University**

**Computational Science and Engineering Association**

Supported by

**Mae Fah Luang University**

**National Electronics and Computer Technology Center**

**NVIDIA**



**NECTEC**  
a member of NSTDA



**ANSCSE14 Mae Fah Luang University, Chiang Rai, Thailand**

This material is reserved for educational use only. It is not allowed for commercial use.

**March 23-26, 2010**

Forbidden to modify the content, and cite the document when use.

## Development of Free Bulge Test Tooling for Flow Stress Curve Determination of Tubular Materials

Perawat Boonpuek<sup>1</sup>, Suwat Jirathearanat<sup>2</sup>, Nattawut Depaiwa<sup>3</sup> and Naoto Ohtake<sup>4,c</sup>

<sup>1</sup> Graduate Student, TAIST Tokyo Tech Automotive Engineering (International Program), International College, King Mongkut's Institute of Technology Ladkrabang, Bangkok 10520, Thailand

<sup>2</sup> National Metal and Materials Technology Center,

National Science and Technology Development Agency, Bangkok, 10400, Thailand

<sup>c</sup> E-mail: K.perawat.b@gmail.com; Fax: (662) 5647001-5; Tel. 089-0789857. (662) 5647000

### ABSTRACT

This study aims to design die inserts for use in free bulge testing to determine flow stress curves of tubular materials. Hwang's Model is used to determine the suitable free bulge shape of tubular materials being tested. The results of Finite Element simulation of free bulge forming are compared with the analytical results of Hwang's Model. The results of this study show that the die inserts designed are able to perform in tubular materials testing with the free bulge shape suitable for proper flow stress curve determination. A numerical study on effects of K and n values on hydroformability of fuel filler pipe is conducted by Finite Element Software, DYNAFORM. STKM 11A carbon steel tubing is evaluated for its plastic deformation through consideration of forming limit diagram and thickness distribution. It is also shown in this study that the hydroformability of the fuel filler pipe is highly sensitive to the magnitude of K and n values. Therefore, proper determination of flow stress curves of tubular materials is of great importance.

Keywords: Tube Hydroforming, Free Bulge Test, Flow Stress Curve

### 1. INTRODUCTION

Hydroforming processes have become popular in various industries, such as bicycle, automotive, aircraft and aerospace, etc., due to increasing demands for lightweight parts, high strength and reducing welding line of parts. This technology is a relatively new manufacturing process able to form more complex shapes compared to stamping. In comparison to conventional metal forming, tube hydroforming has several advantages, such as: (1) reduction in number of workpieces, tool cost and product weight, (2) improvement of structural stability and increase of strength and stiffness of the formed parts, (3) more uniform thickness distribution, and (4) fewer secondary operations, etc. On the other hand, this technology has some disadvantages, such as long cycle time, expensive equipment and lack of effective database for tooling and process design [1-3].

Several studies concerning the axis-symmetric hydraulic bulge forming have been reported in the literature review. Yeong – Maw Hwang, Yi - Kai Lin and T. Altan [4, 5], they proposed an analytical model to evaluate the effects of die entrance radius on the internal pressure and thickness distribution of formed tubes. In their paper, assumption of an elliptical surface for the bulge profile is made. A thin wall thickness of free bulge region is approximated using a quadratic distribution. However, they did not consider the influence of  $R_d/t$  and  $L/OD$  ratios, where  $R_d$ ,  $L$ ,  $t$ ,  $OD$  are die entrance radius, bulge length, thickness and outer diameter of tubes, respectively.

This paper aims at designing proper die inserts for use in tube bulge test considering the effects of  $R_d/t$  and  $L/OD$  ratios. The FEA simulation method is used to investigate the above-mentioned parameters of the die inserts that can form the tubes in the range of proper free bulge shapes. Hwang's model is considered to determine the proper free bulge shape comparing with FEA simulation results. In addition, FEA simulation method is also used to

ANSCSE14 Mae Fah Luang University, Chiang Rai, Thailand

This material is reserved for educational use only. It is not allowed for commercial use.

March 23-26, 2010

Forbidden to modify the content, and cite the document when use.

study effects of strength coefficient (K) and strain-hardening exponent (n) on hydroformability of fuel filler pipe forming.

Nomenclature			
$D_p$	diameter of the forming tube at the pole	$\phi_e$	contact angle
K	strength coefficient	$\rho_a, \rho_\phi$	circumferential and meridian radii of curvature at any point on the tube surface
L	bulge length	$\rho_{ap}, \rho_{\phi p}$	circumferential and meridian radii of curvature at pole p
n	strain hardening exponent	$\epsilon_a, \epsilon_t$	strain at the pole in the hoop and thickness directions
$P_i$	internal pressure	$\bar{\sigma}, \bar{\epsilon}$	effective stress and effective strain
$R_0$	initial tube outer radius	$\sigma_a, \sigma_\phi$	stress in the meridian and circumferential directions
$R_d$	entrance radius of the die	$\sigma_0, \epsilon_0$	initial yield stress and initial yield strain
$R_e, Z_e$	coordinates of contact point e	$\xi$	principal strain ratio
$R_p, R_z$	half length of the minor and major axes of the elliptical tube surface	$\epsilon_1, \epsilon_2$	major strain and minor strain
$t_p$	tube thickness at pole p		

**2. ANALYTICAL MODEL**

In Hwang’s Model, the effective stress and effective strain are derived from the hydraulic bulge profile of tube and internal pressure. Assumptions of free bulge profile are as follows:

- (1) The profile of the forming tube at the free bulge shape is assumed to be of an elliptical curve as shown in Figure 1.
- (2) The two ends of the tube with a bulge length (L) are completely fixed.

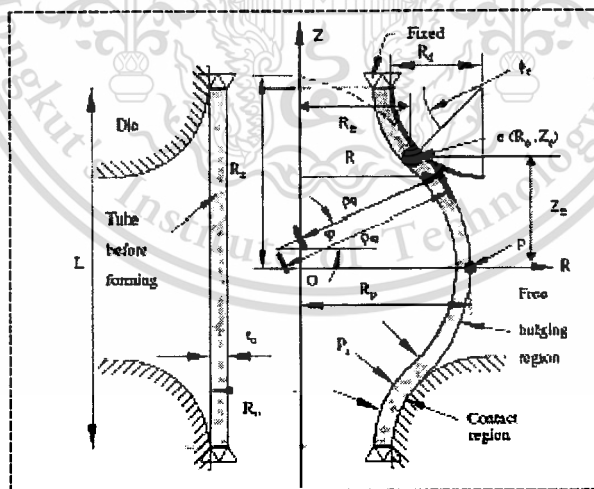


Figure 1. Schematic of tube free-bulge test [4, 5]

From the bulge model (Figure1), the coordinate of contact point e,  $R_e$  and  $Z_e$  can be calculated by Eq. (1) and Eq. (2)

$$R_e = R_0 + R_d(1 - \cos \phi_e) \tag{1}$$

$$Z_e = L/2 - R_d \sin \phi_e \tag{2}$$

where  $\phi_e$ ,  $L$ ,  $R_0$ ,  $R_d$  are the contact angle, bulge length, tube outer diameter, die entrance radius, respectively. The half length of the minor and major axes of the elliptical surface in the free bulge region,  $R_p$ ,  $R_z$  can be obtained by Eq. (3) and Eq. (4).

$$R_p = \sqrt{R_e(R_e + Z_e \tan \phi_e)} \quad (3)$$

$$R_z = \sqrt{Z_e(Z_e + R_e \cot \phi_e)} \quad (4)$$

The circumferential and meridian radii of curvature at pole  $p$  of the tube bulge shape,  $\rho_{\theta p}$  and  $\rho_{\phi p}$ , can be expressed, respectively, as follows:

$$\rho_{\theta p} = R_p \quad (5)$$

$$\rho_{\phi p} = R_z^2 / R_p \quad (6)$$

Eq. (1) – Eq. (6) are used to calculate the  $\rho_{\theta p}$  and  $\rho_{\phi p}$  in the bulge region. Finally, flow stress curve can be derived from the effective stress and effective strain in biaxial stress state of plastic deformation. The flow stress can be expressed using an exponential strain hardening as Eq. (7) [4-6].

$$\bar{\sigma} = K(\epsilon_0 + \bar{\epsilon})^n \quad (7)$$

where  $\bar{\sigma}$ ,  $\bar{\epsilon}$ ,  $K$ ,  $\epsilon_0$ ,  $n$  are the effective stress, effective strain, strength coefficient, initial strain and strain – hardening exponent, respectively,

### 3. DIE INSERT DESIGN for FREE BULGE TEST

#### 3.1 FEA with varied dimensions of die inserts

The objective of this FEA simulation for tooling design is to investigate dimensions of the die inserts ( $R_d$  and  $L$ ) that allow forming of the proper free bulge shapes. The schematic of free bulge study is shown in Figure 2.

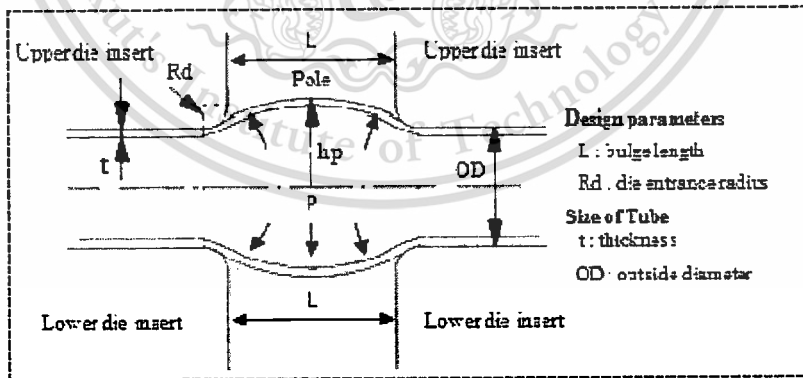


Figure 2. Schematic of free bulge test and the design parameters

From Figure 2,  $R_d$  and  $L$  values are the design parameters of interest.  $R_d$  signifies mobility of the tubes into the die cavities.  $L$  signifies a bulging ability of the tubes. These factors have effects on the thickness distributions. Dimensions of the investigated die insert for FEA simulation are defined in Table 1.  $R_d$  and  $L$  are varied to investigate the forming of the bulge shapes ranging from initial bulge to cracking.

Table 1. Parameters of finite element model

Model	Rd (mm)	t <sub>0</sub> (mm)	Rd/ t <sub>0</sub>	L (mm)	OD (mm)	L/OD
1	5	1	5	25.4	25.4	1
2	5	1	5	38.1	25.4	1.5
3	5	1	5	50.8	25.4	2
4	15	1	15	25.4	25.4	1
5	15	1	15	38.1	25.4	1.5
6	15	1	15	50.8	25.4	2
7	25	1	25	25.4	25.4	1
8	25	1	25	38.1	25.4	1.5
9	25	1	25	50.8	25.4	2

DYNAFORM is used to conduct the FEA simulations of hydro-forming processes. LS - Dyna solver is directly adopted to solve the nonlinear problems. During the simulation, two ends of the tube are fixed in the closed die inserts. For the process design, Models of die inserts are assumed to be rigid body. Plastic deformation behavior of the tube is a biaxial stress state. The material used for tube blank model is mild steel: CQ T36 (USA Standard), OD = 25.4 mm, thickness = 1 mm. Mechanical properties of tubular materials are defined as default of software. In this study, heat and temperature are neglected. A constant friction coefficient ( $\mu$ ) of 0.125 is assumed at the interface between the tube and dies. The model of the tube is meshed by shell elements at the middle surface. Element size of die mesh is maximum size = 2, minimum size = 0.5. Element size of the tube mesh is maximum size = 1, minimum size = 0.5. Feeding distance is zero (fixed). Density of Water =  $9.95e^{-7}$  kg/mm<sup>3</sup> and Bulk = 2200 GPa.

### 3.2 Results of Finite Element Simulation

All the simulation results of the free bulging are analyzed and summarized in this section. The bulge shape from each simulation is considered at the time when a crack is first predicted, Figure 3. Figure 4 shows the forming tube at various intermediate forming steps. The bulge shapes from all 9 cases are compared in Figure 5.

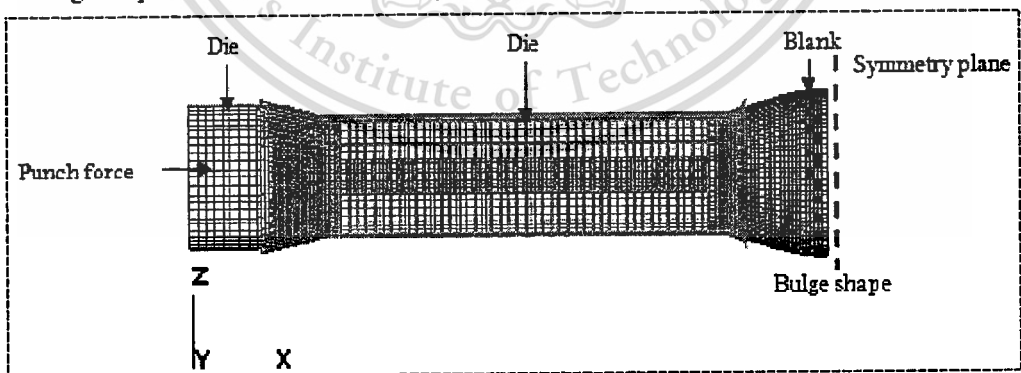


Figure 3. Half model of tube free bulging

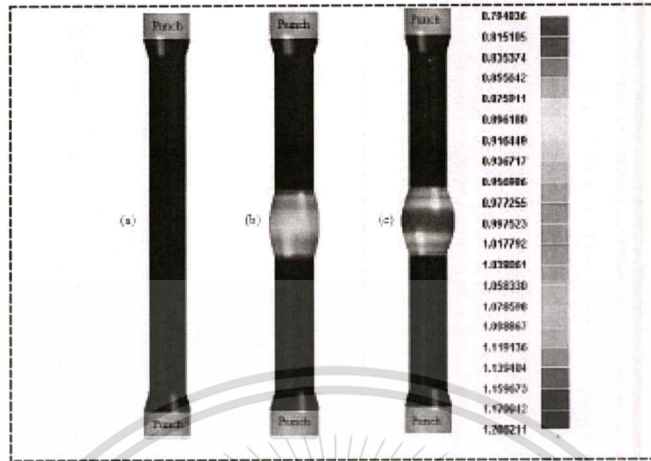


Figure 4. Intermediate forming steps with thickness distribution: (a) tube ends are fixed by punches, (b) early deformation by internal pressurization, (c) end of free bulge forming

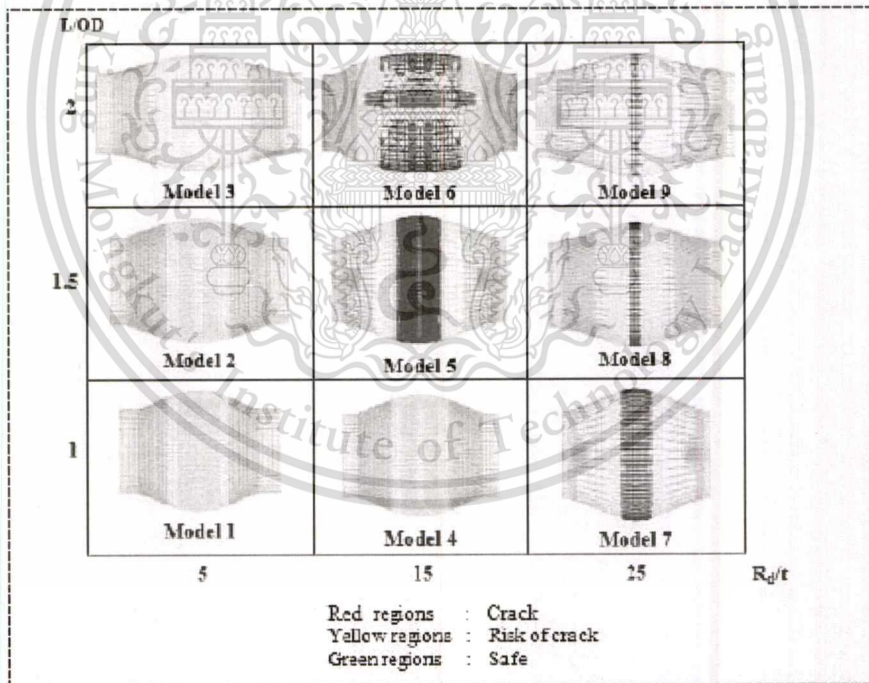


Figure 5. Comparison of predicted bulge shapes from different die insert geometry

The thickness at the pole versus bulge heights is compared for different ratios of  $R_d / t$  and  $L/OD$ , in order to determine a bulge shape suitable for flow stress curve determination of tubes, thus selecting proper tooling dimensions. The thickness versus bulge heights is plotted in Figure 6.

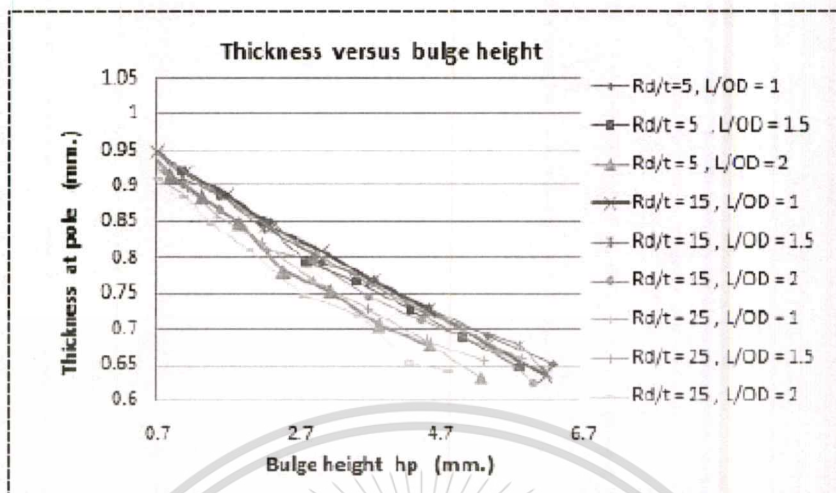


Figure 6 Bulge heights versus thickness at the pole p

From Figure 5, it can be seen that Model #3, Model #5, Model #6, Model #7, Model #8, Model #9 have improper bulge shapes because they do not resemble elliptical shape and crack too early. The 6 out of 9 models (i.e. Model #3, Model #5-Model #9) have cracked by the end of the simulation. This leads to conclude that Model #1, Model #2, Model #4 seem to be suitable for the testing as they form to be large bulges without any cracks. This is confirmed by larger wall thickness of the three models compared to the rest, Figure 6. In order to compare among the Models #1, Models #2 and Models #4, curvature of the bulges (i.e. circumferential radius and meridian radius) are compared with those calculated by Hwang's model (see Figure 7, Figure 8 and Figure 9).

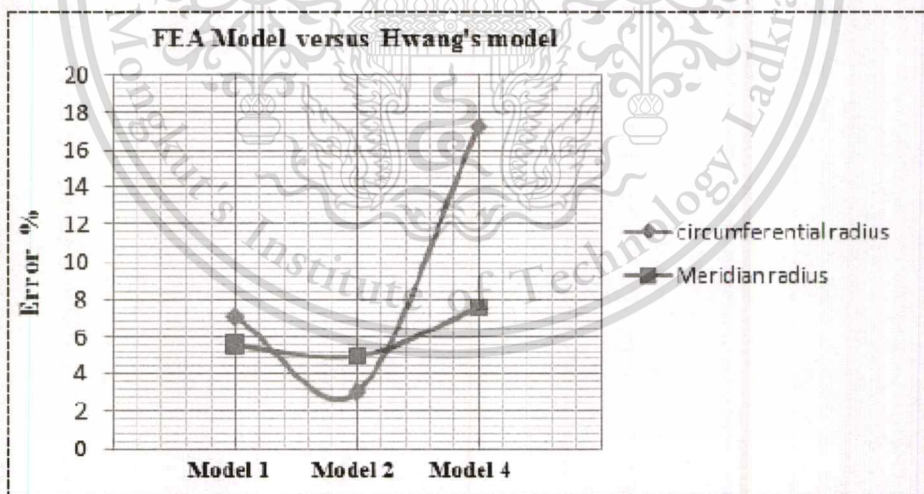


Figure 7. Deviation of simulated bulge shape curvatures from Hwang's model

Figure 7 graphs the curvature deviations of the simulated Model #1, #2, and #4 from the corresponding analytical results based on Hwang's model. Model #2 best fits Hwang's model as it shows the least curvature deviations. Figure 8 and 9 show comparisons of the simulated (i.e. from Model #2) and exact curvature (i.e. from Hwang's model). It can be seen that the bulge curvatures (i.e. both circumferential and meridian) follow Hwang's model well. Therefore, the die geometry of model #2 ( $R_d / t = 5$  and  $L/OD = 1.5$ ) seems to be the proper die geometry for flow stress curve determination experiment. Those values are then chosen for the free bulge test tooling manufacturing.

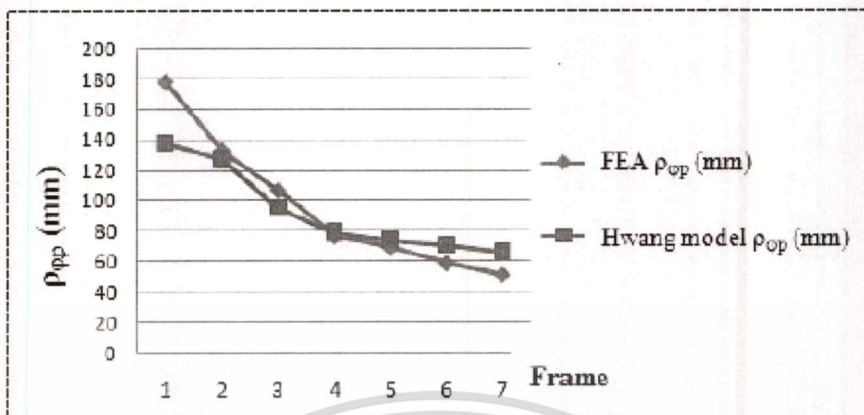


Figure 8. Meridian radius comparison between simulation results and Hwang’s model

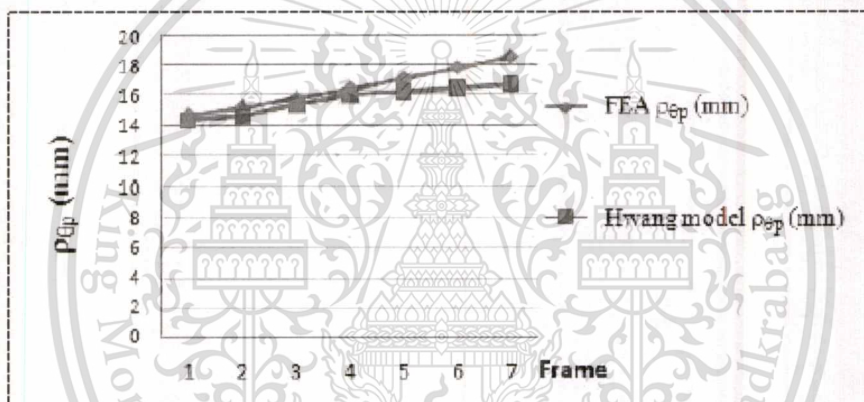


Figure 9. Circumferential radius comparison between simulation results and Hwang’s model

**4. SENSIVITY STUDY of K and n on PART HYDROFORMABILITY**

The objective of this FE simulation is to study the effects of material properties, i.e. varied strength coefficient (K) and strain-hardening exponent (n). To evaluate the effect of these material parameters on hydroformability, the hydroforming of fuel filler pipe is modeled and simulated. The material used for tube blank models is mild steel: CQ T36 (USA Standard), OD=28.6 mm, thickness = 1.2 mm. The FE simulations matrix is summarized in Table 2.

Table 2. FEA for sensitivity study of k, n

No.	Change	K (MPa)	n
1	Default	479.3	0.226
2	10 % K	527.23	0.226 Constant
3	20 % K	575.16	
4	-10 % K	431.37	
5	-20 % K	383.44	
6	10 % n	479.3 Constant	
7	20 % n		0.2486
8	-10 % n		0.2034
9	-20 % n		0.1808

Maximum feeding distance of the punch is defined as 74.4 mm. Friction coefficient ( $\mu$ ) of 0.125 is assumed. The FE model is meshed using shell elements. Element size of die is maximum size = 1 mm, minimum size = 0.5 mm. Element size of the tube is maximum size = 1 mm, minimum size = 0.5 mm. Density of Water =  $9.95e^{-7}$  kg/mm<sup>3</sup> and Bulk = 2200 GPa. FE model is shown in Figure 10.

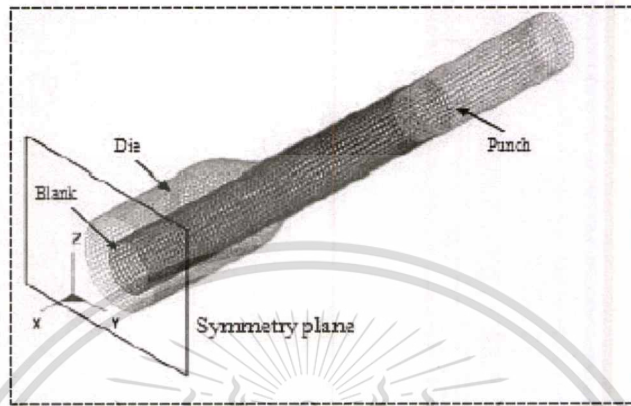
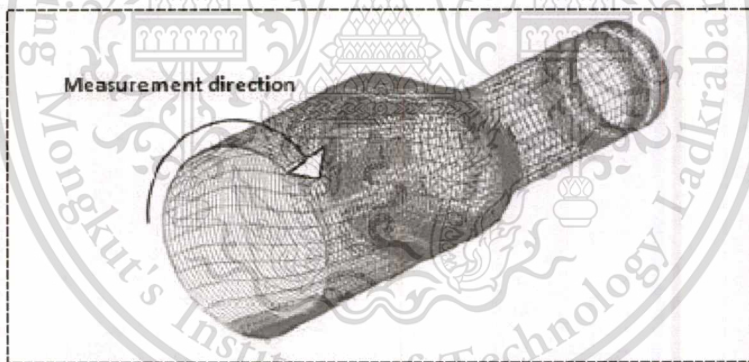
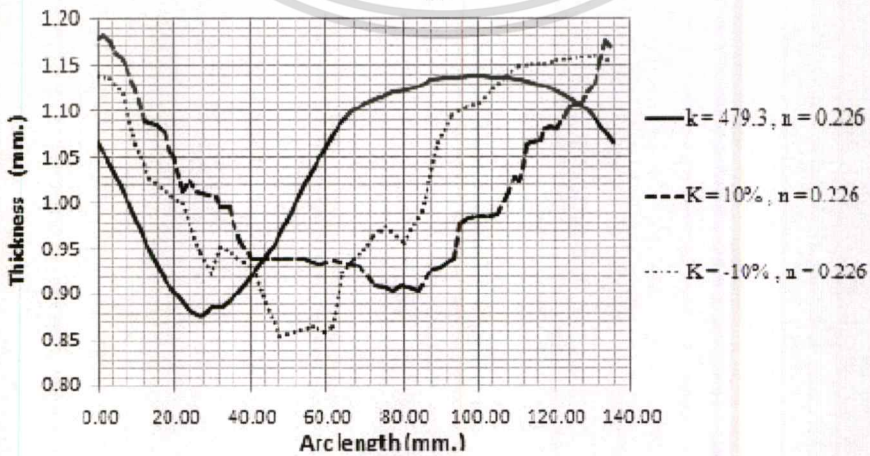


Figure 10. Half FEA mode of hydroforming of fuel filler pipe

Figure 11 shows the thickness distribution along the cutting line shown, which is obtained from some selected FE models (see table 2). Figure 12 shows the strain paths of the element at the pole from all the FE models.



(a)



(b)

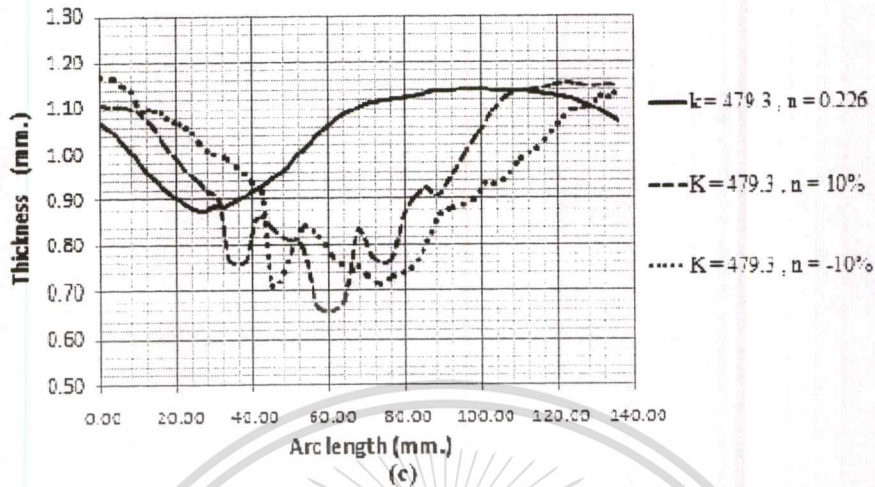


Figure 11. Thickness distribution when (a) FE model, (b) vary  $K$ ,  $n$  constant, (c) vary  $n$ ,  $K$  constant

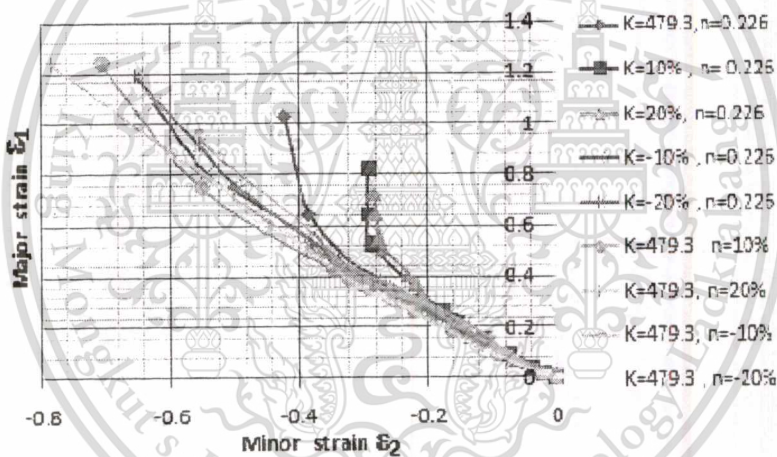


Figure 12. Forming limit diagram

From the simulation results on study of  $K$  and  $n$  effects, it is seen that the fuel filler pipe made of tubes with mechanical properties that are just varied by 10 % of the  $K$  and  $n$  values (see Table 2) have totally different distributions compared to the one with normal  $K$  and  $n$  values. Moreover, the strain paths of the element at the pole from different models seem to have drastic changes in the direction away from the one with normal  $K$  and  $n$  values. This suggests that a light change in the material parameter values (i.e.,  $K$  and  $n$ ) will significantly affect the part thickness distribution and strain paths. This seems more apparent in tube hydroforming process than stamping process.

## 5. CONCLUSION

A FEA approach for determination of proper tube free bulge tooling geometry is proposed. An analytical model for the tube profile at the free bulge region is assumed to be of an elliptical surface. Effect of die entrance radius ( $R_d$ ) and bulge length ( $L$ ) on the bulge shape are investigated by using finite element simulations. Circumferential and meridian radii obtained from FE model measurements are compared with those values calculated from Hwang's model to determine the proper die insert geometry. Finally, the die insert suitable for

free bulge test is found (i.e.,  $R_d = 5$  mm,  $L = 38.1$  mm). In the study of  $K, n$  effects, the results of finite element simulations show that the strength coefficient ( $K$ ) and strain – hardening ( $n$ ) have a pronounced effect on the thickness distributions and hydroformability of fuel filler pipe.

## REFERENCE

1. Muammer Koç, *Hydroforming for advanced Manufacturing*, First Published. England: Woodhead Publishing Limited and CRC Press LLC. 2008
2. F. Dohmann, Ch. Hartl, *Liquid-bulge-forming as a flexible production method*, Journal of Materials Processing Technology 45 (1994) 377
3. F. Dohmann, Ch. Hartl, *Hydroforming—a method to manufacture light-weight parts*. Journal of Materials Processing Technology 60 (1996) 669
4. Y.M. Hwang, Yi-Kai Lin, *Analysis of tube bulge forming in an open die considering anisotropic effect of the tubular material*, Journal of Machine Tools & Manufacture 46 (2006), p. 1921-1928
5. Y.M. Hwang, Yi-Kai Lin, T. Altan: *Evaluation of tubular materials by a hydraulic bulge test*. Journal of Machine Tools & Manufacture 47 (2007), p. 343-351
6. William F. Hosford, Robert M. Caddell, *METAL FORMING Mechanics and Metallurgy*, Third edition, first published, Cambridge University Press, The Edinburgh Building, Cambridge CB2 8RU, UK, 2007

## ACKNOWLEDGMENTS

The authors would like to extend their appreciation to the National Science and Technology Development Agency, Thailand Science Park. The advice and financial support of MTEC are greatly acknowledged. The authors would also thank TAIST Tokyo Tech Automotive Engineering (International Program) International College, King Mongkut's Institute of Technology Ladkrabang, Thailand.

## Appendix B

### Analytical Models and Data of Flow Stress of Tube

**Appendix B-1: SPB model**

**Appendix B-2: Ying Yot's model**

**Appendix B-3: Hwang's model**

**Appendix B-4: Tensile test**

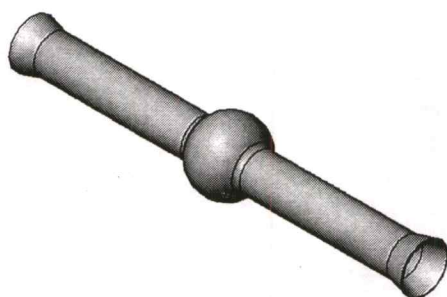
**Appendix B-5: Design of experiments**

**Appendix B-6: Data of flow stress of tube**

#### Appendix B-1: SPB model

Parameters related to expression of bulge shape geometry (**Figure B-1**) are described as follows:

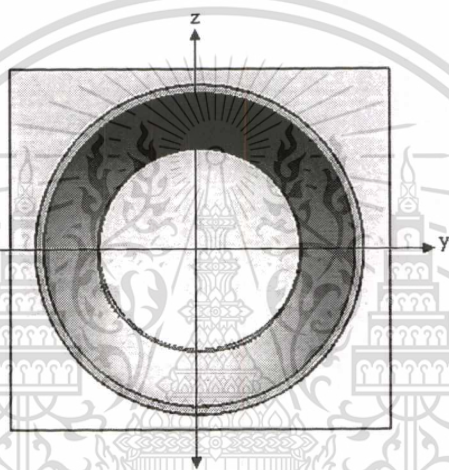
Nomenclature	
$P_i$ internal pressure	$r_e, z_e$ coordinates of contact point (e)
$L_b$ bulge length	$\rho_\theta$ circumferential radius of curvature of bulge shape
$r_o$ initial outer radius of tube	$\rho_\phi$ meridian radius of curvature of bulge shape
$R_d$ die radius	$\rho_{\theta p}$ circumferential radius of curvature of bulge shape at vertex (P)
$t_o$ initial tube thickness	$\rho_{\phi p}$ meridian radius of curvature of bulge shape at vertex (P)
$t_p$ tube thickness at vertex (p)	$\epsilon_1, \epsilon_2$ major strain and minor strain
$K$ strength coefficient of material	$\sigma_o$ initial yield stress of material
$n$ strain hardening of material	$\epsilon_o$ initial yield strain of material
$\phi$ die contact angle	$\epsilon_{\theta p}$ strain in circumferential direction at vertex (P)
$r_p$ half length of minor axes of bulge shape	$\epsilon_{t p}$ strain in thickness direction at vertex (P)
$r_x$ half length of major axes of bulge shape	$\sigma_{\theta p}$ circumferential stress at vertex (P)
$U, V$ displacement of contact point (e)	$\sigma_{\phi p}$ meridian stress at vertex (P)
$h_p$ bulge height	$\bar{\sigma}, \bar{\epsilon}$ effective stress and effective strain



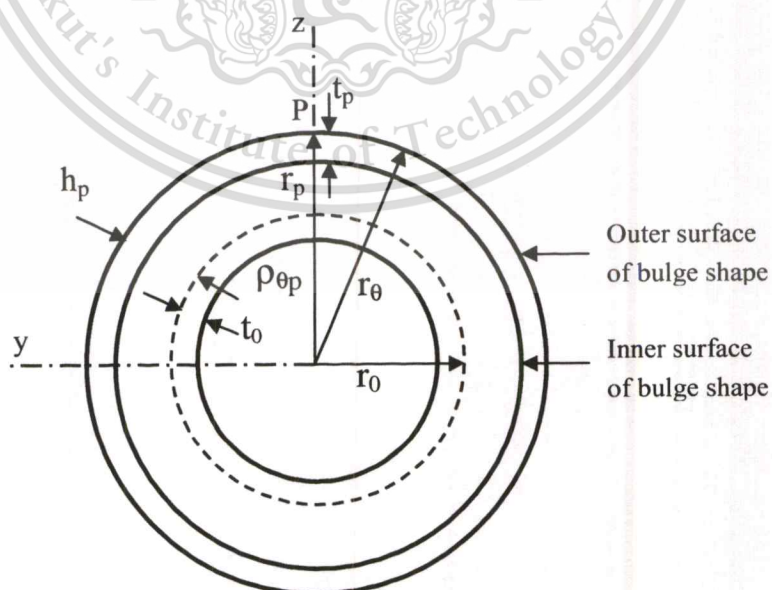
**Figure B-1** A bulge shape of a hydroformed Tube

SPB model, equation can be derived from the following sections.

**1) Cross section cut**



**Figure B-2** Cross section cut



**Figure B-3** SPB model of bulge shape in circumferential direction

**Figure B-3** illustrates tube bulge profile and parameters at vertex (P). According to bulge shape of STKM 11A tube, the junction of the major radius ( $r_x$ ) and minor radius ( $r_p$ ) are the center point of the bulge shape. By considering geometrical relationship, the circumferential strain, the meridian strain and the tube thickness at vertex (P) are postulated. The initial outer radius of the tube ( $r_0$ ) can be expressed as **Equation 1**, **Equation 2**, respectively.

$$r_0 = OD/2 \quad (1)$$

The radius of the bulge at vertex is  $r_p = OD/2 + h_p$  (2)

So, we can get the circumferential radius ( $\rho_{\theta p}$ ) of curvature at the vertex (**Equation 3**).

$$\rho_{\theta p} = r_p \quad (3)$$

The radial radius can be expressed as **Equation 4**.

$$r_{\theta} = r_p \quad (4)$$

The circumferential strain can be expressed as **Equation 5**.

$$\epsilon_{\theta p} = \ln[(r_p)/(r_0)] \quad (5)$$

From volume constancy of thin-walled structure elongating under planar tension state,

$$\epsilon_x + \epsilon_y + \epsilon_z = 0 \quad \text{or} \quad \epsilon_x = -\epsilon_y - \epsilon_z$$

where,

$$\epsilon_x = \epsilon_{\phi p}, \quad \epsilon_y = \epsilon_{tp}, \quad \epsilon_z = \epsilon_{\theta p}$$

Therefore, meridian strain can be expressed as **Equation 6**.

$$\epsilon_{\phi p} = -\epsilon_{tp} - \epsilon_{\theta p} \quad (6)$$

Then, strain in thickness direction can be expressed as **Equation 7**.

$$\epsilon_{tp} = \ln(t_p / t_0) \quad (7)$$

The tube thickness ( $t_p$ ) at the vertex (P) can be obtained from measurement during experimentation. Measuring instrument, dial caliper gauge (KASEDA F-180) is used to measure tube thickness. From von Mises yield criterion, effective strain equation is represented. Therefore, the effective strains at vertex (P) can be expressed as **Equation 8**.

$$\bar{\epsilon} = \frac{2}{\sqrt{3}} \sqrt{\epsilon_{\theta p}^2 + \epsilon_{\theta p} \epsilon_{tp} + \epsilon_{tp}^2} \quad (8)$$

2) Longitudinal section cut

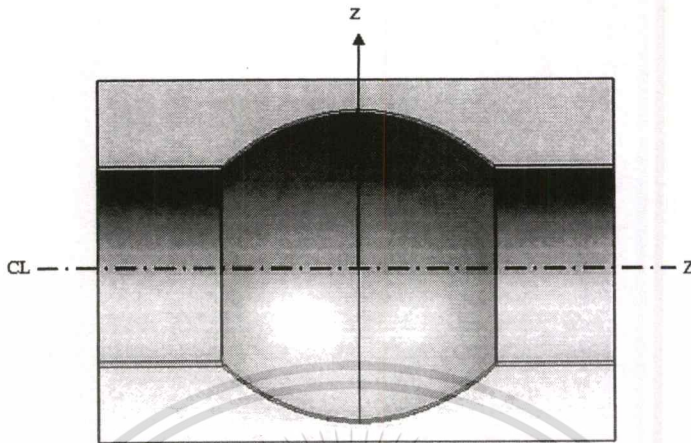


Figure B-4 Longitudinal section cut

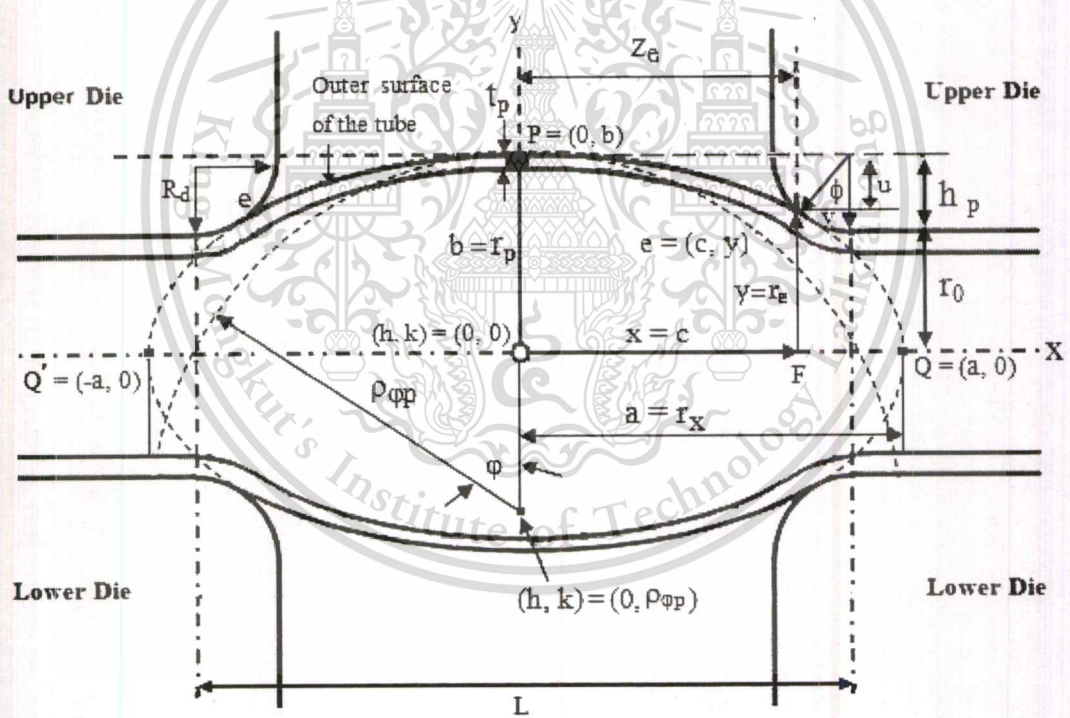


Figure B-5 SPB model of bulge shape profile in meridian plane

For Figure B-5, the contact point (e) at the outer surface (in the right hand side), we can get the contact point radius of the die (Equation 9).

$$r_e = r_0 + (h_p - U) \tag{9}$$

The bulge height ( $h_p$ ) is measured by laser sensor (optoNCDT1302) connected with Data Acquisition System (DAQ). The displacements of the contact point, V and U can be measured in CAD software. Coordinates of the contact point (e),  $z_e$  can be expressed as **Equation 10**.

$$z_e = L/2 - U \tan\phi \quad (10)$$

From the standard form of elliptic,

$$x^2/a^2 + y^2/b^2 = 1,$$

and the bulge shape geometry at point P, we can get these parameters known as follows:

$$c = x = z_e, \quad a = r_x, \quad y = r_e, \quad b = r_p$$

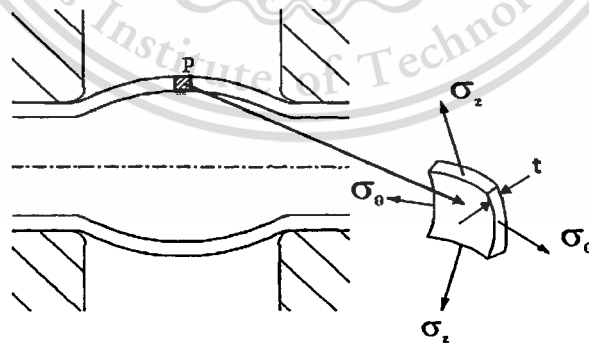
Substituting these parameters into standard form of an elliptic surface, we get **Equation 11**.

$$z_e^2/r_x^2 + r_e^2/r_p^2 = 1 \quad (11)$$

So,  $r_x$  can be expressed as **Equation 12**.

$$r_x = [(r_p^2)(z_e^2) / (r_p^2 - r_e^2)]^{1/2} \quad (12)$$

For Figure B-6, curvature of the smallest element of the thin-walled tube at the vertex (P) can be assumed as circular arc. With biaxial stress state at the vertex (P), meridian radius ( $\rho_{pp}$ ) of the bulge shape can be measured in CAD software. We can use the meridian radius ( $\rho_{pp}$ ) to calculate effective stress in the next step.



**Figure B-6** Biaxial stress state occurred on the thin-walled tube at vertex (P) of the bulge shape

The stress equations based on the theory of cylindrical pressure vessel are derived. Meridian stress and can be expressed as **Equation 13** and **Equation 14**.

$$\sigma_{\varphi p} = \frac{P_i r_{\theta}}{2t_p} \quad (13)$$

$$\sigma_{\varphi p} = \frac{P_i(\rho_{\theta p})}{2t_p} \quad (14)$$

By taking equation of equilibrium of force at the vertex (p) of the bulge shape, circumferential stress can be expressed as follows:

$$\frac{\sigma_{\varphi p}}{\rho_{\varphi p}} + \frac{\sigma_{\theta p}}{\rho_{\theta p}} = \frac{P_i}{t_p} \quad (15)$$

$$\sigma_{\theta p} = \left( \frac{P_i}{t_p} - \frac{\sigma_{\varphi p}}{\rho_{\varphi p}} \right) \rho_{\theta p} \quad (16)$$

Substituting **Equation 14** for **Equation 16**, we can get the circumferential stress (**Equation 17**),

where,  $\rho_{\theta p} = r_p$ .

$$\sigma_{\theta p} = \frac{P_i}{t_p} \rho_{\theta p} - \frac{\sigma_{\varphi p}}{\rho_{\varphi p}} \rho_{\theta p} \quad (17)$$

From von Mises criterion, effective stress can be expressed as **Equation 18**.

$$\bar{\sigma} = \sqrt{\sigma_{\theta p}^2 - \sigma_{\theta p} \sigma_{\varphi p} + \sigma_{\varphi p}^2} \quad (18)$$

Finally, relationship between the effective stress and the effective strain (flow stress curve) is expressed as **Equation 19**. Either **Equation 20** or **Equation 21** is principal expression for flow stress determination. However, these equations depend on material testing conditions.

$$\bar{\sigma} = K(\varepsilon_0 + \bar{\varepsilon})^n \quad (19)$$

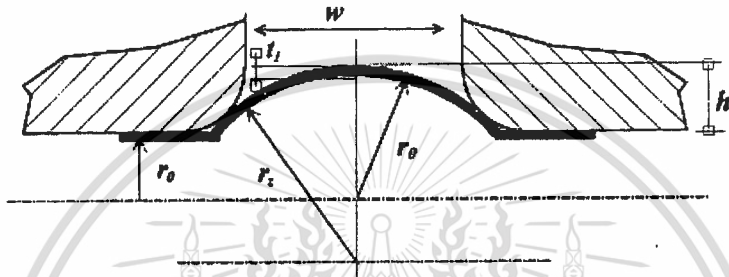
$$\bar{\sigma} = \sigma_0 + K(\bar{\varepsilon})^n \quad (20)$$

$$\bar{\sigma} = K(\bar{\varepsilon})^n \quad (21)$$

**Equation 19**, **Equation 20** and **Equation 21** are exact equations of Swift's law, Ludwik's law, Power law, respectively. If the test tubes are pre-formed by flattening process, flow stress should be expressed in forms of Ludwik's law and Swift's law. If the test tubes are not pre-formed, flow stress should be expressed in form of Power law. Therefore, this flow stress determination with the free bulge test is related to **Equation 21** only. Because we use the tube blank without preforming.

## Appendix B-2: Ying Yot's model

They assumed that the bulge shape of the formed tube is a circular shape that has the curvature at the inner surface. In each forming step, the geometry parameters of the bulge shape are measured by measuring instruments. They proposed three methods for bulge shape analysis as details in literature review section. The bulge shape model is shown in **Figure B-7**. The exact equations for axial stress and axial strain can be derived as follows:



**Figure B-7** YingYot model

The meridional radius of the curvature of the bulge shape can be expressed as **Equation 22**.

$$r_{\theta} = r_0 + h_p \quad (22)$$

The circumferential strain and the meridian strain can be expressed as **Equation 23**, **Equation 24**, respectively.

$$\epsilon_{\theta} = \ln (r_{\theta} / r_0) \quad (23)$$

$$\epsilon_z = \ln (l_1 / l_0) \quad (24)$$

The longitudinal radius (z–axial) of the bulge shape can be expressed as **Equation 25**.

$$r_z = [(W/2)^2 + h_p^2] / 2 h_p \quad (25)$$

Thickness at vertex (P) is measured by dial caliper gauge. Therefore, equation of the strain in thickness direction is expressed as **Equation 26**.

$$\epsilon_r = \epsilon_t = \ln (t_p / t_0) \quad (26)$$

From theory of thin –walled structure, volume constancy is used for axial stain calculation.

$$\epsilon_{\theta} + \epsilon_t + \epsilon_z = 0 \quad \text{or} \quad \epsilon_z = -\epsilon_{\theta} - \epsilon_t$$

The effective strain can be expressed as **Equation 27**.

$$\bar{\epsilon} = ((2/3)(\epsilon_{\theta}^2 + \epsilon_r^2 + \epsilon_z^2))^{1/2} \quad (27)$$

Substituting  $\epsilon_z = -\epsilon_{\theta} - \epsilon_r$  for **Equation 27**. We can get the effective strain equation (**Equation 28**).



$$R_e = R_0 + R_d(1 - \cos\phi_e) \quad (33)$$

$$Z_e = L/2 - R_d \sin\phi_e \quad (34)$$

$$R_p = \sqrt{R_e(R_e + Z_e \tan\phi_e)} \quad (35)$$

$$R_z = \sqrt{Z_e(Z_e + R_e \cot\phi_e)} \quad (36)$$

where,  $t_p$  is tube thickness at vertex. The circumferential strain and the meridian strain can be expressed as **Equation 37** and **Equation 38**, respectively.

$$\varepsilon_\theta = \ln \left( \frac{R_p - t_p/2}{R_0 - t_0/2} \right) \quad (37)$$

$$\varepsilon_t = \ln \left( \frac{t_p}{t_0} \right) \quad (38)$$

From theory of thin-walled structure, von Mises yield criterion and volume constancy are used.

$$\varepsilon_\theta + \varepsilon_t + \varepsilon_z = 0 \quad \text{or} \quad \varepsilon_z = -\varepsilon_\theta - \varepsilon_t$$

The effective strain can be expressed as **Equation 39**.

$$\bar{\varepsilon} = ((2/3)(\varepsilon_\theta^2 + \varepsilon_t^2 + \varepsilon_z^2))^{1/2} \quad (39)$$

Substituting  $\varepsilon_z = -\varepsilon_\theta - \varepsilon_t$  for **Equation 39**. We can get the effective strain as **Equation 40**.

$$\bar{\varepsilon} = \frac{2}{\sqrt{3}} \sqrt{\varepsilon_\theta^2 + \varepsilon_\theta \varepsilon_t + \varepsilon_t^2} \quad (40)$$

The meridian radius and the circumferential radius are expressed as **Equation 41** and **Equation 42**, respectively.

$$\rho_\theta = R_p \quad (41)$$

$$\rho_\phi = R_z^2 / R_p \quad (42)$$

The force equilibrium for shell element of the bulge shape is expressed as **Equation 43**.

$$\frac{\sigma_\phi}{\rho_\phi} + \frac{\sigma_\theta}{\rho_\theta} = \frac{P_i}{t_p} \quad (43)$$

Therefore, the meridian stress can be expressed as **Equation 44**.

$$\sigma_\phi = \frac{P_i(\rho_\theta - t_p)^2}{2t_p(\rho_\theta - t_p/2)^2} \quad (44)$$

Combining **Equation 43** with **Equation 44**, circumferential stress can be expressed as **Equation 45**.

$$\sigma_\theta = \frac{P_i(\rho_\theta - t_p)}{2t_p(\rho_\theta - t_p/2)} (2\rho_\phi - \rho_\theta - t_p) \quad (45)$$

The effective stress equation is **Equation 46**.

$$\bar{\sigma} = \sqrt{\sigma_\theta^2 - \sigma_\theta \sigma_\phi + \sigma_\phi^2} \quad (46)$$

From Swift's law, the flow stress can be expressed as **Equation 47**.

$$\bar{\sigma} = K(\bar{\varepsilon})^n \quad (47)$$

#### Appendix B-4: Tensile test

This study is related to metal forming based on true stress and true strain behaviors; these are defined as below. The true stress is expressed as **Equation 48**.

$$\sigma = \frac{P}{A} \quad (48)$$

where,  $A$  is the current cross-sectional area. The true stress can be determined from the load-extension diagram during the tensile test. Between initial yielding and the maximum load in fact plastic deformation and alloys takes place without any appreciable change in volume. The volume of the gauge section is constant, i.e.

$$A_0 l_0 = A l.$$

and the true stress is **Equation 49**.

$$\bar{\sigma} = \frac{P}{A} \frac{l}{l_0} \quad (49)$$

If the gauge length increases by a small amount,  $dl$ , a suitable definition of the strain is that the strain increment is the small amount per current length as **Equation 50**.

$$d\varepsilon = \frac{dl}{l} \quad (50)$$

For very small strains,  $l \approx l_0$ , the strain increment is very similar to the engineering strain. It does in the tensile test. The strain increment can be integrated to give the true strain as **Equation 51**.

$$\bar{\varepsilon} = \int_0^l \frac{dl}{l} = \ln \frac{l}{l_0} \quad (51)$$

For use of a pre-strain constant, although it requires the determination of three constants, Swift law is useful and will fit a material with a definite yield stress. The constant  $\varepsilon_0$  has been termed a *pre-strain* or *offset strain* constant. If the material is flattened, the effective stress-strain curve of that material can be fitted by Swift's law.

$$\bar{\sigma} = K(\varepsilon_0 + \bar{\varepsilon})^n \quad (52)$$

## Appendix B-5: Design of Experiment

### Internal pressure investigation

**Table B-1** Investigation of yielding internal pressure and bursting internal pressure

Internal forming pressure curve from Test #1(continuous forming) in plastic state of the material			
Internal pressure (MPa)	Investigated internal pressure level	Internal pressure (continuous)	Investigated internal pressure (continuous)
290.0149	Yield point	322.8660	
293.2916		323.9827	
295.0546		326.6946	
296.8735		328.1336	
298.5658		329.3884	
300.9882	P1	330.7254	P4
303.1953		331.4326	
305.0470		331.7993	
306.9465		333.0163	
307.9941		333.7103	
309.5236		334.8220	
310.0739	P2	335.7545	
311.3441		335.5868	
313.7879		336.0884	P5
314.7434		336.5488	
316.3222		337.0800	
317.8467		337.1912	
320.1607	P3	337.7791	Burst point
321.6786			

### Actual Internal forming pressure for absolute experimentation

**Table B-2** Actual internal forming pressure for experimentation

Pressure level	STKM 11A tube, OD =28.6 mm, $t_0$ =1.2 mm			
	Internal pressure (MPa)	Internal pressure (psi)	Time of test	Quantity of tube
P yield	29.00	4205.00	4	4
P1	30.00	4350.00	4	4
P2	31.00	4495.00	4	4
P3	32.00	4640.00	4	4
P4	33.00	4785.00	4	4
P5	33.60	4872.00	4	4
P burst	33.77	4896.65	4	4
Total tube				28

This material is reserved for educational use only, not allowed for commercial use.

Forbidden to modify the content, and cite the document when use.

**Table B-3** Measured parameters of the best hydroformed parts in interrupted forming process

Internal pressure level (MPa)	Thickness $t_p$ at vertex (mm)			Bulge height $h_p$ at vertex (mm)			Measured meridian radius $\rho_{\phi p}$ at vertex (mm) for SPB model		
	Neck point	Near by weld line	Opposite weld line	Neck point	Near by weld line	Opposite weld line	Neck point	Near by weld line	Opposite weld line
Pyield	1.10	1.11	1.10	0.58	0.57	0.575	289.84	289.84	289.84
P1	1.08	1.09	1.09	0.91	0.90	0.895	232.86	232.85	232.86
P2	1.05	1.04	1.04	1.16	1.15	1.130	146.09	146.19	146.26
P3	0.98	0.98	0.99	1.88	1.85	1.845	97.00	100.14	102.04
P4	0.92	0.94	0.94	2.80	2.79	2.725	73.13	76.14	78.03
P5	0.88	0.88	0.90	3.62	3.60	3.550	58.18	60.58	63.19
Pburst	0.83	0.84	0.88	4.70	4.55	4.40	45.43	49.17	59.68

**Appendix B-6: Data of flow stresses of tubes****1) SPB Model, calculated parameters for flow stress curve determination****Table B-4** Flow stress data of Neck point using parameters in **Table B-2** and **Table B-3**

$\phi_e$ (degree)	$r_x$ (mm)	$r_p = \rho_{\theta p}$ (mm)	$\epsilon_{\theta p}$	$\epsilon_{\tau p}$	$\rho_{\phi p}$ (mm)	$\sigma_{\theta p}$ (MPa)	$\sigma_{\phi p}$ (MPa)	$\bar{\epsilon}$	$\bar{\sigma}$ (MPa)
15.00	82.93	14.88	0.040	-0.05	289.84	382.34	196.21	0.055	331.16
18.00	69.17	15.21	0.060	-0.07	232.86	408.70	211.25	0.077	354.01
22.35	61.38	15.46	0.078	-0.09	146.09	432.28	228.21	0.104	374.56
41.00	47.71	16.17	0.123	-0.16	97.00	484.12	264.08	0.174	419.84
47.32	41.58	17.10	0.178	-0.23	73.13	541.65	306.68	0.242	470.45
50.14	34.08	17.92	0.226	-0.27	58.18	578.85	342.10	0.294	504.06
52.04	30.97	19.00	0.284	-0.33	45.43	611.40	386.52	0.360	535.62

**Table B-5** Flow stress data of Nearby Weldline point using parameters in **Table B-2** and **Table B-3**

$\phi_e$ (degree)	$r_x$ (mm)	$r_p = \rho_{\theta p}$ (mm)	$\epsilon_{\theta p}$	$\epsilon_{\tau p}$	$\rho_{\phi p}$ (mm)	$\sigma_{\theta p}$ (MPa)	$\sigma_{\phi p}$ (MPa)	$\bar{\epsilon}$	$\bar{\sigma}$ (MPa)
15.00	82.93	14.87	0.03	-0.04	289.84	378.53	194.24	0.04	327.85
18.00	69.17	15.20	0.06	-0.06	232.85	404.69	209.17	0.07	350.54
22.30	61.38	15.45	0.07	-0.10	146.19	436.19	230.26	0.11	377.95
40.99	47.71	16.15	0.12	-0.168	102.14	484.82	263.67	0.17	420.40
46.52	41.59	17.09	0.17	-0.210	76.14	532.77	300.07	0.22	462.62
48.91	34.12	17.90	0.22	-0.276	60.58	582.61	341.82	0.29	507.08
51.54	31.00	18.85	0.27	-0.322	49.17	612.57	378.90	0.34	535.45

**Table B-6** Flow stress data of Opposite Weldline point using parameters in **Table B-2** and **Table B-3**

$\phi_e$ (degree)	$r_x$ (mm)	$r_p = \rho_{\theta p}$ (mm)	$\epsilon_{\theta p}$	$\epsilon_{\varphi p}$	$\rho_{\varphi p}$ (mm)	$\sigma_{\theta p}$ (MPa)	$\sigma_{\varphi p}$ (MPa)	$\bar{\epsilon}$	$\bar{\sigma}$ (MPa)
15.00	82.95	14.87	0.03	-0.05	289.84	382.09	196.07	0.055	330.94
18.00	69.16	15.19	0.06	-0.07	232.85	408.31	211.04	0.077	353.67
22.30	61.35	15.43	0.07	-0.11	146.26	437.77	231.07	0.116	379.32
40.93	47.49	16.14	0.12	-0.16	102.03	483.01	262.25	0.169	418.81
46.32	40.13	17.02	0.17	-0.21	78.03	532.48	298.84	0.225	462.29
48.14	32.92	17.85	0.22	-0.25	63.19	572.28	333.20	0.276	497.84
50.14	29.95	18.70	0.26	-0.27	59.68	605.20	358.80	0.314	527.12

## 2) Ying Yot's Model (Step forming)

Calculated parameters for flow stress curve determination

**Table B-7** Flow stress data of Neck point using parameters in **Table B-2** and **Table B-3**

$r_{\theta} = \rho_{\theta p}$ (mm)	$\epsilon_{\theta p}$	$\epsilon_{\varphi p}$	$r_z = \rho_{\varphi p}$ (mm)	$\sigma_{\theta p}$ (MPa)	$\sigma_{z p}$ (MPa)	$\bar{\epsilon}$	$\bar{\sigma}$ (MPa)
14.89	0.04	-0.05	310.46	383.01	196.21	0.05	331.73
15.21	0.0	-0.07	199.85	406.42	211.25	0.07	352.06
15.46	0.07	-0.09	157.00	433.96	228.21	0.10	375.99
16.18	0.12	-0.16	97.71	484.44	264.08	0.17	420.11
17.10	0.17	-0.23	66.20	534.15	306.68	0.24	464.28
17.92	0.22	-0.27	51.93	566.17	342.10	0.29	493.86
19.00	0.28	-0.33	40.95	593.73	386.52	0.36	521.94

**Table B-8** Flow stress data of Nearby Weldline point using parameters in **Table B-2** and **Table B-3**

$r_{\theta} = \rho_{\theta p}$ (mm)	$\epsilon_{\theta p}$	$\epsilon_{\varphi p}$	$r_z = \rho_{\varphi p}$ (mm)	$\sigma_{\theta p}$ (MPa)	$\sigma_{z p}$ (MPa)	$\bar{\epsilon}$	$\bar{\sigma}$ (MPa)
14.87	0.03	-0.04	318.62	379.43	194.24	0.04	328.62
15.20	0.06	-0.06	202.06	402.61	209.17	0.07	348.76
15.45	0.07	-0.10	158.35	438.06	230.26	0.11	379.54
16.15	0.12	-0.16	99.00	484.33	263.67	0.17	419.99
17.10	0.17	-0.21	66.31	522.79	300.07	0.22	454.40
17.91	0.22	-0.27	52.13	566.25	341.82	0.29	493.88
18.85	0.27	-0.32	42.15	588.38	378.90	0.34	516.54

**Table B-9** Flow stress data of Opposite Weldline using parameters in **Table B-2** and **Table B-3**

$r_{\theta} = \rho_{\theta p}$ (mm)	$\epsilon_{\theta p}$	$\epsilon_{tp}$	$r_z = \rho_{\phi p}$ (mm)	$\sigma_{\theta p}$ (MPa)	$\sigma_{z p}$ (MPa)	$\bar{\epsilon}$	$\bar{\sigma}$ (MPa)
14.88	0.03	-0.05	315.85	382.92	196.07	0.05	331.65
15.20	0.06	-0.07	203.18	406.30	211.04	0.07	351.95
15.43	0.07	-0.11	161.14	440.02	231.07	0.11	381.23
16.15	0.12	-0.16	99.27	481.85	262.25	0.16	417.84
17.03	0.17	-0.21	67.95	522.81	298.84	0.22	454.31
17.85	0.22	-0.25	52.88	553.94	333.20	0.27	483.01
18.70	0.26	-0.27	43.43	563.15	358.80	0.31	493.77

### 3) Hwang's Model, calculated parameters for flow stress curve determination

**Table B-10** Flow stress data of Neck point using parameters in **Table B-2** and **Table B-3**

$\phi_e$ (degree)	Rz (mm)	$R_p = \rho_{\theta p}$ (mm)	$\epsilon_{\theta p}$	$\epsilon_{tp}$	$\rho_{\phi p}$ (mm)	$\sigma_{\theta p}$ (MPa)	$\sigma_{\phi p}$ (MPa)	$\bar{\epsilon}$	$\bar{\sigma}$ (MPa)
1.30	125.16	14.57	0.02	-0.05	1075.17	352.71	12.16	0.05	346.79
2.15	98.31	14.74	0.03	-0.07	655.54	375.29	12.85	0.07	369.03
3.96	73.92	15.10	0.06	-0.09	361.70	406.41	13.71	0.10	399.73
15.00	41.80	17.25	0.20	-0.16	101.29	485.82	15.38	0.21	478.31
21.81	36.13	18.57	0.27	-0.23	70.31	549.01	17.03	0.29	540.70
30.36	31.84	20.33	0.37	-0.27	49.88	589.99	18.25	0.38	581.08
35.61	29.94	21.50	0.43	-0.33	41.70	622.16	19.55	0.45	612.62

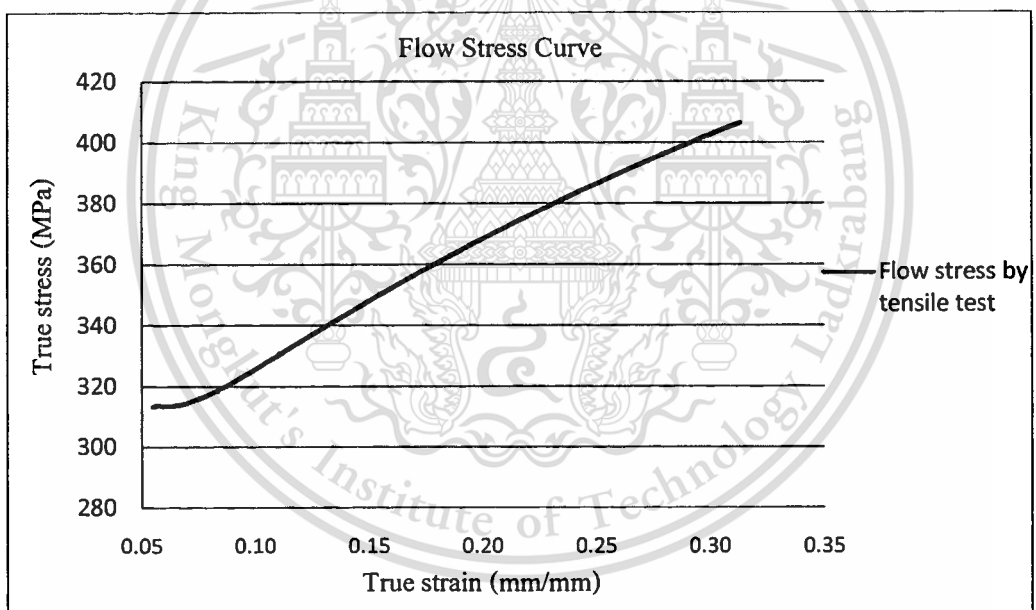
**Table B-11** Flow stress data of Nearby Weldline point using parameters in **Table B-2** and **Table B-3**

$\phi_e$ (degree)	Rz (mm)	$R_p = \rho_{\theta p}$ (mm)	$\epsilon_{\theta p}$	$\epsilon_{tp}$	$\rho_{\phi p}$ (mm)	$\sigma_{\theta p}$ (MPa)	$\sigma_{\phi p}$ (MPa)	$\bar{\epsilon}$	$\bar{\sigma}$ (MPa)
1.30	125.16	14.57	0.02	-0.04	1075.17	349.27	12.04	0.04	343.41
2.15	98.31	14.74	0.03	-0.06	655.54	371.57	12.72	0.06	365.38
3.36	79.73	14.98	0.05	-0.10	424.11	408.44	13.85	0.10	401.69
14.89	41.92	17.22	0.19	-0.16	102.01	485.56	15.38	0.21	478.05
20.51	37.00	18.31	0.26	-0.21	74.74	534.81	16.64	0.27	526.68
29.86	32.05	20.22	0.36	-0.27	50.79	590.26	18.25	0.38	581.34
34.32	30.37	21.20	0.41	-0.32	43.51	617.38	19.29	0.43	607.96

**Table B-12** Flow stress data of Opposite-eldline point using parameters in **Table B-2** and **TableB-3**

$\phi_e$ (degree)	Rz (mm)	$R_p = \rho_{\theta p}$ (mm)	$\epsilon_{\theta p}$	$\epsilon_{\eta p}$	$\rho_{\phi p}$ (mm)	$\sigma_{\theta p}$ (MPa)	$\sigma_{\phi p}$ (MPa)	$\bar{\epsilon}$	$\bar{\sigma}$ (MPa)
1.30	125.16	14.57	0.02	-0.05	1075.17	352.71	12.16	0.05	346.79
2.15	98.31	14.74	0.03	-0.07	655.54	375.29	12.85	0.07	369.03
3.26	80.85	14.96	0.05	-0.11	436.74	410.19	13.92	0.11	403.41
14.78	42.04	17.20	0.19	-0.16	102.74	482.69	15.30	0.21	475.23
20.22	37.20	18.26	0.25	-0.21	75.80	534.34	16.63	0.27	526.22
29.36	32.25	20.11	0.36	-0.25	51.72	576.70	17.82	0.37	568.00
34.15	30.43	21.17	0.41	-0.27	43.76	588.40	18.38	0.42	579.42

4) Tensile test, flow stress curve obtained from tube – flattened tensile test



Strength coefficient (K) = 485.87 MPa

Strain- hardening exponent (n) = 0.172

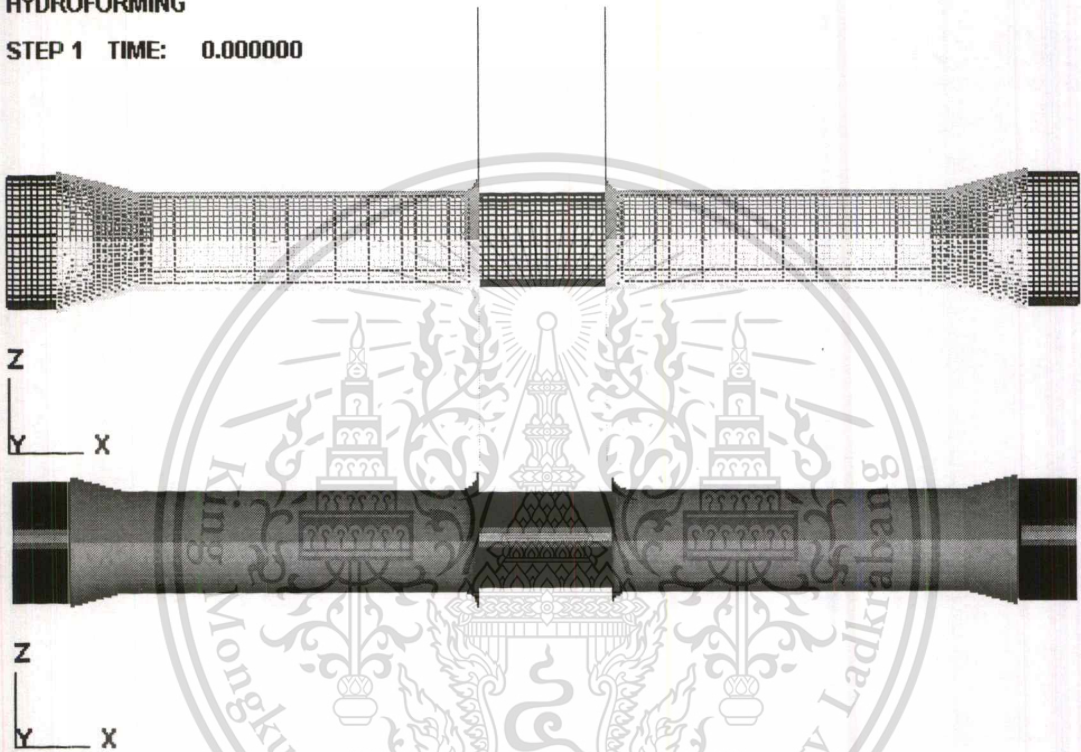
## Appendix C

### Finite Element Simulation

#### Finite Element Simulation Methods

##### HYDROFORMING

STEP 1 TIME: 0.000000



Mesh structure of the tubular material = shell element, middle surface

Mesh size of the tubular material:

- Element size of the die = 2 mm, minimum size = 0.5 mm
- Element size of the tube = 1 mm, minimum size = 0.5 mm

Time step size DT2MS =  $-4 \times 10^{-8} \text{ s}^{-1}$

Frame versus time = 16 Level

Pressure control circle = 200

Fluid pressurization: Density of Water =  $9.95 \times 10^{-7} \text{ kg/mm}^3$  and Bulk = 2200 GPa.

Two side ends of tube are fixed by axial punches.

Static friction coefficient ( $\mu$ ) = 0.125

Heat and temperature = 0

This material is reserved for educational use only, not allowed for commercial use.

Forbidden to modify the content, and cite the document when use.

## Forming pressure versus time

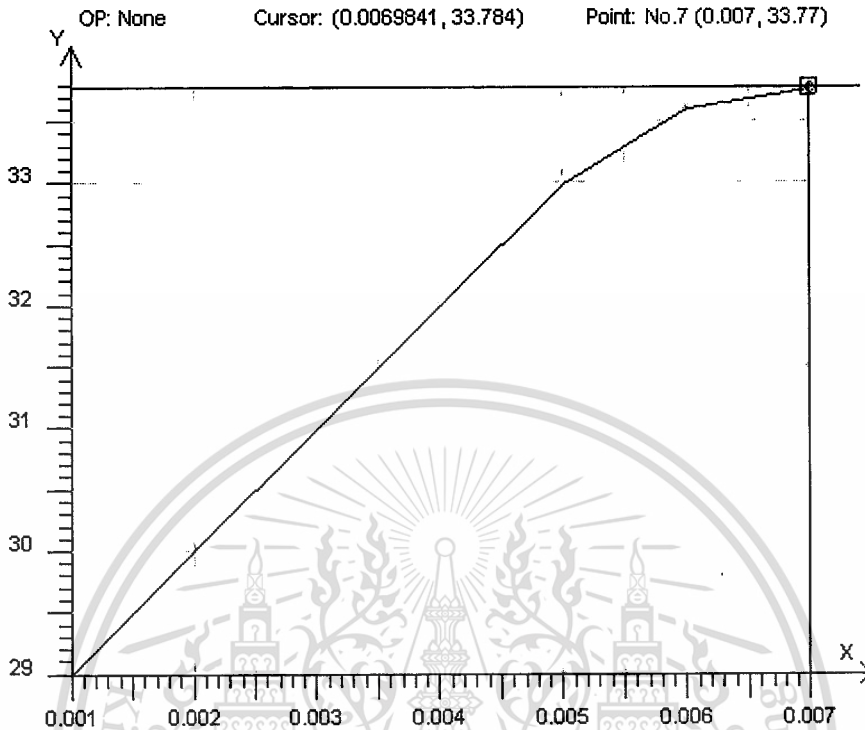


Table C-1 Input data for FE simulation of tube hydroformability evaluation

FEA Model	Material : STKM 11A Steel										
	Mesh type	Obtained data of material properties from analytical models							$\bar{\epsilon}$	$\bar{\sigma}$	Poison ratio
		K	n	Anisotropy							
				R0	R45	R90					
#1 SPB Model	Square	687.48	0.259	1	1	1	input	input	0.28		
#2 SPB Model	Square	659.41	0.244	1	1	1	input	input	0.28		
#3 SPB Model	Square	744.52	0.266	1	1	1	input	input	0.28		
#4 YingYot's Model	Square	680.76	0.251	1	1	1	input	input	0.28		
#5 YingYot's Model	Square	646.21	0.231	1	1	1	input	input	0.28		
#6 YingYot's Model	Square	728.32	0.250	1	1	1	input	input	0.28		

This material is reserved for educational use only, not allowed for commercial use.

Forbidden to modify the content, and cite the document when use.

#7 Hwang's Model	Square	697.33	0.266	1	1	1	input	input	0.28
#8 Hwang's Model	Square	644.70	0.235	1	1	1	input	input	0.28
#9 Hwang's Model	Square	728.32	0.250	1	1	1	input	input	0.28
#10 Tensile test	Square	485.87	0.172	1	1	1	input	input	0.28

**Table C-2** FE simulation for study of anisotropic material effects

FEA Model	FE simulation using NeckPoint flow stresses curves obtained from SPB model							
	Mesh type	Material Properties					Varied anisotropy values	
		K	n	$\bar{\sigma} - \bar{\epsilon}$ curve (Flow stress curve)	R0	R45	R90	
Model #1 (Default of FEA software)	Square	687.48	0.259	Default (Material type T36 SPCC, JIS standard)	1.13	0.95	1.35	
Model #2 anisotropy values R = -0.5	Square	687.48	0.259	Neckpoint_Flow stress determined by SPB model	0.63	0.45	0.85	
Model #3 anisotropy value R = +0.5	Square	687.48	0.259	Neckpoint_Flow stress determined by SPB model	1.63	1.45	1.85	
Model #4 anisotropy value R= +1.74 obtained from tensile test	Square	687.48	0.259	Neckpoint_Flow stress determined by SPB model	2.87	1.69	2.09	

## Appendix D

### Data of Die Design and Tooling Drafts

**Appendix D-1: Data of die designs**

**Appendix D-2: Drafts of die inserts**

**Appendix D-3: Drafts of die bases**

**Appendix D-4: Drafts of axial punches**

**Appendix D-5: Drafts of punch adaptors**

#### Appendix D-1: Data of die designs

**Table D-1** Parameters of FEA model for the die insert design

Model	R <sub>d</sub> (mm)	t <sub>o</sub> (mm)	R <sub>d</sub> / t <sub>o</sub>	L (mm)	OD (mm)	L/OD
1	5	1	5	25.4	25.4	1
2	5	1	5	38.1	25.4	1.5
3	5	1	5	50.8	25.4	2
4	15	1	15	25.4	25.4	1
5	15	1	15	38.1	25.4	1.5
6	15	1	15	50.8	25.4	2
7	25	1	25	25.4	25.4	1
8	25	1	25	38.1	25.4	1.5
9	25	1	25	50.8	25.4	2

**Table D-2** Meridian radius ( $\rho_{\phi P}$ ) and circumferential radius ( $\rho_{\theta P}$ ) of curvature of the bulge shapes from FEA models compared with Hwang's model

Model	Model 1		Model 2		Model 4		
Error %	$\rho_{\phi P}$	$\rho_{\theta P}$	$\rho_{\phi P}$	$\rho_{\theta P}$	$\rho_{\phi P}$	$\rho_{\theta P}$	
		26.5141	1.2233	22.7270	1.9034	25.8815	2.3243
		4.9400	3.8930	4.3908	4.2764	-5.6628	5.5311
		-11.6170	6.2026	10.5424	2.9059	-19.2112	7.2846
		-16.4280	6.8048	-3.7040	2.5949	-30.0628	8.8798
		-18.0560	6.9650	-8.4336	5.1677	-25.1956	8.4078
		-14.2580	6.1501	-20.2715	7.7278	-28.9720	9.5395
	-20.4220	7.6068	-30.3862	10.0000	-37.2850	10.7763	
Sim. frame	7.05	5.5494	3.05	4.9394	17.21	7.5348	

**Table D-3** FEA results of Model#2 ( $L/OD = 1.5$  and  $R_d/t = 1$ ) compared with Hwang's model

Sim. frame	P (MPa)	$R_d$ (mm)	$R_0$ (mm)	hp (mm) Simulation	hp (mm) Hwang model	Thickness at vertex ( $t_p$ )	$R_p$ (mm) Simulation	$R_p$ (mm) Hwang model
1 to 6	0	5	-	-	-	-	-	-
7	2	5	12.2	-	-	-	-	-
8	8	5	12.2	-	-	-	-	-
9	19	5	12.2	-	-	-	-	-
10	26	5	12.2	1.5784	-	0.8874	14.6658	14.3867
11	30	5	12.2	2.1712	-	0.8491	15.2204	14.5695
12	32	5	12.2	2.8277	2.4658	0.8086	15.8364	15.3762
13	33	5	12.2	3.5096	3.0204	0.7688	16.4785	16.0509
14	33	5	12.2	4.2633	3.6364	0.7270	17.1904	16.3020
15	33	5	12.2	5.0252	4.2785	0.6870	17.9123	16.5280
16	32	5	12.2	5.8144	4.9904	0.6469	18.6613	16.7952

**Table D-3** Cont.

Sim. frame	Contact angle ( $\theta$ )	$L = L/2$ (mm)	$R_e$ (mm) Simulation	$R_e$ (mm) Hwang model	$Z_e$ (mm) Simulation	$Z_e$ (mm) Hwang model	$R_z$ (mm) Simulation
1 to 6	-	-	-	-	-	-	-
7	0	24.05	-	-	-	-	-
8	0	24.05	-	-	-	-	-
9	0	24.05	-	-	-	-	-
10	11.13	24.05	12.30	12.2940	23.06	23.0848	51.05
11	12.10	24.05	12.32	12.3110	22.9	23.0019	44.96
12	16.39	24.05	12.40	12.4031	22.63	22.6391	41.10
13	19.95	24.05	12.51	12.5000	22.32	22.3440	35.44
14	21.26	24.05	12.54	12.5402	22.23	22.2370	34.32
15	22.43	24.05	12.58	12.5782	22.13	22.1422	32.40
16	23.80	24.05	12.62	12.6252	22.04	22.0322	30.84

**Table D-3** Cont.

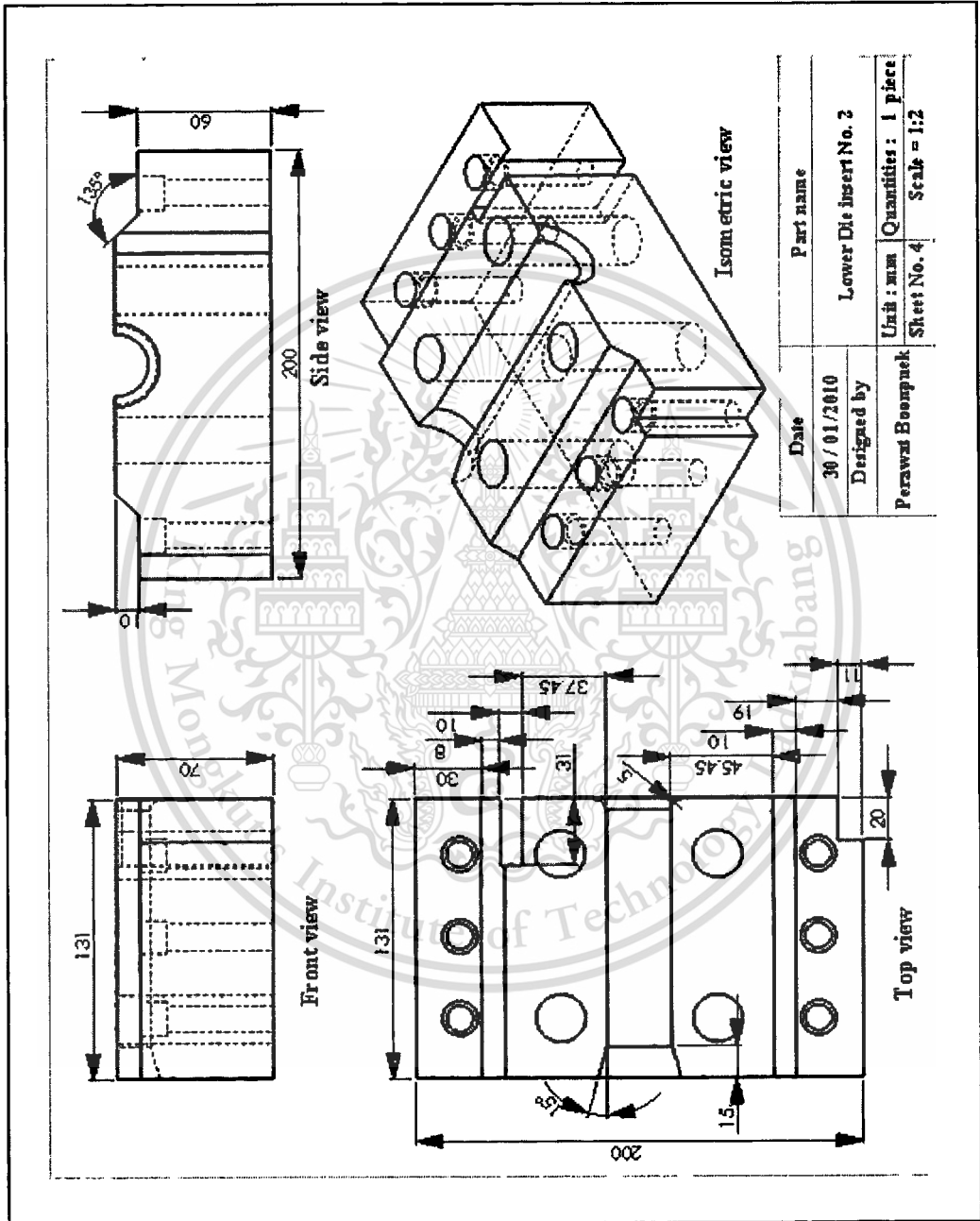
Sim. frame	$R_z$ (mm) Hwang model	$\rho_{\phi P}$ (mm) Simulation	$\rho_{\phi P}$ (mm) Hwang model	Error %	$\rho_{\phi P}$ (mm) Simulation	$\rho_{\phi P}$ (mm) Hwang model	Error%
1 to 9	-	-	-	-	-	-	-
10	44.4463	177.6982	137.3126	22.7270	14.6658	14.3867	1.9034
11	43.0115	132.8086	126.9772	4.3908	15.2204	14.5695	4.2764
12	38.3042	106.6660	95.4207	10.5424	15.8364	15.3762	2.9059

This material is reserved for educational use only, not allowed for commercial use.

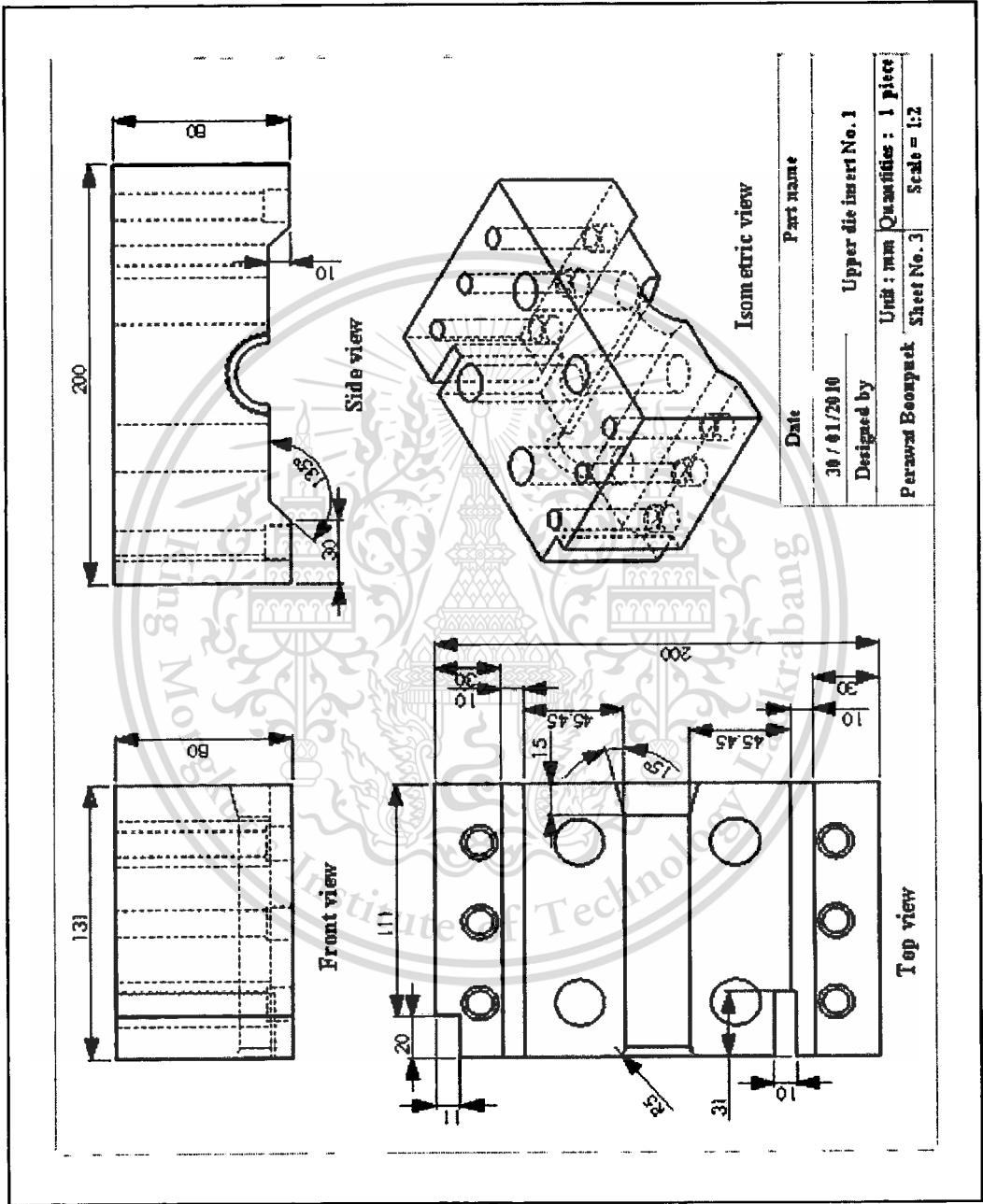
Forbidden to modify the content, and cite the document when use.



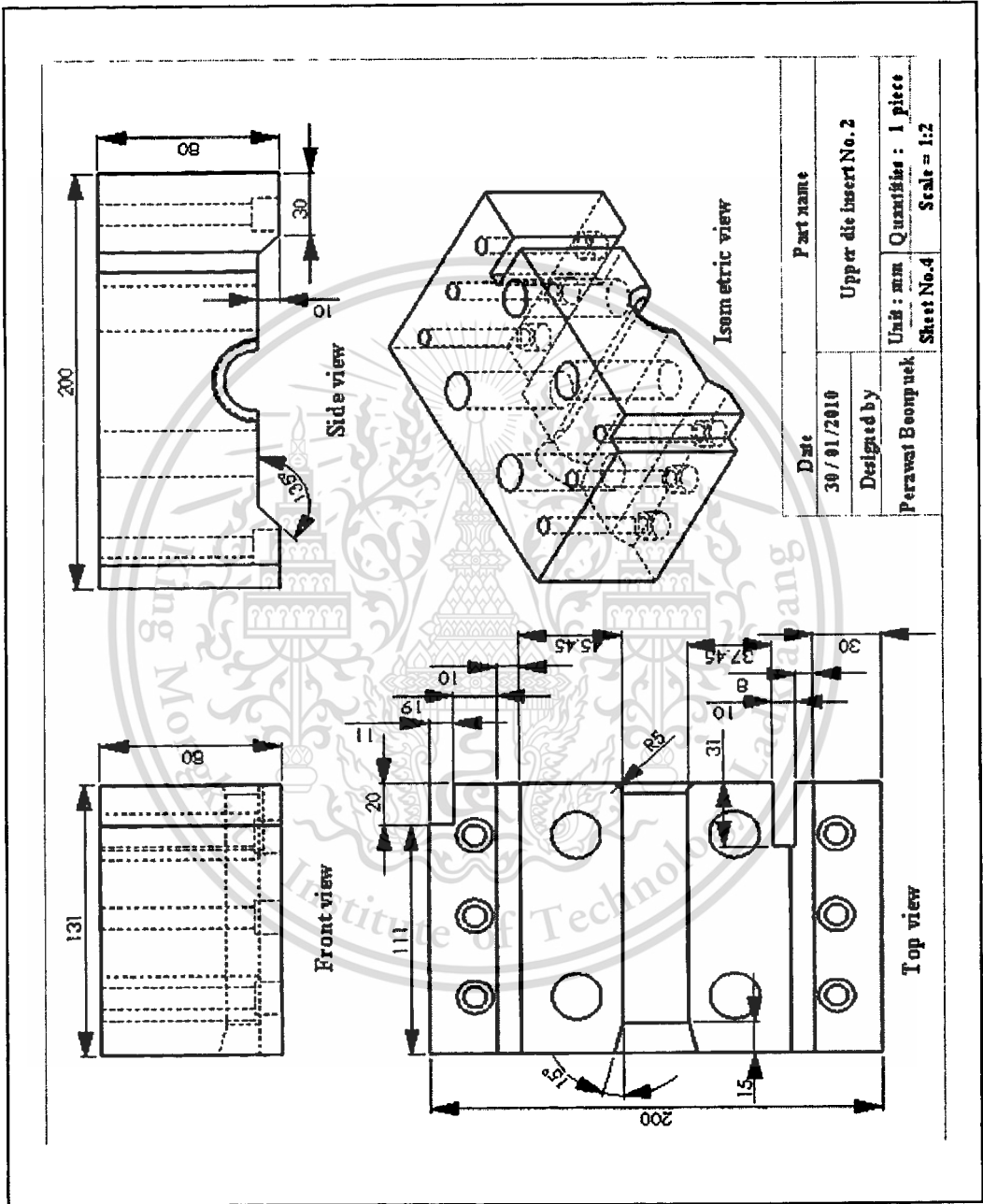
Lower Die Insert No. 2



Upper Die Insert No. 1

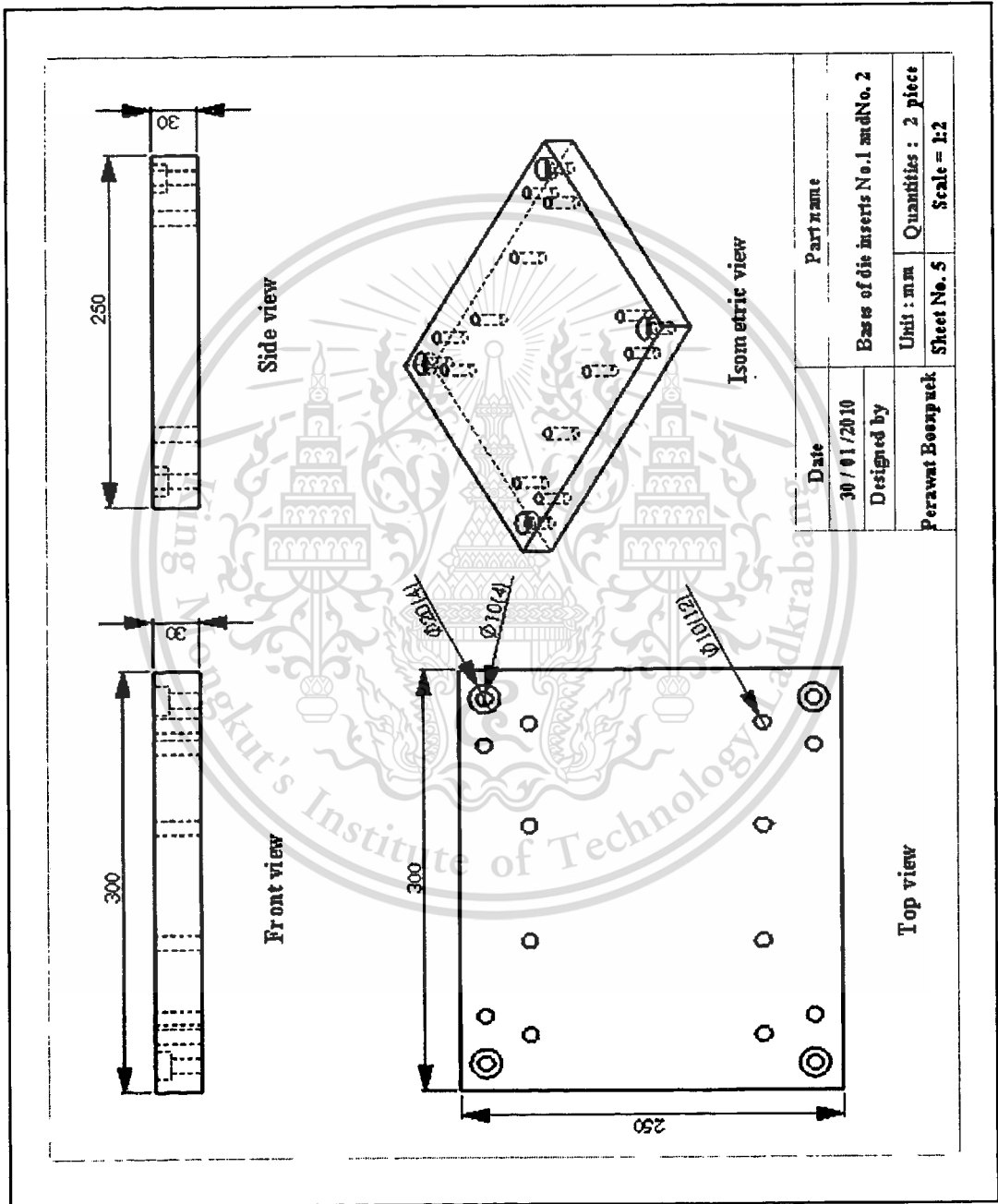


Upper Die Insert No. 2



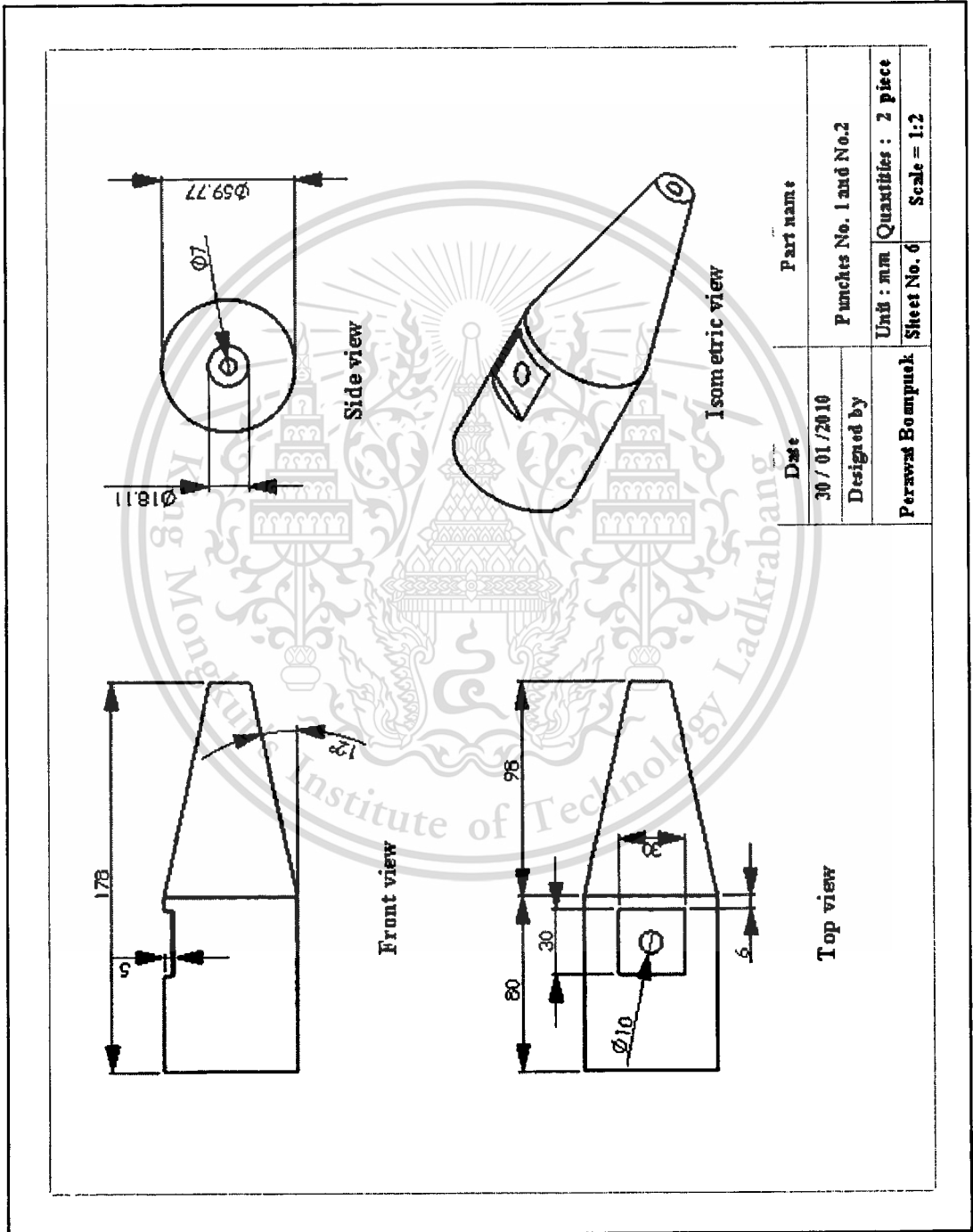
**Appendix D-3: Drafts of die bases**

Upper die base and Lower die base



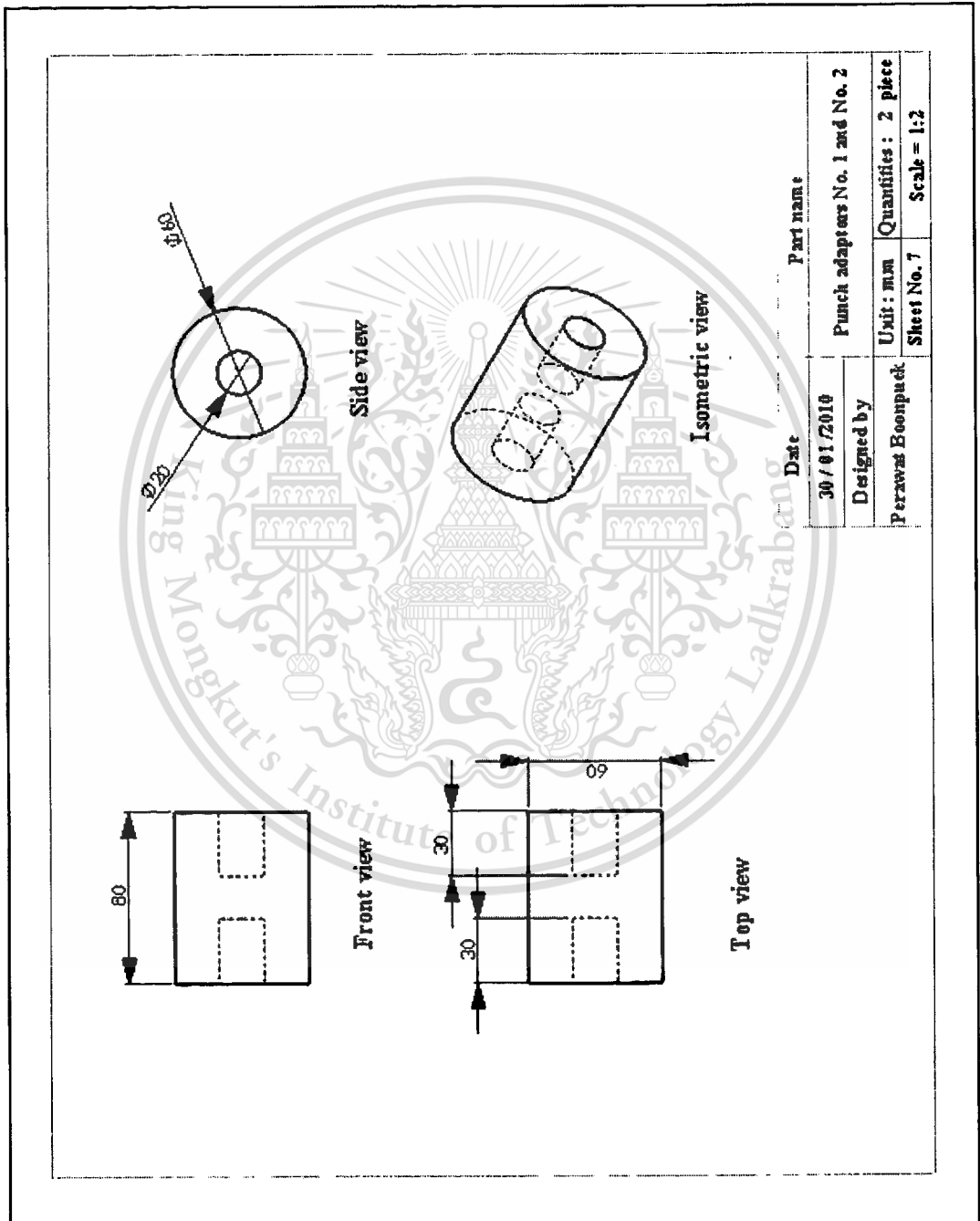
**Appendix D-4: Drafts of axial punches**

Axial punches in the right and left hand side



**Appendix D-5: Drafts of punch adaptors**

Punch adaptors in the right and left hand side



## Author Biography

Name: Perawat  
 Surname: BOONPUEK  
 Gender: Male  
 Date of birth: March 27, 1986  
 Place of birth: Kalasin Province, Thailand  
 Nationality: Thai

### Educations:

1999 - 2004 High school, Samchai school, Kalasin Province, Thailand  
 2004 - 2008 B.Eng. (Mechanical Engineering)  
 Department of Mechanical and Manufacturing Engineering,  
 Faculty of Science and Engineering, Kasetsart University  
 2008 - 2011 M. Eng. (Automotive Engineering), International Program,  
 International College, King Mongkut's Institute of Technology Ladkrabang

### Work experiences:

2010 - 2011 Thai Samsung Electronics Co., Ltd.  
 Design Engineer, Microwave Plant, 24" Electric Oven Team  
 Sahaphat Group Industrial Estate, Chonburi, Thailand

### Publications:

Perawat Boonpuek , Suwat Jirathearnat , Nattawoot Depaiwa and Naoto Ohtake,  
 and Naoto Ohtake, “ **Development of Free Bulge Test Tooling for Flow Stress  
 Curve Determination of Tubular Materials**”, Proceedings of 14th International  
 Annual Symposium on Computational Science and Engineering 2010  
 (ANSCSE14), Mae Fah Luang University, Chiang Rai, Thailand,  
 March 23-26, 2010, pp. 779 - 788